



SCUOLA DI DOTTORATO
UNIVERSITÀ DEGLI STUDI DI MILANO-BICOCCA

Department of Biotechnology and Biosciences

PhD program in Converging Technologies for Biomolecular Systems
Cycle: XXXVI

New approach methodologies-oriented toxicology in *in vitro* systems for implementing the safety-by-design of new nanomaterials

Surname: Motta

Name: Giulia

Registration number: 753117

Tutor: Prof. Paride Mantecca

Supervisor: Dr. Maurizio Gualtieri and Dr. Rossella Bengalli

Coordinator: Prof. Paola Branduardi

ACADEMIC YEAR 2022-2023

Contents

Abstract	1
Introduction	5
Chapter 1: Design and hazard of new nanomaterials	7
1.1 Nanomaterials and Nanoparticles	7
1.1.1 <i>Safety and sustainability by design of new NMs</i>	9
1.1.2 <i>Properties of silver and titania NPs</i>	11
1.2 Exposure to metal NPs	12
1.2.1 <i>Routes of exposure</i>	13
1.2.2 <i>Workplace exposure</i>	16
1.2.3 <i>Toxicological effects of NPs</i>	17
1.3 Anticipating Safety Issues at the Design Stage of NAno Product Development	18
1.3.1 <i>Material safety design criteria</i>	20
1.3.2 <i>NPs used in this thesis</i>	20
1.4 References	22
Chapter 2: New approach methodologies	28
2.1 Tiered approach (monoculture versus co-culture)	28
2.2 Submerged and Air-liquid interface exposure	29
2.3 AOP approach	31
2.3.1 <i>Relevant AOPs for Ag and TiO₂ NPs</i>	32
2.4 Exposure systems	34
2.5 References	35

Chapter 3: Aim of the thesis	39
Chapter 4: Toxicological analysis in a Safe-by-Design and Adverse Outcome Pathway-driven approach on different silver and titania nanoparticles	42
4.1 Introduction	42
4.2 Materials and Methods	45
4.2.1 <i>Chemicals and Reagents</i>	45
4.2.2 <i>NP Suspension Preparation</i>	45
4.2.3 <i>NP Characterization</i>	46
4.2.4 <i>Cell Culture</i>	46
4.2.5 <i>Viability Assay</i>	46
4.2.6 <i>Inflammatory Response</i>	47
4.2.7 <i>Intracellular ROS</i>	47
4.2.8 <i>DNA Damage</i>	47
4.2.9 <i>Cell–Particle Bio-Interaction</i>	47
4.2.10 <i>Statistical Analysis</i>	48
4.3 Results	48
4.3.1 <i>NP Characterization for Toxicological Analyses</i>	48
4.3.2 <i>Cell Viability</i>	51
4.3.3 <i>Reactive Oxygen Species Formation</i>	53
4.3.4 <i>Inflammatory Response (IL-8 Release)</i>	54
4.3.5 <i>Oxidative DNA Damage (yH2AX)</i>	55
4.3.6 <i>Cell–Particle Bio-Interactions</i>	56
4.4 Discussion	57
4.5 Conclusions	60
4.6 Data curation	60

4.7 References	62
----------------	----

Chapter 5: An integrated new approach methodology for risk assessment of Safe and Sustainable by Design

nanomaterials	67
5.1 Introduction	67
5.2 Materials and Methods	71
5.2.1 <i>Nanoparticles and reagents</i>	71
5.2.2 <i>Preparation of the suspensions</i>	72
5.2.3 <i>Environmental monitoring campaign and lung deposition doses</i>	72
5.2.4 <i>Laboratory lung in vitro model exposure</i>	73
5.2.5 <i>Deposition efficiency</i>	75
5.2.6 <i>Air-Liquid Interface Co-culture of A549 and THP-1 derived macrophages</i>	77
5.2.7 <i>Cytotoxicity</i>	78
5.2.8 <i>Cytokines release</i>	78
5.2.9 <i>Data collection and statistical analysis</i>	79
5.3 Results	79
5.3.1 <i>Environmental monitoring campaign and lung deposition modelling</i>	79
5.3.2 <i>Deposition efficiency</i>	81
5.3.3 <i>Estimation of deposition efficiency</i>	82
5.3.4 <i>Cytotoxicity</i>	85
5.3.5 <i>Cytokines release</i>	86
5.3.6 <i>The conceptual framework of the proposed NAM</i>	88
5.4 Discussion	89
5.5 Conclusions	95

5.6 Supplementary	97
5.6.1 Materials and methods	97
5.6.2 Results	101
5.6.3 Supplementary tables	103
5.6.4 Supplementary figures	104
5.7 References	109
Chapter 6: General conclusions and future perspectives	115
6.1 General conclusions	115
6.2 Future perspectives	118
6.3 References	120
List of abbreviations	122
Acknowledgements	124
List of publications	125
Annex I	
Annex II	
Annex III	

Abstract

This work is part of the H2020 European project ASINA which aims to promote Safe-by-Design (SbD) solutions for new nanomaterials (NMs) across all life cycle stages. The adoption of SbD novel approaches for new NMs is of pivotal importance in the framework of the European Commission's Green Deal. Over the past decades, the production and use of NMs have seen substantial growth, raising concerns regarding the potential risk associated with their release and population exposure. Silver (Ag) and titania (TiO₂) nanoparticles (NPs) are among the most widely used NMs and their applications in various products, due to the antibacterial properties of the first and photocatalytic activity of the latter, are increasing.

The aim of this work is to identify the potential hazard posed by newly developed metal based NMs, designed according to a SbD approach, toward human health during their production and use.

The initial step involved testing the newly developed Ag and TiO₂ NPs coated with different agents to compare their toxicological effects to reference uncoated NPs. The endpoints were selected according to an Adverse Outcome Pathway (AOP) approach that enabled the identification of the main events linked to the toxicity of these NPs. Cell viability, inflammatory response, reactive oxygen species levels, oxidative DNA damage, and cell-NPs interactions were analyzed in the alveolar *in vitro* model, A549.

Furthermore, a New Approach Methodology (NAM) was developed to identify and evaluate the hazard of the safer NPs (based on the results of the first part of this study) considering the potential human exposure during NMs production. The goal was to improve their hazard and risk definition. The selection of appropriate exposure doses for hazard assessment has gained increasing importance in the risk assessment framework. To this end, starting

from monitoring campaign data and applying the MPPD model to determine the lung retained dose of NPs, it was possible to estimate the doses representative of a chronic human exposure. The selected *in vitro* model, consisted in a human cell contact co-culture (A549 and THP-1 cells differentiated in macrophages) representative of the alveolar space, cultured, and exposed at the Air-Liquid-Interface (ALI). Exposure to aerosolized NPs was performed by Vitrocell[®] and Cultex[®] commercial systems. This approach allows for more reliable results than by traditional submerged culture systems due to a closer replication of the human physiology. Before exposing the model to the calculated doses, the deposition efficiency (DE) of each NP was determined by using a quartz crystal microbalance (QCM).

The results demonstrated that the functionalization of the NPs has a primary role in driving their toxicity. Moreover, the method of NPs production significantly influenced their toxicity. Different NPs also showed different DE depending on their characteristics. The results obtained from the co-culture indicates the absence of significant hazard for chronic inhalation exposure at environmentally relevant doses, confirming the safety of the NMs and the process developed.

Riassunto

Questo lavoro fa parte del progetto Europeo H2020 ASINA, il quale mira a promuovere delle soluzioni Safe-by-design (SbD) per nuovi nanomateriali (NMs) lungo tutto il loro ciclo vitale. L'adozione di innovativi approcci SbD è di grande importanza nel quadro del Green Deal della Commissione Europea. Negli ultimi decenni, la produzione e l'uso di NMs ha subito una sostanziale crescita, sollevando preoccupazioni a proposito del potenziale rischio associato al loro rilascio e all'esposizione della popolazione. Le nanoparticelle (NPs) di argento (Ag) e di biossido di titanio (TiO₂) sono tra i NMs più ampiamente utilizzati e le loro applicazioni in vari prodotti, a causa delle proprietà antibatteriche delle prime e dell'attività fotocatalitica delle seconde, stanno aumentando.

Lo scopo di questo lavoro è stato di identificare il pericolo posto da NMs metallici di nuova sintesi, disegnati secondo un approccio SbD, verso la salute umana durante la loro produzione e il loro utilizzo.

Il primo passo ha previsto il test delle nuove NPs di Ag e TiO₂ con diversi rivestimenti per confrontare i loro effetti tossicologici con NPs di riferimento senza alcun rivestimento. Gli endpoint sono stati selezionati secondo un approccio Adverse Outcome Pathway (AOP), il quale ha consentito l'identificazione dei principali eventi connessi alla tossicità di queste NPs. La vitalità cellulare, la risposta infiammatoria, i livelli di specie reattive dell'ossigeno, il danno ossidativo al DNA, e le interazioni tra cellule e NPs sono state analizzate nel modello alveolare *in vitro* A549.

In seguito, un New Approach Methodology (NAM) è stato sviluppato per identificare e valutare il rischio delle NPs identificate come più sicure nella prima parte dello studio considerando la potenziale esposizione umana durante la loro produzione. Lo scopo è stato quello di definire meglio il

pericolo di queste NPs. La selezione di dosi di esposizione appropriate per la definizione del pericolo ha un'importanza crescente nel quadro del risk assessment. A tale scopo, partendo dai dati ottenuti da una campagna di monitoraggio e applicando il modello MPPD per determinare la dose di NPs ritenuta a livello alveolare, è stato possibile stimare le dosi rappresentative di un'esposizione umana cronica. Il modello *in vitro* selezionato è composto da una co-coltura (A549 e THP-1 differenziate in macrofagi) rappresentative dello spazio alveolare, coltivate ed esposte all'Air-Liquid-Interface (ALI). L'esposizione all'aerosol di NPs è stata effettuata tramite due sistemi commerciali di Vitrocell® e Cultex®. Questo approccio consente di avere risultati più affidabili rispetto alle tradizionali colture sommerse a causa di una migliore similarità con la fisiologia umana. Prima di esporre il modello alle dosi calcolate, l'efficienza di deposizione (DE) di ogni NP è stata determinata tramite l'uso di una microbilancia.

I risultati dimostrano che la funzionalizzazione delle NPs ha un ruolo primario del determinare la loro tossicità. Inoltre, anche il metodo di produzione è in grado di influenzare in maniera significativa la loro tossicità. Diverse NPs hanno dimostrato diversa DE in base alle loro caratteristiche. I risultati ottenuti dalla co-coltura indicano l'assenza di un pericolo significativo in seguito ad esposizione a dosi rappresentative di una reale inalazione cronica, confermando la sicurezza dei NMs e dei processi sviluppati.

Introduction

This thesis is framed in the context of the H2020 funded European project “Anticipating Safety Issues at the Design Stage of NANO Product Development” (ASINA) (see paragraph 1.3) for the development of a safe by design (SbD) strategy for nanoproducts with antibacterial and photocatalytic properties. The focus of this work is to collect toxicity data to detect the relationship between the physical-chemical (p-chem) properties of the nanomaterials (NMs) and the toxicity outcomes, here including the attempts to develop New Advanced Methodologies (NAMs) for assessing the risk of new NMs. The structure of the thesis is based on introductory chapters (chapters 1 and 2), where the peculiar p-chem and hazardous properties of NPs and NMs (chapter 1) and the recent advancements in the studies related to NAMs (chapter 2) are described. In chapter 3, the aims of the work, in relation to the ASINA specific objectives, are disclosed, with emphasis on the different approaches used in assessing the potential hazards associated with the different forms of nanoparticles (NPs) developed within the project and the contribution to NM risk assessment (RA) frameworks. As preliminary step, a classical *in vitro* toxicological approach is used (Chapter 4 and annex I). NPs toxicity is assessed on a monoculture of alveolar epithelial cells in submerged conditions to highlight how the NPs characteristics influence the selected biological outcomes. From the collected data, we were able to discern the safer and most promising NPs by highlighting the role of NPs coating in modulating their toxicity, according to a SbD approach. These data were also useful for the development of an *in silico* model to predict hazard (annex II). Chapter 5 is based on a submitted paper that aims at providing a NAM (see also chapter 2) to assess the hazard of selected NPs in a co-culture of lung and macrophagic cells, exposed at the air-liquid interface (ALI) to doses relevant for human

inhalation exposure. The results, considering the biological outcomes reported, support that the NPs developed are safe under realistic conditions of exposure and that promising safer antimicrobial and photocatalytic NPs can be synthesized by modulating their surface properties. A final chapter (chapter 6) of general conclusions wrap up all the information collected during the experimental work and provide possible future directions for testing the hazard of NMs, also in the view of the new SbD framework for new chemicals and materials.

Design and hazard of new nanomaterials

1.1 Nanomaterials and Nanoparticles

Nanomaterials (NMs) are natural, incidental, or manufactured materials consisting of solid particles or aggregates where at least 50% of these particles have one or more external dimensions in the range of 1 to 100 nm (“EU Recommendation 2022/C 229/01”).

The prefix “nano” denotes a measure of 10^{-9} units and nano-objects can vary in their shapes, according to differences in the external dimensions in the nanoscale (as depicted in Figure 1.1). Specifically, nanoparticles (NPs) can be defined as particles with all the three external dimensions ranging between 1 to 100 nm.

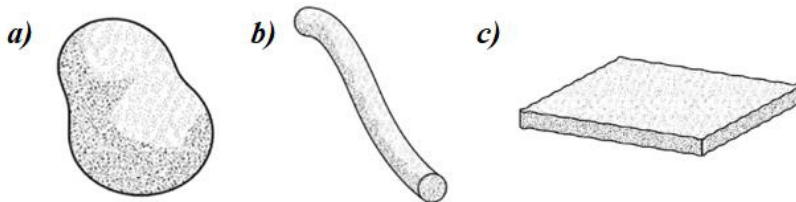


Figure 1.1 - a) Nanoparticle, three external dimensions in the nanoscale; b) Nanofiber, two external dimensions in the nanoscale; c) Nanoplate, one external dimension in the nanoscale. From ISO 80004-1:2023.

The hierarchical relationship between nano-objects and NMs is illustrated in Figure 1.2. Nano-objects may be nanostructured, but it is only when surfaces have been deliberately modified or textured to introduce morphological or chemical variations within the nanoscale that materials are considered “nanostructured materials” (ISO 80004-1:2023).

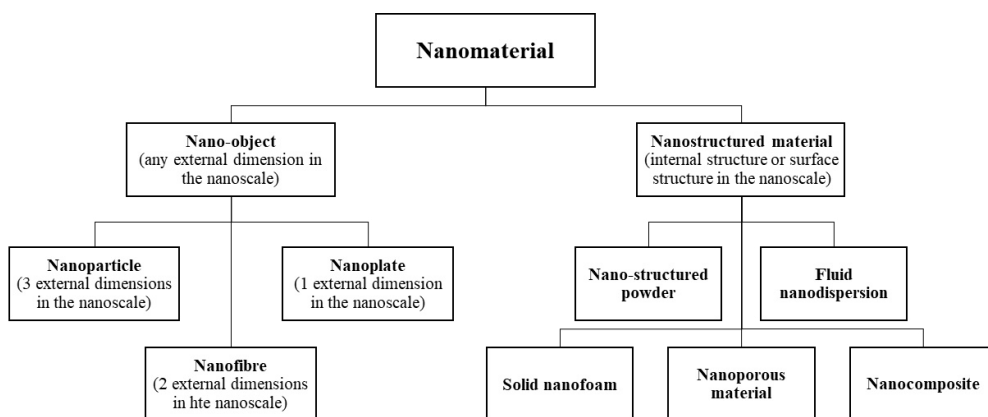


Figure 1.2 - Nanomaterial framework. Adapted from ISO 80004-1:2023.

Nowadays, NMs find extensive applications across a wide range of commercial products, including creams, face masks, clothing, and biomedical devices. In fact, the properties of NPs including mobility, anti-bacterial properties, hardness, magnetization, and colour, makes them attractive for industrial applications. According to the specific application, NPs can serve as chemically inert additives, catalysts, biomaterials, and antimicrobial components (Bapat et al., 2019; Caseri, 2008). Their utility extends to applications like UV protection in cosmetics and the production of colour filters for LCDs (Stark et al., 2015).

NPs offer a versatile, useful, and highly attractive platform for a wide spectrum of biological applications as well, also in relation to their size, comparable to biomolecules like proteins and nucleic acids. Their surface and core characteristics can be designed to suit a single or multiple applications, including biomolecular recognition, therapeutic delivery, biosensing, and bioimaging (De et al., 2008; Gao et al., 2004). Thanks to a greater surface area per volume, compared to the same material of conventional dimensions, NPs possess completely different physical chemical (p-chem) properties and a greater surface reactivity (Schrand et al., 2010). Furthermore, NPs can be tailored using a diverse array of metallic and semiconductor core materials

that provide advantageous features such as fluorescence and magnetic properties (Ferrari, 2005).

1.1.1 Safety and sustainability by design of new NMs

The safe and sustainable by design (SSbD) framework promotes innovation in replacing hazardous substances in both products and processes (European Commission, 2022).

This approach endorses the comprehensive consideration of safety, circularity, and functionality of chemicals and materials throughout their entire life cycle, from initial design to end-of life, including the potential for recycling and reuse. This means acting on the different phases of production of a new NM or a new nano enabled product such as design, development, optimization, production processes and selection of chemicals and materials (Caldeira et al., 2022). By doing so, the SSbD framework aims to prevent or minimize adverse impacts on human health and the environment, facilitating the transition toward a safe and environmentally neutral economy. This is in alignment with the objectives of the European Green Deal (European Commission, 2019), which aims at a transition towards a clean and climate-neutral economy by investing in eco-friendly technologies and implementing initiatives dedicated to restoring biodiversity and reducing pollution (Figure 1.3).



Figure 1.3 – Key drivers and tools for new materials. The policy initiatives of the European Union are in purple, while the essential tools are in green. From Gottardo et al., 2021.

In the SSbD approach, risk analysis and management begin at the material selection stage and continue throughout the entire production phases and beyond, in a life cycle approach, rather than conducting such analyses only downstream the production process, therefore after considerable investment of resources (material and economic) and possible dispersion of NPs in the environment. To implement the SSbD approach effectively, two primary strategies are employed: hazard reduction of the new NPs or NM and exposure minimization toward the target organism (humans, aquatic vertebrates or invertebrates, terrestrial vertebrates or invertebrates and so on), therefore reducing the overall risk related to NPs or NMs release or dispersion. To achieve these goals, different procedure may be employed such as modifying the surface functionalization of nanoparticles with coatings designed to reduce reactivity while preserving material properties or by testing the properties, the possible dispersion, and the overall sustainability (also from an economic

point of view) of newly developed NMs in pilot plants representative of the final industrial plants.

1.1.2 Properties of silver and titania NPs

NPs and NMs can be grouped depending on their chemical composition and structural features including size, shape, and surface modifications (Cho et al., 2013).

The NPs used in this thesis are of similar size and shape and are based on two different cores made of silver (Ag) or titania (TiO₂). The surface of the different NPs is functionalized with different chemicals in order to improve their efficacy or to reduce their toxicity.

Ag NPs are widely employed due to their properties, including high electrical conductivity, chemical stability, optical conductivity (Xia et al., 2011), catalytic activity, as well as antibacterial, antifungal, and antiviral properties (Foldbjerg et al., 2011; Zhang et al., 2016). Ag NPs are extensively integrated into everyday products like textiles, cosmetics, cleaning agents, food packaging, and are also employed in coating of biomedical items such as silicone heart valves, catheters, orthodontic devices, surgical instruments and wounds dressings (Grunkemeier et al., 2006; Huang et al., 2007). The use of Ag NPs in medical devices is reported to minimize the risk of bacterial infections and post-surgical complications (Ge et al., 2014; Tomankova et al., 2015). The antimicrobial properties of Ag NPs make these particles a valid alternative for treating various infections tackling the overall spreading of the antibiotic resistance of some bacterial strains (Marassi et al., 2018).

From an environmental point of view, these NPs play a pivotal role in wastewater treatment, alongside to TiO₂ NPs (Mukhopadhyay et al., 2022).

TiO₂ NPs, in fact, exhibit photocatalytic properties, making them valuable for the photocatalytic degradation of pollutants, and water and air purification. Furthermore, they also find application in the production of sunscreens, tattoo

inks, paint, and photovoltaic cells. TiO₂ NPs have also been applied to biomedical applications for drug delivery (Chen and Selloni, 2014). Additionally, TiO₂ NPs enable the creation of smog-reducing barriers that actively degrade indoor and outdoor pollutants. In fact, through the absorption of UV light, these NPs can participate in surface photochemical processes, resulting in the complete breakdown of various organic and inorganic compounds into CO₂ and H₂O (Mills and Lee, 2002). When TiO₂ is doped, for example, with nitrogen or cobalt, it becomes photocatalytic even under visible light (Shah et al., 2019), extending its photocatalytic capabilities to indoor conditions, eliminating the need for UV radiation (Chen et al., 2012).

1.2 Exposure to metal NPs

The production and use of NMs in many different fields is growing exponentially (<https://single-market-economy.ec.europa.eu/>). This entails an increased risk of human exposure that translates into a growing concern for public health and safety. In fact, the peculiar characteristics of NPs can determine an emerging and increasing risk to human and environmental safety. The entire life cycle of NMs, considering their fate once dispersed in the environment needs to be carefully addressed to avoid unwanted or unpredicted risk (Figure 1.4). This involves the examination of the exposure routes, internalization processes, distribution, and degradation of NPs within living organisms, as well as an investigation into the mechanisms of toxicity associated with their p-chem properties (Colvin, 2003; Hoyt and Mason, 2008). Among the various p-chem parameters, size, shape, core chemistry, agglomeration state, surface characteristics, can influence the interactions between the NP and the cells or the environment (Levard et al., 2012).

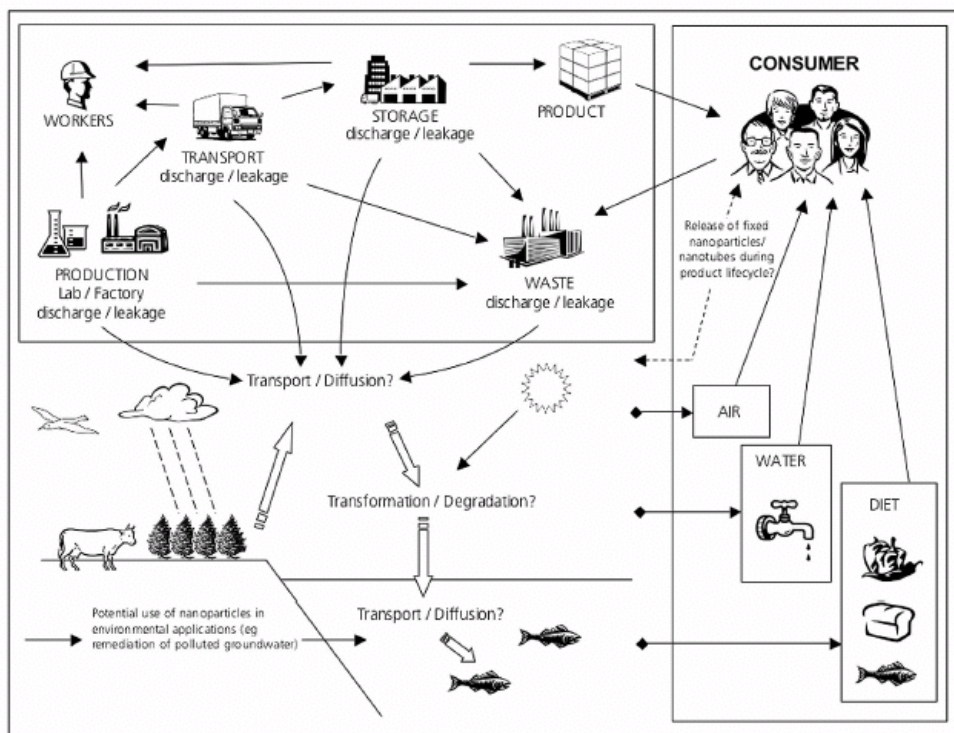


Figure 1.4 – Possible exposure routes for nanoparticles. From Klöpffer et al., 2007.

1.2.1 Routes of exposure

NPs may be released during various stages of their life cycle, starting from the manufacturing process, and extending through product use, all the way to their disposal. Consequently, human exposure to these NPs may occur at any point, and the specific route of exposure vary depending on the characteristics of the nanomaterial and specific process determining the interaction such as from unintended releases or intentional exposure, as in the case of NPs injected for drug delivery (Neha Desai et al., 2021). In the case of unintentional exposure, NPs can enter the body through the skin, the respiratory system, or the gastrointestinal tract. Among these routes, inhalation is regarded as the primary mode of exposure for humans, carrying the highest expected risk (Bierkandt et al., 2018) and, consequently, receiving the most extensive attention in the field of nanotoxicology (Gao et al., 2021).

When NPs are inhaled, their deposition within the airways is influenced by factors such as their shape, size, and chemical characteristics. The mechanisms of deposition of the NPs in the different parts of the respiratory system are shown in Figure 1.5.

Deposition mechanisms in respiratory tract

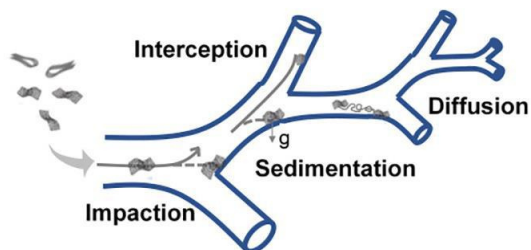


Figure 1.5 - Mechanisms of respiratory tract deposition for NPs. From Gao et al., 2021.

Because of their small dimensions, NPs primarily accumulate in the nose and in the alveolar region of the lungs (Gao et al., 2021). Upon interaction with the blood-air barrier, they have the potential to translocate into the bloodstream (Gwinn and Vallyathan, 2006), ultimately reaching other organs like the nervous system or the liver (Gheshlaghi et al., 2008; Tomankova et al., 2015; Zhang et al., 2016). In fact, the size of NPs increases their ability to permeate biological barriers, as well as cell membranes (Suliman Y et al., 2015).

The clearance in the lungs is promoted by the alveolar macrophages, although they can also be removed from the upper respiratory tract via the mucociliary escalator system and then ingested. Direct ingestion of NPs, occurring via contaminated water or food or by eating products containing NPs, and secondary ingestion, subsequent to inhalation and mucociliary clearance, are therefore the two main pathways that may determine the exposure of the gastro-intestinal tract (Szakal et al., 2014).

After ingestion, NPs have the capacity to interact with the entire gastrointestinal system, potentially being absorbed at the intestinal level, and also interacting with the gut microbiome (Jiang et al., 2018).

Skin absorption is typically expected to be less efficient than inhalation because intact skin serves as an efficient barrier against NPs (Larese Filon et al., 2015). Anyway, absorption can be facilitated in cases of skin lesions and usually occur following the use of cosmetic products containing NPs, such as sunscreens (Wu et al., 2009). Exposure of other species, according to the environmental compartment they live in and the specific anatomic characteristics, occurs through similar processes as those here describe for humans (Figure 1.6).

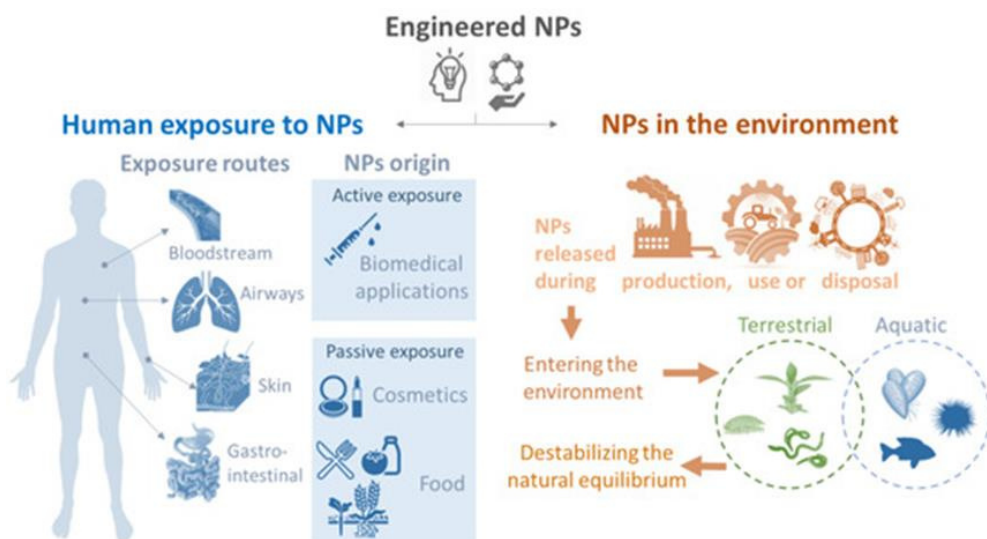


Figure 1.6 – The different exposure routes of NPs that. From Swartzwelter et al., 2021.

Additionally, NPs may be present in the soil due to their incorporation in agricultural products or after deposition of air dispersed particles and, also through wastewater treatment, NPs can also find their way into aquatic environments (Mittal et al., 2020). Upon entering the environment, NPs can

interact with a variety of living organisms, potentially becoming ingested by species of commercial interest (Khosravi-Katuli et al., 2017). Moreover, they may undergo a biomagnification process as they progress through the food chain (Judy et al., 2011)(Judy et al., 2011; Yoo-iam et al., 2014) posing an additional concern for human health and the environment. In the environment, NPs interact with both biotic and abiotic components, undergoing a range of processes including dissolution, speciation, degradation, biological or chemical-physical transformation, agglomeration, deposition, and mineralization. Different types of NPs are also capable of adsorbing and transporting polycyclic aromatic hydrocarbons, effectively serving as carriers for other types of pollutants (Wang et al., 2008).

1.2.2 Workplace exposure

The primary site of uncontrolled NP inhalation has been identified in the workplace, particularly where nanomaterials are manufactured or utilized (Suliman Y et al., 2015). This risk arises from the possibility of the NPs to be unintentionally dispersed in the ambient air during the manufacturing process, thereby presenting a hazard to workers. Various activities involved in nanomaterial production, such as powder or suspension handling, grinding, filtration, and material weighing, can result in the release of NPs (Bierkandt et al., 2018). Whether in the form of powders, liquid suspensions, or aerosol dispersed directly into the atmosphere during production, these NPs are susceptible to inhalation by workers (Paur et al., 2011). Hence, to better understand the health risk for workers, the NPs life cycle, the routes of human exposure, and the interactions of NPs within the human body must be addressed considering the specific production phases. In fact, workers are more likely to experience an earlier and higher exposures compared to the general population (Bergamaschi, 2009; Nasterlack et al., 2008) and represent therefore a sub-population at potential higher risk.

1.2.3 Toxicological effects of NPs

The possibility of NPs to determine adverse effects requires the primary interaction between NPs and cells membrane. NPs can be internalized by cells, often through processes like endocytosis, or they can disrupt the cell membrane to enter (Jugan et al., 2012). Once in the cell, the specific outcome depends on the specific p-chem of the NPs. NPs can release ions or directly interact with specific organelles or DNA (Zhang et al., 2016). These biological effects typically manifest as alterations in cell morphology, increase in the intracellular concentration of reactive oxygen species (ROS), genotoxicity, disruption in mitochondrial function, generation of inflammatory mediators, and ultimately cell death via apoptosis or necrosis (Riaz Ahmed et al., 2017). Considering the relation between p-chem and possible adverse effects, typically, NPs exhibit higher toxicity as their size decreases, primarily due to an increased uptake capacity by cells and a greater surface area available for interactions with molecules (Haase et al., 2012). Positively charged particles tend to be more toxic due to their enhanced ability to interact with cell membranes (Loo et al., 2022). The elemental composition of both the core and surface of NPs plays a role in determining their toxicity, as different materials exhibit varying toxicity profiles (Moschini et al., 2013), and surface functionalization is an effective means of modulating the intensity of toxicity (Colombo et al., 2017). Additionally, the shape or morphology of NPs is an important parameter to be considered, as spherical NPs tend to penetrate cells more effectively, whereas fibrous NPs can disrupt the endocytosis process, leading to membrane rupture and improper closure (Boyles et al., 2015). For Ag and TiO₂ NPs, their ability to induce cellular damage has been well investigated (Figure 1.7).

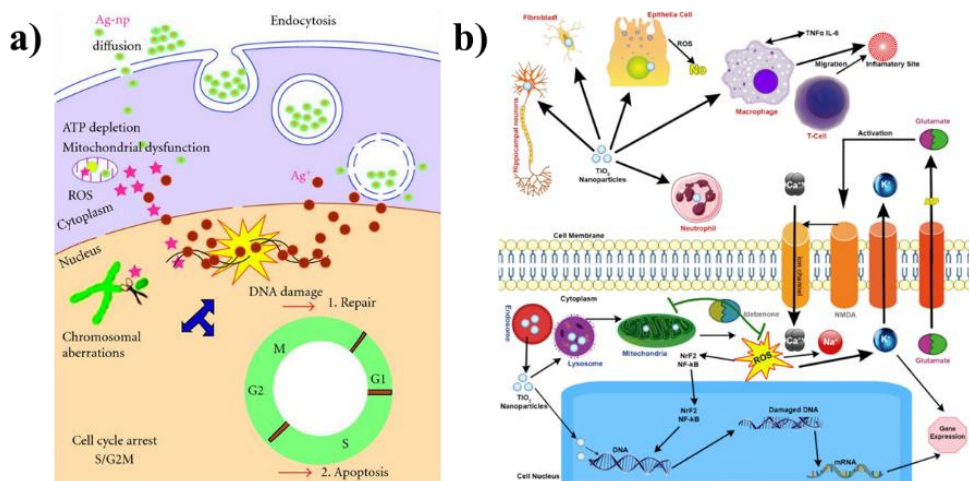


Figure 1.7 – Schematic diagram of the toxicity of Ag and TiO₂ NPs. From Dicks and Heunis, 2010; Shabbir et al., 2021.

Several studies have revealed that both Ag and TiO₂ NPs are able to trigger inflammatory and immunological responses in cells (Loret et al., 2016; Wang et al., 2008), in addition to generating ROS (Carlson et al., 2008; Ma et al., 2012). Furthermore, they can induce genotoxicity through oxidative stress (Park et al., 2008; Suliman Y et al., 2015), ultimately leading to apoptosis (Gurunathan et al., 2015; Shi et al., 2010). It is worth noting that TiO₂ NPs seems to exhibit a higher potential for genotoxic effects compared to Ag NPs, but the latter demonstrate a greater cytotoxic potential (Tomankova et al., 2015).

1.3 Anticipating Safety Issues at the Design Stage of NANO Product Development

This research is conducted within the framework of the European project “Anticipating Safety Issues at the Design Stage of NANO Product Development” (<https://www.asina-project.eu/>). The project’s primary objective is the development of a Safe-by-Design (SbD) strategy for

nanoproducts, with a specific focus on the production of two representative categories of nano-enabled products:

1. Anti-microbial, anti-biofilm, and depolluting coatings used in clean technology, including photocatalytic filters and coated textiles.
2. Nanostructured capsules designed for delivering active components in cosmetic products, such as antiaging and antibacterial creams.

The strategy under development serves as a foundation for establishing design hypotheses and decisions using a data-driven approach and methodology. The ultimate goal of the project is to encourage consumer acceptance and the growth of reference industrial sectors. This will be achieved by maximizing the positive impacts of novel products aimed at enhancing environmental quality and human health. The project is expected to have an impact on various aspects, including:

- Implementation of SbD approaches and tools during the early stages of nanomaterial development.
- Quality workplaces that ensure maximum technical and economic performance while adhering to acceptable risk levels.
- Control and mitigation of the exposure after the release of NMs from products.
- Development and validation of cost-effective techniques for conducting an integrating exposure-driven risk assessment and the associated design of the necessary post-use monitoring.
- Increased industrial competitiveness.
- Impact on human health, the environment, and regulatory frameworks.

1.3.1 Material safety design criteria

Within the ASINA project, the focus of this research is to collect toxicity data to fill gaps for an early identification of hazard potential. The data collected on the hazard of NMs in *in vitro* models or by *in silico* approaches are used to detect the relationship between p-chem properties and toxicity outcomes. The *in vitro* testing is performed also by considering Adverse Outcome Pathways (AOPs, see paragraph 2.4) relevant for human exposure to NMs and by analysing relevant biomarkers of effects for implementing the hazard assessment and the SbD strategy. The testing strategy is therefore based on a tiered approach starting from the identification of the exposure scenarios of NPs, the identification of the p-chem parameters that modulate the biological outcomes, and risk assessment and definition of the product safety requirements in compliance with regulatory frameworks.

1.3.2 NPs used in this thesis

The toxicity data were obtained by comparing commercially available NPs to the NPs developed in the ASINA project to improve some characteristics. To increase Ag dispersion, hydroxyethyl cellulose (HEC) was selected as coating. HEC has the ability to stabilize the Ag NPs in suspension. Two different HEC/Ag molar ratios (5.5 and 6.4) were used as an attempt to increase the antimicrobial properties of the NPs in order to apply a lower dose in the final nano-enabled products. AgHEC NPs were formulated as suspension or powder depending on the final use of the product. AgHEC was intended to be sprayed on textiles, while AgHECp was originally designed to be included in antibacterial creams. Curcumin was selected as coating with the aim of using a stabilizing agent with proven antioxidant and anti-inflammatory properties (Mary et al., 2018; Peng et al., 2021), but it also has an antimicrobial activity (Adamczak et al., 2020). Nitrogen-doped titania (TiO₂-N) has the ability to be photoactivated under visible light (Shah et al., 2019), while TiO₂ can only be

activated by UV light. This doping extends the applicability of these NPs since their antipollution properties can be exploited in indoor environments, reducing the exposure to UV radiation and improving the safety and sustainability of the final products.

1.4 References

- Adamczak, A., Ożarowski, M., Karpiński, T.M., 2020. Curcumin, a Natural Antimicrobial Agent with Strain-Specific Activity. *Pharm.* 2020, Vol. 13, Page 153 13, 153. <https://doi.org/10.3390/PH13070153>
- ASINA project | Safe-by-design of Nano Product Development [WWW Document], n.d. URL <https://www.asina-project.eu/> (accessed 10.15.23).
- Bapat, R.A., Joshi, C.P., Bapat, P., Chaubal, T. V., Pandurangappa, R., Jnanendrapa, N., Gorain, B., Khurana, S., Kesharwani, P., 2019. The use of nanoparticles as biomaterials in dentistry. *Drug Discov. Today* 24, 85–98. <https://doi.org/10.1016/J.DRUDIS.2018.08.012>
- Bergamaschi, E., 2009. Occupational exposure to nanomaterials: Present knowledge and future development. <http://dx.doi.org/10.1080/17435390903037038> 3, 194–201. <https://doi.org/10.1080/17435390903037038>
- Bierkandt, F.S., Leibrock, L., Wagener, S., Laux, P., Luch, A., 2018. The impact of nanomaterial characteristics on inhalation toxicity. *Toxicol. Res. (Camb)*. 7, 321. <https://doi.org/10.1039/C7TX00242D>
- Boyles, M.S.P., Young, L., Brown, D.M., MacCalman, L., Cowie, H., Moisala, A., Smail, F., Smith, P.J.W., Proudfoot, L., Windle, A.H., Stone, V., 2015. Multi-walled carbon nanotube induced frustrated phagocytosis, cytotoxicity and pro-inflammatory conditions in macrophages are length dependent and greater than that of asbestos. *Toxicol. Vitro*. 29, 1513–1528. <https://doi.org/10.1016/J.TIV.2015.06.012>
- Caldeira, C., Farcial, R., Garmendia Aguirre, I., Mancini, L., Tosches, D., Amelio, A., Rasmussen, K., Rauscher, H., Riego Sintes, J. and Sala, S., 2022. Safe and sustainable by design chemicals and materials - Framework for the definition of criteria and evaluation procedure for chemicals and materials [WWW Document]. EUR 31100 EN, Publ. Off. Eur. Union, Luxemb. <https://doi.org/10.2760/487955>, JRC128591
- Carlson, C., Hussein, S.M., Schrand, A.M., Braydich-Stolle, L.K., Hess, K.L., Jones, R.L., Schlager, J.J., 2008. Unique Cellular Interaction of Silver Nanoparticles: Size-Dependent Generation of Reactive Oxygen Species. *J. Phys. Chem. B* 112, 13608–13619. <https://doi.org/10.1021/JP712087M>
- Caseri, W., 2008. INORGANIC NANOPARTICLES AS OPTICALLY EFFECTIVE ADDITIVES FOR POLYMERS. *Chem. Eng. Commun.* 196, 549–572. <https://doi.org/10.1080/00986440802483954>
- Chen, H., Xie, Z., Jin, X., Luo, C., You, C., Tang, Y., Chen, D., Li, Z., Fan, X., 2012. TiO₂ and N-doped TiO₂ induced photocatalytic inactivation of staphylococcus aureus under 405nm LED blue light irradiation. *Int. J. Photoenergy* 2012. <https://doi.org/10.1155/2012/848401>
- Chen, X., Selloni, A., 2014. Introduction: Titanium Dioxide (TiO₂) Nanomaterials. *Chem. Rev.* 114, 9281–9282. <https://doi.org/10.1021/CR500422R>
- Cho, E.J., Holback, H., Liu, K.C., Abouelmagd, S.A., Park, J., Yeo, Y., 2013. Nanoparticle characterization: State of the art, challenges, and emerging technologies. *Mol. Pharm.* 10, 2093–2110. <https://doi.org/10.1021/MP300697H/ASSET/IMAGES/MEDIUM/MP-2012->

00697H_0005.GIF

- Colombo, A., Saibene, M., Moschini, E., Bonfanti, P., Collini, M., Kasemets, K., Mantecca, P., 2017. Teratogenic hazard of BPEI-coated silver nanoparticles to *Xenopus laevis*. *Nanotoxicology* 11, 405–418. <https://doi.org/10.1080/17435390.2017.1309703>
- Colvin, V.L., 2003. The potential environmental impact of engineered nanomaterials. *Nat. Biotechnol.* 2003 2110 21, 1166–1170. <https://doi.org/10.1038/nbt875>
- De, M., Ghosh, P.S., Rotello, V.M., 2008. Applications of nanoparticles in biology. *Adv. Mater.* 20, 4225–4241. <https://doi.org/10.1002/ADMA.200703183>
- Dicks, L.M.T., Heunis, T.D.J., 2010. Nanofibers offer alternative ways to the treatment of skin infections. *J. Biomed. Biotechnol.* 2010. <https://doi.org/10.1155/2010/510682>
- EU COMMISSION RECOMMENDATION of 10 June 2022 on the definition of nanomaterial [WWW Document], n.d. URL <https://eur-lex.europa.eu/legal-content/EN/TXT/?uri=CELEX%3A32022H0614%2801%29> (accessed 10.19.23).
- European Commission, 2022. Commission recommendation of 8.12.2022 establishing a European assessment framework for ‘safe and sustainable by design’ chemicals and materials [WWW Document]. URL https://research-and-innovation.ec.europa.eu/news/all-research-and-innovation-news/recommendation-safe-and-sustainable-chemicals-published-2022-12-08_en (accessed 10.13.23).
- European Commission, 2019. Communication from the Commission to the European Parliament, the European Council, the Council, the European Economic and Social Committee and the Committee of the Regions The European Green Deal.
- European Commission, n.d. Nanomaterials - Internal Market, Industry, Entrepreneurship and SMEs [WWW Document]. URL https://single-market-economy.ec.europa.eu/sectors/chemicals/reach/nanomaterials_en (accessed 10.19.23).
- Ferrari, M., 2005. Cancer nanotechnology: opportunities and challenges. *Nat. Rev. Cancer* 2005 53 5, 161–171. <https://doi.org/10.1038/nrc1566>
- Foldbjerg, R., Dang, D.A., Autrup, H., 2011. Cytotoxicity and genotoxicity of silver nanoparticles in the human lung cancer cell line, A549. *Arch. Toxicol.* 85, 743–750. <https://doi.org/10.1007/S00204-010-0545-5/FIGURES/5>
- Gao, H., Hammer, T., Zhang, X., He, W., Xu, G., Wang, J., 2021. Quantifying respiratory tract deposition of airborne graphene nanoplatelets: The impact of plate-like shape and folded structure. *NanoImpact* 21, 100292. <https://doi.org/10.1016/J.IMPACT.2021.100292>
- Gao, X., Cui, Y., Levenson, R.M., Chung, L.W.K., Nie, S., 2004. In vivo cancer targeting and imaging with semiconductor quantum dots. *Nat. Biotechnol.* 2004 228 22, 969–976. <https://doi.org/10.1038/nbt994>
- Ge, L., Li, Q., Wang, M., Ouyang, J., Li, X., Xing, M.M.Q., 2014. Nanosilver particles in medical applications: synthesis, performance, and toxicity. *Int. J. Nanomedicine* 9, 2399. <https://doi.org/10.2147/IJN.S55015>
- Gheshlaghi, Z.N., Riazi, G.H., Ahmadian, S., Ghafari, M., Mahinpour, R., 2008.

- Toxicity and interaction of titanium dioxide nanoparticles with microtubule protein. *Acta Biochim. Biophys. Sin. (Shanghai)*. 40, 777–782.
<https://doi.org/10.1093/ABBS/40.9.777>
- Gottardo, S., Mech, A., Drbohlavová, J., Małyska, A., Bøwadt, S., Riego Sintes, J., Rauscher, H., 2021. Towards safe and sustainable innovation in nanotechnology: State-of-play for smart nanomaterials. *NanoImpact* 21, 100297. <https://doi.org/10.1016/J.IMPACT.2021.100297>
- Grunkemeier, G.L., Jin, R., Starr, A., 2006. Prosthetic Heart Valves: Objective Performance Criteria Versus Randomized Clinical Trial. *Ann. Thorac. Surg.* 82, 776–780. <https://doi.org/10.1016/j.athoracsur.2006.06.037>
- Gurunathan, S., Jeong, J.K., Han, J.W., Zhang, X.F., Park, J.H., Kim, J.H., 2015. Multidimensional effects of biologically synthesized silver nanoparticles in *Helicobacter pylori*, *Helicobacter felis*, and human lung (L132) and lung carcinoma A549 cells. *Nanoscale Res. Lett.* 2015 101 10, 1–17.
<https://doi.org/10.1186/S11671-015-0747-0>
- Gwinn, M.R., Vallyathan, V., 2006. Nanoparticles: Health Effects—Pros and Cons. *Environ. Health Perspect.* 114, 1818. <https://doi.org/10.1289/EHP.8871>
- Haase, A., Rott, S., Manton, A., Graf, P., Plendl, J., Thünemann, A.F., Meier, W.P., Taubert, A., Luch, A., Reiser, G., 2012. Effects of Silver Nanoparticles on Primary Mixed Neural Cell Cultures: Uptake, Oxidative Stress and Acute Calcium Responses. *Toxicol. Sci.* 126, 457–468.
<https://doi.org/10.1093/TOXSCI/KFS003>
- Hoyt, V.W., Mason, E., 2008. Nanotechnology. *J. Chem. Heal. Saf.* 15, 10–15.
<https://doi.org/10.1016/J.JCHAS.2007.07.015>
- Huang, Y., Li, X., Liao, Z., Zhang, G., Liu, Q., Tang, J., Peng, Y., Liu, X., Luo, Q., 2007. A randomized comparative trial between Acticoat and SD-Ag in the treatment of residual burn wounds, including safety analysis. *Burns* 33, 161–166. <https://doi.org/10.1016/J.BURNS.2006.06.020>
- ISO 80004-1:2023 - Nanotechnologies – Vocabulary — Part 1: Core vocabulary [WWW Document], n.d. URL <https://www.iso.org/standard/79525.html> (accessed 10.12.23).
- Jiang, Z., Jacob, J.A., Li, J., Wu, X., Wei, G., Vimalanathan, A.P., Mani, R., Nainangu, P., Rajadurai, U.M., Chen, B., 2018. Influence of diet and dietary nanoparticles on gut dysbiosis. *Microb. Pathog.* 118, 61–65.
<https://doi.org/10.1016/J.MICPATH.2018.03.017>
- Judy, J.D., Unrine, J.M., Bertsch, P.M., 2011. Evidence for biomagnification of gold nanoparticles within a terrestrial food chain. *Environ. Sci. Technol.* 45, 776–781.
https://doi.org/10.1021/ES103031A/SUPPL_FILE/ES103031A_SI_001.PDF
- Jugan, M.L., Barillet, S., Simon-Deckers, A., Herlin-Boime, N., Sauvaigo, S., Douki, T., Carriere, M., 2012. Titanium dioxide nanoparticles exhibit genotoxicity and impair DNA repair activity in A549 cells. *Nanotoxicology* 6, 501–513. <https://doi.org/10.3109/17435390.2011.587903>
- Khosravi-Katuli, K., Prato, E., Lofrano, G., Guida, M., Vale, G., Libralato, G., 2017. Effects of nanoparticles in species of aquaculture interest. *Environ. Sci. Pollut. Res.* 2017 2421 24, 17326–17346. <https://doi.org/10.1007/S11356-017-9360-3>

- Klöpffer, W., Heijungs, R., Koehler, A., Olsen, S., Frankl, Paolo, Curran, M., 2007. Nanotechnology and Life Cycle Assessment: A Systems Approach to Nanotechnology and the Environment.
- Larese Filon, F., Mauro, M., Adami, G., Bovenzi, M., Crosera, M., 2015. Nanoparticles skin absorption: New aspects for a safety profile evaluation. *Regul. Toxicol. Pharmacol.* 72, 310–322. <https://doi.org/10.1016/J.YRTPH.2015.05.005>
- Levard, C., Hotze, E.M., Lowry, G. V., Brown, G.E., 2012. Environmental transformations of silver nanoparticles: Impact on stability and toxicity. *Environ. Sci. Technol.* 46, 6900–6914. https://doi.org/10.1021/ES2037405/ASSET/IMAGES/LARGE/ES-2011-037405_0005.JPEG
- Loo, C.Y., Siew, E.L., Young, P.M., Traini, D., Lee, W.H., 2022. Toxicity of curcumin nanoparticles towards alveolar macrophage: Effects of surface charges. *Food Chem. Toxicol.* 163, 112976. <https://doi.org/10.1016/J.FCT.2022.112976>
- Loret, T., Peyret, E., Dubreuil, M., Aguerre-Chariol, O., Bressot, C., le Bihan, O., Amodeo, T., Trouiller, B., Braun, A., Egles, C., Lacroix, G., 2016. Air-liquid interface exposure to aerosols of poorly soluble nanomaterials induces different biological activation levels compared to exposure to suspensions. *Part. Fibre Toxicol.* 13, 1–21. <https://doi.org/10.1186/S12989-016-0171-3/FIGURES/10>
- Ma, H., Brennan, A., Diamond, S.A., 2012. Photocatalytic reactive oxygen species production and phototoxicity of titanium dioxide nanoparticles are dependent on the solar ultraviolet radiation spectrum. *Environ. Toxicol. Chem.* 31, 2099–2107. <https://doi.org/10.1002/ETC.1916>
- Marassi, V., Di Cristo, L., Smith, S.G.J., Ortelli, S., Blosi, M., Costa, A.L., Reschiglian, P., Volkov, Y., Prina-Mello, A., 2018. Silver nanoparticles as a medical device in healthcare settings: a five-step approach for candidate screening of coating agents. *R. Soc. Open Sci.* 5. <https://doi.org/10.1098/RSOS.171113>
- Mary, C.P.V., Vijayakumar, S., Shankar, R., 2018. Metal chelating ability and antioxidant properties of Curcumin-metal complexes – A DFT approach. *J. Mol. Graph. Model.* 79, 1–14. <https://doi.org/10.1016/J.JMGM.2017.10.022>
- Mills, A., Lee, S.K., 2002. A web-based overview of semiconductor photochemistry-based current commercial applications. *J. Photochem. Photobiol. A Chem.* 152, 233–247. [https://doi.org/10.1016/S1010-6030\(02\)00243-5](https://doi.org/10.1016/S1010-6030(02)00243-5)
- Mittal, D., Kaur, G., Singh, P., Yadav, K., Ali, S.A., 2020. Nanoparticle-Based Sustainable Agriculture and Food Science: Recent Advances and Future Outlook. *Front. Nanotechnol.* 2, 579954. <https://doi.org/10.3389/FNANO.2020.579954/BIBTEX>
- Moschini, E., Gualtieri, M., Colombo, M., Fascio, U., Camatini, M., Mantecca, P., 2013. The modality of cell–particle interactions drives the toxicity of nanosized CuO and TiO₂ in human alveolar epithelial cells. *Toxicol. Lett.* 222, 102–116. <https://doi.org/10.1016/J.TOXLET.2013.07.019>
- Mukhopadhyay, R., Sarkar, B., Khan, E., Alessi, D.S., Biswas, J.K., Manjaiah,

- K.M., Eguchi, M., Wu, K.C.W., Yamauchi, Y., Ok, Y.S., 2022. Nanomaterials for sustainable remediation of chemical contaminants in water and soil. *Crit. Rev. Environ. Sci. Technol.* 52, 2611–2660.
<https://doi.org/10.1080/10643389.2021.1886891>
- Nasterlack, M., Zober, A., Oberlinner, C., 2008. Considerations on occupational medical surveillance in employees handling nanoparticles. *Int. Arch. Occup. Environ. Health* 81, 721–726. <https://doi.org/10.1007/S00420-007-0245-5/METRICS>
- Neha Desai, Momin, M., Khan, T., Gharat, S., Ningthoujam, R.S., Omri, A., 2021. Metallic nanoparticles as drug delivery system for the treatment of cancer. *Expert Opin. Drug Deliv.* 18, 1261–1290.
<https://doi.org/10.1080/17425247.2021.1912008>
- Park, E.J., Yi, J., Chung, K.H., Ryu, D.Y., Choi, J., Park, K., 2008. Oxidative stress and apoptosis induced by titanium dioxide nanoparticles in cultured BEAS-2B cells. *Toxicol. Lett.* 180, 222–229.
<https://doi.org/10.1016/J.TOXLET.2008.06.869>
- Paur, H.R., Cassee, F.R., Teeguarden, J., Fissan, H., Diabate, S., Aufderheide, M., Kreyling, W.G., Hänninen, O., Kasper, G., Riediker, M., Rothen-Rutishauser, B., Schmid, O., 2011. In-vitro cell exposure studies for the assessment of nanoparticle toxicity in the lung—A dialog between aerosol science and biology. *J. Aerosol Sci.* 42, 668–692.
<https://doi.org/10.1016/J.JAEROSCI.2011.06.005>
- Peng, Y., Ao, M., Dong, B., Jiang, Y., Yu, L., Chen, Z., Hu, C., Xu, R., 2021. Anti-Inflammatory Effects of Curcumin in the Inflammatory Diseases: Status, Limitations and Countermeasures. *Drug Des. Devel. Ther.* 15, 4503–4525.
<https://doi.org/10.2147/DDDT.S327378>
- Riaz Ahmed, K.B., Nagy, A.M., Brown, R.P., Zhang, Q., Malghan, S.G., Goering, P.L., 2017. Silver nanoparticles: Significance of physicochemical properties and assay interference on the interpretation of in vitro cytotoxicity studies. *Toxicol. Vitr.* 38, 179–192. <https://doi.org/10.1016/J.TIV.2016.10.012>
- Schrand, A.M., Rahman, M.F., Hussain, S.M., Schlager, J.J., Smith, D.A., Syed, A.F., 2010. Metal-based nanoparticles and their toxicity assessment. *Wiley Interdiscip. Rev. Nanomedicine Nanobiotechnology* 2, 544–568.
<https://doi.org/10.1002/WNAN.103>
- Shabbir, S., Kulyar, M.F. e. A., Bhutta, Z.A., Boruah, P., Asif, M., 2021. Toxicological Consequences of Titanium Dioxide Nanoparticles (TiO₂NPs) and Their Jeopardy to Human Population. *Bionanoscience* 11, 621–632.
<https://doi.org/10.1007/S12668-021-00836-3/FIGURES/1>
- Shah, Z., Nazir, S., Mazhar, K., Abbasi, R., Samokhvalov, I.M., 2019. PEGylated doped- and undoped-TiO₂ nanoparticles for photodynamic Therapy of cancers. *Photodiagnosis Photodyn. Ther.* 27, 173–183.
<https://doi.org/10.1016/J.PDPDT.2019.05.019>
- Shi, Y., Wang, F., He, J., Yadav, S., Wang, H., 2010. Titanium dioxide nanoparticles cause apoptosis in BEAS-2B cells through the caspase 8/t-Bid-independent mitochondrial pathway. *Toxicol. Lett.* 196, 21–27.
<https://doi.org/10.1016/J.TOXLET.2010.03.014>
- Stark, W.J., Stoessel, P.R., Wohlleben, W., Hafner, A., 2015. Industrial applications

- of nanoparticles. *Chem. Soc. Rev.* 44, 5793–5805.
<https://doi.org/10.1039/C4CS00362D>
- Suliman Y, A.O., Ali, D., Alarifi, S., Harrath, A.H., Mansour, L., Alwasel, S.H., 2015. Evaluation of cytotoxic, oxidative stress, proinflammatory and genotoxic effect of silver nanoparticles in human lung epithelial cells. *Environ. Toxicol.* 30, 149–160. <https://doi.org/10.1002/TOX.21880>
- Swartzwelter, B.J., Mayall, C., Alijagic, A., Barbero, F., Ferrari, E., Hernadi, S., Michelini, S., Pacheco, N.I.N., Prinelli, A., Swart, E., Auguste, M., 2021. Cross-Species Comparisons of Nanoparticle Interactions with Innate Immune Systems: A Methodological Review. *Nanomater.* 2021, Vol. 11, Page 1528 11, 1528. <https://doi.org/10.3390/NANO11061528>
- Szkal, C., Roberts, S.M., Westerhoff, P., Bartholomaeus, A., Buck, N., Illuminato, I., Canady, R., Rogers, M., 2014. Measurement of nanomaterials in foods: Integrative consideration of challenges and future prospects. *ACS Nano* 8, 3128–3135.
https://doi.org/10.1021/NN501108G/ASSET/IMAGES/LARGE/NN-2014-01108G_0005.JPEG
- Tomankova, K., Horakova, J., Harvanova, M., Malina, L., Soukupova, J., Hradilova, S., Kejlova, K., Malohlava, J., Licman, L., Dvorakova, M., Jirova, D., Kolarova, H., 2015. Cytotoxicity, cell uptake and microscopic analysis of titanium dioxide and silver nanoparticles in vitro. *Food Chem. Toxicol.* 82, 106–115. <https://doi.org/10.1016/J.FCT.2015.03.027>
- Wang, X., Lu, J., Xu, M., Xing, B., 2008. Sorption of pyrene by regular and nanoscaled metal oxide particles: Influence of adsorbed organic matter. *Environ. Sci. Technol.* 42, 7267–7272.
https://doi.org/10.1021/ES8015414/SUPPL_FILE/ES8015414_SI_001.PDF
- Wu, J., Liu, W., Xue, C., Zhou, S., Lan, F., Bi, L., Xu, H., Yang, X., Zeng, F.D., 2009. Toxicity and penetration of TiO₂ nanoparticles in hairless mice and porcine skin after subchronic dermal exposure. *Toxicol. Lett.* 191, 1–8.
<https://doi.org/10.1016/J.TOXLET.2009.05.020>
- Xia, Y., Zhou, Y., Tang, Z., 2011. Chiral inorganic nanoparticles : origin, optical properties and bioapplications. *Nanoscale* 3, 1374–1382.
<https://doi.org/10.1039/C0NR00903B>
- Yoo-iam, M., Chaichana, R., Satapanajaru, T., 2014. Toxicity, bioaccumulation and biomagnification of silver nanoparticles in green algae (*Chlorella* sp.), water flea (*Moina macrocopa*), blood worm (*Chironomus* spp.) and silver barb (*Barbonymus gonionotus*). *Chem. Speciat. Bioavailab.* 26, 257–265.
<https://doi.org/10.3184/095422914X14144332205573>
- Zhang, X.F., Shen, W., Gurunathan, S., 2016. Silver Nanoparticle-Mediated Cellular Responses in Various Cell Lines: An in Vitro Model. *Int. J. Mol. Sci.* 2016, Vol. 17, Page 1603 17, 1603. <https://doi.org/10.3390/IJMS17101603>

New approach methodologies

New Approach Methodologies (NAMs) are strategies based on *in vitro* and, *in silico* or *in chemico* methods that can provide information on the hazard and risk assessment of chemicals without involving animal testing (ECHA, 2016). Consequently, these methods serve as alternatives or complementary methods to traditional animal testing. This approach is a valuable tool for reducing the number of animals used for scientific purposes and for enhancing the acquisition of toxicological data to perform next generation risk assessment. The development and application of NAMs for risk assessment aligns with the principles of the 3R: replacement, reduction, and refinement of conventional animal experiments (Directive 2010/63/EU).

NAMs are included in the “Next Generation Risk Assessment” (NGRA) process to identify the existence of hazard and to minimize harm. This process involve the use of a tiered approach to use relevant data for a comprehensive assessment of safety risks of chemicals. In the NGRA the focus is more than just the toxicological endpoint. In fact, it considers the entire process starting from the exposure to a substance, down to the final adverse outcome.

2.1 Tiered approach (monoculture versus co-culture)

A tiered approach is structured with a sequence of assessments, starting with tests that use existing data or basic biological techniques. As the process advances, more complex tests and models come into play.

In this thesis, both models used for the evaluation of the toxicity of NPs are *in vitro*. Tier 1 involved the use of a simple monoculture of A549 cells (adenocarcinomic human alveolar epithelial cells) in submerged conditions. This particular cell line is widely employed in nanotoxicology to assess

cytotoxicity at the alveolar level (Gliga et al., 2014; Simon-Deckers et al., 2008). A monoculture is a simple model, which allow to obtain data in a brief time. As tier 2 model, a co-culture of A549 cells and macrophages (derived from the monocyte line THP-1) is used. This co-culture was cultured before the exposure to NPs at the Air-Liquid Interface (ALI, see paragraph 2.3) to allow epithelial cells differentiation. A co-culture is a more realistic model compared to a single cell line since it allows the examination of inter-cellular interactions that naturally occur in the human lung. In fact, it replicates the interaction between lung epithelial cells and immune system cells. In recent years, the use of multi-cultures has been promoted due to their advantages, providing more valuable insights into the actual effects of the substance being tested (James Kirkpatrick et al., 2007; Miki et al., 2012). Moreover, the Tier2 approach here used, by culturing and exposing lung cells at the ALI, improve the representativeness of the *in vitro* model to the human lung alveolar sacs, where the interaction among inhaled pollutants (particle, gases, viruses etc.) happen at the interface between the inhaled air and the lung membranes. Additional advanced models are now based also on 3D models namely lung organoids (Barkauskas et al., 2017). These spherical systems, although providing relevant 3D cell to cell interactions still require further assessment and development before application to NPs hazard evaluation, being model used essentially in submerged conditions.

2.2 Submerged and Air-liquid interface exposure

In vitro models representative of the lung epithelia can be cultured in different ways. Traditionally, they are submerged in culture media to provide them all the required nutrients and growth factors. Alternatively, lung *in vitro* models can be cultured on supports such as inserts or scaffolds, enabling ALI cultivation and exposure. In these systems, the nutrients and growth factors are provided to the cells from the basal side, therefore mimicking the actual *in*

in vivo situation. While exposures under classical conditions are simpler from an experimental standpoint, ALI exposures are more physiologically accurate and thus biologically more significant. Some studies indicate that, when comparing the responses of cultures exposed to NPs in submerged and ALI conditions, the response tends to be more pronounced under ALI conditions (Diabaté et al., 2020; Lenz et al., 2013). Submerged exposure involves directly introducing NPs into the cell culture medium, therefore the cell-NPs interaction does not reflect real-life situations, where lung cells are exposed to the surrounding air (Joris et al., 2013). Factors such as surface charge, solubility, agglomeration, and surface structure are altered when NPs are in solution, depending on the composition of the medium (Limbach et al., 2005). These alterations significantly affect the toxicity of the NPs because the biological response of the model is influenced by their p-chem properties (Lee et al., 2009; Monopoli et al., 2011; Rothen-Rutishauser et al., 2008). It's important to acknowledge that in such exposure scenarios, determining or calculating the precise dose of NPs reaching the cells is a challenging task (Lenz et al., 2013). This difficulty arises from the fact that a portion of the particles remains suspended in the culture medium or adheres to the culture vessel's side walls. These factors not only impact the effective NP dosage but also influence their interaction with cells. Additionally, there is a limitation related to the NPs dispersed in the cell culture medium, as they have the potential to bind with proteins and other organic molecules present in the medium, giving rise to the formation of a protein corona that can alter the particles' toxicity (Barbero et al., 2017; Garvas et al., 2015; Zanganeh et al., 2016). On the other hand, in an ALI exposure, NPs suspended in the air are deposited directly onto cells cultivated on supports. These supports enable the model to be exposed directly to the surrounding air on the apical side, while the cell culture medium is situated at the bottom of the support on the basal side of the model. NPs interact directly with the cells without undergoing any

alterations caused by any medium (Paur et al., 2011). This setup allows for the precise calculation or direct measurement of the actual exposure dose.

2.3 AOP approach

NAMs are frameworks aimed at developing and testing new methodologies to evaluate the hazard and assess the risk of target compounds or to test new drugs or molecules in pharmacology-oriented tests. On the other hand, the biological endpoints to be evaluated in a newly developed NAM may be diverse as targeting a specific pathway or following an untargeted approach and using classical or omics techniques. The OECD (Organization for Economic Co-operation and Development) defines an Adverse Outcome Pathway (AOP) as a conceptual framework that outlines a step-by-step sequence of linked events occurring at various biological levels, leading to an adverse health or ecotoxicological effect (OECD ILibrary). An AOP-centered approach enables the connection of the p-chem properties of NPs with the mechanistic aspects of their biological interactions, ultimately linking them to potential health impacts in both humans and other organisms. AOPs are now recognized as a pivotal tool for replacing animal testing with scientifically valid alternative methods to support regulatory decisions (Halappanavar et al., 2019). AOPs are structured as organized diagrammatic representations that establish connections across diverse biological levels. They start with an event known as molecular initiating event (MIE), which involves the interaction between a toxic substance and the biological system. This sequence then progresses through a series of intermediate key events (KE), connected by key event relationships (KER), culminating in the ultimate adverse outcome (AO) (Figure 2.1).

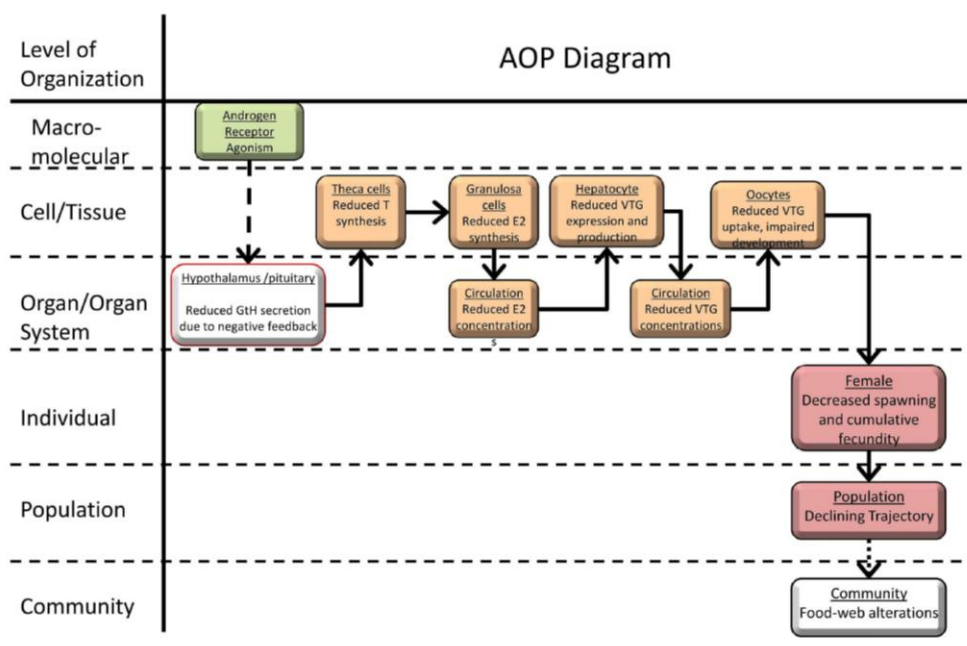


Figure 2.1 – Graphical representation of an AOP with the different levels of organization. From AOP-Wiki.

2.3.1 Relevant AOPs for Ag and TiO₂ NPs

Several AOPs have been proposed covering diverse human diseases and biological responses (<https://aopwiki.org/>). Among the different AOPs, here the ones more relevant or directly connected to NPs exposure are reported. Three AOPs have been documented in the literature regarding the mechanisms of Ag NPs toxicity:

1. Ma et al., (2018) describe how ROS production in zebrafish gonad tissue, which can be triggered by Ag NPs, leads to oxidative stress, then germ cell apoptosis and finally impaired reproduction.
2. Jeong et al., (2018) describe how NADPH oxidase activation leads to reproductive failure in *C. elegans*, identifying Ag NPs as prototypical stressor. The KEs from this AOP are related to oxidative stress, hypoxic stress, DNA damage and repair, and apoptosis.

3. Nicholas et al., (2021) describe Ag NPs toxicity towards the respiratory tract. After acute exposure, they identify as MIE the ROS production. The two KE identified are the upregulation of neutrophil chemokines and the recruitment of neutrophils. The final AO is lung tissue damage. For TiO₂, there are two AOPs identified in the literature and three published on the AOP wiki:

1. Brand et al., (2020) proposed an AOP that describes a series of KEs that link TiO₂ endocytic lysosomal uptake (MIE) to liver fibrosis (AO1), liver oedema (AO2), and steatosis (AO3).
2. Braakhuis et al., (2021) describe how cellular uptake of TiO₂ NPs in the intestine (MIE) leads to intestinal tumors (AO). The series of KEs linking the MIE and the AOP encompass oxidative stress, inflammation, proliferation of intestinal cells and DNA damage, which are toxicity mechanisms frequently reported to explain TiO₂ NP toxicity.
3. From the wiki (AOP-Wiki), AOP260 describes how protein adduct formation and CYP2E1 activation (MIEs) can lead to neurodegeneration (AO). AOP208 and AOP282 describe cellular pathways that are activated by photoactive stressors. AOP208 includes UV-activated TiO₂ NPs as a stressor and was developed to describe their toxicity towards the nematode *C. elegans*. The putative AOP282 describes how photoactivation of the stressor leads to inflammation via oxidation of lipids/proteins.

It is remarkable to observe that Ag and TiO₂ NPs exhibit a similar overarching mechanism of toxicity: oxidative stress, inflammation, DNA damage and repair, as well as apoptosis, collectively play a central role in the toxicity of both types of NPs.

2.4 Exposure systems

In the existing literature, various systems have been employed for exposing ALI-cultured cells to NPs (Aufderheide et al., 2017; Leroux et al., 2022; Nair et al., 2020; Rach et al., 2014; Steinritz et al., 2013). Among the commercially available systems, notable examples include the Vitrocell® and Cultex® systems, both designed to facilitate the uniform deposition of aerosols onto ALI-cultured cells. For this thesis, two systems were used.

The Vitrocell® Cloud α 12 (Figure 2.2a) allows to generate a cloud of aerosol particles, of dimension varying in the range 2 to 10 μm , from a NPs suspension. The aerosol droplet containing the NPs are effectively delivered to the cells through total gravimetric deposition. The system is equipped with a microbalance, allowing for the precise measurement the actual mass of NPs deposited during the exposure, with a resolution of 10 ng/cm^2 per second.

The Cultex® RFS Compact module (Figure 2.2b) enables cell exposure to an aerosol generated from a suspension or directly sampled from the test atmosphere (generated in the lab or ambient atmosphere). In this system, external air is drawn in, passes over the cells, and the deposition relies on the interplay between gravitational forces and the Brownian motion of the NPs. The doses of exposure can be calculated according to the physical laws of a particle in a fluid (air in this case).

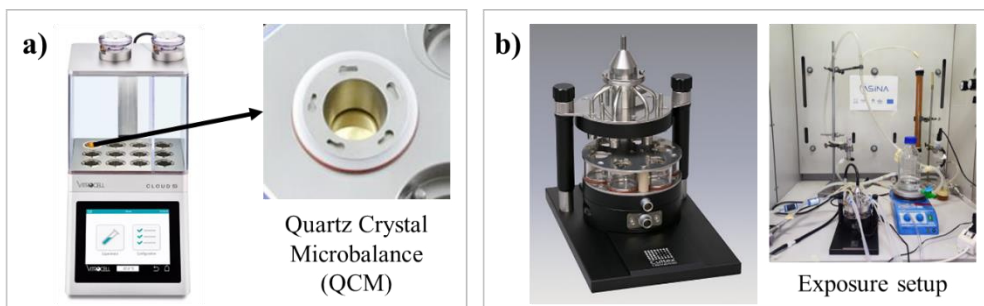


Figure 2.2 – Exposure systems used during this thesis. a) The Vitrocell® cloud α 12 and the QCM; b) The Cultex® RFS Compact module and, on the right, the setup of the experiment for the exposure of the cell to a generated aerosol of NPs. From Vitrocell® Website and Cultex® Website.

2.5 References

- AOP-Wiki*. (n.d.). Retrieved October 23, 2023, from <https://aopwiki.org/>
- Aufderheide, M., Heller, W. D., Krischenowski, O., Möhle, N., & Hochrainer, D. (2017). Improvement of the CULTEX® exposure technology by radial distribution of the test aerosol. *Experimental and Toxicologic Pathology*, *69*(6), 359–365. <https://doi.org/10.1016/J.ETP.2017.02.004>
- Barbero, F., Russo, L., Vitali, M., Piella, J., Salvo, I., Borrajo, M. L., Busquets-Fité, M., Grandori, R., Bastús, N. G., Casals, E., & Puentes, V. (2017). Formation of the Protein Corona: The Interface between Nanoparticles and the Immune System. *Seminars in Immunology*, *34*, 52–60. <https://doi.org/10.1016/J.SMIM.2017.10.001>
- Barkauskas, C. E., Chung, M. I., Fioret, B., Gao, X., Katsura, H., & Hogan, B. L. M. (2017). Lung organoids: current uses and future promise. *Development*, *144*(6), 986–997. <https://doi.org/10.1242/DEV.140103>
- Braakhuis, H. M., Gosens, I., Heringa, M. B., Oomen, A. G., Vandebriel, R. J., Groenewold, M., & Cassee, F. R. (2021). Mechanism of Action of TiO₂: Recommendations to Reduce Uncertainties Related to Carcinogenic Potential. <https://doi.org/10.1146/Annurev-Pharmtox-101419-100049>, *61*, 203–223. <https://doi.org/10.1146/ANNUREV-PHARMTOX-101419-100049>
- Brand, W., Peters, R. J. B., Braakhuis, H. M., Maślankiewicz, L., & Oomen, A. G. (2020). Possible effects of titanium dioxide particles on human liver, intestinal tissue, spleen and kidney after oral exposure. *Nanotoxicology*, *14*(7), 985–1007. <https://doi.org/10.1080/17435390.2020.1778809>
- Cultex® website*. (n.d.). Retrieved October 23, 2023, from <https://www.cultex-technology.com/>
- Diabaté, S., Armand, L., Murugadoss, S., Dilger, M., Fritsch-Decker, S., Schlager, C., Béal, D., Arnal, M. E., Biola-Clier, M., Ambrose, S., Mülhopt, S., Paur, H. R., Lynch, I., Valsami-Jones, E., Carriere, M., & Weiss, C. (2020). Air–Liquid Interface Exposure of Lung Epithelial Cells to Low Doses of Nanoparticles to Assess Pulmonary Adverse Effects. *Nanomaterials 2021, Vol. 11, Page 65*, *11*(1), 65. <https://doi.org/10.3390/NANO11010065>
- Directive 2010/63/EU of the European Parliament and of the Council of 22 September 2010 on the protection of animals used for scientific purposes Text with EEA relevance*. (n.d.). Retrieved October 23, 2023, from <https://eur-lex.europa.eu/legal-content/EN/TXT/?uri=CELEX:32010L0063>
- European Chemicals Agency. (2016). *New approach methodologies in regulatory science: proceedings of a scientific workshop: Helsinki, 19-20 April 2016*. European Chemicals Agency. <https://doi.org/doi/10.2823/543644>
- Garvas, M., Testen, A., Umek, P., Gloter, A., Koklic, T., & Strancar, J. (2015). Protein Corona Prevents TiO₂ Phototoxicity. *PLOS ONE*, *10*(6), e0129577. <https://doi.org/10.1371/JOURNAL.PONE.0129577>
- Gliga, A. R., Skoglund, S., Odnevall Wallinder, I., Fadeel, B., & Karlsson, H. L. (2014). Size-dependent cytotoxicity of silver nanoparticles in human lung cells: The role of cellular uptake, agglomeration and Ag release. *Particle and Fibre Toxicology*, *11*(1), 1–17. <https://doi.org/10.1186/1743-8977-11-11/FIGURES/8>

- Halappanavar, S., Ede, J. D., Shatkin, J. A., & Krug, H. F. (2019). A systematic process for identifying key events for advancing the development of nanomaterial relevant adverse outcome pathways. *NanoImpact*, *15*, 100178. <https://doi.org/10.1016/J.IMPACT.2019.100178>
- James Kirkpatrick, C., Fuchs, S., Iris Hermanns, M., Peters, K., & Unger, R. E. (2007). Cell culture models of higher complexity in tissue engineering and regenerative medicine. *Biomaterials*, *28*(34), 5193–5198. <https://doi.org/10.1016/J.BIOMATERIALS.2007.08.012>
- Jeong, J., Song, T., Chatterjee, N., Choi, I., Cha, Y. K., & Choi, J. (2018). Developing adverse outcome pathways on silver nanoparticle-induced reproductive toxicity via oxidative stress in the nematode *Caenorhabditis elegans* using a Bayesian network model. *Nanotoxicology*, *12*(10), 1182–1197. <https://doi.org/10.1080/17435390.2018.1529835>
- Joris, F., Manshian, B. B., Peynshaert, K., De Smedt, S. C., Braeckmans, K., & Soenen, S. J. (2013). Assessing nanoparticle toxicity in cell-based assays: influence of cell culture parameters and optimized models for bridging the in vitro–in vivo gap. *Chemical Society Reviews*, *42*(21), 8339–8359. <https://doi.org/10.1039/C3CS60145E>
- Lee, J., Lilly, D., Doty, C., Podsiadlo, P., & Kotov, N. (2009). In vitro Toxicity Testing of Nanoparticles in 3D Cell Culture. *Small*, *5*(10), 1213–1221. <https://doi.org/10.1002/SMLL.200801788>
- Lenz, A. G., Karg, E., Brendel, E., Hinze-Heyn, H., Maier, K. L., Eickelberg, O., Stoeger, T., & Schmid, O. (2013). Inflammatory and oxidative stress responses of an alveolar epithelial cell line to airborne zinc oxide nanoparticles at the air-liquid interface: A comparison with conventional, submerged cell-culture conditions. *BioMed Research International*, *2013*. <https://doi.org/10.1155/2013/652632>
- Leroux, M. M., Hocquel, R., Bourge, K., Kokot, B., Kokot, H., Koklič, T., Štrancar, J., Ding, Y., Kumar, P., Schmid, O., Rihn, B. H., Ferrari, L., & Joubert, O. (2022). Aerosol–Cell Exposure System Applied to Semi-Adherent Cells for Aerosolization of Lung Surfactant and Nanoparticles Followed by High Quality RNA Extraction. *Nanomaterials*, *12*(8), 1362. <https://doi.org/10.3390/NANO12081362/S1>
- Limbach, L. K., Li, Y., Grass, R. N., Brunner, T. J., Hintermann, M. A., Muller, M., Gunther, D., & Stark, W. J. (2005). Oxide nanoparticle uptake in human lung fibroblasts: Effects of particle size, agglomeration, and diffusion at low concentrations. *Environmental Science and Technology*, *39*(23), 9370–9376. https://doi.org/10.1021/ES051043O/SUPPL_FILE/ES051043OSI20050825_114251.PDF
- Ma, Y. B., Lu, C. J., Junaid, M., Jia, P. P., Yang, L., Zhang, J. H., & Pei, D. S. (2018). Potential adverse outcome pathway (AOP) of silver nanoparticles mediated reproductive toxicity in zebrafish. *Chemosphere*, *207*, 320–328. <https://doi.org/10.1016/J.CHEMOSPHERE.2018.05.019>
- Miki, Y., Ono, K., Hata, S., Suzuki, T., Kumamoto, H., & Sasano, H. (2012). The advantages of co-culture over mono cell culture in simulating in vivo environment. *The Journal of Steroid Biochemistry and Molecular Biology*, *131*(3–5), 68–75. <https://doi.org/10.1016/J.JSBMB.2011.12.004>

- Monopoli, M. P., Walczyk, D., Campbell, A., Elia, G., Lynch, I., Baldelli Bombelli, F., & Dawson, K. A. (2011). Physical-Chemical aspects of protein corona: Relevance to in vitro and in vivo biological impacts of nanoparticles. *Journal of the American Chemical Society*, 133(8), 2525–2534. https://doi.org/10.1021/JA107583H/SUPPL_FILE/JA107583H_SI_001.PDF
- Nair, V., Tran, M., Behar, R. Z., Zhai, S., Cui, X., Phandthong, R., Wang, Y., Pan, S., Luo, W., Pankow, J. F., Volz, D. C., & Talbot, P. (2020). Menthol in electronic cigarettes: A contributor to respiratory disease? *Toxicology and Applied Pharmacology*, 407, 115238. <https://doi.org/10.1016/J.TAAP.2020.115238>
- Nicholas, T. P., Boyes, W. K., Scoville, D. K., Workman, T. W., Kavanagh, T. J., Altemeier, W. A., & Faustman, E. M. (2021). The effects of gene × environment interactions on silver nanoparticle toxicity in the respiratory system: An adverse outcome pathway. *Wiley Interdisciplinary Reviews: Nanomedicine and Nanobiotechnology*, 13(5), e1708. <https://doi.org/10.1002/WNAN.1708>
- OECD Series on Adverse Outcome Pathways | OECD iLibrary. (n.d.). Retrieved October 23, 2023, from https://www.oecd-ilibrary.org/environment/oecd-series-on-adverse-outcome-pathways_2415170x
- Paur, H. R., Cassee, F. R., Teeguarden, J., Fissan, H., Diabate, S., Aufderheide, M., Kreyling, W. G., Hänninen, O., Kasper, G., Riediker, M., Rothen-Rutishauser, B., & Schmid, O. (2011). In-vitro cell exposure studies for the assessment of nanoparticle toxicity in the lung—A dialog between aerosol science and biology. *Journal of Aerosol Science*, 42(10), 668–692. <https://doi.org/10.1016/J.JAEROSCI.2011.06.005>
- Rach, J., Budde, J., Möhle, N., & Aufderheide, M. (2014). Direct exposure at the air–liquid interface: evaluation of an in vitro approach for simulating inhalation of airborne substances. *Journal of Applied Toxicology*, 34(5), 506–515. <https://doi.org/10.1002/JAT.2899>
- Rothen-Rutishauser, B., Blank, F., Mühlfeld, C., & Gehr, P. (2008). In vitro models of the human epithelial airway barrier to study the toxic potential of particulate matter. *Expert Opinion on Drug Metabolism & Toxicology*, 4(8), 1075–1089. <https://doi.org/10.1517/17425255.4.8.1075>
- Simon-Deckers, A., Gouget, B., Mayne-L’Hermite, M., Herlin-Boime, N., Reynaud, C., & Carrière, M. (2008). In vitro investigation of oxide nanoparticle and carbon nanotube toxicity and intracellular accumulation in A549 human pneumocytes. *Toxicology*, 253(1–3), 137–146. <https://doi.org/10.1016/J.TOX.2008.09.007>
- Steinritz, D., Möhle, N., Pohl, C., Papritz, M., Stenger, B., Schmidt, A., Kirkpatrick, C. J., Thiermann, H., Vogel, R., Hoffmann, S., & Aufderheide, M. (2013). Use of the Cultex® Radial Flow System as an in vitro exposure method to assess acute pulmonary toxicity of fine dusts and nanoparticles with special focus on the intra- and inter-laboratory reproducibility. *Chemico-Biological Interactions*, 206(3), 479–490. <https://doi.org/10.1016/J.CBI.2013.05.001>
- Vitrocell® website. (n.d.). Retrieved October 23, 2023, from <https://www.vitrocell.com/>
- Zanganeh, S., Spitler, R., Erfanzadeh, M., Alkilany, A. M., & Mahmoudi, M. (2016). Protein corona: Opportunities and challenges. *The International Journal of*

Biochemistry & Cell Biology, 75, 143–147.
<https://doi.org/10.1016/J.BIOCEL.2016.01.005>

Aim of the thesis

This research is focused on establishing criteria for material safety design by identifying the potential hazard toward human health that may arise during the production and use of nano enabled products containing metal-based nanoparticles (NPs). The main goals of the thesis are:

- To define the potential correlation of physical-chemical (p-chem) properties with negative biological effects.
- To investigate how distinct NPs may pose hazard to human health after their interaction with *in vitro* models of the lung alveolar epithelium.
- To develop novel methodologies to evaluate the hazard and provide relevant information for risk assessment.

We aim to provide evidence concerning the presence or absence of potential hazards associated with the new NPs, developed during the ASINA project (see paragraph 1.3), prior their pre-commercial exploitation. The possibility to reach the goals of the thesis will provide relevant information to minimize or remove any unwanted or unpredicted risk after intentional or unintentional exposure, thanks to the early evaluation of NPs safety and eventual re-design. In particular, the subsequent chapters will focus on different research activities performed to reach the thesis's goals.

Chapter 4 is focused on the study of the biological effects of Ag and TiO₂ NPs differing in size and surface properties on a monoculture of type II pneumocytes cultivated and exposed in submerged conditions (Figure 3.1). The goal is to assess the influence of the NP p-chem characteristics, as designed during the production process, on the modulation of selected biological endpoints, defined according to an Adverse Outcome Pathway (AOP) approach (see paragraph 2.3). This study allows to discern the safer

(less hazardous) and most promising NPs synthesized within the ASINA project, in accordance with the SbD framework (see paragraph 1.1.1).

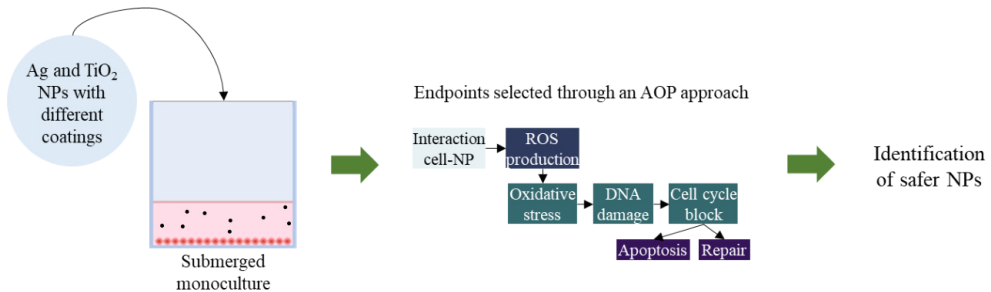


Figure 3.1 – Graphical abstract of chapter 4. The selection of different NPs in deep characterized for their main *p*-chem properties is followed by a classical toxicological approach. The biological outcomes tested are selected according to an AOPs approach to identify the hazard of the different NPs in relation to their *p*-chem characteristics.

Chapter 5 is focused on developing a New Approach Methodology (NAM, see chapter 2) that incorporates environmental monitoring, exposure modelling, and NP *p*-chem and *in vitro* inhalation toxicity data to assess the risk of selected NPs (Figure 3.2). The most promising NPs (selected through the study shown in chapter 4) were tested on a co-culture of human type II pneumocytes and macrophages cultivated and exposed at the ALI (see paragraph 2.2) through commercial systems for aerosol exposure (see paragraph 2.4). The doses were selected based on lung-retained doses calculated through an *in silico* model, using input data collected during a monitoring campaign at a manufacturing site of nano enabled materials (coated textiles). In addition to suggest a new NAM, this study contributed to the definition of the NPs hazard at realistic conditions of exposure, therefore providing information useful for risk assessment.

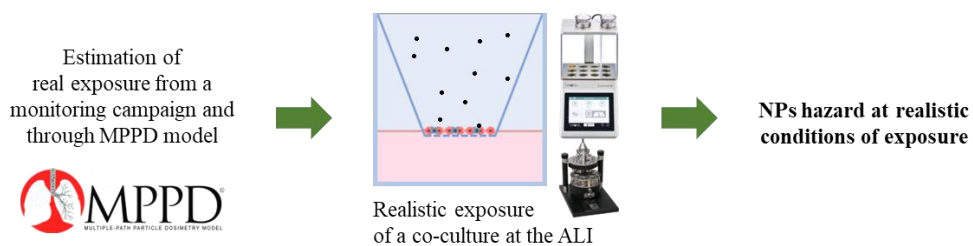


Figure 3.2 – Graphical abstract of chapter 5. The integration of the *in silico* approach with the ALI exposure systems is reported. The data collected at the relevant exposure doses are providing information for hazard evaluation and risk assessment.

Toxicological analysis in a Safe-by-Design and Adverse Outcome Pathway-driven approach on different silver and titania nanoparticles: assessment of acute responses in A549 cells

This chapter is largely based on the published paper “Preliminary Toxicological Analysis in a Safe-by-Design and Adverse Outcome Pathway-Driven Approach on Different Silver Nanoparticles: Assessment of Acute Responses in A549 Cells (Motta et al., 2020. Annex I). The results have been integrated with unpublished data on the toxicity of TiO₂ (TiO₂NKD) and nitrogen-doped TiO₂ (TiO₂-N), and of additional Ag-based NPs: Ag-doped with curcumin (AgCUR) and Ag-doped with hydroxyethylcellulose in suspension form with a HEC/Ag molar ratio of 6.4 (AgHEC_{S6.4}).

4.1 Introduction

Silver and titania nanoparticles (Ag and TiO₂ NPs) are among the most widely used metal-based nanomaterials (NMs) for several applications. Such important use is mainly due to their peculiar properties. In fact, thanks to their antibacterial capability (Nowack et al., 2011), Ag NPs are nowadays used in several fields, from the textile industry to biomedical application (Beyene et al., 2017; Shanmuganathan et al., 2019). Moreover, their use as antimicrobial materials is gaining relevance for their capability to combat pathogens causing infections *in vitro* and *in vivo* (Bruna et al., 2021). Ag NPs are present in different products, health care and fitness, cleaning, food packaging, household equipment, electronic devices and even toys (Natsuki, 2015; Tortella et al., 2020). The photocatalytic properties of TiO₂ NPs are relevant for several applications, including the formulation of sun creams, tattoo inks,

paint, purification products, and photovoltaic cells. Additionally, these NPs are employed in biomedicine, particularly in drug delivery (Chen and Selloni, 2014).

The widespread uses inevitably increase the possibility of accidental release of these NPs to the environment, with a consequent increase in the exposure of humans and other organisms (Burduşel et al., 2018). The various routes of exposure for humans are therefore multiple: ingestion, inhalation, dermal contact and, at times, directly in systemic circulation via intravenous injection. NMs may cause inflammatory response or reactive oxygen species (ROS) production (Huang et al., 2010); these are processes that can alter the cell membrane and damage organelles (Ahmadian et al., 2018). It has been observed (De Matteis and Rinaldi, 2018) that Ag NPs induce ROS production and cell apoptosis through a caspase-dependent intracellular pathway in liver hepatocellular adenocarcinoma cell line (HepG2). Other authors also observed the induction of ROS production and a reduction in glutathione (GH) after Ag NP exposure due to the release of free Ag⁺ ions. The increase in ROS caused adverse effects on cell viability and cell membrane integrity in several cell lines, both human and murine (Gurunathan et al., 2018). Therapeutic synthesized Ag NP exposure showed a dose- and time-dependent inhibition of cell viability, cell proliferation and cell morphology in A549 cells because of the increased oxidative stress (Han et al., 2014).

TiO₂ NPs are often associated to genotoxic effects, induced by ROS generation according to the particle's reactivity (Jugan et al., 2012). In fact, in cells representative of the alveolar-capillary barrier, TiO₂ NPs were found to induce the generation of ROS, apoptosis induction, and DNA damage (Hanot-Roy et al., 2016). Moreover, these NPs may impair the activity of mitochondrial dehydrogenase and reduce the mitochondrial membrane potential, possibly resulting in apoptosis (Ghosh et al., 2013).

Noteworthy, after entering in contact with cells, NPs can undergo different possible transformations in terms of their pristine physical-chemical (p-chem) properties; for several metal oxide NPs, dissolution has been reported as a major process, and agglomeration and other surface modifications are reported to play a key role in NP effects (Gulumian and Cassee, 2021).

Although these possible drawbacks, NPs and nano-enabled products (NEPs) are gaining relevance in everyday life. In light of this, to reduce the uncertainty of the potential adverse impact of NPs or NEPs on human health and the environment, already starting from the first steps of nanomaterial (NM) conceptualization and production and onwards, the application of the safe-by-design (SbD) strategy has been proposed and applied (Halappanavar et al., 2020). Among the different toxicological tests suggested for a SbD approach, viability and the generation of reactive oxygen species should be considered. In addition to this, additional biological endpoints, such as inflammation, and the stability of the NM itself should be considered. In this context, and in view of the 3Rs principle, *in vitro* studies are gaining prominent relevance to collect significant data to sustain the lack or reduce the unwanted and undesired intrinsic hazards of NPs and NEPs, in a life cycle-oriented approach.

In this study, six different Ag NPs and two TiO₂ NPs were selected to investigate how their p-chem properties might modulate the interactions with cells in a simple *in vitro* system (human alveolar adenocarcinoma A549 cells in monoculture). The biological endpoints were selected considering the main adverse outcome pathways (AOPs) related to chronic inflammation. The AOP 173 (<https://aopwiki.org/aops/173>), with its molecular-initiating event (MIE), key events (KE) (oxidative stress and inflammatory cytokines release) and the final adverse outcome (AO) is related to lung fibrosis and was mainly considered in this work. Indeed, this AOP was recently reported to appropriately describe the toxicological impact of some NMs that interact with cell membrane components (e.g., receptors and lipids) (MIE) and lead to lung

fibrosis, such as carbon nanotubes, TiO₂ or cerium oxide nanoparticles (Zhou et al., 2019; Ma et al., 2017; Roda et al., 2019; Sun et al., 2015; Wang et al., 2017). In addition to the above mentioned KE, DNA damage and cell cycle alteration were also considered for further assessing the possible adverse effects of NPs on lung epithelial cells, and because DNA damage is a consequence of oxidative stress and inflammation while cell cycle arrest is a consequence of DNA damage. Other AOPs relevant for NPs toxicity but not directly related to lung adverse outcomes are reported in Chapter 2 and not further described here.

4.2 Materials and Methods

The materials and methods of this chapter are briefly reported in the following sections. For more details, refer to Annex I.

4.2.1 Chemicals and Reagents

We selected different Ag and TiO₂ NPs both commercial and synthesized in the framework of the ASINA European project. The Ag and TiO₂ without coating (AgNKD and TiO₂NKD, as reference materials) and Ag with PVP surface coating (AgPVP) were selected as commercially available NPs. The nitrogen-doped titania (TiO₂-N) and Ag NPs coated with curcumin (AgCUR) or hydroxyethylcellulose delivered as powder form (AgHECp) or as colloidal suspension (AgHECs), in this latter case with two different HEC/Ag molar ratio (AgHECs_{5.5} and AgHECs_{6.4}). Additional information on the other relevant chemicals and reagents are reported in Annex I.

4.2.2 NP Suspension Preparation

NP suspensions for characterization and treatments were prepared in MilliQ water to reach an initial stock suspension of 1 mg/mL of Ag or TiO₂ NPs (considering the mass of Ag or TiO₂ core as reference, the concentrations here

reported are to be considered as mass of Ag or mass of TiO₂ per mL). The NPs in powder form (AgNKD, AgPVP, AgHECp, TiO₂NKD and TiO₂-N) were sonicated with an ultra-sonicator by applying in total 40W for 10 min (1 s pulse, 1 s pause cycle). NPs in colloidal suspension form (AgHECs_{5.5}, AgHECs_{6.4} and AgCUR) were vortexed and directly diluted in MilliQ water to reach the desired concentration. Additional information on the suspensions' preparation is reported in Annex I.

4.2.3 NP Characterization

NPs were characterized in terms of size, shape, surface charges (ζ -potential), agglomeration state and dispersion by Dynamic Light Scattering (DLS) analysis and by transmission electron Microscopy (TEM) after being diluted in MilliQ at 100 $\mu\text{g}/\text{mL}$. All the suspensions were analyzed by DLS at time 0, just after preparation, and after 24 h of incubation at RT without vortexing to assess NP stability in solution.

4.2.4 Cell Culture

Human alveolar epithelial cells (A549 cell line) were used as a model to evaluate NPs cytotoxicity. They were cultivated in DMEM medium supplemented with 10% fetal bovine serum and 1% antibiotics. Cells were treated with concentrations of NPs ranging from 0 to 100 $\mu\text{g}/\text{mL}$ for 24 h and then processed for further analysis. Additional information on the used protocols is in the Annex I.

4.2.5 Viability Assay

The cell viability was assessed with the Alamar Blue assay 24 h after the exposure to the NPs. The fluorescence emission at 590 nm was recorded and the viability is expressed as relative variation over the control ratio. Additional information on the protocol is reported in the Annex I.

4.2.6 Inflammatory Response

The inflammatory potency of the tested NPs was assessed by measuring the release of Interleukin 8 (IL-8 ELISA matched antibody pair kit) in the supernatants collected after 24 h of exposure. The samples absorbance was measured at the wavelength of 450 nm. Data are expressed as fold increase with respect to the control. Additional information on the protocol is reported in the Annex I.

4.2.7 Intracellular ROS

The intracellular ROS level was measured using 2',7'-dichlorodihydrofluorescein diacetate (H₂DCFDA) probe. H₂O₂ was used as positive control. Fluorescence was measured using flow cytometry with an excitation wavelength of 488 nm and an emission wavelength of 525 nm. Detailed information on the protocol used is reported in Annex I.

4.2.8 DNA Damage

γ H2AX was evaluated as a marker for DNA double-strand breaks (DSBs). The samples were stained using Phospho-Histone H2A.X (Ser139) (20E3) Rabbit mAb (Alexa Fluor® 488 Conjugate) following the manufacturer instructions. Fluorescence was measured using flow cytometry with an excitation wavelength of 488 nm and an emission wavelength of 525 nm. Additional information is available in Annex I.

4.2.9 Cell-Particle Bio-Interaction

At the end of the exposure, the samples were analyzed using a CytoFlex with an excitation wavelength of 488 nm. The side scatter signal (SSC) was recorded as proxy variable of the particle-cell interaction (both at cell membrane and/or after internalization).

4.2.10 Statistical Analysis

Data are expressed as the mean \pm standard error (SE) or standard deviation (SD) of at least three biological independent experiments ($N > 3$, if not otherwise stated). Statistical analyses were performed using R software, using one-way ANOVA test followed by Dunnett's post hoc test if the homogeneity of variance was confirmed by Levene's test; conversely, the pairwise Wilcoxon test was applied to determine statistical differences; values of $p < 0.05$ were considered statistically significant.

4.3 Results

4.3.1 NP Characterization for Toxicological Analyses

Except for TiO₂NKD, NPs hydrodynamic diameters showed a general tendency to reduce over the time; among the different NPs, the AgHECS_{5.5}, AgHECp and especially AgCUR NPs showed the lower variation of the hydrodynamic diameter over 24 h (Table 4.1).

*Table 4.1. NP characterization for cell exposure. Dynamic Light Scattering (DLS) analysis performed for Ag NPs (AgNKD, AgPVP, AgHECS_{5.5}, AgHECS_{6.4}, AgHECp and AgCUR) and TiO₂ NPs (TiO₂NKD and TiO₂-N) in MilliQ water. The measurements were performed at two different time points, 0 and 24 h, and two concentrations (10 and 100 $\mu\text{g}/\text{mL}$) were considered. In the table are reported the values of z-average (nm) \pm SD and PDI \pm SD, for each particle is indicated the value ζ -potential (mV) in MilliQ water at the concentration of 100 $\mu\text{g}/\text{mL}$. * = mean of two replicates.*

NPs	Time (h)	ppm	z-average (nm) ± SD	PdI ± SD
AgNKD ζ-potential (mV ± SD): -27.57 ± 0.60	0	100	270.76 ± 53.18	0.45 ± 0.04
	24	100	109.35 ± 22.42	0.34 ± 0.08
	0	10	266.29 ± 35.96	0.47 ± 0.01
	24	10	142.52 ± 51.02	0.29 ± 0.05
AgPVP ζ-potential (mV ± SD): -6.07 ± 0.59	0	100	695.91 ± 617.49	0.7 ± 0.26
	24	100	227.06 ± 159.62	0.45 ± 0.15
	0	10	1515.88 ± 928.18	0.92 ± 0.14
	24	10	591.67 ± 192.93	0.81 ± 0.16
AgHECs _{5.5} ζ-potential (mV ± SD): -4.71 ± 0.24	0	100	122.16 ± 5.89	0.14 ± 0.02
	24	100	115.70 ± 5.37	0.15 ± 0.01
	0	10	122.04 ± 10.16	0.14 ± 0.02
	24	10	109.41 ± 8.36	0.15 ± 0.003
AgHECs _{6.4} ζ-potential (mV ± SD): +21.1 ± 0.9	0	100	353.20 ± 152.61	0.31 ± 0.06
	24	100	158.75 ± 63.33*	0.40 ± 0.15*
	0	10	254.489 ± 149.05	0.40 ± 0.09
	24	10	173.92 ± 7.75*	0.36 ± 0.11*
AgHECp ζ-potential (mV ± SD): +9.92 ± 0.37	0	100	304.89 ± 34.89	0.37 ± 0.07
	24	100	261.63 ± 26.86	0.36 ± 0.06
	0	10	293.83 ± 6.76	0.41 ± 0.06
	24	10	219.33 ± 5.13	0.4 ± 0.01
AgCUR ζ-potential (mV ± SD): -34.13 ± 1.59	0	100	91.27 ± 5.79	0.31 ± 0.01
	24	100	86.17 ± 4.42	0.33 ± 0.02
	0	10	93.30 ± 7.02	0.34 ± 0.03
	24	10	90.78 ± 7.52	0.33 ± 0.01
TiO ₂ NKD ζ-potential (mV ± SD): +18.26 ± 3.97	0	100	210.43 ± 10.34	0.13 ± 0.04
	24	100	227.59 ± 70.54	0.13 ± 0.01
	0	10	223.57 ± 36.07	0.17 ± 0.05
	24	10	476.59 ± 410.76	0.47 ± 0.15
TiO ₂ -N ζ-potential (mV ± SD): -17.45 ± 3.36	0	100	1838.76 ± 912.16	0.96 ± 0.05
	24	100	472.69 ± 84.53	0.74 ± 0.08
	0	10	10379.41 ± 2719.64	0.76 ± 0.17
	24	10	161.69 ± 59.01	0.34 ± 0.06

The ζ-potential resulted highly negative for AgCUR, AgNKD and TiO₂-N (respectively -34.13, -27.57 and -17.45 mV), slightly negative for AgPVP and

Ag-HECs_{5.5} (-6.07 mV and -4.71 mV, respectively) and positive for AgHECp, AgHECs_{6.4} and TiO₂NKD (+9.92, +21.1 and +18.26 mV). This differential surface property of the different NPs is related to the different doping and the particle delivery forms, the ζ -potential of HECs and HECp being different.

NP suspensions, prepared in MilliQ water, were also analyzed by transmission electron microscopy (TEM) to qualitatively evaluate their morphology and agglomeration state (Figure 4.1). All the NPs showed primary particles with a spherical shape in the range of 20 to 30 nm. AgHECs_{5.5}, AgHECp and AgCUR resulted better dispersed compared to the other NPs, which were characterized by agglomerates in the order of hundreds of nm, as already observed by DLS analysis. This difference in agglomeration is a relevant outcome of the different surface modifications which allow for a better dispersion during manufacturing processes, such as spray coating of textile, at the same time, agglomeration state greatly affects bio-interactions and effects in living cells.

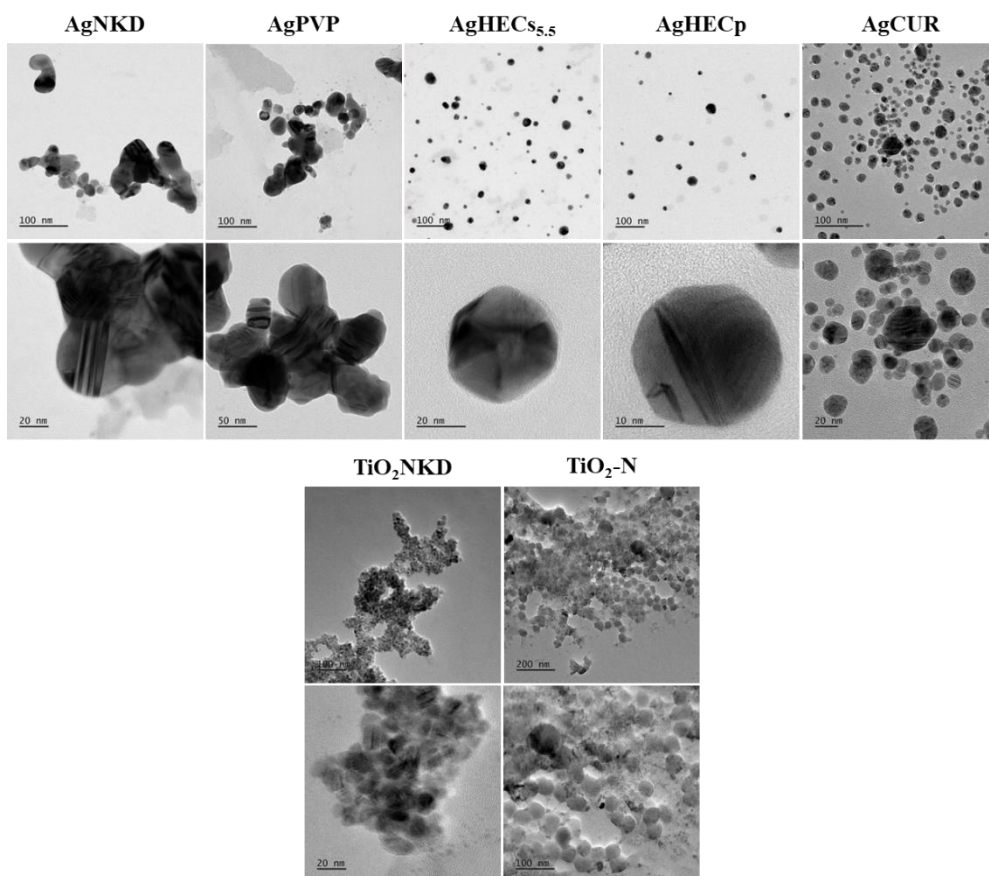


Figure 4.1. Transmission electron microscopy images of Ag and TiO₂ NP suspensions. NPs in MilliQ water were analyzed by TEM. The images show how particle suspensions are dispersed and a detail of small agglomerates or single particles.

4.3.2 Cell Viability

Viability decreased concentration-dependently for all the Ag particles tested, but the AgCUR and AgHECS_{5.5}, with a clearer effect for the AgHECp NPs and, especially, AgHECS_{6.4} (this latter not further tested due to the high cytotoxicity). TiO₂ NPs showed no effect on cell viability at the tested concentrations (Figure 4.2 and 4.3). Given the general low cytotoxicity of these NPs, the 24 h IC₅₀ was calculated only for AgHECp and AgHECS_{6.4}

(Table 4.2) while for the other NPs we assume the IC₅₀ to be higher than 100 µg/mL.

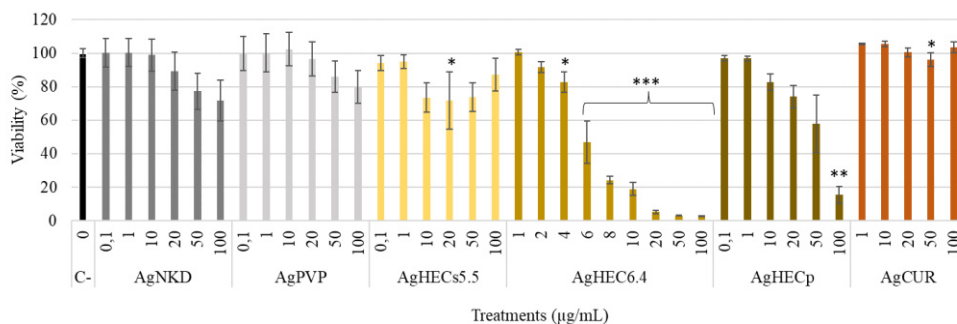


Figure 4.2. Cell viability after Ag NPs exposure. The graphs show the percentages of cell viability compared to the negative control, assessed by Alamar Blue assay after 24 h of treatment. Data are presented as the mean of at least three independent experiments ± SE. Statistical analysis: one-way ANOVA followed by Dunnett’s test. * $p < 0.05$ compared to control; ** $p < 0.01$ compared to control; *** $p < 0.001$ compared to control group.

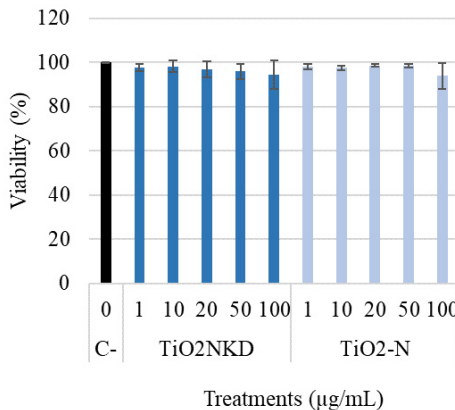


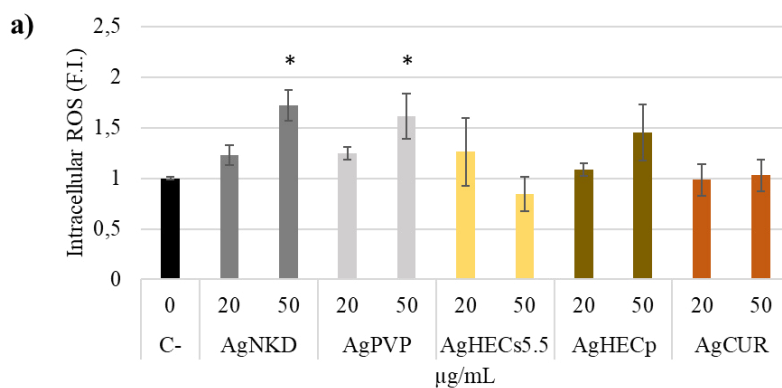
Figure 4.3. Cell viability after TiO₂ NPs exposure. The graphs show the percentages of cell viability compared to the negative control, assessed by Alamar Blue assay after 24 h of treatment. Data are presented as the mean of at least three independent experiments ± SE. Statistical analysis: one-way ANOVA followed by Dunnett’s test. * $p < 0.05$ compared to control; ** $p < 0.01$ compared to control; *** $p < 0.001$ compared to control group.

Table 4.2. IC₅₀ after 24h of exposure to NPs. Given the high cytotoxic effect at the concentrations used for the experiments, the lower and upper EC50 limits for AgHECs_{6.4} were not calculated by the statistical analysis.

	Estimate	Lower limit	Upper limit
AgHECs _{6.4}	7,29	-	-
AgHECp	57,05	47,61	70,01

4.3.3 Reactive Oxygen Species Formation

After 90 min of treatment, AgNKD and AgPVP at the exposure concentration of 50 µg/mL and TiO₂NKD at the exposure concentration of 100 µg/mL induced a significant increase in intracellular ROS. A non-significant increase was observed in AgHECp and TiO₂-N exposed cells, while absence of modulation was observed in AgHECs_{5.5} and AgCUR treatments (Figure 4.4).



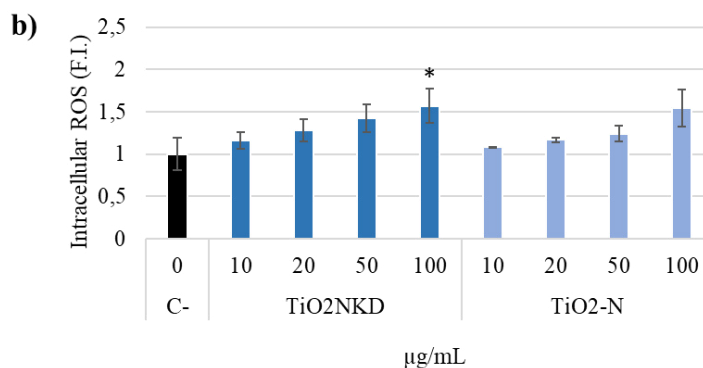
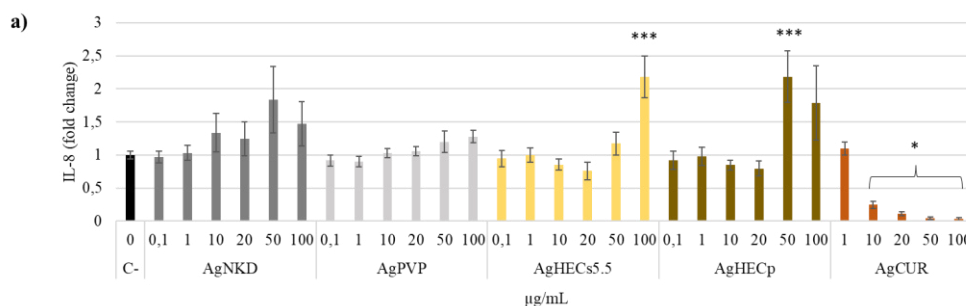


Figure 4.4. Reactive oxygen production after 90 min of treatment. a) Ag NPs treatments; b) TiO₂ NPs treatments. Data are presented as the mean of at least three independent experiments \pm SE. Statistical analysis: one-way ANOVA followed by Dunnett's test. * $p < 0.05$ compared to control non exposed cells.

4.3.4 Inflammatory Response (IL-8 Release)

The release of the inflammatory mediator (IL-8) in A549 cells after 24 h of exposure to Ag NPs was modulated differently by the different NPs (Figure 4.5a). Although some increase of IL-8 in treated samples, statistically significant increases were observed only for the higher concentrations of AgHECs_{5.5} (100 µg/mL) and at the concentration for 50 µg/mL of AgHECp. AgPVP was the least active in inducing IL-8 modulation. Interestingly, AgCUR NPs reduced the release of IL-8 in a concentration-dependent fashion, with significant reduction already at 10 µg/mL. TiO₂ NPs had no significant modulation on IL-8 release (Figure 4.5b).



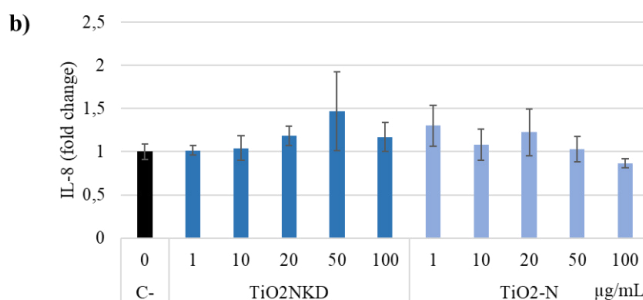
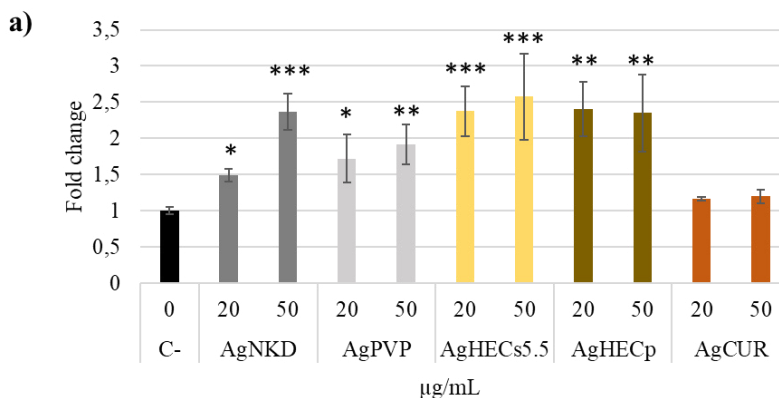


Figure 4.5. The inflammatory response (IL-8 release). IL-8 protein concentration was differently modulated by the NPs. a) Ag NPs treatments; b) TiO₂ NPs treatments. Data are presented as the mean of at least three independent experiments \pm SE. Statistical analysis: one-way ANOVA followed by Dunnett's test. * $p < 0.05$ and *** $p < 0.001$ compared to control group.

4.3.5 Oxidative DNA Damage (γ H2AX)

The increase in the fluorescent signal of H2AX (Figure 4.6) after A549 treatment with the different NPs was significant for all the Ag NPs at the concentrations tested (20 and 50 μ g/mL), except for AgCUR NPs. The AgHEC NPs showed a high increase in H2AX phosphorylation at the concentration of exposure of 20 μ g/mL. TiO₂ NPs exposure caused an increase in H2AX phosphorylation, significant only for TiO₂-N at 50 and 100 μ g/mL.



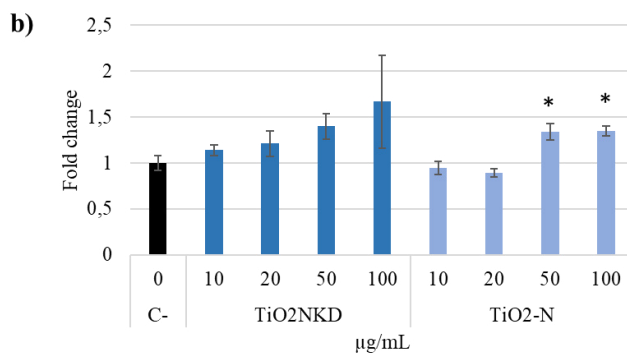


Figure 4.6. DNA damage (expressed as FC of γ H2AX) was determined by quantifying the increase in the γ H2AX protein. a) Ag NPs treatments; b) TiO₂ NPs treatments. Data are presented as the mean of at least three independent experiments \pm SE. Statistical difference analyzed by one-way ANOVA and Dunnett's test. * $p < 0.05$ compared to control; ** $p < 0.01$ compared to control; *** $p < 0.001$ compared to control.

4.3.6 Cell-Particle Bio-Interactions

The SSC reported show (Figure 4.7) that A549 cells treated with AgCUR, TiO₂-N, AgNKD and AgPVP had the lowest scattering values and the Ag-treated were statistically different from the control only at the higher concentration of exposure (except for AgCUR NPs that showed no statistical significance at the concentration tested, maybe due to their higher stability in suspension that may reduce the number of depositing NPs and their lower interactions with cell membrane due to the negative surface charge). On the contrary, cells treated with AgHECs_{5.5} and AgHECp resulted in higher SSC values and therefore higher cell-particle interactions (significant values different from the controls already at the concentration of 10 μ g/mL, $p < 0.001$). Cells treated with TiO₂NKD NPs had the higher scattering values, statistically significant at all the tested concentrations, while for TiO₂-N only the higher concentrations (50 and 100 μ g/mL) were significant.

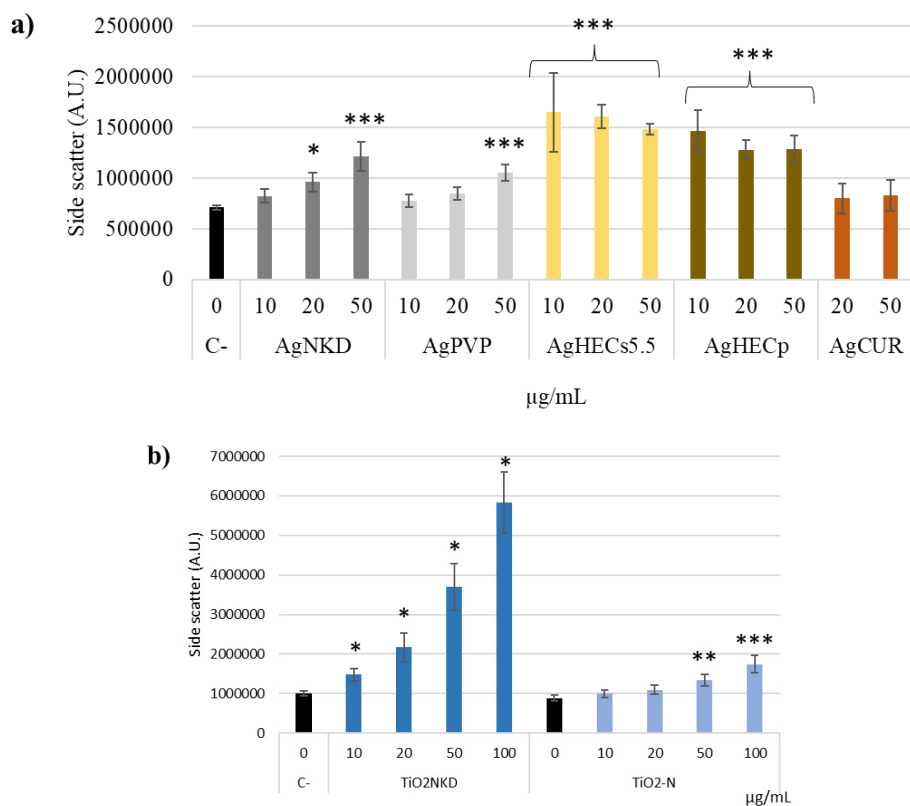


Figure 4.7. Bio-interaction analysis. The side scatter (SSC) values of cells exposed at different concentrations of the different NPs. a) Ag NPs treatments; b) TiO₂ NPs treatments. Data are presented as the mean of at least three independent experiments \pm SE. Statistical analysis: one-way ANOVA followed by Dunnett's test; * p -value = 0.05; *** p -value = 0.001 compared to control.

4.4 Discussion

Ensuring the safety of NMs and NEPs is crucial due to their potential intrinsic hazard at the nanoscale (Demir, 2021; Schmutz et al., 2020). Typically, toxicological evaluations are performed after synthesis to determine if these particles pose a risk to humans and the environment. SbD approaches aim to provide early evidence of safety throughout the life cycle of NMs, minimizing unexpected risks post-exposure (Delrue et al., 2016; Ma et al., 2017). Key questions revolve around the predictive capacity of SbD for chronic effects, given the absence of acute toxicity. AOPs have offered a novel framework for

supporting SbD approaches (Delrue et al., 2016). Within the framework of AOPs, we identified AOP #173 related to lung fibrosis of substances interacting with the membrane components (e.g., receptors and lipids) of lung cells, leading to fibrosis. The induction of lung fibrosis due to NP exposure has been proposed by several researchers (Ma et al., 2017; Roda et al., 2019; Sun et al., 2015; Wang et al., 2017). Data indicates the interaction of Ag NPs with cell membranes, with internalization playing a significant role in cytotoxicity. Indeed, the capability of some metal or metal oxide NPs to exert their adverse effects through the intracellular release of metal ions after internalization is largely reported (Glinski et al., 2021; Lubick, 2008; Niu and Tang, 2022; Studer et al., 2010). Internalized NPs might interact with cellular macromolecules according to their affinity or by generating ROS (Capasso et al., 2014; Niu and Tang, 2022). TiO₂ NPs proved to be safer, despite being able to be internalized by the cells, TiO₂NKD was only able to induce ROS production at the higher dose, while TiO₂-N was effective in inducing H2AX phosphorylation, with a minor entity with respect to Ag NPs. In the literature, it is proven that TiO₂ NPs are able to induce the formation of ROS and inflammatory response, but the entity of their cytotoxicity strongly depends on the cell line and the exposure conditions (Bacova et al., 2022; Brandão et al., 2020). Although the relatively low TiO₂-induced acute toxicity, and considering its ability to accumulate into the cells, particular attention should be dedicated to the chronic cytotoxic effects of this insoluble and persistent particles since their long-term toxicity is reported (Armand et al., 2016; Coccini et al., 2015; Shajari et al., 2021).

The results here reported show a significant increase in ROS after 90 min of exposure for Ag NPs, according to the expected oxidative burst usually reported few hours after exposure of *in vitro* or *in vivo* models to NPs (Capasso et al., 2014; Martins et al., 2017; Moschini et al., 2013; Rahmanian et al., 2021). We would like to speculate, that the absence of positive results with

the HEC coated NPs, may be related to a quenching effect or a masking effect of the HEC over the fluorescent probe used to test ROS. In fact, according to the short life of reactive species in cells, we observed, also in HEC coated Ag NPs, the increase in H2AX, a marker of oxidative damage of the DNA, that is also related to precedent ROS formation (Hoffmann and Griffiths, 2018; Zhao et al., 2016). ROS generation and inflammatory mediator release have been associated (Castranova, 2004; Delgado-Roche and Mesta, 2020; Geering et al., 2013; Sharma et al., 2021), contributing to the modulation of IL-8 we reported here. The activation of the inflammation a significant key event in lung fibrosis (Alessandri et al., 2013; Gomez-Mejiba et al., 2009; Nissinen and Kähäri, 2014; Selman and Pardo, 2020). The differences we have observed between the differentially coated NPs are relevant in the SbD concept. AgCUR NPs appeared to induce fewer adverse events related to the selected AOP, compared to AgNKD and AgPVP, whereas AgHEC NPs exhibit differences in toxicity based on the HEC coating. AgHECp display higher toxicity, determining the highest cytotoxicity and IL-8 modulation, while the DNA damaging potency was similar between the two AgHEC NPs. The higher toxicity of AgHEC NPs could be related to both their higher stability and lower agglomeration in toxicological media as compared to reference Ag NPs (Ciekot et al., 2021; Sheikhi et al., 2019), and the direct effect of the HEC coating in favouring the internalization of the Ag NPs (Ciekot et al., 2021). The lower toxicity of AgCUR NPs may be explained through the well-known antioxidant and anti-inflammatory properties of curcumin (Mary et al., 2018; Peng et al., 2021). The results here reported support that curcumin may counteract the adverse effects of Ag NPs after doping particles surface, being a safer solution. Nonetheless the capability of curcumin to alter the inflammatory response pathway should be considered in relation to the specific application the NPs are intended. Finally, in the context of SbD and AOP outcomes, the production and use of AgHEC NPs should

involve wet procedures rather than drying the NPs for subsequent applications, given the different toxic effects reported for these two NPs. The increased hazard of AgHEC in powder form may relate to potential p-chem transformations of the coating polymer during the processes, although specific analyses are needed to define the actual chemical or physical transformation of the doping molecule.

4.5 Conclusions

In conclusion, novel NPs were characterized and tested in parallel for their hazards according to a SbD approach combined with relevant AOP events. The combination of these two relevant frameworks showed efficacy in characterizing the hazards of different NPs and defining which production and use procedure should be considered with lower expected risk. The doping of the surface of NPs seems to have a primary role in driving the toxicity of the newly synthesized particles and the selection of coated NPs with lower intrinsic hazards should be favored for subsequent testing and use in manufacturing procedure.

4.6 Data curation

The data collected during the toxicological analysis were useful for the development of quantitative models to predict hazard (Annex II). The collected data were curated and merged for the development of new approach methodologies based on regression and classification machine learning algorithms, aiming at predicting a hazard class. The probabilistic model developed is based on Bayesian networks to predict hazard, achieving an average accuracy of around 78%. This work demonstrates the practical application of the SbD approach, providing quantitative hazard criteria for safer NMs synthesis, highlighting challenges, and paving the way for future

criteria that can guide material engineers and enable a fast and cost-efficient *in silico* toxicological screening of new NMs.

4.7 References

- Ahmadian, E., Dizaj, S.M., Rahimpour, E., Hasanzadeh, A., Eftekhari, A., Hosain zadegan, H., Halajzadeh, J., Ahmadian, H., 2018. Effect of silver nanoparticles in the induction of apoptosis on human hepatocellular carcinoma (HepG2) cell line. *Mater. Sci. Eng. C* 93, 465–471. <https://doi.org/10.1016/J.MSEC.2018.08.027>
- Alessandri, A.L., Sousa, L.P., Lucas, C.D., Rossi, A.G., Pinho, V., Teixeira, M.M., 2013. Resolution of inflammation: Mechanisms and opportunity for drug development. *Pharmacol. Ther.* 139, 189–212. <https://doi.org/10.1016/J.PHARMTHERA.2013.04.006>
- Armand, L., Tarantini, A., Beal, D., Biola-Clier, M., Bobyk, L., Sorieul, S., Pernet-Gallay, K., Marie-Desvergne, C., Lynch, I., Herlin-Boime, N., Carriere, M., 2016. Long-term exposure of A549 cells to titanium dioxide nanoparticles induces DNA damage and sensitizes cells towards genotoxic agents. *Nanotoxicology* 10, 913–923. <https://doi.org/10.3109/17435390.2016.1141338>
- Bacova, J., Knotek, P., Kopecka, K., Hromadko, L., Capek, J., Nyvltova, P., Bruckova, L., Schröterova, L., Sestakova, B., Palarcik, J., Motola, M., Cizkova, D., Bezrouk, A., Handl, J., Fiala, Z., Rudolf, E., Bilkova, Z., Macak, J.M., Rousar, T., 2022. Evaluating the Use of TiO₂ Nanoparticles for Toxicity Testing in Pulmonary A549 Cells. *Int. J. Nanomedicine* 17, 4211–4225. <https://doi.org/10.2147/IJN.S374955>
- Beyene, H.D., Werkneh, A.A., Bezabh, H.K., Ambaye, T.G., 2017. Synthesis paradigm and applications of silver nanoparticles (AgNPs), a review. *Sustain. Mater. Technol.* 13, 18–23. <https://doi.org/10.1016/J.SUSMAT.2017.08.001>
- Brandão, F., Fernández-bertólez, N., Rosário, F., Bessa, M.J., Fraga, S., Pásaro, E., Teixeira, J.P., Laffon, B., Valdíglesias, V., Costa, C., 2020. Genotoxicity of TiO₂ Nanoparticles in Four Different Human Cell Lines (A549, HEPG2, A172 and SH-SY5Y). *Nanomater.* 2020, Vol. 10, Page 412 10, 412. <https://doi.org/10.3390/NANO10030412>
- Bruna, T., Maldonado-Bravo, F., Jara, P., Caro, N., 2021. Silver Nanoparticles and Their Antibacterial Applications. *Int. J. Mol. Sci.* 2021, Vol. 22, Page 7202 22, 7202. <https://doi.org/10.3390/IJMS22137202>
- Burduşel, A.C., Gherasim, O., Grumezescu, A.M., Mogoantă, L., Ficiu, A., Andronescu, E., 2018. Biomedical Applications of Silver Nanoparticles: An Up-to-Date Overview. *Nanomater.* 2018, Vol. 8, Page 681 8, 681. <https://doi.org/10.3390/NANO8090681>
- Capasso, L., Camatini, M., Gualtieri, M., 2014. Nickel oxide nanoparticles induce inflammation and genotoxic effect in lung epithelial cells. *Toxicol. Lett.* 226, 28–34. <https://doi.org/10.1016/J.TOXLET.2014.01.040>
- Castranova, V., 2004. Signaling Pathways Controlling The Production Of Inflammatory Mediators in Response To Crystalline Silica Exposure: Role Of Reactive Oxygen/Nitrogen Species. *Free Radic. Biol. Med.* 37, 916–925. <https://doi.org/10.1016/J.FREERADBIOMED.2004.05.032>
- Chen, X., Selloni, A., 2014. Introduction: Titanium Dioxide (TiO₂) Nanomaterials. *Chem. Rev.* 114, 9281–9282. <https://doi.org/10.1021/CR500422R>

- Ciekot, J., Psurski, M., Jurec, K., Boratyński, J., 2021. Hydroxyethylcellulose as a methotrexate carrier in anticancer therapy. *Invest. New Drugs* 39, 15–23. <https://doi.org/10.1007/S10637-020-00972-9/TABLES/6>
- Coccini, T., Grandi, S., Lonati, D., Locatelli, C., De Simone, U., 2015. Comparative cellular toxicity of titanium dioxide nanoparticles on human astrocyte and neuronal cells after acute and prolonged exposure. *Neurotoxicology* 48, 77–89. <https://doi.org/10.1016/J.NEURO.2015.03.006>
- De Matteis, V., Rinaldi, R., 2018. Toxicity assessment in the nanoparticle era. *Adv. Exp. Med. Biol.* 1048, 1–19. https://doi.org/10.1007/978-3-319-72041-8_1/COVER
- Delgado-Roche, L., Mesta, F., 2020. Oxidative Stress as Key Player in Severe Acute Respiratory Syndrome Coronavirus (SARS-CoV) Infection. *Arch. Med. Res.* 51, 384–387. <https://doi.org/10.1016/J.ARCMED.2020.04.019>
- Delrue, N., Sachana, M., Sakuratani, Y., Gourmelon, A., Leinala, E., Diderich, R., 2016. The Adverse Outcome Pathway Concept: A Basis for Developing Regulatory Decision-making Tools. <https://doi.org/10.1177/026119291604400504> 44, 417–429. <https://doi.org/10.1177/026119291604400504>
- Demir, E., 2021. A review on nanotoxicity and nanogenotoxicity of different shapes of nanomaterials. *J. Appl. Toxicol.* 41, 118–147. <https://doi.org/10.1002/JAT.4061>
- Geering, B., Stoeckle, C., Conus, S., Simon, H.U., 2013. Living and dying for inflammation: neutrophils, eosinophils, basophils. *Trends Immunol.* 34, 398–409. <https://doi.org/10.1016/J.IT.2013.04.002>
- Ghosh, M., Chakraborty, A., Mukherjee, A., 2013. Cytotoxic, genotoxic and the hemolytic effect of titanium dioxide (TiO₂) nanoparticles on human erythrocyte and lymphocyte cells in vitro. *J. Appl. Toxicol.* 33, 1097–1110. <https://doi.org/10.1002/JAT.2863>
- Glinski, A., Lima de Souza, T., Zablocki da Luz, J., Bezerra Junior, A.G., Camargo de Oliveira, C., de Oliveira Ribeiro, C.A., Filipak Neto, F., 2021. Toxicological effects of silver nanoparticles and cadmium chloride in macrophage cell line (RAW 264.7): An in vitro approach. *J. Trace Elem. Med. Biol.* 68, 126854. <https://doi.org/10.1016/J.JTEMB.2021.126854>
- Gomez-Mejiba, S.E., Zhai, Z., Akram, H., Pye, Q.N., Hensley, K., Kurien, B.T., Scofield, R.H., Ramirez, D.C., 2009. Inhalation of environmental stressors & chronic inflammation: Autoimmunity and neurodegeneration. *Mutat. Res. Toxicol. Environ. Mutagen.* 674, 62–72. <https://doi.org/10.1016/J.MRGENTOX.2008.09.016>
- Gulumian, M., Cassee, F.R., 2021. Safe by design (SbD) and nanotechnology: a much-discussed topic with a prudence? Part. *Fibre Toxicol.* 18, 1–4. <https://doi.org/10.1186/S12989-021-00423-0/METRICS>
- Gurunathan, S., Kang, M.H., Qasim, M., Kim, J.H., 2018. Nanoparticle-Mediated Combination Therapy: Two-in-One Approach for Cancer. *Int. J. Mol. Sci.* 2018, Vol. 19, Page 3264 19, 3264. <https://doi.org/10.3390/IJMS19103264>
- Halappanavar, S., Van Den Brule, S., Nymark, P., Gaté, L., Seidel, C., Valentino, S., Zhernovkov, V., Høgh Danielsen, P., De Vizcaya, A., Wolff, H., Stöger, T., Boyadziev, A., Poulsen, S.S., Sørli, J.B., Vogel, U., 2020. Adverse

- outcome pathways as a tool for the design of testing strategies to support the safety assessment of emerging advanced materials at the nanoscale. *Part. Fibre Toxicol.* 17, 1–24. <https://doi.org/10.1186/s12989-020-00344-4>
- Han, J.W., Gurunathan, S., Jeong, J.K., Choi, Y.J., Kwon, D.N., Park, J.K., Kim, J.H., 2014. Oxidative stress mediated cytotoxicity of biologically synthesized silver nanoparticles in human lung epithelial adenocarcinoma cell line. *Nanoscale Res. Lett.* 9, 1–14. <https://doi.org/10.1186/1556-276X-9-459/FIGURES/10>
- Hanot-Roy, M., Tubeuf, E., Guilbert, A., Bado-Nilles, A., Vigneron, P., Trouiller, B., Braun, A., Lacroix, G., 2016. Oxidative stress pathways involved in cytotoxicity and genotoxicity of titanium dioxide (TiO₂) nanoparticles on cells constitutive of alveolo-capillary barrier in vitro. *Toxicol. Vitro.* 33, 125–135. <https://doi.org/10.1016/J.TIV.2016.01.013>
- Hoffmann, M.H., Griffiths, H.R., 2018. The dual role of Reactive Oxygen Species in autoimmune and inflammatory diseases: evidence from preclinical models. *Free Radic. Biol. Med.* 125, 62–71. <https://doi.org/10.1016/J.FREERADBIOMED.2018.03.016>
- Huang, Y.W., Wu, C.H., Aronstam, R.S., 2010. Toxicity of Transition Metal Oxide Nanoparticles: Recent Insights from in vitro Studies. *Mater.* 2010, Vol. 3, Pages 4842–4859 3, 4842–4859. <https://doi.org/10.3390/MA3104842>
- Jugan, M.L., Barillet, S., Simon-Deckers, A., Herlin-Boime, N., Sauvaigo, S., Douki, T., Carriere, M., 2012. Titanium dioxide nanoparticles exhibit genotoxicity and impair DNA repair activity in A549 cells. *Nanotoxicology* 6, 501–513. <https://doi.org/10.3109/17435390.2011.587903>
- Lubick, N., 2008. Nanosilver toxicity: Ions, nanoparticles - Or both? *Environ. Sci. Technol.* 42, 8617. https://doi.org/10.1021/ES8026314/ASSET/IMAGES/MEDIUM/ES-2008-026314_0001.GIF
- Ma, J., Bishoff, B., Mercer, R.R., Barger, M., Schwegler-Berry, D., Castranova, V., 2017. Role of epithelial-mesenchymal transition (EMT) and fibroblast function in cerium oxide nanoparticles-induced lung fibrosis. *Toxicol. Appl. Pharmacol.* 323, 16–25. <https://doi.org/10.1016/J.TAAP.2017.03.015>
- Martins, A. da C., Azevedo, L.F., de Souza Rocha, C.C., Carneiro, M.F.H., Venancio, V.P., de Almeida, M.R., Antunes, L.M.G., de Carvalho Hott, R., Rodrigues, J.L., Ogunjimi, A.T., Adeyemi, J.A., Barbosa, F., 2017. Evaluation of distribution, redox parameters, and genotoxicity in Wistar rats co-exposed to silver and titanium dioxide nanoparticles. *J. Toxicol. Environ. Heal. Part A* 80, 1156–1165. <https://doi.org/10.1080/15287394.2017.1357376>
- Mary, C.P.V., Vijayakumar, S., Shankar, R., 2018. Metal chelating ability and antioxidant properties of Curcumin-metal complexes – A DFT approach. *J. Mol. Graph. Model.* 79, 1–14. <https://doi.org/10.1016/J.JMGM.2017.10.022>
- Moschini, E., Gualtieri, M., Colombo, M., Fascio, U., Camatini, M., Mantecca, P., 2013. The modality of cell–particle interactions drives the toxicity of nanosized CuO and TiO₂ in human alveolar epithelial cells. *Toxicol. Lett.* 222, 102–116. <https://doi.org/10.1016/J.TOXLET.2013.07.019>
- Natsuki, J., 2015. A Review of Silver Nanoparticles: Synthesis Methods, Properties and Applications. *Int. J. Mater. Sci. Appl.* 4, 325.

- <https://doi.org/10.11648/J.IJMSA.20150405.17>
- Nissinen, L., Kähäri, V.M., 2014. Matrix metalloproteinases in inflammation. *Biochim. Biophys. Acta - Gen. Subj.* 1840, 2571–2580. <https://doi.org/10.1016/J.BBAGEN.2014.03.007>
- Niu, Y., Tang, M., 2022. In vitro review of nanoparticles attacking macrophages: Interaction and cell death. *Life Sci.* 307, 120840. <https://doi.org/10.1016/J.LFS.2022.120840>
- Nowack, B., Krug, H.F., Height, M., 2011. 120 years of nanosilver history: Implications for policy makers. *Environ. Sci. Technol.* 45, 1177–1183. https://doi.org/10.1021/ES103316Q/SUPPL_FILE/ES103316Q_SI_001.PDF
- Peng, Y., Ao, M., Dong, B., Jiang, Y., Yu, L., Chen, Z., Hu, C., Xu, R., 2021. Anti-Inflammatory Effects of Curcumin in the Inflammatory Diseases: Status, Limitations and Countermeasures. *Drug Des. Devel. Ther.* 15, 4503–4525. <https://doi.org/10.2147/DDDT.S327378>
- Rahmanian, N., Shokrzadeh, M., Eskandani, M., 2021. Recent advances in γ H2AX biomarker-based genotoxicity assays: A marker of DNA damage and repair. *DNA Repair (Amst)*. 108, 103243. <https://doi.org/10.1016/J.DNAREP.2021.103243>
- Roda, E., Bottone, M.G., Biggiogera, M., Milanese, G., Coccini, T., 2019. Pulmonary and hepatic effects after low dose exposure to nanosilver: Early and long-lasting histological and ultrastructural alterations in rat. *Toxicol. Reports* 6, 1047–1060. <https://doi.org/10.1016/J.TOXREP.2019.09.008>
- Schmutz, M., Borges, O., Jesus, S., Borchard, G., Perale, G., Zinn, M., Sips, Á.A.J.A.M., Soeteman-Hernandez, L.G., Wick, P., Som, C., 2020. A Methodological Safe-by-Design Approach for the Development of Nanomedicines. *Front. Bioeng. Biotechnol.* 8, 509010. <https://doi.org/10.3389/FBIOE.2020.00258/BIBTEX>
- Selman, M., Pardo, A., 2020. The leading role of epithelial cells in the pathogenesis of idiopathic pulmonary fibrosis. *Cell. Signal.* 66, 109482. <https://doi.org/10.1016/J.CELLSIG.2019.109482>
- Shajari, Z., Golestani, A., Nowrouzi, A., 2021. Acute cytotoxic effects of Titanium dioxide (TiO₂) and chronic exposure to safe dose of nanoparticle on Hepatocarcinoma cell line (HepG2). *Nanomedicine Res. J.* 6, 269–278. <https://doi.org/10.22034/NMRJ.2021.03.007>
- Shanmuganathan, R., Karuppusamy, I., Saravanan, M., Muthukumar, H., Ponnuchamy, K., Ramkumar, V.S., Pugazhendhi, A., 2019. Synthesis of Silver Nanoparticles and their Biomedical Applications - A Comprehensive Review. *Curr. Pharm. Des.* 25, 2650–2660. <https://doi.org/10.2174/1381612825666190708185506>
- Sharma, A., Tewari, D., Nabavi, S.F., Nabavi, S.M., Habtemariam, S., 2021. Reactive oxygen species modulators in pulmonary medicine. *Curr. Opin. Pharmacol.* 57, 157–164. <https://doi.org/10.1016/J.COPH.2021.02.005>
- Sheikhi, A., Hayashi, J., Eichenbaum, J., Gutin, M., Kuntjoro, N., Khorsandi, D., Khademhosseini, A., 2019. Recent advances in nanoengineering cellulose for cargo delivery. *J. Control. Release* 294, 53–76. <https://doi.org/10.1016/J.JCONREL.2018.11.024>
- Studer, A.M., Limbach, L.K., Van Duc, L., Krumeich, F., Athanassiou, E.K.,

- Gerber, L.C., Moch, H., Stark, W.J., 2010. Nanoparticle cytotoxicity depends on intracellular solubility: Comparison of stabilized copper metal and degradable copper oxide nanoparticles. *Toxicol. Lett.* 197, 169–174. <https://doi.org/10.1016/J.TOXLET.2010.05.012>
- Sun, B., Wang, X., Ji, Z., Wang, M., Liao, Y.P., Chang, C.H., Li, R., Zhang, H., Nel, A.E., Xia, T., 2015. NADPH Oxidase-Dependent NLRP3 Inflammasome Activation and its Important Role in Lung Fibrosis by Multiwalled Carbon Nanotubes. *Small* 11, 2087–2097. <https://doi.org/10.1002/SMLL.201402859>
- Tortella, G.R., Rubilar, O., Durán, N., Diez, M.C., Martínez, M., Parada, J., Seabra, A.B., 2020. Silver nanoparticles: Toxicity in model organisms as an overview of its hazard for human health and the environment. *J. Hazard. Mater.* 390, 121974. <https://doi.org/10.1016/J.JHAZMAT.2019.121974>
- Wang, Z., Wang, C., Liu, S., He, W., Wang, L., Gan, J., Huang, Z., Wang, Z., Wei, H., Zhang, J., Dong, L., 2017. Specifically Formed Corona on Silica Nanoparticles Enhances Transforming Growth Factor β 1 Activity in Triggering Lung Fibrosis. *ACS Nano* 11, 1659–1672. https://doi.org/10.1021/ACSNANO.6B07461/SUPPL_FILE/NN6B07461_SI_006.XLS
- Zhao, X., Takabayashi, F., Ibuki, Y., 2016. Coexposure to silver nanoparticles and ultraviolet A synergistically enhances the phosphorylation of histone H2AX. *J. Photochem. Photobiol. B Biol.* 162, 213–222. <https://doi.org/10.1016/J.JPHOTOBIO.2016.06.046>
- Zhou, Y., Ji, J., Ji, L., Wang, L., Hong, F., 2019. Respiratory exposure to nano-TiO₂ induces pulmonary toxicity in mice involving reactive free radical-activated TGF- β /Smad/p38MAPK/Wnt pathways. *J. Biomed. Mater. Res. Part A* 107, 2567–2575. <https://doi.org/10.1002/JBM.A.36762>

An integrated new approach methodology for risk assessment of Safe and Sustainable by Design nanomaterials

5.1 Introduction

The regulatory system for chemical safety assessment relies largely on *in vivo* approaches while the European Commission is trying to reduce the use of animal models in compliance with the 3R principle (reduction, replacement, and refinement of animal employment for scientific purposes). *In vivo* testing is expensive, time-consuming, and banned in Europe for cosmetic testing (Regulation EC No 1223/2009). In this scenario, *in vitro* and *in silico* systems offer progressively reliable and advanced alternatives, also through the development of new approach methodologies (NAMs) for hazard and risk assessment of chemicals. NAMs are strategies based on *in vitro* and *in silico* methods that can provide information on the hazard and risk assessment of chemicals without involving animal testing (ECHA, 2016).

Depending on their structure, NAMs can be a practical tool that allow using available data for designing new experiments and models, with the purpose of generating data that give helpful information for human risk assessment prediction. NAMs may also represent completely new testing strategy that, avoiding the use of animals, deliver reliable data relevant for human physiology and risk assessment (El Yamani et al., 2022). Therefore, through a NAMs approach is possible to improve the understanding of the toxicological mechanisms of a new NM and to evaluate in advance its toxicity proposing new materials or refining the NM to lower the undesired negative effects already starting at the early stages of production (Nymark et al., 2020). In the context of new NAMs, data collection through monitoring campaigns,

in silico modeling, and *in vitro* testing are relevant alternative to classical *in vivo* toxicological approaches.

The use of NAMs for the hazard assessment of chemicals, including nanoparticles (NPs) and nano-enabled products (NEPs), is rapidly increasing, due also to the request of the European Commission to promote new tools for the development of safe and sustainable by design (SSbD) materials (Caldeira et al., 2022).

Some attempts of introducing NAMs in toxicity testing were done by integrating different strategies. Turley et al., (2019) conducted a comparison between ToxCast and *in vivo* toxicity data to evaluate the program accuracy in predicting the bioactivity of indirect food additives in the context of safety assessment. In another study, Mannerström et al., (2022) employed various *in vitro* tests coupled to a focused analysis of different substances representative of indoor air samples tested. The aim was to establish a connection between the composition of the samples and their biological effects.

The results of these two studies showed that the proposed NAMs need improvements for their direct application to risk assessment; nonetheless, the development of NAMs is important to provide information on the mechanism of action of chemicals, useful for safety screening of new materials and for the definition of novel approaches reducing the use of animals. More recently Ramanarayanan et al. (2022) proposed a NAM for pesticides based on an integration between source characterization and *in vitro* models, aiming at defining human exposure concentrations relevant for risk assessment.

In the last decades, the production of new nanomaterials (NMs) increased, since their broad range of properties translates into an extensive variety of practical applications and an attractive commercial impact (Mazari et al., 2021). When nanomaterials are produced or used in various industrial processes, NPs can be released into the environment and workers can be exposed. The release of NPs can occur through various routes, such as

airborne release, water release or direct contact. The airborne release is the most common during manufacturing processes such as spraying, milling, grinding, or simply by handling of powders. These airborne particles can be dispersed in the environment, inhaled by workers therefore resulting in continuous and prolonged exposure.

In time, some attempts to create a guideline to assess the occupational exposure to airborne NPs have been developed (CEN, 2018; ISO, 2007; OECD, 2015), given that many workers are potentially exposed to these new pollutants by inhalation.

The understanding of the release of NPs during the production process is a valuable resource for conducting risk assessment and implementing effective risk management strategies. The proper evaluation of the environmental concentration of NPs in selected environments, by field monitoring campaign (Boccuni et al., 2020; Trabucco et al., 2022) or laboratory simulations (Natale et al., 2022), can provide the metrics (particles number or mass concentrations) for the evaluation of human exposure by inhalation. The evaluation of human realistic exposure doses is becoming increasingly important in the risk assessment framework, since the effects of NPs on health are affected not only by their physical chemical properties and the route of exposure, but also by the delivered dose (Paur et al., 2011).

Currently performed *in vitro* toxicological studies use unrealistically high concentrations of NPs (Cao et al., 2021; Mittal et al., 2020; Tomankova et al., 2015), while realistic doses might differ and be lower, also considering control measure normally used in workplaces (Ling et al., 2011; Salmatonidis et al., 2019). Therefore, to test realistic doses on an *in vitro* model, it is essential the evaluation, by computational models, of the most likely deposited lung dose(s) of a person exposed to NPs during the production of NMs.

Computational models represent a valid instrument to translate data obtained from field monitoring studies into deposited lung doses. Among the different

options, the Multiple Path Particle Dosimetry (MPPD) model (<https://www.ara.com/mppd/>) is a well-established computational model that allow to calculate the deposition and the clearance of an aerosol of NPs. The model requires input data such as NPs number and mass concentrations, and size distribution to estimate the regional deposition of the NPs and the retention dose of the aerosol. This model is broadly applied with the purpose of assessing the deposition of aerosols in the respiratory tract of humans and laboratory animals (Amoatey et al., 2022; Kuprat et al., 2021; Manojkumar et al., 2019).

The realistic doses calculated by computational models can then be used as reference for providing relevant hazard data thank to the use of *in vitro* models, as closer as possible to the physiology of the target organ, that represent the proper closure to obtain risk assessment data according to NAM and 3R frameworks.

The main aim of this study is to provide a NAM that integrates environmental, modelling, physical chemical, and toxicological information to define the hazard of silver (Ag)- and titanium dioxide (TiO₂)-based NMs designed with different coatings according to a Safe and Sustainable by Design approach (SSbD). The NPs were synthesized with the aims of reducing their toxicity (curcumin coating) and improving their stability (hydroxyethyl cellulose – HEC coating) in suspension still maintaining their antimicrobial (Ag-based NPs) or their photocatalytic properties (Ti-based NPs) with respect to commercial uncoated NPs. Given their commercial interest, these NPs are here tested according to a new NAM procedure. In this study, the lung-retained dose of two selected NPs was determined from monitoring campaign data elaborated through the MPPD model. The model-estimated doses, representative of a chronic human exposure, were used for the exposure of an *in vitro* model of the alveolar space (a contact air liquid interface – ALI co-culture model of A549 and macrophages derived from THP-1 cells) by means

of an aerosol exposure system. The alveolar space is expected to be one of the main targets of aerosolized NPs and the region for gas exchanges which physiology is essential for well-being of humans. We also provide information on using two different exposure modules, one based on generation of aerosol droplet allowing deposition by gravitation settling (Vitrocell Cloud α) and the other requiring the ad hoc generation of the desired NPs aerosol but allowing for deposition by random movement and gravitation settling (Cultex Compact Module). The different steps for replicating the proposed NAM are described together with the relevant steps for correctly determining the actual dose of exposure of the *in vitro* model with an ALI exposure system.

5.2 Materials and Methods

5.2.1 Nanoparticles and reagents

The nanoparticles (NPs) used in this study have a silver (Ag) or titanium dioxide (TiO₂) core with different coatings. Ag NPs are used uncoated (AgNKD) or coated with polyvinylpyrrolidone (PVP), hydroxyethyl cellulose (AgHECs and AgHECp) or curcumin (AgCUR). AgNKD and AgPVP NPs were obtained by Sigma Aldrich (#484059 and #576832, Milano, Italy) while AgHEC, already as colloidal suspension (AgHECs) or as freeze-dried powder (AgHECp), and AgCUR were synthesized and provided by the Italian National Research Council (ISSMC-CNR, former ISTECC-CNR, Faenza, Italy). TiO₂ NPs are used without modifications (TiO₂NKD, reference material) or in a nitrogen-doped form (TiO₂-N). Reference TiO₂ NPS (namely, NM105) were obtained from the European Union Joint Research Centre, while TiO₂-N NPs were synthesized by Colorobbia Italia, SPA (Sovigliana Vinci, FI, Italy) and freeze-dried by ISSMC-CNR. All chemicals and reagents were purchased from Sigma Aldrich (Milano, Italy) if not stated elsewhere.

5.2.2 Preparation of the suspensions

The NPs stock suspensions were prepared in Milli-Q water and used for both characterization and exposure. The NPs provided already as suspensions (AgHECs and AgCUR) were simply vortexed for 30 s and then diluted in Milli-Q water to reach the final concentration of 1 mg Ag/mL, considering the mass ratio between the Ag core and the surface doping molecules. For the NPs provided in powder form (AgNKD, AgPVP, TiO₂NKD and TiO₂-N) the NPs were weighted and diluted in a 50 mL falcon tube with Milli-Q water to reach the concentration of 1 mg of Ag or TiO₂/mL. Then, the tubes were placed in an insulation box filled with ice and sonicated with an ultra-sonicator (Sonopuls HD3100, Bandelin, Berlin, Germany) equipped with a 2 mm probe. NP suspensions were sonicated by applying an electrical power of 40 W for 10 min (with cycles of 1 s pulse and 1 s pause). AgHECp NPs were directly diluted in Milli-Q water and vortexed for their high dispersibility in water. Stock suspensions were then further diluted at the final concentration of 100 µg of Ag or TiO₂/mL in Milli-Q water for TEM and DLS characterization or diluted at the desired concentration for deposition efficiency measurement and cell exposures in Milli-Q containing 0.5% of PBS.

5.2.3 Environmental monitoring campaign and lung deposition doses

A dedicated monitoring campaign was performed at a site of nano enabled products manufacturing as previously reported (Koivisto et al., 2022; Trabucco et al., 2022). Briefly, monitoring of the NPs present in the atmosphere of a pilot plant was performed during normal production phases of nano enabled products (NEPs, in the specific case textiles functionalized with AgHECs and TiO₂-N NPs, the other NPs used for toxicological hazard evaluation have been selected for comparative scope, in accordance with the SSbD approach). Particle number size and mass concentrations were obtained in real time by deploying the following instruments: an SMPS (L-DMA and

CPC mod. 5403, Grimm Aerosol Technik, Ainring, Germany), an OPC (mod 11 D Grimm Aerosol Technik, Ainring, Germany) and an aerosol photometer (DustTrack II mod. 8530, TSI Inc., Shoreview, MN, USA). Monitoring was performed at different distances from the spray coating machinery: at Near Field (NF) position, in proximity to the spray chamber and at heights from 1 to 1.3 m, into the spray coating cabinet and at Far Field (FF) to account for environmental contribution to NPs distribution. NF data, subtracted from interferences from the background, were then used to determine the average size of airborne particles and the average density of the particles. These values were then used to calculate, according to mass concentration values, the expected alveolar retained dose with the MPPD 4.01 software.

5.2.4 Laboratory lung in vitro model exposure

The *in vitro* co-culture model (paragraph 5.2.6) was exposed to the different NPs in a Vitrocell® Cloud alpha 12 system equipped with a nebulizer with a droplet MMAD ranging from 4.0 to 6.0 μm and a Quartz Crystal Microbalance (QCM) for the measuring of the deposited mass. For each NP, 200 μL of a suspension, at concentration defined according to the deposition efficiency of the selected NP, were loaded in the nebulizer, and completely aerosolized for 25 seconds. Then the obtained cloud (NPs plus dispersion medium) was left to settle for 15 minutes. These procedures were performed under a sterile hood. The exposed cells were then transferred to a CO₂ incubator for 24 hours before measuring the biological endpoints.

Between one spray and the next, the nebulizer was cleaned by vaporizing two time consecutively 400 μL of Milli-Q water. Three separate nebulizers were used, one for the negative control (0.5% PBS in Milli-Q), one for the Ag NPs and one for the TiO₂ NPs. The mass contribution of the suspension medium (Milli-Q with 0.5% of PBS) was preliminary measured and then subtracted to the final deposited mass of each NP suspension. Furthermore, to evaluate and

reduce the contribution of the PBS salts to the measured mass, without affecting the nebulizer functioning, solutions containing different concentrations of PBS (50, 10, 5 and 0.5%) were nebulized and the deposited mass was measured.

Additional tests were performed with the same co-culture model but with an alternative approach by using the Cultex® RFS Compact module and the AgHECs only. The system is not provided with a nebulizing system but allow to expose the cell at a flux of particles, mimicking the inspiration flux. Particles in this model deposit according to their physical properties rather than as total gravimetric deposition such as in the Vitrocell® Cloud alpha 12 system. Briefly, the RFS Compact module was placed under a chemical bench and connected to a sampling line deriving from an expansion chamber (see Figure S6). Particle were generated by a Collison nebulizer (BGI, Inc.) filled with 60 mL of a 100 µg Ag/mL of AgHECs particles. Particle size distribution generated by the Collison was preliminary controlled by dedicated experiments (data not shown). Particles nebulized were dried to allow counting with a DiSC mini (Schaefer, Italy) instrument while part of the generated flux was derived to the expansion chamber where temperature was set to 30 °C and relative humidity of the aerosol increased at around 50-60%. The Cultex® module allowed to expose three inserts to the particles arriving from the expansion chamber while three inserts were exposed to the same flux of filtered air. The deposited mass of the generated aerosol is provided according to (Gualtieri et al., 2022). The two models differ substantially on the way the particles are dispersed and delivered to the cell culture. The Cloud system relies on vibrating mesh nebulizers having droplet median mass aerodynamic diameter (MMAD, i.e., the average size of particles constituting the deposited aerosol) ranges of 2.5 – 6.0 µm, 2.5 – 4.0 µm and 4.0 – 6.0 µm. The nebulizers therefore generate an aerosol which droplet are at least one order of magnitude bigger than the nebulized nanoparticles. This is functional

to depositing most of the mass present in the nebulizer considering gravitational deposition as the main process. On the contrary, the Cultex model is not provided directly with a nebulizing system and different approaches may be selected to provide the aerosol to the system. The aerosol is delivered to the cell culture model by a strictly controlled air flux and the forces that drive particles deposition are both gravitational settling and random movements according to the properties (such as diameter, shape, and density) of the original particle. This main difference in the two system must be carefully considered for a proper understanding of the reported results.

5.2.5 Deposition efficiency

To define the concentration of the suspension of NPs to be nebulized in the Vitrocell® Cloud alpha 12 system to obtain a desired deposited mass, the measurement of the deposition efficiency is a mandatory step to avoid misinterpretation of the results, above all when comparing different NPs. To measure this parameter the deposited mass of the different NPs is to be evaluated, starting from a suspension at known concentration (150, 250 or 500 µg of Ag or TiO₂/mL in the experiments here reported). To measure the deposited mass the same procedure used for cell exposure was applied except that, after settling of the cloud, the nebulizer chamber was removed for 5 minutes to let the water to evaporate, a required step for correct mass measurement with a dedicated quartz crystal microbalance (QCM). For the mass measuring, the chamber was placed back and the reading with the QCM started. The microbalance was allowed to stabilize for 5 minutes and until a stable signal was recorded. The last thirty (30) consecutive values of the stable signal from the QCM were then averaged to obtain the actual deposited mass for the different NPs.

The deposition efficiency of each NP requires the definition of the expected maximal theoretical deposited mass, calculated according to equation (1)

$$\text{expected dep.} = \frac{c * V_{neb}}{A_c} \quad (1)$$

where c is the concentration of a given NP suspension, V_{neb} is the volume of suspension nebulized (200 μL in our experiments) and A_c is the cross-sectional area of the aerosol chamber (141.5 cm^2). A limiting factor to calculate the maximal deposition is the definition of the concentration c for each NPs. This concentration should permit the dispersion of the whole content of NPs without artefacts. According to preliminary experiments, the following suspensions in Milli-Q with 0.5% PBS were used for the different NPs: AgNKD suspensions at 500, 250 and 150 $\mu\text{g/mL}$; AgPVP, AgCUR, TiO_2NKD and $\text{TiO}_2\text{-N}$ suspensions at 250 $\mu\text{g/mL}$; AgHECs and AgHECp suspensions at 150 $\mu\text{g/mL}$.

The actual deposited mass, as measured by the QCM, was then used to determine the deposition efficiency (DE) for each NP according to equation (2).

$$\text{deposition efficiency (DE)} = \frac{\text{measured deposited dose}}{\text{expected deposited dose}} * 100 \quad (2)$$

Each NP, having specific physical and chemical properties, was tested for its deposition efficiency. DE was then used to determine the concentration of the different suspensions to be nebulized to obtain the desired dose of exposure according to equation (3).

$$\text{Conc} = \frac{\left[\frac{\text{Dose of exposure}}{\text{DE}} * 100 * \frac{A_c}{V_{neb}} \right]}{1000} \quad (3)$$

Where Dose of exposure is the final desired dose of exposure to be obtained after spraying, DE is the efficiency of deposition specific for each NP calculated according to (2), A_c is the area of the Vitrocell Cloud chamber, while V_{neb} is the volume of suspension to be nebulized (200 μ L in the experiments here reported).

The experiments here reported were performed considering the MPPD derived average retained alveolar doses (Table 5.1) considering 1, 6 or 12 months of workplace related human exposure.

5.2.6 Air-Liquid Interface Co-culture of A549 and THP-1 derived macrophages

Both cell lines used for the formation of the co-culture were cultivated in OptiMEM medium (Life Technologies Monza, Italy) supplemented with 10% fetal bovine serum (FBS; Gibco Life Technologies, Monza, Italy) and antibiotics (penicillin/streptomycin, 100 U/mL; Euroclone, Pero, Italy). Human alveolar epithelial cells (A549 cell line, ATCC® CCL-185™ ATCC, Manassas, VA, USA) and human monocytes (THP-1 cell line, ATCC® TIB202™) were cultivated in submerged conditions prior co-culture set-up. Cells were maintained in an incubator at 37°C and 5% CO₂. A549 were seeded on the apical side of the porous membrane (with a pore diameter of 1.0 μ m) of 12 well inserts (cellQART, SABEU GmbH & Co. KG, Northeim, Germany) at a density of 5×10^4 cell/insert and allowed to grow for 48 hours. THP-1 cells were differentiated (dTHP-1) for 24 h with 20 ng/mL of Phorbol 12-myristate 13-acetate (PMA). After differentiation, the medium was removed, and cells were allowed to recover for 24 h in fresh medium. The co-culture was then formed by adding differentiated dTHP-1 directly in contact with the A549 cells with a ratio of 1:10. dTHP-1 cells were left to seed for 4 h, then the medium in the apical side of the inserts were removed and fresh

medium was added in the basal side of the well. After 24 h of differentiation at the Air-Liquid Interface (ALI), the co-culture was considered established. The exposure of the co-culture to the different NPs was performed as already described.

The morphology of the co-culture was observed through scanning electron microscopy (SEM) using a TESCAN Vega®XM 5136 SEM operating at 20 kV acceleration voltage (Figure S5).

5.2.7 Cytotoxicity

The cytotoxicity of the co-culture was assessed through the CyQUANT™ LDH Cytotoxicity Assay (Invitrogen Life Technologies, Monza, Italy). 24 h after the exposure to the NPs, the medium from the basolateral compartments of control and exposed cells was collected and the level of LDH (Lactate Dehydrogenase) was assessed immediately to avoid any loss of activity, following manufacturer's instructions. As a positive control, the Lysis buffer included in the kit was added to an insert for 45 minutes to lysate all the cells cultured on the insert obtaining the maximal amount of LDH. 50 µL of each sample were transferred in triplicate in a 96 multiwell plate and 50 µL of the reaction mixture were added. The plate was incubated at room temperature and in the dark for 30 minutes. Then, 50 µl of stop solution were added and the absorbance was measured at 490 nm, with a reference of 680 nm, using a TECAN Infinite M200 Pro microplate reader (TECAN, Männedorf, Switzerland). The cytotoxicity is expressed as relative variation over the positive control performed by complete lysis of the cells.

5.2.8 Cytokines release

As an index of pro-inflammatory activity, the quantification of three selected cytokines was done through ELISA assays (Invitrogen Life Technologies, Monza, Italy) according to manufacturer's instructions. The quantification of

the release of Interleukin 8 (IL-8), Interleukin 6 (IL-6) and Interleukin 1 β (IL-1 β) was performed on the media of the basolateral side collected from each insert after 24h of exposure to the NPs. The supernatants were stored at -80°C until analysis. The absorbance of the samples was measured using a TECAN Infinite M200 Pro microplate reader (TECAN, Männedorf, Switzerland). The concentration of interleukins was calculated based on standard curves and data are shown as fold change compared to the negative control.

5.2.9 Data collection and statistical analysis

Data of deposition efficiency are expressed as the mean \pm standard deviation of mean (SD) of at least three independent experiments ($N > 3$, if not otherwise stated). For the cytotoxicity, three technical replicas for each biological replicate were analyzed. Statistical analyses were performed using the R software (R Core Team, 2022), applying the one-way ANOVA test followed by Dunnett's post hoc test. The homogeneity of the variance was confirmed by Levene's test. Values of $p < 0.05$ were considered statistically significant.

5.3 Results

5.3.1 Environmental monitoring campaign and lung deposition modelling

The particle number size distribution at a factory processing textile by spray techniques for nano-coating are reported in Trabucco et al., (2022). The data collected were used to determine the measured geometric mean concentration (39 and 94 $\mu\text{g}/\text{m}^3$ for AgHEC and TiO₂-N respectively) and average density (6.5 g/cm^3 and 2.1 g/cm^3 for AgHEC and TiO₂-N, respectively) of the particles, while polydisperse particle distributions obtained from field campaign data were used as count median distribution (CMD). These values were then used in the MPPD 4.01 software to obtain the lung deposited dose also considering clearance (Table 5.1). A classical shift of 8 hours for 5 consecutive days a week was considered for estimating worker exposure.

Deposition was modelled in an adult considering a human symmetric lung geometry with 24 consecutive segments, a total lung capacity (TLC) of 5558.09 mL, a functional residual volume (FRC) of 3300 mL, a scaling tree factor of 1.053, a lung distal volume of 2850 mL and a volume of conducting airways of 171.31 mL. The breathing frequency was considered equal to 20 breathing per minute (1.5 sec for inhalation and 1.5 sec for exhalation), the tidal volume was set to 1100 mL and the nasopharyngeal death space equal to 50 mL. The low number and mass concentration of nanoparticles measured at the working area determined a low mass of AgHEC and TiO₂ nanoparticles deposited at the alveolar region on daily basis that was in the order of few ng per square cm. These values considering the high density adopted for the calculation may be even lower for other materials with lower density. Considering a cumulative deposition (Table 5.1), over a year of continuous exposure, the expected retained dose reached the order of hundreds of nanograms (232 and 324 ng/cm² for Ag and TiO₂ respectively).

Table 5.1. Average alveolar retention dose. The doses representative of an exposure of one week shift, 1 month, 6 months and 1 year for the two representative NPs used during the monitoring campaign are reported in the table, the values calculated by the MPPD model are highlighted in grey.

Average Alveolar Retention dose				
	5 days	1 month	6 months	1 year
AgHEC	4.47 ng/cm ²	19 ng/cm ²	116 ng/cm ²	232 ng/cm ²
TiO₂-N	6.23 ng/cm ²	27 ng/cm ²	162 ng/cm ²	324 ng/cm ²

5.3.2 Deposition efficiency

The measurement of deposition efficiency typical for each NPs is essential to reproduce *in vitro* the deposited dose calculated through the MPPD model. To calculate the deposition efficiency for each NP, the maximal theoretical deposition was obtained, for different NPs concentrations, according to equation (1) and the results are reported in Table 5.2.

Table 5.2. Maximal theoretical deposition for each single nebulization based on the suspension concentration in $\mu\text{g/mL}$ of NPs.

	μg in each spray	$\mu\text{g}/\text{cm}^2$	ng/cm^2
Deposit expected for 500 $\mu\text{g/mL}$:	100	0.71	707
Deposit expected for 250 $\mu\text{g/mL}$:	50	0.35	353
Deposit expected for 150 $\mu\text{g/mL}$:	30	0.21	212

The actual deposited dose was measured by the QCM for each NP. A preliminary assessment of the mass deposited by the spraying medium (Milli-Q with PBS) was performed to obtain the mass attributable to the selected spraying medium that is to be subtracted to obtain the final NPs mass. The suspending medium, Milli-Q with 0.5% of PBS, was finally selected for NPs exposures and deposition efficiency measurements. The QCM measured deposited doses are reported in Table 5.3.

Table 5.3. Measured deposition of Ag and TiO_2 . The results are obtained by spraying different $\mu\text{g/mL}$ of NP to estimate the best conditions. The mass of Ag or TiO_2 was calculated considering the mass ratio of Ag or TiO_2 over the doping molecules in the different NPs (for AgHECs the silver is 8.04%, for AgHECp it is 7.7% and for AgCUR it is 47.5%. For all the other NPs, the amount of Ag or TiO_2 is close to 100%). * = NPs not tested on the biological model.

	$\mu\text{g/mL}$	PBS (%)	Deposited mass (ng/cm^2) \pm SD
AgNKD	250	0.5	109.65 \pm 15.08
AgPVP*	250	0.5	179.11 \pm 37.93
AgHECs	150	0.5	175.57 \pm 13.11
AgHECp*	150	0.5	136.85 \pm 16.11
AgCUR	250	0.5	307.81 \pm 25.99
TiO₂NKD	250	0.5	259.66 \pm 64.15
TiO₂-N	250	0.5	145.84 \pm 16.82

The NPs concentration of the suspensions to be sprayed were defined *a priori* based on the peculiar properties of each NP suspension. NPs were characterized for their hydrodynamic properties once in solution, their surface charge (ζ -potential) and their physical properties (size and shape) (see supplementary materials and methods, supplementary results, and supplementary Figure S1 and Table S1). In fact, for some NPs, solutions at high concentration were not compatible with the nebulizing system. As an example, a clogging effect was encountered during nebulization of AgHECs and AgHECp NPs at the concentrations of 250 and 200 $\mu\text{g/mL}$ (Figure S3A). The high viscosity of these suspensions determined the deposition over the spraying grid of big aggregates of NPs that impaired a complete and homogeneous nebulization process. Therefore, only suspensions up to 150 $\mu\text{g/mL}$ were nebulized for these NPs. Similarly, after the nebulization of a suspension of 500 $\mu\text{g/mL}$ of AgNKD NPs, it was noticed that part of the NPs remained clogged in the mesh of the vibrating membrane (Figure S3B).

5.3.3 Estimation of deposition efficiency

The results obtained by spraying the different solution were used to calculate the deposition efficiency specific for each NP, according to the equation (2).

The different NPs have different deposition efficiency (Table 5.4) depending on their characteristics. In detail, Ag NPs coated with HEC or CUR have a higher deposition efficiency while AgPVP and especially AgNKD showed the lower ones. TiO₂NKD has a deposition efficiency that is much higher with respect to TiO₂-N. These results suggests that the p-chem properties of the NPs could determine the possibility to spray the different solutions. In fact, lower deposition efficiency is found in the NPs with the higher agglomeration tendencies. Although the low number of data available, it was possible to analyze Spearman correlations between the different p-chem and the efficiency of deposition or of deposited mass. The only significant result was a negative association between the deposition of efficiency and the hydrodynamic diameter measure just after the preparation of a working solution. The correlations were negative and significant both considering the hydrodynamic diameter of a solution of 10 µg-ml⁻¹ (spearman correlation equal to -0.786, $p < 0.05$) or a solution of 100 µg-ml⁻¹ (spearman correlation equal to -0.893, $p < 0.05$).

*Table 5.4. Deposition efficiency for each suspension nebulized. * = NPs not tested on the biological model.*

	µg/mL	PBS (%)	Deposition efficiency (%) ± SD
AgNKD	250	0.5	31.03 ± 4.27
AgPVP*	250	0.5	50.69 ± 10.73
AgHECs	150	0.5	82.81 ± 6.19
AgHECp*	150	0.5	64.55 ± 7.60
AgCUR	250	0.5	87.11 ± 7.35
TiO₂NKD	250	0.5	73.48 ± 18.15
TiO₂-N	250	0.5	41.27 ± 4.76

Based on these results, the concentrations required for each NP to obtain the final exposure doses were calculated (Table 5.5) and prepared prior to each exposure experiment.

Table 5.5. Concentrations of the suspensions calculated according to (3) for each different NPs to be nebulized to obtain the final exposure dose considering the DE reported in Table 5.4.

Nanoparticle \ Dose of exposure	19 ng/cm ²	116 ng/cm ²	232 ng/cm ²
	AgNKD	43.321 µg/mL	264.486 µg/mL
AgHECs	16.233 µg/mL	99.106 µg/mL	198.213 µg/mL
AgCUR	15.432 µg/mL	94.214 µg/mL	188.428 µg/mL
	27 ng/cm ²	162 ng/cm ²	324 ng/cm ²
TiO₂NKD	25.997 µg/mL	155.981 µg/mL	311.962 µg/mL
TiO₂-N	46.287 µg/mL	277.720 µg/mL	555.440 µg/mL

Calculated deposited mass and number of silver nanoparticles in the Cultex module are reported in Table 6. Considering the aerosol size number distribution, the average number and mass of deposited NPs were calculated. As a reference for mass deposition, the average mass concentration of silver generated by the Collison nebulizer is reported (for details refers to supplementary Figure S6).

Table 5.6. A) Deposited average number and mass calculated for the Cultex RFS Compact module. Average total mass of nebulized particles is in the order of $9.0 + 1.6$ ng per square centimeter, while total deposited number where in the order of $1.7 \cdot 10^{+06} + 3.0 \cdot 10^{+05}$ particles per square centimeter. Mass deposition is also reported as Ag relative deposited mass. B) The relative mass contribution of Ag to

the total mass was measure on the Teflon filter placed just before the exhaust exit line (see Figure S6). A 12% contribution of Ag to the total mass of the sampled particle was determined by ICP-OES (details on this procedure may be found in Trabucco et al. (2022)).

A		Deposited number (\pm sd)	Deposited mass (\pm sd)
		#/cm²	μg/cm²
Total deposition		1.69*10 ⁺⁰⁶ (\pm 2.98*10 ⁺⁰⁵)	9.02*10 ⁻⁰³ (\pm 1.59*10 ⁻⁰³)
Deposition reported as Ag mass		nd	1.05*10 ⁻⁰³ (\pm 1.85*10 ⁻⁰⁴)

B		Total mass concentration (\pm sd)	Total Ag concentration (\pm sd)
		μg/m³	μg/m³
Generated particle concentrations		1025.41 (\pm 201.48)	119.39 (\pm 42.54)

5.3.4 Cytotoxicity

The cytotoxicity of NPs at the exposure doses reported was assessed measuring the levels of LDH released by the cells in the media. The results (Figure 5.1) show no significant increase or reduction of LDH in the cells treated with the different NPs. Cytotoxicity from test with the alternative exposure module Cultex RFS model were not significantly changed (data not shown) according to the low exposure doses obtained with the exposure procedure (Supplementary Table S3).

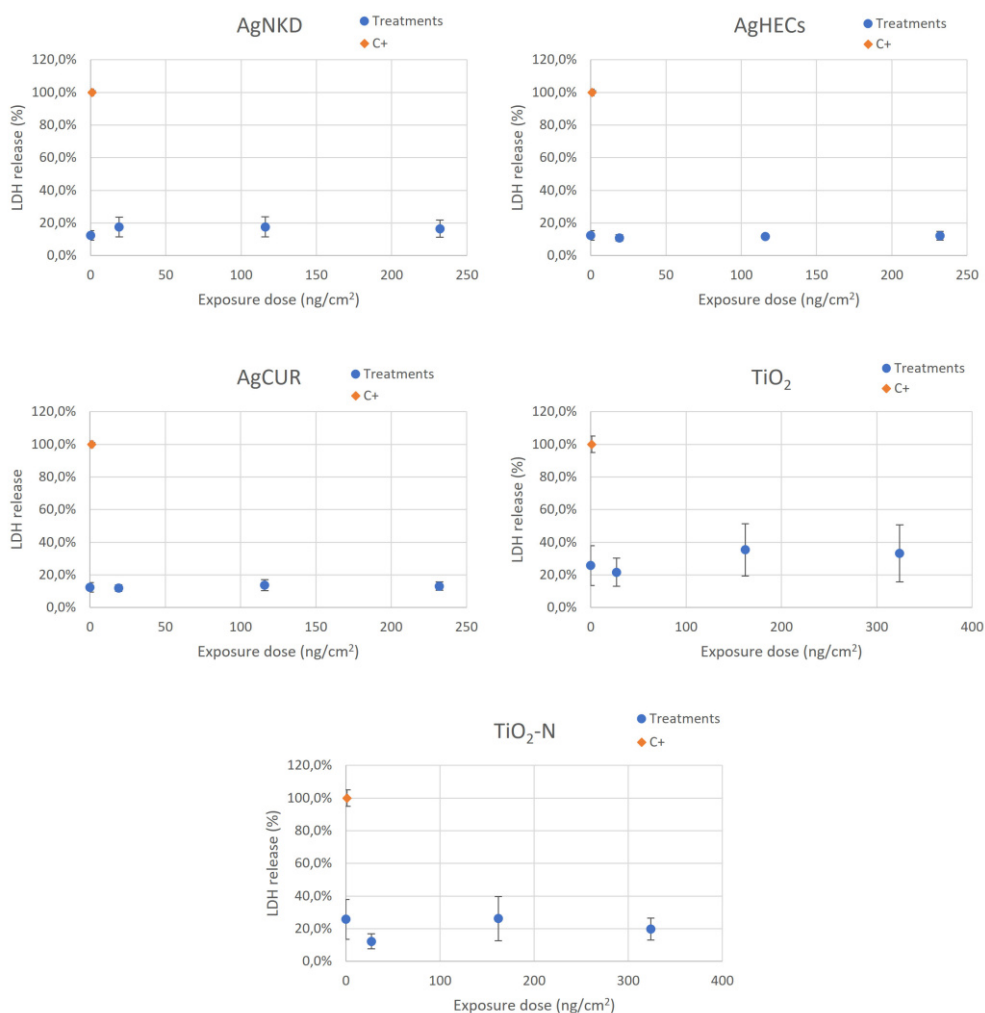


Figure 5.1. Cytotoxicity. The graphs show the percentage of LDH release compared to the positive control (black dot equal to 100% cell death). The cytotoxicity was assessed 24 h after NPs nebulization and it was measured through LDH assay. Data are shown as the mean of three independent experiments \pm SD. Statistical analysis: one-way ANOVA.

5.3.5 Cytokines release

At the tested doses, the release of the measured inflammatory mediators IL-8, IL-6 and IL-1 β (Figure 5.2) was not modulated by the NPs except for TiO₂-N. For this NP, there is a significant decrease of IL-1 β release in the media for cells treated with all the tested concentrations. There's also a non-significant

increase of IL-6 in cells treated with TiO₂-N. Ag NPs induced no modulation. Similar results were obtained with the Cultex RFS exposure module (data not shown). Noteworthy, ALI exposure of the co-culture model to LPS (positive control for inflammation, dose of exposure 10.42 μg/cm² induced a significant release of IL-8, for more detail supplementary materials and methods and supplementary Figure S8). However, the lack of cytokine release in the cell supernatants may be also related to an actual communication between the cell types in co-culture. In fact, the cytokines released from macrophages may be captured by lung cells receptors, and vice versa, therefore removing them from the supernatant and masking the pro-inflammatory effect of the tested NPs.

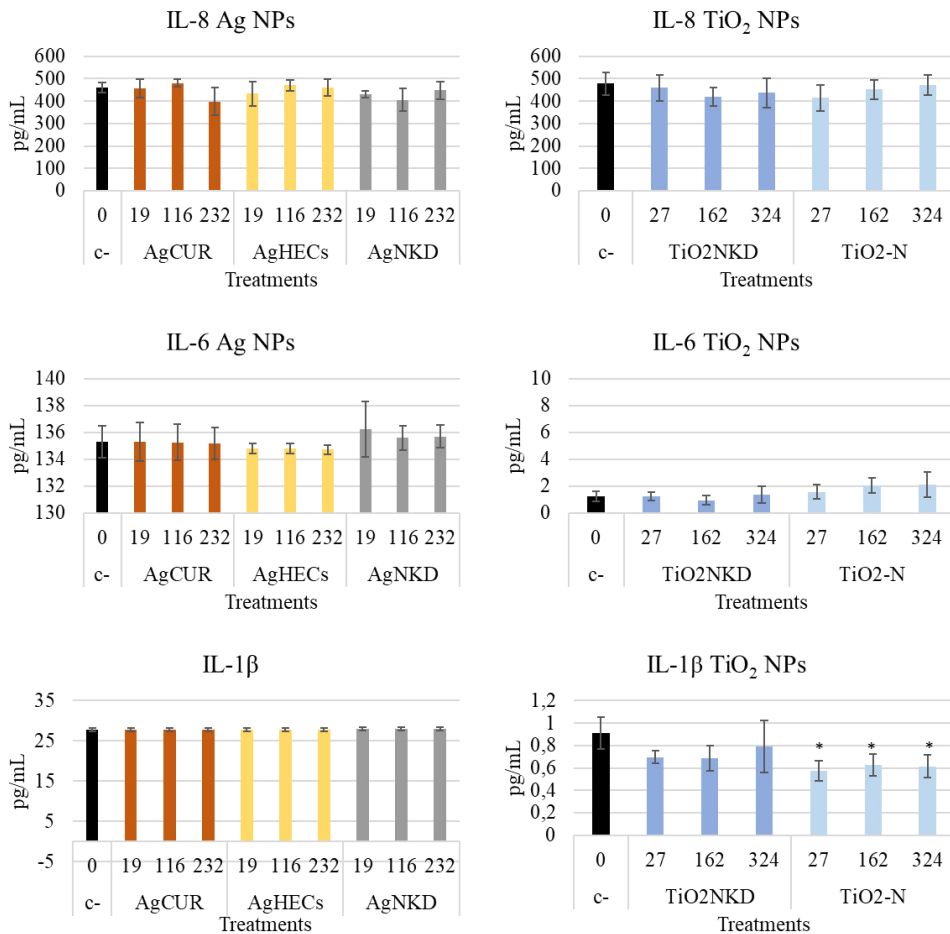


Figure 5.2. Cytokines release (IL-8, IL-6 and IL-1 β). The release of cytokines in the media was measured 24 h after the NPs nebulization. There is a significant decrease of IL-1 β release in cells exposed to TiO₂-N at all tested concentrations. Data are shown as the mean of three independent experiments \pm SD. Statistical analysis: one-way ANOVA followed by Dunnett's test. * $p < 0.05$ compared to the control group. As a reference we report here the average and SD of ILs in control cells kept in incubator after ALI differentiation: 492,00 + 67,89 for IL8; 0,99 + 0,13 for IL-6 and 0,95 + 0,21 for IL-1b.

5.3.6 The conceptual framework of the proposed NAM

The conceptual framework of the proposed NAM is based on three main blocks, environment data collection and human exposure dose calculation; *in vitro* model definition and preparation and laboratory efficiency of deposition; *in vitro* model exposure and biological responses evaluation (Figure 5.3). Ambient monitoring at the site (production site here) of interest is performed to collect data on the NPs size number distribution and particle density, if not available, these data are used to run a lung deposition model, the MPPD model in our case. The retained alveolar dose, or the deposited alveolar dose, is therefore modelled and used for defining the exposure doses to be performed under lab-controlled conditions. The definition of the *in vitro* model to be tested may be defined according to the specific research interest or the laboratory protocols. Here, the lung alveolar model is obtained according to the protocols previously described: after differentiation of monocytes, dTHP-1 cells are seeded on top of the inserts seeded A549 (ratio of number of dTHP-1:A549 equal to 1:10). Then, the culture medium in the apical side of the insert is removed to let the cells at the ALI for at 24 hours.

The lung epithelial model is finally exposed to the NPs through the Vitrocell® Cloud alpha 12. After exposure, the inserts are placed in a CO₂ incubator for the time needed to activate the biological responses (24 hour in this case). At the end of the incubation time post-exposure, the lung model is tested for the

selected biological outcomes, here: cytotoxicity, cytokine release, and morphology by SEM.

Relevant variation in the proposed NAM may be related to the lung model to be used, to the model used to define the lung deposited or retained dose, to the equipment selected to expose the cells (see for example the procedure reported here for the Cultex Compact module (supplementary materials and methods, supplementary Figure S6 and Figure S7), to the time of incubation to be selected after the exposure and, to the biological endpoints that can take advantage also of omics approaches.

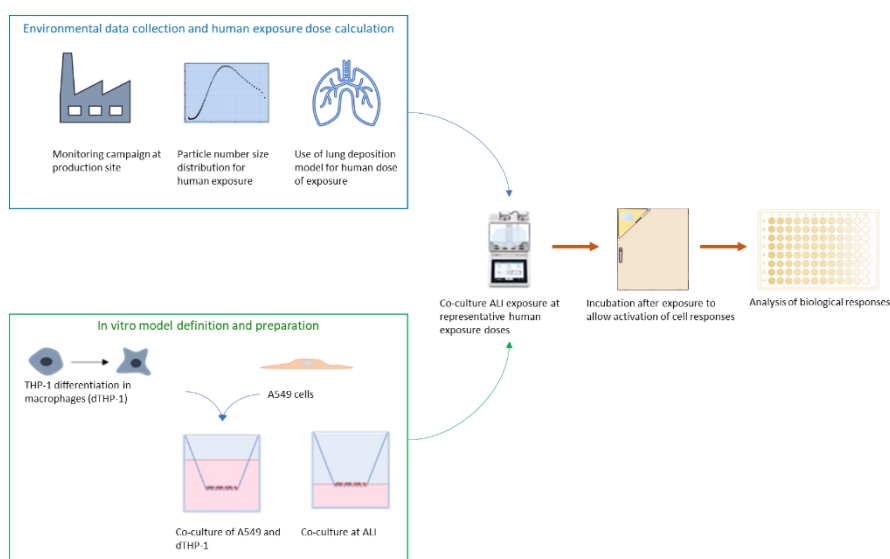


Figure 5.3. Workflow of the proposed NAM. The three conceptual blocks required to perform the NAM framework are briefly reported and integrated. The specific solution here adopted are briefly depicted.

5.4 Discussion

New nanomaterials (NMs) are continuously developed, and their wide use (Nowack et al., 2011) leads to the release of nanoparticles (NPs) in different environments. The presence of NPs in the environment increases the risk of human exposure by different routes, mostly inhalation, ingestion, and contact.

Such exposures can happen also during the use of new NMs or during their production (Kuhlbusch et al., 2018). Furthermore, according to the Safety and sustainable by Design (SSbD) paradigm the safety of a NM has to be assessed during all its life cycle phases.

The proper evaluation of the risk assessment of new NMs is relevant for human health protection therefore, beside environmental, also working place exposure requires specific attention. It has been recently reported (Belosi et al., 2023) that the production processes of nano-enabled material (NEM) may determine local release of NPs in the atmosphere with potential of human exposure. Also, NPs hazard definition should consider, to the best of the knowledge, doses of exposure of biological models that are relevant for humans, to provide data that can be useful in the risk assessment framework (Paur et al., 2011).

Accordingly, we provide here a NAM (Figure 5.3) to define the hazard of new Ag and TiO₂ based NMs based on human exposure doses definition (based on monitoring campaign and MPPD modelling) and on an *in vitro* model (representative of the alveolar space) exposed by a well characterized ALI procedure. The proposed NAM represents a step forward since most *in vitro* studies on the toxicological effects of NPs are limited, since monocultures are exposed in submerged conditions (Andreoli et al., 2021; Lovén et al., 2021) at unrealistic concentrations, without considering lung physiology and complexity (Lenz et al., 2013; Paur et al., 2011). Here, beside using an *in vitro* model representative of the alveolar space, we provide a detailed workflow to adopt ALI exposure systems after preliminary and relevant characterizations (Medina-Reyes et al., 2020; Meldrum et al., 2022). In fact, to get closer to real human exposure conditions, three parameters are important to consider: the biological model, the exposure protocol, and the doses of exposure.

The *in vitro* model should be selected to mimic the interaction between the different cell types of the target organ thus being more reliable model for the

pathway of exposure and the biological response. In this context, here we used a co-culture of epithelial cells and macrophages differentiated at the ALI (Cappellini et al., 2020; Loret et al., 2016), although other co-culture models have been proposed (Chary et al., 2019).

The exposure procedure should mimic as much as possible lung deposition: for (nano)particle toxicology, normally adopted models can be summarized in submerged, *quasi*-ALI, and ALI. For submerged exposure protocols, it is hard, if not impossible, to define the effective dose of NPs that reaches the cells (Upadhyay and Palmberg, 2018), since part of the NPs are absorbed in the walls of the wells or stay in suspension (Cappellini et al., 2020). Also, under submerged exposure protocols the NPs interact with the medium of culture modifying their surface by protein (and other molecules) corona, affecting in the end the interaction between the NPs and the biological model (Ke et al., 2017; Liu et al., 2020; Moore et al., 2015; Zanganeh et al., 2016). *Quasi*-ALI exposure conditions are seldom used since they take advantage of lung model cultured at the ALI, but the exposure is still obtained by pipetting small volume (tens of microliters, depending on the culture surface) of a solution of NPs dispersed in an appropriate medium. On the contrary, ALI exposure mimics the actual interaction between the lung epithelial cells and the inhaled particles since the NPs interact with the cell membrane at the interface with the air without the need of a medium as vehicle to deliver the NPs to the cells. Finally, the exposure doses used in the majority of *in vitro* studies are usually in the order of tens of micrograms (Leibrock et al., 2019; Lin et al., 2006). To our knowledge, exposure of an *in vitro* model at ultra-low concentration is reported by Giovanni et al. (2015). The authors used nanograms or picograms of different metal-based NPs to expose, in submerged conditions, murine macrophages showing an increased inflammatory response also at these low concentrations. Nonetheless, this approach, based on submerged cell exposure, can be useful to highlight the overall mechanism of action of the

new NPs, it does not allow the prediction of the hazard, since these conditions are far from being representative of real human exposure. While this approach can be useful to highlight the overall mechanism of action of the new NPs, it does not allow the prediction of the hazard, since these conditions are far from being representative of real human exposure.

The new integrated methodology here reported overcame these limitations (such as representativeness of the exposure procedure, ALI vs submerged, coherence with expected human exposure doses, relevance of the *in vitro* model for human alveolar space in terms of culturing, ALI vs submerged, and cell types, alveolar cells, and macrophages). Starting from data on NPs released in a work environment during the production of textiles coated with silver (Ag) or titania (TiO₂) NPs (Koivisto et al., 2022), the expected lung retained dose was calculated (MPPD model 4.01 considering working shift of 8 h/day for 5 working days/week) and used as reference parameter to expose the *in vitro* model. The exposure doses here applied are in the order of hundred(s) of ng/cm² which, representing an integrated (six months to one year) exposure at the production site, are relevant for human exposure and risk assessment. Tilly et al., (2023) recently reported metal oxide effects at ALI working at concentration of tens to hundreds of micrograms/cm²; similarly, Medina-Reyes and colleagues (2020) tested TiO₂-based materials in the range of micrograms/cm². Interestingly, Wang et al., (2020) reported effects of SiO₂-Ag in a co-culture of A549 and THP-1 cells exposed to 576 ng/cm². Future ALI testing should focus on more human relevant exposure doses, to provide hazard data transferable to risk assessment approaches.

A key step in properly controlling the *in vitro* model exposure doses, and reproducing *in silico* derived human exposure doses, is the evaluation of the deposition efficiency of the different NPs tested. Despite the increasing use of ALI exposure modules, few studies have reported the evaluation of this parameter (Bannuscher et al., 2022; di Cristo et al., 2020; He et al., 2021) in

spite of the significant difference that different NPs solutions may have and the impact of the effective exposure doses in the biological models.

For example, Lenz et al., (2009) nebulized various solutions (NaCl, (NH₄)₂SO₄) and NPs suspensions (ZnO, Au) by means of the air-liquid interface cell exposure system (ALICE) and found a deposition efficiency of $57 \pm 0.07\%$ for all the tested substances, showing also a similar efficiency of deposition using different solution concentrations. Similarly, in our exposure model different concentrations of nebulized AgNKD showed a stable deposition efficiency (equal to 33.66, 31.16, 35.85% for 500, 250 and 150 $\mu\text{g/mL}$ starting concentrations, respectively). Hu et al., (2020) studied the anti-inflammatory effect of curcumin in both submerged and ALI conditions through the Vitrocell® Cloud Starter Kit aerosol exposure system. Instead of using a QCM, they relied on the autofluorescence of curcumin to determine the delivered dose. In this case, starting from different doses of curcumin (10, 20, 50, 100 μM) they found different deposition factors (0.697, 0.806, 0.545 and 0.668). Bannuscher et al., (2022) used the Vitrocell® Cloud12 system to nebulize concentrations of 0, 125, 250 and 500 $\mu\text{g/mL}$ of DQ12 (crystalline silica quartz) and TiO₂ and assessed the deposition efficiency through the QCM. They obtained a linear correspondence between particle concentration and particle deposition, in agreement with our results for AgNKD (data not shown) and PBS.

Here we provide an additional interesting observation, i.e., the deposition efficiency may be controlled, rather than by the pristine dimension of the particles, or of the z-potential of the nanomaterial, by the agglomeration tendency that the particles have once dispersed in the working media. Lower is the resulting hydrodynamic diameter, higher will be the final efficiency of deposition. In fact, in our study the deposition of efficiency was higher for AgCUR > AgHECs > TiO₂NKD > AgHECp > AgPVP > TiO₂-N > AgNKD, similarly to what observed with the hydrodynamic diameter values that was

the lowest for AgCUR < AgHECs < TiO₂NKD < AgHECp < AgNKD < AgPVP < TiO₂-N.

The results obtained by assessing cytotoxicity after the nebulization on the co-culture of five of these NPs (AgNKD, AgHECs, AgCUR, TiO₂NKD and TiO₂-N) at the selected doses indicate the absence of a significant LDH release in the cell medium. The quantification of the release of three selected cytokines also showed no statistical differences between the control and the cells treated with AgNKD, AgHECs, AgCUR and TiO₂NKD. It was observed a reduction of the release of IL-1 β in cells treated with TiO₂-N. Similar doses (30 and 278 ng/cm²) were used by Herzog et al. (2013) to investigate the effects of citrate-coated Ag NPs on a tri-culture of A549, macrophages and dendritic cells, exposed at the ALI. In agreement with our results, the authors did not observe any significant LDH release from the cells. They also evaluated the production of TNF- α and IL-8 and observed no pro-inflammatory effects at the tested doses. Wang et al., (2020), using a similar co-culture model showed lack of cytotoxicity, by LDH release, using an exposure dose of 576 ng/cm², nonetheless the authors reported inflammatory effects. Loret et al., (2016) studied the effects of three different TiO₂-NPs on both a monoculture of A549 and on a co-culture of A549 and macrophages cultured and exposed at the ALI. The doses used in the study were higher (1, 3 and 10 μ g/cm²) to what we report and a higher release of various cytokines (TNF- α , IL-8, IL-6 and IL-1 β) on the ALI co-culture was reported. The authors also showed a higher sensibility of the co-culture model with respect to the A549 in the same exposure conditions, and higher effects on the models exposed at the ALI compared to the submerged conditions. Giovanni et al. (2015) tested the pro-inflammatory response of Ag and TiO₂ NPs using concentrations between 10⁻⁷ μ g/mL and 10 μ g/mL on a mouse macrophage cell line in submerged conditions. They observed a moderate pro-inflammatory response, starting from the lower concentration in case of TiO₂-

treated cells. Even though the lower concentrations used can be compared to the present study, the exposure conditions and the model used are different. Future steps of improvement are related to possible optimizations of the *in vitro* model since this has been shown to be a relevant factor in properly assessing NPs and other molecules deposition and hazard (He et al., 2021; Lee et al., 2023; Rothen-Rutishauser et al., 2023). Moreover, for future relevant toxicological studies using this system, prolonged and/or repeated exposures, coupled with the measurement of biological endpoints using omics, are desirable. Also, from a technical point of view, exposure allow a proper mimicking of particle deposition in the lungs, therefore considering gravitational settling and random impaction, should be developed, although the required complex nebulization procedure we report here. The possibility to use lung-on-a-chip systems, coupled with other organ-on-a-chip, should be envisaged as well, given the reported predictability of these models for human health. Finally, the need of generating sound a robust data through NAMs will require further collaboration and integration of expertise from different areas, such as *in vitro* toxicology, human health, air pollution and *in silico* modelling.

5.5 Conclusions

The NAM here reported allowed for the evaluation of the hazard of new NMs at realistic doses of exposure. It is shown that different NPs have a different DE depending on their physical chemical properties such as their size and their agglomeration state. Because of that, the determination of the DE is a critical step for properly defining the concentration of NPs to be nebulized, in order to obtain the final doses of exposure. Doses representative of real environmental concentrations, obtained through a field monitoring campaign and *in silico* modelling, allow for the evaluation of NMs safety mimicking the actual human exposure. The choice of the model used to assess NMs toxicity should be done considering the similarity of the model to the target organ to

obtain results as reliable as possible. The results of this study suggest the lack of hazard for chronic inhalation exposure and confirm the safety of the NMs and process developed. As additional step, intercomparison among different laboratories should test the framework here presented, as relevant differences among laboratories have been reported when working with ALI exposure modules (Bannuscher et al., 2022; Braakhuis et al., 2023).

5.6 Supplementary

5.6.1 Materials and methods

Nanoparticles characterization

The NPs were characterized in terms of size, shape, and agglomeration state by Transmission Electron Microscopy (TEM). The TEM samples were prepared by adding a droplet (5 μL) of the 100 $\mu\text{g}/\text{mL}$ suspension on a Formvar-carbon support film coated copper grid (200 mesh) and let dry overnight. The samples were observed under the Jeol Jem 2100 Plus TEM Microscope (Jeol Ltd., Tokio, Japan).

The NPs suspensions were also characterized in terms of hydrodynamic diameter (z-average) and polydispersity (PDI) by the Dynamic Light Scattering (DLS), and in terms of surface charge (ζ -potential) by the Electrophoretic Light Scattering (ELS) using the Zetasizer Nano ZS90 (Malvern Ltd., Warwickshire, UK). The 100 $\mu\text{g}/\text{mL}$ suspensions were analyzed freshly prepared (time 0) and after 24 h resting at room temperature, to assess the time stability of the NP suspensions.

THP-1 differentiation into macrophages

THP-1 cells were differentiated for 24 h using a concentration of 20 ng/mL of PMA (Phorbol 12-myristate 13-acetate). After differentiation, the medium was changed, and cells were allowed to recover for 24 h. The success of THP-1 differentiation was verified using a CD11b Recombinant Rabbit Monoclonal Antibody (Invitrogen, JU93-81), following the producer's instructions (Figure S4).

Assessment of cytokines production

To assess the capability of the co-culture to produce pro-inflammatory cytokines, cells were exposed to Lipopolysaccharides from *E. coli* (LPS obtained by Sigma Aldrich, Milano, Italy) at a concentration of 10.42 $\mu\text{g}/\text{cm}^2$

and the quantification of three selected cytokines was done 24h after the nebulization through ELISA assays (Invitrogen Life Technologies, Monza, Italy) according to manufacturer's instructions. The quantification of the release of Interleukin 8, Interleukin 6, and Interleukin 1 β was performed on the media of the basolateral side collected from each insert after 24h of exposure to the NPs. The supernatants were stored at -80°C until analysis. The absorbance of the samples was measured using a TECAN Infinite M200 Pro microplate reader (TECAN, Männedorf, Switzerland). The concentration of interleukins was calculated based on standard curves and data are shown as fold change compared to the negative control.

Deposition efficiency

Part of the AgNKD, AgHECs and AgHECp NPs were not nebulized by the system and stayed attached to the upper side of the vibrating mesh (Figure S3), resulting in a reduction of the deposition. The deposition of AgHECs and AgHECp was probably affected by the higher amount of HEC in these concentrations that increased the viscosity of the suspensions. The high viscosity resulted in the formation of foam that clogged the pores of the mesh. For AgNKD, cleaning the mesh by vaporizing 400 μ L of Milli-Q twice was enough for the residues of silver to pass through the pores.

Framework limitation

The framework we reported is affected by some limitations related to the different procedures adopted. Among the limitations that requires, in future developments, a better understanding one of relevance is a better evaluation by a sensitivity analysis of the retained doses calculated by the MPPD model. Some of the components that determine the uncertainties of the MPPD model, and the calculation of the deposition fractions in fact are the input parameters since the accuracy of the deposition fraction calculations heavily relies on the

accuracy of the input parameters used in the model. Uncertainties in parameters such as particle size distribution, breathing patterns, and lung geometry impact the prediction of deposition fractions significantly. Also, the MPPD model assumes specific properties of particles, such as density and shape. However, variations in these properties for different types of particles can introduce uncertainties in the deposition fraction calculations. The MPPD model makes certain assumptions about the behaviour of particles in the respiratory system. These assumptions may not hold true for all scenarios, leading to uncertainties in the calculated deposition fractions. The model did not consider inter-individual variability in lung anatomy, breathing patterns, and physiological parameters. This can introduce uncertainties in the deposition fraction calculations. The MPPD model provides average values, but individual variations may not be accurately captured. Another source of possible variation of the results are the experimental data in input to the model. The MPPD model relies on experimental data for validation and calibration. However, uncertainties in the experimental data, such as measurement errors or limited data availability, can propagate into the model calculations. Finally, a recent report from the OECD (2021) reported that for the MPPD model the variables affecting the most the results are the tidal volume, kept constant in our runs, air concentrations, the particle diameter, that during the different measurements resulted constant, and the GSD. Performing a simple analysis, we obtained that the variation in the retained dose associated to GSD variations was on average 9% for titania NPs and 35% for silver-based NPs. The airborne mass concentration on the contrary resulted to primarily affect the modelled retained alveolar mass. In fact, for titania-based NPs the percentage variability was 46% while for silver-based NPs the variation was 75%. This variation should be, in future experiments also consider for defining the doses of exposure of the *in vitro* models and for risk assessment considerations.

The protocols followed to evaluate the airborne concentration of NPs at the facility site are quite standard for airborne pollutant monitoring. The data collected with the online monitors for measuring the number and mass concentration of particles came from instruments well described in the literature (SMPS and OPC) and their accountability have been largely discussed. More detail on the instrumentation deployed and the results that may be obtained may be found in Trabucco et al., (2022). Variations are therefore associated with actual variation in the airborne concentration of the pollutants rather than to uncertainties related to the procedures adopted. The variability in airborne concentration we observed was higher than 50% for both the NPs. Again, this variation should be considered in future experiments as a source of possible different scenarios to test under the same controlled exposure protocol for *in vitro* model.

References

- OECD 2021 Evaluation of Tools and Models for Assessing Occupational and Consumer Exposure to Manufactured Nanomaterials – Part I: Compilation of tools/models and analysis for further evaluation. Series on the Safety of Manufactured Nanomaterials No. 99 Series on Testing and Assessment, No. 346. ENV/CBC/MONO(2021)27/REV
- Trabucco, S., Koivisto, A.J., Ravegnani, F., Ortelli, S., Zanoni, I., Blosi, M., Costa, A.L., Belosi, F., 2022. Measuring TiO₂N and AgHEC Airborne Particle Density during a Spray Coating Process. *Toxics* 10, 498. <https://doi.org/10.3390/TOXICS10090498/S1>

5.6.2 Results

NPs Characterization

Representative NPs pictures recorded by transmission electron microscopy (TEM) are reported in Figure S1. All the NPs showed a spherical shape with different primary size among the various NPs. AgNKD and AgPVP have a primary size between 30 and 50 nm and show the presence, after suspension drying, of agglomerates in the order of hundreds of nm, while AgHECs and AgHECp NPs are better dispersed and have a smaller primary size, between 20 and 40 nm. AgCUR NPs are heterogeneous in size, since it is possible to identify at least three subpopulations of NPs sizing from 5 nm up to 50 nm. Both TiO₂NKD and TiO₂-N NPs show a strong agglomeration that makes it difficult to determine the primary size of these NPs. The different agglomeration state, especially for Ag NPs, is due to the different surface coatings that provide a better dispersion during the spray coating procedures for which these NPs are synthesized.

The NPs suspensions characterization performed by DLS and ELS is shown in Table S1. The lower z-average was measured for AgCUR and AgHECs NPs. AgHECp, AgNKD, AgPVP and TiO₂NKD show a z-average in the order of hundreds of nm possibly in relation to the formation of bigger agglomerates when the NPs are dispersed, while TiO₂-N NPs showed a z-average in the order of μm at time 0. The analysis performed after 24 hours shows that AgHECs, AgCUR and TiO₂NKD NPs z-average was stable. On the contrary, the z-average decreased for AgNKD, AgPVP, AgHECp and TiO₂-N probably due to the precipitation of the bigger agglomerates at the bottom of the cuvette. Among the different NPs, TiO₂-N NPs showed the highest PdI suggesting the presence of different particles/agglomerates populations compared to the other NPs. The ζ -potential values obtained were negative for all the NPs but AgHECp and TiO₂NKD NPs. Among the different NPs only AgCUR NPs showed a strong negative ζ -potential supporting the lowest z-average here

reported. Our data confirm that the coating with HEC in solution allow a higher stability of the NPs over 24h, avoiding unwanted agglomeration. Similarly, the curcumin coating showed the absence of agglomeration over time. These two NPs were characterized by the lowest hydrodynamic diameter compared to the other NPs tested supporting the choice of these two doping molecules for improving dispersion and NPs properties, such in the case of curcumin.

5.6.3 Supplementary tables

Table S1. NPs characterization by DLS and ELS. The analysis was performed on the NPs suspended in Milli-Q water at the concentration of 100 $\mu\text{g/mL}$. The measurements with the DLS technique were performed right after preparation ($t=0$ h) and after 24 h, while ELS analysis was performed at time 0. A) Data published in Motta et al. (2023), B) data from the present article. In the table, the values of z-average, PDI and ζ -potential \pm SD are reported.

A)	NPs	Medium	Time (h)	$\mu\text{g/mL}$	z-average (nm) \pm SD	PdI \pm SD	ζ -potential (mV) \pm SD
	AgNKD	Milli-Q	0	100	270.76 \pm 53.18	0.45 \pm 0.04	-27.57 \pm 0.60
			24	100	109.35 \pm 22.42	0.34 \pm 0.08	
	AgPVP	Milli-Q	0	100	695.91 \pm 617.49	0.7 \pm 0.26	-6.07 \pm 0.59
			24	100	227.06 \pm 159.62	0.45 \pm 0.15	
	AgHECs	Milli-Q	0	100	122.16 \pm 5.89	0.14 \pm 0.02	-4.71 \pm 0.24
			24	100	115.7 \pm 5.37	0.15 \pm 0.01	
	AgHECp	Milli-Q	0	100	304.89 \pm 34.89	0.37 \pm 0.07	+9.92 \pm 0.37
			24	100	261.63 \pm 26.86	0.36 \pm 0.06	

B)	NPs	Medium	Time (h)	$\mu\text{g/mL}$	z-average (nm) \pm SD	PdI \pm SD	ζ -potential (mV) \pm SD
	AgCUR	Milli-Q	0	100	91.27 \pm 5.79	0.31 \pm 0.01	-34.13 \pm 1.59
			24	100	86.17 \pm 4.42	0.32 \pm 0.02	
	TiO ₂ NKD	Milli-Q	0	100	210.43 \pm 10.34	0.13 \pm 0.04	+18.26 \pm 3.97
			24	100	227.59 \pm 70.54	0.13 \pm 0.01	
	TiO ₂ -N	Milli-Q	0	100	1838.76 \pm 912.16	0.96 \pm 0.05	-17.45 \pm 3.36
			24	100	472.69 \pm 84.53	0.74 \pm 0.08	

Table S2. To evaluate QCM efficiency, PBS at different concentrations (50, 10, 5, 0.5%) were performed. Deposited mass determined by the PBS solution alone (in ng/cm^2) is here reported with the relative standard deviation.

	%	ng/cm^2 (\pm SD)
PBS	50	4925 \pm 326
	10	1067 \pm 163
	5	561 \pm 61
	0.5	66 \pm 9

5.6.4 Supplementary figures

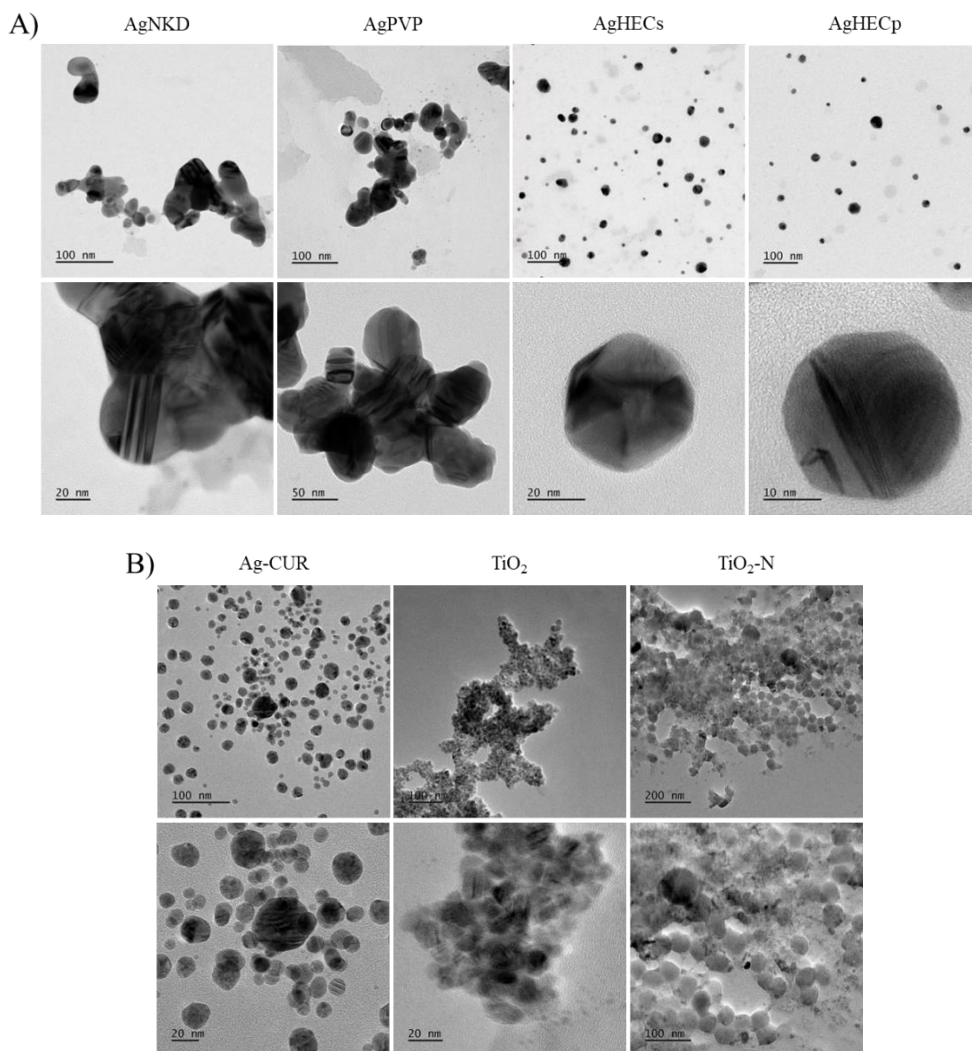


Figure S1. TEM pictures of Ag and TiO₂ NPs suspensions at different magnifications. A) Pictures published in Motta et al. (2023). B) Pictures published in the present paper.

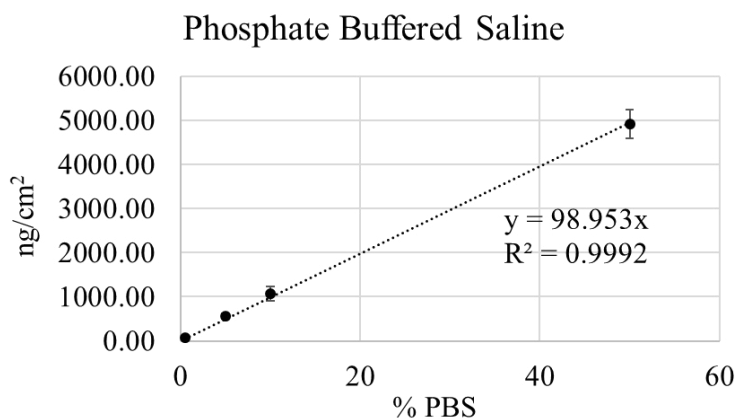


Figure S2. Deposited PBS mass (reported in Table S2) and interpolating linear curve. The linearity between the amount of PBS and the mass measured by the QCM is supported by the high R^2 here reported.

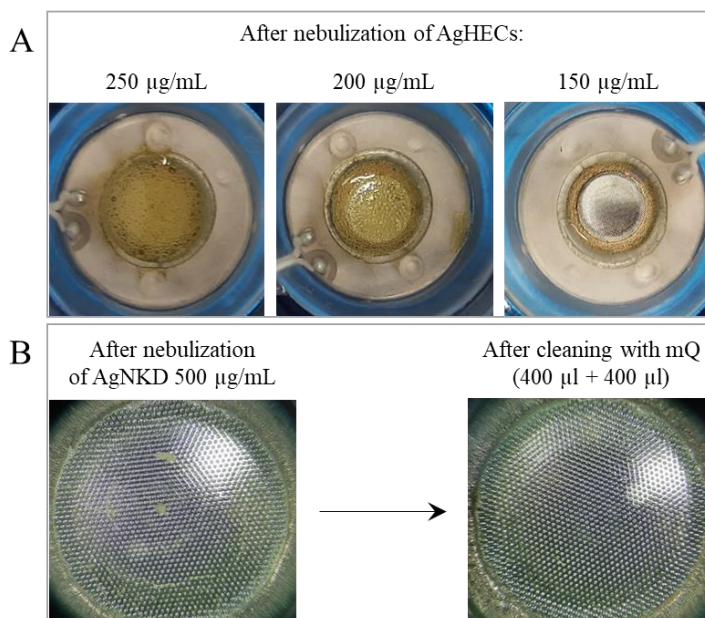


Figure S3. Images of the apical side of the vibrating mesh of the nebulizer after the spray of AgHECs and AgNKD. A) Pictures of the mesh after the nebulization of different concentrations of AgHECs showing the clogging of the pores. B) Pictures of the mesh after the nebulization of a suspension of 500 $\mu\text{g/mL}$ of AgNKD in which are visible the agglomerates of the NPs (arrow); and after the cleaning of the mesh.

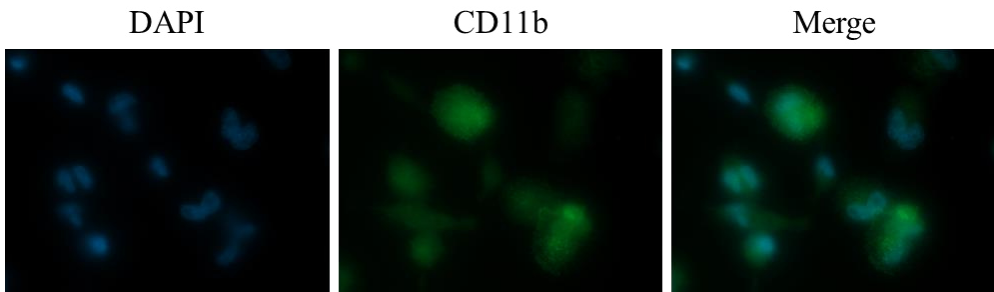


Figure S4. CD11b expression on the surface of dTHP-1. A) Nuclei staining (DAPI, blue), B) CD11b staining (Alexa-488, green) and C) Merge of A) and B). Differentiated cells showed overlapping signals from the two staining, considering the round shaped morphology of macrophagic cells (see also Figure S5).

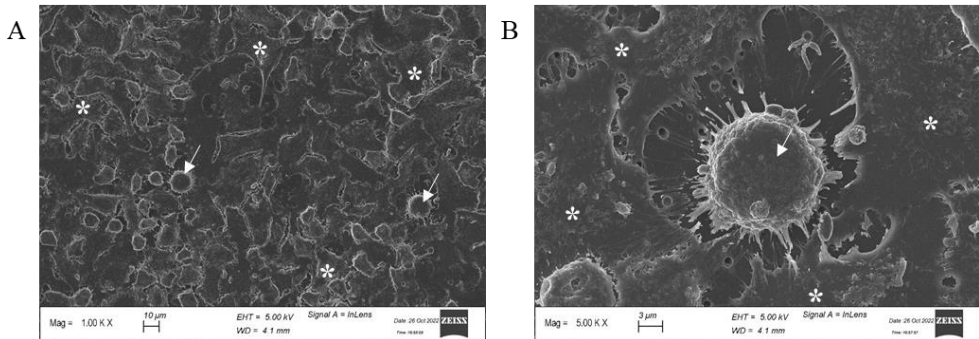


Figure S5. SEM images showing the co-culture morphology. In the representative images of the untreated co-culture, 48 h after addition of the macrophages, is possible to appreciate the distribution of the two cell lines. A) The homogeneous distribution of A549 cells is visible, and the presence of macrophages is shown with an arrow; B) detail of a macrophage, surrounded by A549 (*).

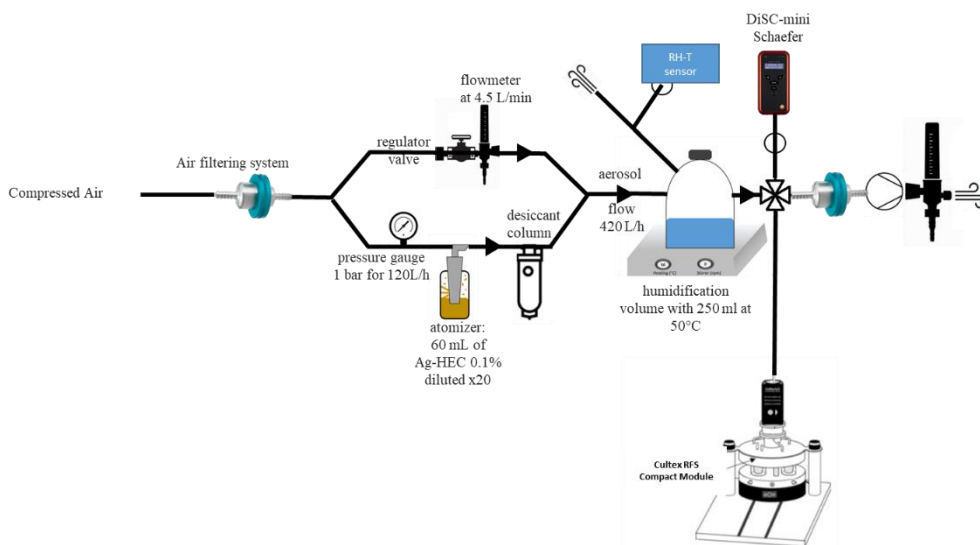


Figure S6. Scheme of the nebulization protocol adopted in the Cultex RFS exposure tests. Briefly, compressed air was filtered by an absolute filter to remove any particle deriving from the compressed air line. The flux was split according to the Collison nebulizer requirement, operating at 1 bar controlled by a pressure gauge. The nebulized particles passed through a desiccator to allow subsequent particle total number concentration by a DiSC-mini (Schaefer, Italy), the flux to the DiSC-mini was deviated by a flow splitter when needed. Part of the generated nebulized particles passed through a glass humidification chamber, filled with sterile water. The relative humidity (RH) and temperature (T) of the exiting air was measured by a RH and T sensor. 1 L/min were constantly sampled from the humidifying chamber to the Cultex RFS Compact module for the cell exposure tests. A pre-weighed Teflon filters was places just before the exhaust exit line to allow for particle sampling and further analysis. Total mass was determined after filter equilibration, by gravimetric analysis while, Ag deposited mass was determined by ICP-OES analysis (see Table S3).

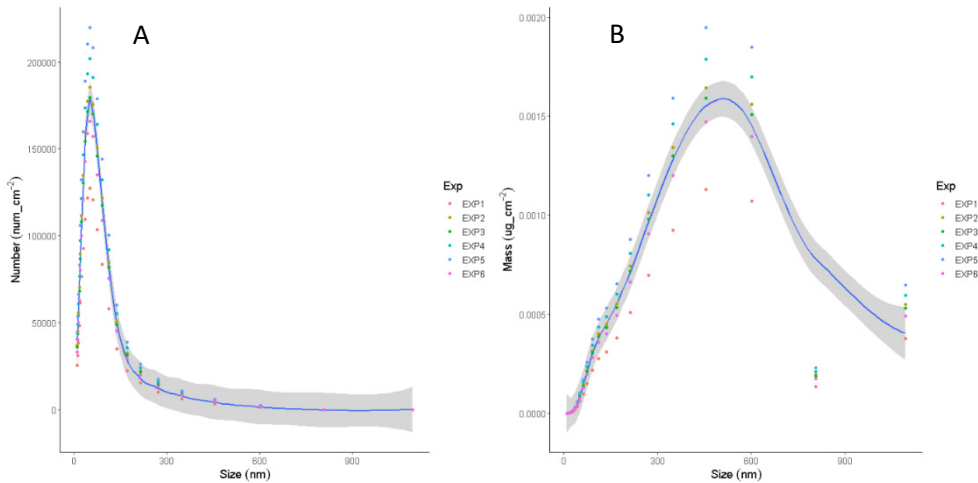


Figure S7. Deposited particle number (A) and particle mass (B) calculated for the Cultex RFS Compact module. The data interpolation curve (blue line) and its confidence interval (grey areas) are reported. Maximal number deposition is at particle size range between 25 and 75 nm (with max deposition at 50 nm), while maximal mass deposition was at particle size range between 350 and 600 nm (with max deposition around 450 nm).

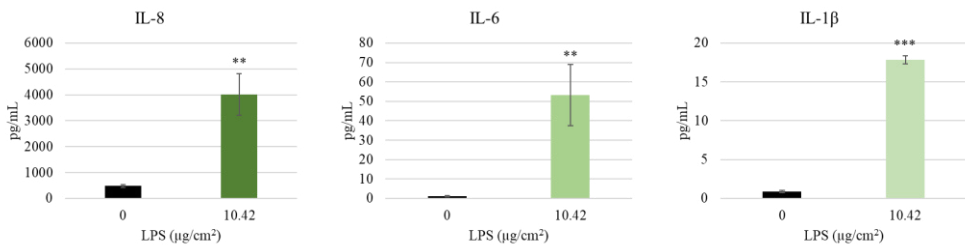


Figure S8. Cytokines release (IL-8, IL-6 and IL-1 β) in the media of the co-culture after 24h of exposure to 10.42 $\mu\text{g}/\text{cm}^2$ of nebulized LPS. Data are shown as the mean of three independent experiments \pm SD. Statistical analysis: one-way ANOVA followed by Dunnett's test. * $p < 0.05$ compared to the control group.

5.7 References

- Amoatey, P., Omidvarborna, H., Al-Jabri, K., Al-Harthy, I., Baawain, M.S., Al-Mamun, A., 2022. Deposition Modeling of Airborne Particulate Matter on Human Respiratory Tract During Winter Seasons in Arid-Urban Environment. *Aerosol Sci. Eng.* 6, 71–85. <https://doi.org/10.1007/S41810-021-00125-2/FIGURES/6>
- Andreoli, C., Prota, V., De Angelis, I., Facchini, E., Zijno, A., Meccia, E., Barletta, B., Butteroni, C., Corinti, S., Chatgialiloglu, C., Krokidis, M.G., Masi, A., Condello, M., Meschini, S., Di Felice, G., Barone, F., 2021. A harmonized and standardized in vitro approach produces reliable results on silver nanoparticles toxicity in different cell lines. *J. Appl. Toxicol.* 41, 1980–1997. <https://doi.org/10.1002/JAT.4178>
- Bannuscher, A., Schmid, O., Drasler, B., Rohrbasser, A., Braakhuis, H.M., Meldrum, K., Zwart, E.P., Gremmer, E.R., Birk, B., Rissel, M., Landsiedel, R., Moschini, E., Evans, S.J., Kumar, P., Orak, S., Doryab, A., Erdem, J.S., Serchi, T., Vandebriel, R.J., Cassee, F.R., Doak, S.H., Petri-Fink, A., Zienolddiny, S., Clift, M.J.D., Rothen-Rutishauser, B., 2022. An inter-laboratory effort to harmonize the cell-delivered in vitro dose of aerosolized materials. *NanoImpact* 28, 100439. <https://doi.org/10.1016/J.IMPACT.2022.100439>
- Belosi, F., Koivisto, A.J., Furxhi, I., de Ipiña, J.L., Nicosia, A., Ravegnani, F., Ortelli, S., Zanoni, I., Costa, A., 2023. Critical aspects in occupational exposure assessment with different aerosol metrics in an industrial spray coating process. *NanoImpact* 30, 100459. <https://doi.org/10.1016/J.IMPACT.2023.100459>
- Boccuni, F., Ferrante, R., Tombolini, F., Natale, C., Gordiani, A., Sabella, S., Iavicoli, S., 2020. Occupational exposure to graphene and silica nanoparticles. Part I: workplace measurements and samplings. *Nanotoxicology* 14, 1280–1300. https://doi.org/10.1080/17435390.2020.1834634/SUPPL_FILE/INAN_A_1834634_SM9739.DOCX
- Braakhuis, H.M., Gremmer, E.R., Bannuscher, A., Drasler, B., Keshavan, S., Rothen-Rutishauser, B., Birk, B., Verlohner, A., Landsiedel, R., Meldrum, K., Doak, S.H., Clift, M.J.D., Erdem, J.S., Foss, O.A.H., Zienolddiny-Narui, S., Serchi, T., Moschini, E., Weber, P., Burla, S., Kumar, P., Schmid, O., Zwart, E., Vermeulen, J.P., Vandebriel, R.J., 2023. Transferability and reproducibility of exposed air-liquid interface co-culture lung models. *NanoImpact* 31, 100466. <https://doi.org/10.1016/j.impact.2023.100466>
- Caldeira, C., Farcas, R., Garmendia Aguirre, I., Mancini, L., Tosches, D., Amelio, A., Rasmussen, K., Rauscher, H., Riego Sintes, J. and Sala, S., 2022. Safe and sustainable by design chemicals and materials - Framework for the definition of criteria and evaluation procedure for chemicals and materials [WWW Document]. EUR 31100 EN, Publ. Off. Eur. Union, Luxemb. <https://doi.org/10.2760/487955, JRC128591>
- Cao, Y., Dhahad, H.A., El-Shorbagy, M.A., Alijani, H.Q., Zakeri, M., Heydari, A., Bahonar, E., Slouf, M., Khatami, M., Naderifar, M., Irvani, S., Khatami, S.,

- Dehkordi, F.F., 2021. Green synthesis of bimetallic ZnO–CuO nanoparticles and their cytotoxicity properties. *Sci. Reports* 2021 111 11, 1–8. <https://doi.org/10.1038/s41598-021-02937-1>
- Cappellini, F., Di Bucchianico, S., Karri, V., Latvala, S., Malmlöf, M., Kippler, M., Elihn, K., Hedberg, J., Wallinder, I.O., Gerde, P., Karlsson, H.L., 2020. Dry Generation of CeO₂ Nanoparticles and Deposition onto a Co-Culture of A549 and THP-1 Cells in Air-Liquid Interface—Dosimetry Considerations and Comparison to Submerged Exposure. *Nanomater.* 2020, Vol. 10, Page 618 10, 618. <https://doi.org/10.3390/NANO10040618>
- CEN, 2018. EN 17058 - Workplace exposure - assessment of inhalation exposure to nano-objects and their agglomerates and aggregates [WWW Document]. URL <https://www.en-standard.eu/csn-en-17058-workplace-exposure-assessment-of-exposure-by-inhalation-of-nano-objects-and-their-agglomerates-and-agglomerates/> (accessed 7.11.23).
- Chary, A., Serchi, T., Moschini, E., Hennen, J., Cambier, S., Ezendam, J., Blömeke, B., Gutleb, A.C., 2019. An in vitro coculture system for the detection of sensitization following aerosol exposure. *ALTEX - Altern. to Anim. Exp.* 36, 403–418. <https://doi.org/10.14573/ALTEX.1901241>
- Cristo, L. Di, Boccuni, F., Iavicoli, S., Sabella, S., 2020. A Human-Relevant 3D In Vitro Platform for an Effective and Rapid Simulation of Workplace Exposure to Nanoparticles: Silica Nanoparticles as Case Study. *Nanomater.* 2020, Vol. 10, Page 1761 10, 1761. <https://doi.org/10.3390/NANO10091761>
- El Yamani, N., Mariussen, E., Gromelski, M., Wyrzykowska, E., Grabarek, D., Puzyn, T., Tanasescu, S., Dusinska, M., Rundén-Pran, E., 2022. Hazard identification of nanomaterials: In silico unraveling of descriptors for cytotoxicity and genotoxicity. *Nano Today* 46, 101581. <https://doi.org/10.1016/J.NANTOD.2022.101581>
- European Chemicals Agency, 2016. New approach methodologies in regulatory science : proceedings of a scientific workshop : Helsinki, 19-20 April 2016. European Chemicals Agency. <https://doi.org/doi/10.2823/543644>
- Giovanni, M., Yue, J., Zhang, L., Xie, J., Ong, C.N., Leong, D.T., 2015. Pro-inflammatory responses of RAW264.7 macrophages when treated with ultralow concentrations of silver, titanium dioxide, and zinc oxide nanoparticles. *J. Hazard. Mater.* 297, 146–152. <https://doi.org/10.1016/J.JHAZMAT.2015.04.081>
- Gualtieri, M., Berico, M., Grollino, M.G., Cremona, G., La Torretta, T., Malaguti, A., Petralia, E., Stracquadanio, M., Santoro, M., Benassi, B., Piersanti, A., Chiappa, A., Bernabei, M., Zanini, G., 2022. Emission Factors of CO₂ and Airborne Pollutants and Toxicological Potency of Biofuels for Airplane Transport: A Preliminary Assessment. *Toxics* 2022, Vol. 10, Page 617 10, 617. <https://doi.org/10.3390/TOXICS10100617>
- He, R.W., Braakhuis, H.M., Vandebriel, R.J., Staal, Y.C.M., Gremmer, E.R., Fokkens, P.H.B., Kemp, C., Vermeulen, J., Westerink, R.H.S., Cassee, F.R., 2021. Optimization of an air-liquid interface in vitro cell co-culture model to estimate the hazard of aerosol exposures. *J. Aerosol Sci.* 153, 105703. <https://doi.org/10.1016/J.JAEROSCI.2020.105703>
- Hu, Y., Sheng, Y., Ji, X., Liu, P., Tang, L., Chen, G., Chen, G., 2020. Comparative

- anti-inflammatory effect of curcumin at air-liquid interface and submerged conditions using lipopolysaccharide stimulated human lung epithelial A549 cells. *Pulm. Pharmacol. Ther.* 63, 101939.
<https://doi.org/10.1016/J.PUPT.2020.101939>
- ISO, 2007. ISO/TR 27628: Workplace atmospheres - Ultrafine, nanoparticle and nanostructured aerosols - Inhalation exposure characterization and assessment.
- Ke, P.C., Lin, S., Parak, W.J., Davis, T.P., Caruso, F., 2017. A Decade of the Protein Corona. *ACS Nano* 11, 11773–11776.
https://doi.org/10.1021/ACSNANO.7B08008/ASSET/IMAGES/LARGE/NN-2017-08008A_0001.JPEG
- Koivisto, A.J., Del Secco, B., Trabucco, S., Nicosia, A., Ravegnani, F., Altin, M., Cabellos, J., Furxhi, I., Blosi, M., Costa, A., de Ipiña, J.L., Belosi, F., 2022. Quantifying Emission Factors and Setting Conditions of Use According to ECHA Chapter R.14 for a Spray Process Designed for Nanocoatings—A Case Study. *Nanomaterials* 12, 596. <https://doi.org/10.3390/NANO12040596/S1>
- Kuhlbusch, T.A.J., Wijnhoven, S.W.P., Haase, A., 2018. Nanomaterial exposures for worker, consumer and the general public. *NanoImpact* 10, 11–25.
<https://doi.org/10.1016/j.impact.2017.11.003>
- Kuprat, A.P., Jalali, M., Jan, T., Corley, R.A., Asgharian, B., Price, O., Singh, R.K., Colby, S., Darquenne, C., 2021. Efficient bi-directional coupling of 3D computational fluid-particle dynamics and 1D Multiple Path Particle Dosimetry lung models for multiscale modeling of aerosol dosimetry. *J. Aerosol Sci.* 151, 105647. <https://doi.org/10.1016/J.JAEROSCI.2020.105647>
- Lee, R.E., Reidel, B., Nelson, M.R., Macdonald, J.K., Kesimer, M., Randell, S.H., 2023. Air-Liquid interface cultures to model drug delivery through the mucociliary epithelial barrier. *Adv. Drug Deliv. Rev.* 198, 114866.
<https://doi.org/10.1016/J.ADDR.2023.114866>
- Leibrock, L., Wagener, S., Singh, A.V., Laux, P., Luch, A., 2019. Nanoparticle induced barrier function assessment at liquid–liquid and air–liquid interface in novel human lung epithelia cell lines. *Toxicol. Res. (Camb)*. 8, 1016–1027.
<https://doi.org/10.1039/C9TX00179D>
- Lenz, A.G., Karg, E., Brendel, E., Hinze-Heyn, H., Maier, K.L., Eickelberg, O., Stoeger, T., Schmid, O., 2013. Inflammatory and oxidative stress responses of an alveolar epithelial cell line to airborne zinc oxide nanoparticles at the air-liquid interface: A comparison with conventional, submerged cell-culture conditions. *Biomed Res. Int.* 2013. <https://doi.org/10.1155/2013/652632>
- Lenz, A.G., Karg, E., Lentner, B., Dittrich, V., Brandenberger, C., Rothen-Rutishauser, B., Schulz, H., Ferron, G.A., Schmid, O., 2009. A dose-controlled system for air-liquid interface cell exposure and application to zinc oxide nanoparticles. *Part. Fibre Toxicol.* 6, 1–17.
<https://doi.org/10.1186/1743-8977-6-32/FIGURES/9>
- Lin, W., Huang, Y., Wern, Zhou, X.D., Ma, Y., 2006. In vitro toxicity of silica nanoparticles in human lung cancer cells. *Toxicol. Appl. Pharmacol.* 217, 252–259. <https://doi.org/10.1016/J.TAAP.2006.10.004>
- Ling, M.P., Chio, C.P., Chou, W.C., Chen, W.Y., Hsieh, N.H., Lin, Y.J., Liao, C.M., 2011. Assessing the potential exposure risk and control for airborne titanium dioxide and carbon black nanoparticles in the workplace. *Environ.*

- Sci. Pollut. Res. 18, 877–889. <https://doi.org/10.1007/S11356-011-0447-Y/TABLES/3>
- Liu, N., Tang, M., Ding, J., 2020. The interaction between nanoparticles-protein corona complex and cells and its toxic effect on cells. *Chemosphere* 245, 125624. <https://doi.org/10.1016/J.CHEMOSPHERE.2019.125624>
- Loret, T., Peyret, E., Dubreuil, M., Aguerre-Chariol, O., Bressot, C., le Bihan, O., Amodeo, T., Trouiller, B., Braun, A., Egles, C., Lacroix, G., 2016. Air-liquid interface exposure to aerosols of poorly soluble nanomaterials induces different biological activation levels compared to exposure to suspensions. *Part. Fibre Toxicol.* 13, 1–21. <https://doi.org/10.1186/S12989-016-0171-3/FIGURES/10>
- Lovén, K., Dobric, J., Bölükbas, D.A., Kåredal, M., Tas, S., Rissler, J., Wagner, D.E., Isaxon, C., 2021. Toxicological effects of zinc oxide nanoparticle exposure: an in vitro comparison between dry aerosol air-liquid interface and submerged exposure systems. *Nanotoxicology* 15, 494–510. https://doi.org/10.1080/17435390.2021.1884301/SUPPL_FILE/INAN_A_1884301_SM1109.DOCX
- Manojkumar, N., Srimuruganandam, B., Shiva Nagendra, S.M., 2019. Application of multiple-path particle dosimetry model for quantifying age specified deposition of particulate matter in human airway. *Ecotoxicol. Environ. Saf.* 168, 241–248. <https://doi.org/10.1016/J.ECOENV.2018.10.091>
- Marika, M., Marketa, D., Lada, S., Marian, R., Filip, K., Adam, V., Věra, V., Kristina, K., Dagmar, J., Tuula, H., 2022. New approach methods for assessing indoor air toxicity. *Curr. Res. Toxicol.* 3, 100090. <https://doi.org/10.1016/J.CRTOX.2022.100090>
- Mazari, S.A., Ali, E., Abro, R., Khan, F.S.A., Ahmed, I., Ahmed, M., Nizamuddin, S., Siddiqui, T.H., Hossain, N., Mubarak, N.M., Shah, A., 2021. Nanomaterials: Applications, waste-handling, environmental toxicities, and future challenges – A review. *J. Environ. Chem. Eng.* 9, 105028. <https://doi.org/10.1016/J.JECE.2021.105028>
- Medina-Reyes, E.I., Delgado-Buenrostro, N.L., Leseman, D.L., Déciga-Alcaraz, A., He, R., Gremmer, E.R., Fokkens, P.H.B., Flores-Flores, J.O., Cassee, F.R., Chirino, Y.I., 2020. Differences in cytotoxicity of lung epithelial cells exposed to titanium dioxide nanofibers and nanoparticles: Comparison of air-liquid interface and submerged cell cultures. *Toxicol. Vitro.* 65, 104798. <https://doi.org/10.1016/J.TIV.2020.104798>
- Meldrum, K., Evans, S.J., Vogel, U., Tran, L., Doak, S.H., Clift, M.J.D., 2022. The influence of exposure approaches to in vitro lung epithelial barrier models to assess engineered nanomaterial hazard. *Chemosphere* 295, 114–134. <https://doi.org/10.1080/17435390.2022.2051627>
- Mittal, J., Pal, U., Sharma, L., Verma, A.K., Ghosh, M., Sharma, M.M., 2020. Unveiling the cytotoxicity of phytosynthesised silver nanoparticles using *Tinospora cordifolia* leaves against human lung adenocarcinoma A549 cell line. *IET Nanobiotechnology* 14, 230–238. <https://doi.org/10.1049/IET-NBT.2019.0335>
- Moore, T.L., Rodriguez-Lorenzo, L., Hirsch, V., Balog, S., Urban, D., Jud, C.,

- Rothen-Rutishauser, B., Lattuada, M., Petri-Fink, A., 2015. Nanoparticle colloidal stability in cell culture media and impact on cellular interactions. *Chem. Soc. Rev.* 44, 6287–6305. <https://doi.org/10.1039/C4CS00487F>
- Motta, G., Gualtieri, M., Saibene, M., Bengalli, R., Briigliadori, A., Carrière, M., Mantecca, P., 2023. Preliminary Toxicological Analysis in a Safe-by-Design and Adverse Outcome Pathway-Driven Approach on Different Silver Nanoparticles: Assessment of Acute Responses in A549 Cells. *Toxics* 2023, Vol. 11, Page 195 11, 195. <https://doi.org/10.3390/TOXICS11020195>
- MPPD: Multiple-Path Particle Dosimetry Model [WWW Document], n.d. URL <https://www.ara.com/mppd/>
- Natale, C., Ferrante, R., Boccuni, F., Tombolini, F., Sarto, M.S., Iavicoli, S., 2022. Occupational Exposure to Silica Nanoparticles: Evaluation of Emission Fingerprints by Laboratory Simulations. *Sustain.* 2022, Vol. 14, Page 10251 14, 10251. <https://doi.org/10.3390/SU141610251>
- Nowack, B., Krug, H.F., Height, M., 2011. 120 years of nanosilver history: Implications for policy makers. *Environ. Sci. Technol.* 45, 1177–1183. https://doi.org/10.1021/ES103316Q/SUPPL_FILE/ES103316Q_SI_001.PDF
- Nymark, P., Bakker, M., Dekkers, S., Franken, R., Fransman, W., García-Bilbao, A., Greco, D., Gulumian, M., Hadrup, N., Halappanavar, S., Hongisto, V., Hougaard, K.S., Jensen, K.A., Kohonen, P., Koivisto, A.J., Dal Maso, M., Oosterwijk, T., Poikkimäki, M., Rodriguez-Llopis, I., Stierum, R., Sørli, J.B., Grafström, R., 2020. Toward Rigorous Materials Production: New Approach Methodologies Have Extensive Potential to Improve Current Safety Assessment Practices. *Small* 16, 1904749. <https://doi.org/10.1002/SMLL.201904749>
- OECD, 2015. Harmonized tiered approach to measure and assess the potential exposure to airborne emissions of engineered nano-objects and their agglomerates and aggregates at workplaces. *Ser. Saf. Manuf. Nanomater.* 55, JT03378848.
- Paur, H.R., Cassee, F.R., Teeguarden, J., Fissan, H., Diabate, S., Aufderheide, M., Kreyling, W.G., Hänninen, O., Kasper, G., Riediker, M., Rothen-Rutishauser, B., Schmid, O., 2011. In-vitro cell exposure studies for the assessment of nanoparticle toxicity in the lung—A dialog between aerosol science and biology. *J. Aerosol Sci.* 42, 668–692. <https://doi.org/10.1016/J.JAEROSCI.2011.06.005>
- Ramanarayanan, T., Szarka, A., Flack, S., Hinderliter, P., Corley, R., Charlton, A., Pyles, S., Wolf, D., 2022. Application of a new approach method (NAM) for inhalation risk assessment. *Regul. Toxicol. Pharmacol.* 133, 105216. <https://doi.org/10.1016/J.YRTPH.2022.105216>
- Regulation (EC) No 1223/2009 of the European Parliament and of the Council of 30 November 2009 on cosmetic products [WWW Document], n.d. URL <https://eur-lex.europa.eu/legal-content/EN/TXT/?uri=CELEX%3A02009R1223-20221217> (accessed 8.7.23).
- Rothen-Rutishauser, B., Gibb, M., He, R., Petri-Fink, A., Sayes, C.M., 2023. Human lung cell models to study aerosol delivery – considerations for model design and development. *Eur. J. Pharm. Sci.* 180, 106337. <https://doi.org/10.1016/J.EJPS.2022.106337>

- Salmattonidis, A., Ribalta, C., Sanf elix, V., Bezantakos, S., Biskos, G., Vulpoi, A., Simion, S., Monfort, E., Viana, M., 2019. Workplace Exposure to Nanoparticles during Thermal Spraying of Ceramic Coatings. *Ann. Work Expo. Heal.* 63, 91–106. <https://doi.org/10.1093/ANNWEH/WXY094>
- Tilly, T.B., Ward, R.X., Morea, A.F., Tyler Nelson, M., Robinson, S.E., Eiguren-Fernandez, A., Lewis, G.S., Lednický, J.A., Sabo-Attwood, T., Hussain, S.M., Wu, C.-Y., 2023. Toxicity assessment of CeO₂ and CuO nanoparticles at the air-liquid interface using bioinspired condensational particle growth. *Hyg. Environ. Heal. Adv.* 7, 100074. <https://doi.org/10.1016/J.HEHA.2023.100074>
- Tomankova, K., Horakova, J., Harvanova, M., Malina, L., Soukupova, J., Hradilova, S., Kejlova, K., Malohlava, J., Licman, L., Dvorakova, M., Jirova, D., Kolarova, H., 2015. Cytotoxicity, cell uptake and microscopic analysis of titanium dioxide and silver nanoparticles in vitro. *Food Chem. Toxicol.* 82, 106–115. <https://doi.org/10.1016/J.FCT.2015.03.027>
- Trabucco, S., Koivisto, A.J., Ravegnani, F., Ortelli, S., Zandoni, I., Bloisi, M., Costa, A.L., Belosi, F., 2022. Measuring TiO₂N and AgHEC Airborne Particle Density during a Spray Coating Process. *Toxics* 10, 498. <https://doi.org/10.3390/TOXICS10090498/S1>
- Turley, A.E., Isaacs, K.K., Wetmore, B.A., Karmaus, A.L., Embry, M.R., Krishan, M., 2019. Incorporating new approach methodologies in toxicity testing and exposure assessment for tiered risk assessment using the RISK21 approach: Case studies on food contact chemicals. *Food Chem. Toxicol.* 134, 110819. <https://doi.org/10.1016/J.FCT.2019.110819>
- Upadhyay, S., Palmberg, L., 2018. Air-Liquid Interface: Relevant In Vitro Models for Investigating Air Pollutant-Induced Pulmonary Toxicity. *Toxicol. Sci.* 164, 21–30. <https://doi.org/10.1093/TOXSCI/KFY053>
- Wang, Y., Adamcakova-Dodd, A., Steines, B.R., Jing, X., Salem, A.K., Thorne, P.S., 2020. Comparison of in vitro toxicity of aerosolized engineered nanomaterials using air-liquid interface mono-culture and co-culture models. *NanoImpact* 18, 100215. <https://doi.org/10.1016/J.IMPACT.2020.100215>
- Zanganeh, S., Spitler, R., Erfanzadeh, M., Alkilany, A.M., Mahmoudi, M., 2016. Protein corona: Opportunities and challenges. *Int. J. Biochem. Cell Biol.* 75, 143–147. <https://doi.org/10.1016/J.BIOCEL.2016.01.005>

General conclusions and future perspectives

6.1 General conclusions

This work, as part of the EU H2020 ASINA project, contributes to develop Safe-by-Design (SbD) strategies aiming at anticipating and preventing the risk toward environmental and human health of innovative nanomaterials (NMs) and nano-enabled products (NEPs). In particular, silver (Ag) and titania (TiO₂)-based NMs have been extensively characterized for their hazard profile, considering their exploitation as textile antimicrobial coating agents and photocatalytic air purifying systems. The innovative approaches used to characterize exposure and hazard during the different NMs life cycle stages will likely fit into the new frameworks under development for Safe and Sustainable by Design (SSbD) new chemicals and materials (Caldeira et al., 2022), providing always greener products to next generations. To deliver relevant contributions to such new frameworks, the research on New Approach Methodologies (NAMs) should be prioritized.

Accordingly, the use of advanced *in vitro* methods is at the core of the present work. *In vitro* models, as alternatives to animal experiments, align with the directive on the protection of animals used for scientific purposes (Directive 2010/63/EU) and adhere to the 3R principles.

The use of NPs offers various benefits due to the advantageous surface-volume ratio which minimizes the quantity of metal used, thereby reducing production costs, and enhancing selected performances compared to their bulk counterparts. However, it is well established that NPs can have adverse effects on both environmental systems and living organisms (Fard et al., 2015). As a result, investigating these effects and implementing methods to mitigate potential toxic outcomes are of fundamental importance.

By employing a SbD approach in conjunction with an Adverse Outcome Pathway (AOP) strategy, this study characterizes the hazard associated with various newly synthesized TiO₂ and Ag nanoparticles (NPs). These are nitrogen doped TiO₂ and Ag functionalized with either polyvinylpyrrolidone (PVP), hydroxyethylcellulose (HEC), or curcumin (CUR). The results demonstrated that the functionalization of the NPs has a primary role in driving their toxicity (Feng et al., 2018; Sharma et al., 2014). Furthermore, the method of NPs production also plays a significant role in determining their toxicity. For instance, Ag NPs coated with HEC exhibited a higher toxicity following a freeze-drying postproduction process. Consequently, newly developed NPs should be designed and synthesized using coatings and management processes aimed at minimizing potential hazard. Moreover, new NMs should be tested starting from the very beginning of manufacturing procedures (material selection, doping molecules definition etc.) to early highlight potential hazard, also in the view of re-designing the materials, according to the SbD framework. Noteworthy, the toxicity of Ag NPs was effectively reduced through functionalization with curcumin, possibly counteracting the oxidative effects of these NPs, often reported as the leading mechanism in NPs toxicity (Cypriyana P J et al., 2021).

Another interesting result that can be of relevance in a risk assessment framework is that the ratio between the coating and the NP is a parameter that may modulate the particles adverse effects. In fact, AgHEC NPs with a higher molar ratio of HEC (ratio HEC/Ag of 6.4 compared to the lower ratio of 5.5) were highly toxic, since the interaction of Ag with the cells was probably favoured by the higher amount of HEC.

TiO₂ NPs proved to be relatively safe, under the exposure conditions applied. TiO₂NKD was only able to induce reactive oxygen species (ROS) production at the higher dose, while TiO₂-N was effective in inducing H2AX phosphorylation, but with lower effect compared to Ag NPs.

In addition to a traditional toxicological approach, this study also embraces a more advanced and realistic methodology by employing a model and exposure systems that better replicate real environmental conditions. The NAM here reported enables the evaluation of the hazard of new NMs at realistic exposure doses, considering human inhalation as the primary exposure pathway. High doses are useful to highlight the mechanisms of toxicity behind a new NPs, but exposures at realistic doses can give more representative and predictive information. The use of a co-culture model of the alveolar space, cultured and exposed at the Air-Liquid Interface (ALI), allows for more reliable results, since the experimental setup reflects better the physiological interactions between different cell's types resident in the lungs. The study further underlines the significance of integrating diverse experimental approaches. The use of doses representative of real environmental concentrations may be determined only through a dedicated field monitoring campaign and using the data from this campaign to run an *in silico* model to obtain the human lung deposited or retained doses. This integration ensures the evaluation of NMs safety that closely resembles real human exposure and provide data ready for risk assessment. Keeping in mind the limitation of the study (i.e. single-dose exposure versus chronic inhalation processes; few toxicological outcomes measured), the results reported indicate the absence of significant hazard for inhalation exposure and confirm the acceptable safety profile of the NMs and processes developed in ASINA project.

6.2 Future perspectives

The development of nanotechnologies must be strongly supported by toxicological analyses, particularly from a SSbD perspective. New NMs require the evaluation of their safety and sustainability taking advantage of *in vitro* models, using NPs well characterized in terms of physical-chemical (p-chem) characteristics and applying toxicological procedures that can reduce false interpretations, also by considering AOPs-oriented approaches and other NAMs. However, it is worth noting that the development of complete and validated AOPs for each newly synthesized NM remains a challenge due to the current unavailability of toxicological data.

Greater research efforts are essential to identify the effect concentrations of NMs and, consequently, to establish accurate exposure limit values, thereby enhancing the precision of risk assessment. Employing *in vitro* systems representative of the alveolar epithelium, coupled with exposure methods that closely mimic human physiology, along with realistic exposure doses, are of critical importance in evaluating the potential hazard posed by various NPs, especially within the context of a SSbD approach.

In the future, it will be valuable to explore more in detail toxicity endpoints typically associated with NPs, such as genotoxicity and oxidative changes of proteins and lipids (Paciorek et al., 2020; Xie et al., 2011). Additionally, assessing the same endpoints considered in this study but at different exposure times could help in identifying both early and late responses, which is essential to interpret possible sub-chronic and chronic effects. The use of omics approaches (genomic, transcriptomic and proteomic), may provide information in a more refined way, indicating for example changes in the expression of the genes involved in the different response pathways activated after sub-acute exposure conditions.

Selecting and developing more accurate biological models to assess NMs toxicity should be also prioritized, especially considering 3D models that

enhance the similarity of the *in vitro* system to the target organ, thus improving the reliability of the results obtained. By increasing the complexity of the model, it's possible to obtain more realistic and informative data. Therefore, it would also be useful to use biological models that better mimic the lung, whether by increasing the complexity of the model by incorporating additional cell lines (such as endothelial cells) or by using more advanced models like spheroids (Klein et al., 2013; Licciardello et al., 2023; Shiraishi et al., 2019). As an additional step, it would be beneficial to carry out intercomparisons involving different laboratories to test the framework presented in this study, as relevant differences among laboratories have been reported when working with ALI exposure modules (Bannuscher et al., 2022; Braakhuis et al., 2023). Finally, it will be of interest to promote in the future a call for data among researchers or projects dealing with NPs hazard evaluation and risk assessment to refine or develop *de novo in silico* methods that can help to prioritize the hazard expected from newly developed NPs. This will, ideally, restrict the number of new NMs to be tested in complex *in vitro* models increasing the possible endpoints to be characterized in a cost-effective way. The new generated data will provide additional input to furthermore refine the *in silico* methods converging to modelling systems that will be reliable to assess NPs risk.

6.3 References

- Bannuscher, A., Schmid, O., Drasler, B., Rohrbasser, A., Braakhuis, H.M., Meldrum, K., Zwart, E.P., Gremmer, E.R., Birk, B., Rissel, M., Landsiedel, R., Moschini, E., Evans, S.J., Kumar, P., Orak, S., Doryab, A., Erdem, J.S., Serchi, T., Vandebriel, R.J., Cassee, F.R., Doak, S.H., Petri-Fink, A., Zienolddiny, S., Clift, M.J.D., Rothen-Rutishauser, B., 2022. An inter-laboratory effort to harmonize the cell-delivered in vitro dose of aerosolized materials. *NanoImpact* 28, 100439. <https://doi.org/10.1016/J.IMPACT.2022.100439>
- Braakhuis, H.M., Gremmer, E.R., Bannuscher, A., Drasler, B., Keshavan, S., Rothen-Rutishauser, B., Birk, B., Verlohner, A., Landsiedel, R., Meldrum, K., Doak, S.H., Clift, M.J.D., Erdem, J.S., Foss, O.A.H., Zienolddiny-Narui, S., Serchi, T., Moschini, E., Weber, P., Burla, S., Kumar, P., Schmid, O., Zwart, E., Vermeulen, J.P., Vandebriel, R.J., 2023. Transferability and reproducibility of exposed air-liquid interface co-culture lung models. *NanoImpact* 31, 100466. <https://doi.org/10.1016/j.impact.2023.100466>
- Caldeira, C., Farcas, R., Garmendia Aguirre, I., Mancini, L., Tosches, D., Amelio, A., Rasmussen, K., Rauscher, H., Riego Sintes, J. and Sala, S., 2022. Safe and sustainable by design chemicals and materials - Framework for the definition of criteria and evaluation procedure for chemicals and materials [WWW Document]. EUR 31100 EN, Publ. Off. Eur. Union, Luxemb. <https://doi.org/10.2760/487955>, JRC128591
- Cypriyana P J, J., S, S., Angalene J, L.A., Samrot, A. V., Kumar S, S., Ponniah, P., Chakravarthi, S., 2021. Overview on toxicity of nanoparticles, it's mechanism, models used in toxicity studies and disposal methods – A review. *Biocatal. Agric. Biotechnol.* 36, 102117. <https://doi.org/10.1016/J.BCAB.2021.102117>
- Directive 2010/63/EU of the European Parliament and of the Council of 22 September 2010 on the protection of animals used for scientific purposes Text with EEA relevance [WWW Document], n.d. URL <https://eur-lex.europa.eu/legal-content/EN/TXT/?uri=CELEX:32010L0063> (accessed 10.23.23).
- Feng, Q., Liu, Y., Huang, Jian, Chen, K., Huang, Jinxing, Xiao, K., 2018. Uptake, distribution, clearance, and toxicity of iron oxide nanoparticles with different sizes and coatings. *Sci. Reports* 2018 81 8, 1–13. <https://doi.org/10.1038/s41598-018-19628-z>
- Khalili Fard, J., Jafari, S., Eghbal, M.A., 2015. A Review of Molecular Mechanisms Involved in Toxicity of Nanoparticles. *Adv. Pharm. Bull.* 5, 447–54. <https://doi.org/10.15171/apb.2015.061>
- Klein, S.G., Serchi, T., Hoffmann, L., Blömeke, B., Gutleb, A.C., 2013. An improved 3D tetra-culture system mimicking the cellular organisation at the alveolar barrier to study the potential toxic effects of particles on the lung. *Part. Fibre Toxicol.* 10, 1–18. <https://doi.org/10.1186/1743-8977-10-31/FIGURES/11>
- Licciardello, M., Sgarminato, V., Ciardelli, G., Tonda-Turo, C., 2023. Development of biomimetic co-culture and tri-culture models to mimic the complex structure of the alveolar-capillary barrier. *Biomater. Adv.* 154, 213620.

- <https://doi.org/10.1016/J.BIOADV.2023.213620>
- Paciorek, P., Zuberek, M., Grzelak, A., 2020. Products of Lipid Peroxidation as a Factor in the Toxic Effect of Silver Nanoparticles. *Mater.* 2020, Vol. 13, Page 2460 13, 2460. <https://doi.org/10.3390/MA13112460>
- Sharma, V.K., Siskova, K.M., Zboril, R., Gardea-Torresdey, J.L., 2014. Organic-coated silver nanoparticles in biological and environmental conditions: Fate, stability and toxicity. *Adv. Colloid Interface Sci.* 204, 15–34. <https://doi.org/10.1016/J.CIS.2013.12.002>
- Shiraishi, K., Nakajima, T., Shichino, S., Deshimaru, S., Matsushima, K., Ueha, S., 2019. In vitro expansion of endogenous human alveolar epithelial type II cells in fibroblast-free spheroid culture. *Biochem. Biophys. Res. Commun.* 515, 579–585. <https://doi.org/10.1016/J.BBRC.2019.05.187>
- Xie, H., Mason, M.M., Wise, J.P., 2011. Genotoxicity of metal nanoparticles. *Rev. Environ. Health* 26, 251–268. <https://doi.org/10.1515/REVEH.2011.033/MACHINEREADABLECITATION/RIS>

List of abbreviations

Ag	Silver
ALI	Air-Liquid Interface
AO	Adverse Outcome
AOP	Adverse Outcome Pathway
ASINA	Anticipating Safety Issues at the design stage of NAno product development
CMD	Count Median Distribution
CUR	Curcumin
DSBs	Double Strand Breaks
DE	Deposition Efficiency
DiSC	Diffusion Size Classifier
DLS	Dynamic Light Scattering
dTHP-1	differentiated THP-1 cells
ELS	Electrophoretic Light Scattering
FF	Far Field
FRC	Functional Residual Volume
HEC	HydroxyEthyl Cellulose
ICP-OES	Inductively Coupled Plasma – Optical Emission Spectroscopy
IL-1 β	Interleukin 1 β
IL-6	Interleukin 6
IL-8	Interleukin 8
KE	Key Event
KER	Key Event Relationship
LDH	Lactate DeHydrogenase
LPS	LipoPolySaccharide
MIE	Molecular Initiating Event
MPPD	Multiple Path Particle Dosimetry
NAMs	New Approach Methodologies

NGRA	Next Generation Risk Assessment
NEPs	Nano-Enabled Products
NF	Near Field
NMs	NanoMaterials
NPs	NanoParticles
OPC	Optical Particle Counter
p-chem	Physical Chemical
PMA	Phorbol 12-Myristate 13-Acetate
PVP	PoliVinilPirrolidone
QCM	Quartz Crystal Microbalance
RA	Risk Assessment
RFS	Radial Flow System
ROS	Reactive Oxygen Species
SD	Standard Deviation
SE	Standard Error
SMPS	Scanning Mobility Particle Sizer
SbD	Safe by Design
SSbD	Safe and Sustainable by Design
SSC	Side SCatter
TEM	Transmission Electron Microscopy
TiO ₂	Titania
TLC	Total Lung Capacity

Acknowledgements

This project was made possible thanks to the project “Anticipating Safety Issues at the Design Stage of NAno Product Development” (ASINA), funded by the European Union’s Horizons 2020 research and innovation programme under grant agreement N° 862444 (<https://www.asina-project.eu/>).



List of publications

This thesis is based on:

Annex I - Giulia Motta, Maurizio Gualtieri, Melissa Saibene, Rossella Bengalli, Andrea Brigliadori, Marie Carrière, Paride Mantecca. Preliminary Toxicological Analysis in a Safe-by-Design and Adverse Outcome Pathway-Driven Approach on Different Silver Nanoparticles: Assessment of Acute Responses in A549 Cells. *Toxics* 2023, 11, 195. <https://doi.org/10.3390/toxics11020195>

Giulia Motta, Maurizio Gualtieri, Rossella Bengalli, Melissa Saibene, Franco Belosi, Alessia Nicosia, Joan Cabellos, Paride Mantecca. An integrated new approach methodology for inhalation risk assessment of Safe and Sustainable by Design nanomaterials. *Environment International*. Volume 183, January 2024, 108420. <https://doi.org/10.1016/j.envint.2024.108420>

Annex II - Irini Furxhi, Rossella Bengalli, Giulia Motta, Paride Mantecca, Ozge Kose, Marie Carriere, Ehtsham Ul Haq, Charlie O'Mahony, Magda Blosi, Davide Gardini, Anna Costa. Data-Driven Quantitative Intrinsic Hazard Criteria for Nanoproduct Development in a Safe-by-Design Paradigm: A Case Study of Silver Nanoforms. *ACS Appl. Nano Mater.* 2023, 6, 5, 3948–3962. <https://doi.org/10.1021/acsnm.3c00173>

Other publications:








Annex III - Patrizia Bonfanti, Anita Colombo, Melissa Saibene, Giulia Motta, Francesco Saliu, Tiziano Catelani, Dora Mehn, Rita La Spina, Jessica Ponti, Claudia Cella, Pamela Floris, Paride Mantecca. Microplastics from miscellaneous plastic wastes: Physico-chemical characterization and impact on fish and amphibian development. *Ecotoxicology and Environmental Safety*, Volume 225, 1 December 2021, 112775. <https://doi.org/10.1016/j.ecoenv.2021.112775>

ANNEX

I

Article

Preliminary Toxicological Analysis in a Safe-by-Design and Adverse Outcome Pathway-Driven Approach on Different Silver Nanoparticles: Assessment of Acute Responses in A549 Cells

Giulia Motta ^{1,2} , Maurizio Gualtieri ^{2,3,*} , Melissa Saibene ^{2,3} , Rossella Bengalli ^{2,3} , Andrea Brigliadori ⁴ , Marie Carrière ⁵  and Paride Mantecca ^{2,3} 

- ¹ Department of Biotechnology and Biosciences, University of Milano-Bicocca, Piazza della Scienza 2, 20126 Milan, Italy
 - ² Research Centre POLARIS, Department of Earth and Environmental Sciences, University of Milano-Bicocca, 20126 Milan, Italy
 - ³ Department of Earth and Environmental Sciences, University of Milano-Bicocca, Piazza della Scienza 1, 20126 Milan, Italy
 - ⁴ National Research Council of Italy, Institute of Science, Technology and Sustainability for Ceramics (CNR-ISSMC former CNR-ISTEC), Via Granarolo 64, 48018 Faenza, Italy
 - ⁵ Univ. Grenoble-Alpes, CEA, CNRS, IRIG, SyMMES, CIBEST, 38000 Grenoble, France
- * Correspondence: maurizio.gualtieri@unimib.it; Tel.: +39-026-448-2110

Abstract: Silver nanoparticles (Ag NPs) are among the most widely used metal-based nanomaterials (NMs) and their applications in different products, also as antibacterial additives, are increasing. In the present manuscript, according to an adverse outcome pathway (AOP) approach, we tested two safe-by-design (SbD) newly developed Ag NPs coated with hydroxyethyl cellulose (HEC), namely AgHEC powder and AgHEC solution. These novel Ag NPs were compared to two reference Ag NPs (naked and coated with polyvinylpyrrolidone—PVP). Cell viability, inflammatory response, reactive oxygen species, oxidative DNA damage, cell cycle, and cell–particle interactions were analyzed in the alveolar in vitro model, A549 cells. The results show a different toxicity pattern of the novel Ag NPs compared to reference NPs and that between the two novel NPs, the AgHEC solution is the one with the lower toxicity and to be further developed within the SbD framework.

Keywords: nano-enabled products; adverse outcomes pathway; safe-by-design; in vitro lung cells; nanotoxicity; silver nanoparticle hazard



Citation: Motta, G.; Gualtieri, M.; Saibene, M.; Bengalli, R.; Brigliadori, A.; Carrière, M.; Mantecca, P. Preliminary Toxicological Analysis in a Safe-by-Design and Adverse Outcome Pathway-Driven Approach on Different Silver Nanoparticles: Assessment of Acute Responses in A549 Cells. *Toxics* **2023**, *11*, 195. <https://doi.org/10.3390/toxics11020195>

Academic Editor: Yang Song

Received: 23 January 2023

Revised: 8 February 2023

Accepted: 10 February 2023

Published: 20 February 2023



Copyright: © 2023 by the authors. Licensee MDPI, Basel, Switzerland. This article is an open access article distributed under the terms and conditions of the Creative Commons Attribution (CC BY) license (<https://creativecommons.org/licenses/by/4.0/>).

1. Introduction

Silver nanoparticles (Ag NPs) are among the most widely used metal-based nanomaterials (NMs) for several applications (e.g., for food packaging, cosmetics, textiles, and health care). Such important use is mainly due to their antimicrobial properties [1]. In fact, thanks to their antibacterial capability [1], Ag NPs are nowadays used in several fields, from the textile industry to biomedical application [2,3]. Moreover, their use as antimicrobial materials is gaining relevance for their capability to combat pathogens causing infections in vitro and in vivo [4].

Ag NPs are present in different products, health care and fitness, cleaning, food packaging, household equipment, electronic devices and even toys [5,6]. These widespread uses inevitably increase the possibility of accidental release of these NPs to the environment, with a consequent increase in the exposure of humans and other organisms [7]. The various routes of exposure to Ag NPs for humans are therefore multiple: ingestion, inhalation, dermal contact and, at times, directly in systemic circulation via intravenous injection.

Although the detailed anti-pathogenic mechanism of Ag NPs remains to be fully clarified, nano-enabled products (NEPs) based on Ag NPs are of interest for their capability

to exert antimicrobial functions through microbial membrane and microbial subcellular structure damages (i.e., mitochondria, ribosomes, and vacuoles), caused by the release of free Ag^+ ions and consequent formation of reactive oxygen species (ROS) [8]. The ROS production is therefore a key feature of the antibacterial properties of Ag NPs, but this may pose a hazard to human and other organisms, if cell damage occurs in unwanted species. When considering human health, several mechanisms have been proposed to explain how Ag NPs exert their toxicity. NMs may cause inflammatory response or reactive oxygen species (ROS) production; these are processes that can alter the cell membrane and damage organelles [9]. It has been observed [10] that Ag NPs induce ROS production and cell apoptosis through a caspase-dependent intracellular pathway in liver hepatocellular adenocarcinoma cell line (HepG2). Other authors also observed the induction of ROS production and a reduction in glutathione (GH) after Ag NP exposure due to the release of free Ag^+ ions. The increase in ROS caused adverse effects on cell viability and cell membrane integrity in several cell lines, both human and murine [11]. Therapeutic synthesized Ag NP exposure showed a dose- and time-dependent inhibition of cell viability, cell proliferation and cell morphology in A549 cells because of the increased oxidative stress [12]. The increase in ROS and subsequent cell death in Ag NP-exposed cells was also related to the formation of autophagosomes and autolysosomes and to a decrease in mitochondrial transmembrane potential (MTP) [13].

Noteworthy, after entering in contact with cells, NPs can undergo different possible transformations in terms of their pristine physico-chemical (p-chem) properties; for several metal oxide NPs, dissolution has been reported as a major process, and agglomeration and other surface modifications are reported to play a key role in NP effects [14].

Although these are possible drawbacks, NPs and nano-enabled products (NEPs, i.e., new products in which NPs are intentionally added to improve specific properties of the product or to substitute materials of fossil origin) are gaining relevance in everyday life. In light of this, to reduce the uncertainty of the potential adverse impact of NPs or NEPs on human health and the environment, already starting from the first steps of nanomaterial (NM) conceptualization and production and onwards, the application of the safe-by-design (SbD) strategy has been proposed and applied [15]. As reported by the authors, among the different toxicological tests suggested for a SbD approach, viability (by MTT, XTT, MTS and WST or Alamar Blue or neutral red) and the generation of reactive oxygen species (such as using 2'-7'-dichloro-fluorescein—DCFH) should be considered. In addition to this, the authors suggest considering additional biological endpoints, such as inflammation, and the stability of the NM itself. In this context, and in view of the 3Rs principle, *in vitro* studies are gaining prominent relevance to collect significant data to sustain the lack or reduce the unwanted and undesired intrinsic hazards of NPs and NEPs, in a life cycle-oriented approach.

In this study, four different Ag NPs were selected to investigate how their p-chem properties might modulate the interactions with cells in a simple *in vitro* system (human alveolar adenocarcinoma A549 cells in monoculture). The particles selected have a similar nominal diameter but different surface coating agents. Two Ag NPs, namely the NPs coated with hydroxyethyl cellulose (HEC), were developed *ex novo* while two other NPs are commercially available, namely the naked Ag (used here as reference Ag NPs) and the NPs coated with polyvinylpyrrolidone (PVP). The novel AgHEC were synthesized in solution (AgHECs) and dried as a powder (AgHECp). The novel NPs were thoroughly characterized with different analytical methods to provide their relevant chemical and physical properties; all the Ag NPs were characterized, prior the toxicological exposures, in terms of size, shape, surface charge and agglomeration state to provide a common characterization, useful for understanding the biological effects. The acute toxic effects and the influence of Ag NP properties on A549 responses (cell viability, cell death, inflammatory response, ROS production and bio-interactions between cells and Ag NPs) after 24 h of exposure were evaluated. The biological endpoints were selected according to the adverse outcome pathway (AOP) 173 (<https://aopwiki.org/aops/173> accessed on 9 January 2023)

being a molecular-initiating event (MIE) or a key event (KE) determining the final adverse outcome (AO) of the AOP, that is lung fibrosis. Indeed, this AOP was recently reported to appropriately describe the toxicological impact of some NMs that interact with cell membrane components (e.g., receptors and lipids) (MIE) and lead to lung fibrosis, such as carbon nanotubes or cerium oxide nanoparticles [16–19]. This AOP would also possibly describe the toxicological pathways of Ag NPs, which have been reported to induce lung fibrosis [20]. In addition to these endpoints, DNA damage (assessed by γ H2AX) and cell cycle alteration were considered as outcomes of interest for further assessing the possible adverse effects of Ag NPs on lung epithelial cells, and because DNA damage is a consequence of oxidative stress and inflammation while cell cycle arrest is a consequence of DNA damage.

2. Materials and Methods

2.1. Chemicals and Reagents

All chemicals and reagents were purchased from Sigma Aldrich (Milano, Italy) if not stated elsewhere. In the framework of the ASINA European project, we selected different Ag NPs. Ag naked (#484059, AgNKD) and Ag with PVP surface coating (#576832, AgPVP) were purchased from Sigma Aldrich (Milano, Italy) as benchmark materials for toxicological profiles comparison against the ASINA produced NMs, namely Ag with HEC doping obtained in suspension or in powder form (hereinafter defined as AgHECs and AgHECp, respectively). These two NPs were kindly provided by the Italian National Research Council (ISSMC-CNR, former ISTECC-CNR, Faenza, Italy). Briefly, a solution of AgNO_3 0.05 M (Sigma-Aldrich, Milan, Italy) was mixed and stirred for five minutes with a solution of hydroxyethyl cellulose (Dow Chemical, Midland, MI, USA) to a final molar ratio Ag/HEC of 5.5. The hydrogel was formed by adding a 1 M solution of NaOH (Sigma-Aldrich, Milan, Italy). The final nanosol dispersion was obtained after 24 h from hydrogel formation by adding MilliQ water. The Ag HEC nanosol was in case granulated, by means of spray freeze drying, dehydrated to also obtain the AgHEC powder sample. More details on AgHEC NP preparation are reported in [21–25]. Reference NPs AgNKD and AgPVP were obtained according to [25].

2.2. NP Suspension Preparation

Ag NP suspensions for characterization and treatments were prepared in MilliQ water to reach an initial stock suspension of 1 mg/mL of Ag NPs (considering the same mass of Ag content for all the tested NPs). For AgNKD and AgPVP NPs in powder form, the following sonication method was followed: NP suspensions, prepared in sterile glass vials or a 50 mL falcon tube, were put in an insulation box filled with ice and sonicated by means of an ultra-sonicator (Sonopuls HD3100, Bandelin, Berlin, Germany) equipped with a 2 mm probe. NP suspensions were sonicated by applying in total 40 W for 10 min (1 s pulse, 1 s pause cycle). AgHECs, after vortexing the stock suspension for 30–60 s with an angle of 45°, were directly diluted in MilliQ water to reach the desired concentration. AgHECp, after being weighed, were pre-wet NPs with a few mL (0.5–1 mL) of ultrapure MilliQ water, vortex for 30–60 s with an angle of 45° and left to set for at least 30 min (better overnight), then the desired amount of MilliQ water was added to reach the concentration of 1 mg/mL. No sonication was applied for these two NPs. All NP stock suspensions were characterized for their stability over time and kept at 4 °C. For NP characterization in MilliQ water or in cell culture medium, stock suspensions (up to 1 month old) were vortexed and diluted to obtain the desired concentrations.

2.3. Ag NP Characterization

The novel Ag NPs, namely AgHECs and AgHECp, were submitted prior to their use in toxicological experiments to a set of analytical characterizations. Morphology, crystalline structure, and particle size were characterized by transmission electron (TEM) analyses using a FEI (Hillsboro, OR, USA) Tecnai F20 microscope operating at 200 keV. AgHECp

was dispersed in isopropyl alcohol and sonicated for 15 min. AgHECs is sonicated for 15 min. The obtained suspensions are deposited on a perforated carbon film supported by a gold grid. The preparation was then dried at 40 °C. Phase contrast images were recorded to evaluate the morphology of the nanoparticles. High resolution (HR-TEM) and selected area electron diffraction (SAED) were used to study the crystalline domains. The electron microscope was also equipped with the STEM accessory, these pictures were recorded using a high-angle annular dark-field (HAADF) detector and then they were used for the size distribution analysis.

X-rays diffraction (XRD) was performed with a with Bruker (Billerica, MA, USA) D8 Advance (Cu K α 1.5406 Å), working conditions: 2 θ interval 10–80°, step 0.04°, step time 0.5 s. Few droplets of AgHECs suspension (500 mg/L) were deposited on a glass substrate and dried at 80 °C, the procedure was repeated to obtain a homogenous layer. AgHECp was directly pressed into the sample holder.

UV–Vis absorption properties of the AgHEC NPs were recorded by a Perkin Elmer (Waltham, MA, USA) Lambda 750 spectrophotometer. AgHECs was diluted to 6 mg/L with MilliQ while AgHECp was dispersed in MilliQ at the concentration of 6 mg/L. The solutions were placed in a quartz cuvette and directly submitted to analysis.

Finally, Fourier transform infrared spectroscopy (FTIR) spectra were acquired by a Thermo Scientific (Waltham, MA, USA) Nicolet iS5 equipped with iD7 an attenuated total reflectance (ATR, with a diamond window) by directly using the AgHECs and AgHECp in their pristine forms, i.e., as particles solution (5000 mg/L) or as powder. The following parameters were considered during the FTIR analysis: scan range 4000–420 cm⁻¹, resolution 0.121 cm⁻¹ and twenty-four scans per sample acquisition.

Ag NP suspensions for toxicological analyses were characterized in terms of size, shape, surface charges (ζ -potential), agglomeration state and dispersion by Dynamic Light Scattering (DLS) analysis using the Zetasizer Nano ZS90 (Malvern Ltd., Warwickshire, UK) and by transmission electron Microscopy (TEM) by a Jeol JEM (Jeol Ltd., Tokio, Japan). Ag NPs were prepared in MilliQ water or cell culture medium (DMEM supplemented with 10% *v/v* of fetal bovine serum, FBS) also considering two different working temperatures, RT for samples in MilliQ and 37 °C for sample in DMEM. For DLS analysis, Ag NP suspensions were prepared at the concentration of 10 and 100 $\mu\text{g}/\text{mL}$. All the suspensions were analyzed at time 0, just after preparation, and after 24 h of incubation at RT to assess NP stability in solution. Regarding TEM analysis, Ag NP suspensions were prepared in MilliQ water at the concentration of 100 $\mu\text{g}/\text{mL}$; 5 μL of suspension were deposited on a TEM grid (Formvar-carbon support film, 200 mesh, copper) and let dry overnight. All the samples were observed under the Jeol Jem 2100 Plus TEM Microscope (Jeol Ltd., Tokio, Japan).

2.4. Cell Culture

Human alveolar epithelial cells (A549 cell line, ATCC[®] CCL-185, American Type Culture Collection, Manassas, VA, USA) were cultivated (passages between 9 and 25) in DMEM medium (Sigma Aldrich, Milano, Italy) supplemented with 10% fetal bovine serum (FBS; Gibco Life Technologies, Monza, Italy) and antibiotics (penicillin/streptomycin, 100 U/mL; Euroclone, Pero, Italy). Cells were maintained in an incubator at 37 °C and 5% CO₂. Cells were treated with different concentrations of Ag NPs (0.1–1–10–20–50–100 $\mu\text{g}/\text{mL}$) in submerged condition for 24 h and then processed for further analysis. Untreated cells were considered as negative control. Routinely mycoplasma detection was performed as reported in Appendix A and Figure A7.

2.5. Viability Assay

The viability of the cells was assessed through the Alamar Blue assay (Invitrogen Life Technologies, Monza, Italy) and MTT assay (described in Appendix A) (although its limitation with Ag NPs reported in [26]). Cells were seeded on a 6 multiwell plate (2.5 \times 10⁵ cell/well); after 24 h, cells were treated with different concentrations of Ag NPs (0.1–1–10–20–50–100 $\mu\text{g}/\text{mL}$, in DMEM medium with 1% serum content) for 24 and 48 h

and untreated cells were considered as Negative Control. After the exposure to NPs, cell medium was removed, and cells were washed with PBS. 800 μ L of cell culture medium with 10% of the Alamar Blue test solution were added to each well. Cells were then incubated at 37 °C and 5% CO₂ for 2 h to allow the viable cells to reduce resazurin in resorufin. Then, 200 μ L from each well were pipetted in triplicate in a 96-well black plate and the fluorescence was measured at an excitation wavelength of 560 nm and a gain of 82 with a TECAN Infinite M200 Pro microplate reader (TECAN, Männedorf, Switzerland). The emission at 590 nm was recorded and the viability expressed as relative variation over the control ratio. To evaluate specific cell death pathways, namely necrosis and apoptosis, A549 cells were seeded on 6 multiwell plate (2.5×10^5 cell/well) and treated for 24 h with different concentrations of Ag NPs (10–20–50 μ g/mL); untreated cells were considered as negative control. At the end of the exposure, cells were rinsed with phosphate buffered saline (PBS), detached by gently trypsinization and stained with Annexin V and Propidium Iodide (PI). Cytofluorimetric analysis (CytoFLEX, Beckman Coulter, Cassina de Pecchi, Italy) was then performed on cell pellets by analyzing the green (FITC channel) and red fluorescence (ECD channel) of 10,000 cells per sample.

2.6. Inflammatory Response

Cells were seeded on 6 multiwell plates at the density of 2.5×10^5 cell/well and after 24 h they were treated with different concentrations of Ag NPs (0.1–1–10–20–50–100 μ g/mL). The release of Interleukin 8 (IL-8) was evaluated in the supernatants collected after 24 h of exposure, centrifuged at 1200 rpm for 6 min and then stored at -80 °C until analysis. The quantification of released IL-8 was performed with IL-8 ELISA matched antibody pair kit (Invitrogen, Life Technologies, Monza, Italy) according to the manufacturer's instruction. The sample absorbance was measured by a multiplate reader (Infinite 200 Pro, TECAN, Männedorf, Switzerland) at the wavelength of 450 nm; the concentration of interleukins was calculated based on standard curves and data were shown as p g/mL. Untreated cells were considered as negative control.

2.7. Intracellular ROS

The intracellular ROS level was measured using 2',7'-dichlorodihydrofluorescein diacetate (H₂DCFDA, Thermo Fisher Invitrogen, Waltham, MA, USA) probe. A549 cells were seeded (2.5×10^5 cell/well) in a 6 multi-well cell culture plate and incubated overnight. Cells were treated with 20 and 50 μ g/mL of Ag NPs for 90 min and 24 h. We exposed two wells for each concentration to evaluate the background fluorescence in absence of the probe. H₂O₂ 0.03% was used as positive control. When the treatment was removed, cells were washed with PBS. Depending on the well, they were loaded with PBS alone or containing 10 μ M of probe for 20 min in the dark at 37 °C. When the solution was removed, cells were washed with PBS twice, detached using trypsin and collected by centrifugation (1200 rpm, 6 min). Fluorescence was measured immediately with a CytoFlex (Beckman Coulter, Cassina de Pecchi Italy) using an excitation wavelength of 488 nm and an emission wavelength of 525 nm and measuring 10,000 events for each sample. The fluorescence intensity of cells not treated with the probe was subtracted to the respective treated cells to have the real fluorescence emission.

2.8. DNA Damage

γ H2AX was evaluated as a marker for DNA double-strand breaks (DDS). The phosphorylation of the histone H2AX is in fact related to the formation of DDS in response to several toxicant, oxidative stress and after cell cycle arrest [27,28] and γ H2AX has been proposed as the most informative marker of double-strand breaks [29]. A549 cells were seeded (2.5×10^5 cells/well) in a 6-well cell culture plate and incubated overnight. Cells were treated with 20 or 50 μ g/mL of silver NPs for 24 h or with etoposide (1.65 μ M) as a positive control. At the end of the treatment, cells were washed with PBS, collected by centrifugation, fixed using 4% PFA for 15 min and permeabilized with ice-cold 90/10%

methanol/PBS for 10 min. The samples were stained using Phospho-Histone H2A.X (Ser139) (20E3) Rabbit mAb (Alexa Fluor® 488 Conjugate) (Cell Signaling Technology, Danvers, MA, USA) following the manufacturer instructions. γ H2AX fluorescence intensity was measured using flow cytometry (CytoFlex, Beckman Coulter, Cassina de Pecchi, Italy). Fluorescence was measured immediately using an excitation wavelength of 488 nm and an emission wavelength of 525 nm and measuring 10,000 events for each sample.

2.9. The Cell Cycle

Cell cycle analysis was performed by staining the DNA with PI followed by flow cytometry. A549 cells were seeded (2.5×10^5 cells/well) in a 6-well cell culture plate and incubated overnight. Cells were treated with 20 and 50 $\mu\text{g}/\text{mL}$ of Ag NPs for 24 h. Etoposide (1.65 μM) was used as a positive control. Then, the suspension was removed, cells were washed with PBS, collected by centrifugation, and suspended in ice-cold ethanol/PBS solution (90%/10% *v/v*). The cells were suspended in PBS containing 20 $\mu\text{g}/\text{mL}$ of RNase DNase-free inhibitor (Sigma-Aldrich, Milan, Italy) for 30 min at 37 °C. PI 10 μM was added and the samples were analyzed using a CytoFlex (Beckman Coulter, Cassina de Pecchi, Italy) with an excitation wavelength of 488 nm and an emission wavelength of 610 nm and measuring 10,000 events per sample.

2.10. Cell-Particle Bio-Interaction

Quantitative analysis: Cells were seeded on 6 multiwell plates at the density of 2.5×10^5 cell/well and after 24 h, they were treated with different concentrations of Ag NPs (1–10–20–50 $\mu\text{g}/\text{mL}$) for additional 24 h. At the end of the exposure, the cells were recovered by trypsinization, and the samples were analyzed using a CytoFlex (Beckman Coulter, Cassina de Pecchi, Italy) with an excitation wavelength of 488 nm. The side scatter signal (SSC) of the gated cell population was recorded as proxy variable of the particle-cell interaction (both at cell membrane and/or after internalization).

Qualitative analysis: A549 cells were seeded on coverslip in 6 well plates (3×10^5 cell/well). After 24 h, cells were exposed with 20 $\mu\text{g}/\text{mL}$ of AgHECp, and AgPVP for an additional 24 h. At the end of the exposure, cells were washed 2 times with sterile PBS and fixed in a solution of 2.5% glutaraldehyde in phosphate buffer (pH 7.4) for 1 h. Then, after washings in the same buffer, cells were post-fixed in 1% osmium tetroxide aqueous solution for 2 h at 4 °C in the dark. Dehydration in ethanol (50, 70, 90, 96 and 100%) and infiltration in epoxy resin were the following steps. Embedded samples were cut with an ultramicrotome (Reichert-Jung Ultracut E) to obtain thin sections (60–70 nm) to be observed under the transmission electron microscope (TEM). Before observation, the sections were stained for 30 min with an aqueous solution of Uranyl Acetate (1%).

2.11. Statistical Analysis

Data are expressed as the mean \pm standard error (SE) of at least three biological independent experiments ($N > 3$, if not otherwise stated). Fold change values were log2 transformed and reported and analyzed as such. Statistical analyses were performed using R software [30], using one-way ANOVA test followed by Dunnett's post hoc test if the homogeneity of variance was confirmed by Levene's test; conversely, the pairwise Wilcoxon test was applied to determine statistical differences; values of $p < 0.05$ were considered statistically significant.

3. Results

3.1. Novel AgHEC Particles Characterization

The novel AgHEC particles were specifically designed, and a series of different analytical approaches were used to characterize their morphological and functional properties. TEM analysis allowed to characterize the morphology and the crystalline structure of the NPs (Figure 1). Both AgHECs and AgHECp have a rather narrow size distribution (3–20 nm and 5–50 nm for AgHECs and AgHECp, respectively) and their diffraction pat-

terns (HRTEM-SAED analysis) confirmed their crystalline structure, formed by twinned domain's structure.

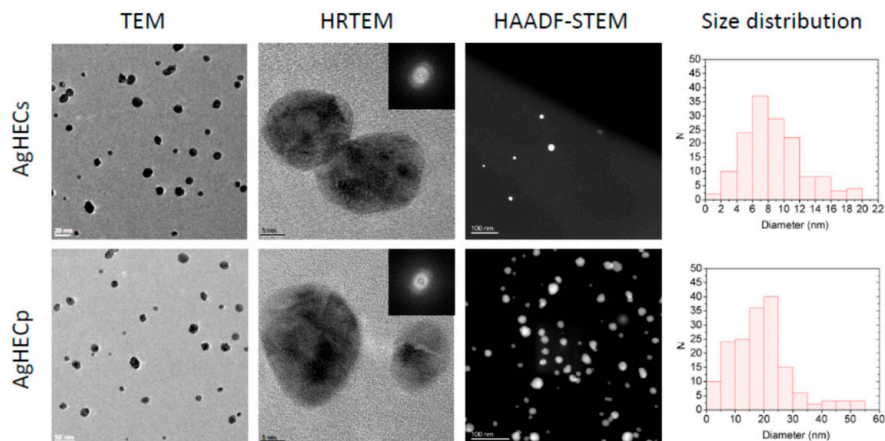


Figure 1. Transmission electron microscopy images of AgHEC NPs. TEM pictures were used for the morphological characterization of the NPs, HRTEM were used to determine the diffraction patterns of the novel particles while the HAADF-STEM to determine the size distribution of the particles.

The XRD results (Figure 2) show a typical XRD pattern of Ag NPs, the main peaks detected can be indexed as a Face-Centered Cubic (FCC) structure (JCPDS, file no. 4-0783). The patterns obtained show the presence of diffraction peaks at 38, 44, 64 and 77°, corresponding, respectively, to (111), (200), (220) and (311) Ag planes.

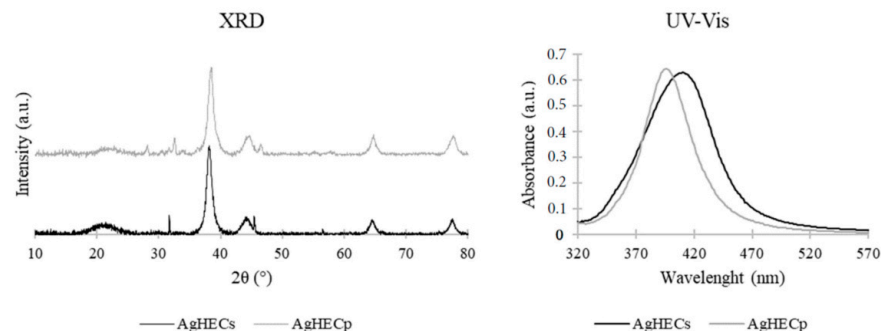


Figure 2. X-ray diffraction and UV-Vis spectra of novel NPs. XRD peaks typical of Ag NPs are reported together with other minor peaks related to the synthesis process. The UV-Vis absorption spectra agree with the silver core nature of the novel NPs.

Crystallite size was determined using the Scherrer method on the main diffraction peak (111). AgHECs has a crystallite size of 8.8 nm, and AgHECp of 9.1 nm. The two samples show similar crystallite size and the AgHECs value is aligned with the TEM size (9 nm), while TEM analysis for AgHECp showed a larger size (19 nm). This may be due to the spray freeze-drying leading to an aggregation, but the low temperature does not allow the recombination of crystal seeds.

Other diffraction peaks may be related to synthesis byproducts, mainly sodium chloride (NaCl), while the amorphous region at approximately 20°, more evident for AgHECs, is due to the amorphous glass substrate. UV-Vis absorption spectra showed the typical Surface Plasmon Resonance peak of Ag NPs. In this case, the maximum absorption falls

at 410 nm for AgHECs and at 397 nm for AgHECp, typical wavelengths of spheroidal Ag NPs with a size of approximately 10–20 nm.

FTIR spectra confirmed the presence of the HEC shell around the NPs. The AgHECs gave lower signals due the presence of the dispersant (water). Cleared peaks were recorded for the AgHECp (Appendix B, Figure A1)

3.2. Ag NP Characterization for Toxicological Analyses

Ag NPs physical properties in the different solutions tested were comparable considering the two concentrations (10 and 100 µg/mL, Table 1). Ag NP hydrodynamic diameters showed a general tendency to reduce over the time in both MilliQ and DMEM solutions; among the different NPs, the AgHECs and AgHECp NPs showed a lower tendency to modify their hydrodynamic diameter over 24 h, when dispersed in aqueous solution compared to the reference NPs (AgNKD) (Table 1).

Table 1. Ag NP characterization for cell exposure. Dynamic Light Scattering (DLS) analysis performed for Ag NPs (AgNKD, AgPVP, AgHECs and AgHECp) in MilliQ water and cell culture medium (CCM). The measurements were performed at two different time points, 0 and 24 h, and two concentrations (10 and 100 µg/mL) were considered. In the table are also reported the values of z-average (nm) ± SD and PDI ± SD. In addition, for each particle is indicated the value ζ-potential (mV) in MilliQ water at the concentration of 100 µg/mL.

NPs	Medium	Time (h)	µg/mL	z-Average (nm) ± SD	PdI ± SD
AgNKD ζ-potential: −27.57 (100µg/mL in mQ)	mQ	0	10	266.29 ± 35.96	0.47 ± 0.01
		24	10	142.52 ± 51.02	0.29 ± 0.05
		0	100	270.76 ± 53.18	0.45 ± 0.04
		24	100	109.35 ± 22.42	0.34 ± 0.08
	DMEM 1% FBS	0	10	624.32 ± 106.24	0.75 ± 0.09
		24	10	128.99 ± 15.32	0.24 ± 0.06
		0	100	328.71 ± 76.9	0.37 ± 0.13
		24	100	167.57 ± 7.55	0.33 ± 0.1
AgPVP ζ-potential: −6.07 (100µg/mL in mQ)	mQ	0	10	1515.88 ± 928.18	0.92 ± 0.14
		24	10	591.67 ± 192.93	0.81 ± 0.16
		0	100	695.91 ± 617.49	0.7 ± 0.26
		24	100	227.06 ± 159.62	0.45 ± 0.15
	DMEM 1% FBS	0	10	545.96 ± 386.17	0.69 ± 0.26
		24	10	165.92 ± 58.32	0.21 ± 0.15
		0	100	361.4 ± 110.43	0.43 ± 0.06
		24	100	185.11 ± 7.62	0.2 ± 0.14
AgHECs ζ-potential: −4.71 (100µg/mL in mQ)	mQ	0	10	122.04 ± 10.16	0.14 ± 0.02
		24	10	109.41 ± 8.36	0.15 ± 0.003
		0	100	122.16 ± 5.89	0.14 ± 0.02
		24	100	115.7 ± 5.37	0.15 ± 0.01
	DMEM 1% FBS	0	10	72.57 ± 6.26	0.23 ± 0.04
		24	10	77.82 ± 0.82	0.23 ± 0.03
		0	100	80.37 ± 2.4	0.2 ± 0.02
		24	100	75.23 ± 4.91	0.21 ± 0.05
AgHECp ζ-potential: 9.92 (100µg/mL in mQ)	mQ	0	10	293.83 ± 6.76	0.41 ± 0.06
		24	10	219.33 ± 5.13	0.4 ± 0.01
		0	100	304.89 ± 34.89	0.37 ± 0.07
		24	100	261.63 ± 26.86	0.36 ± 0.06
	DMEM 1% FBS	0	10	62.72 ± 10.85	0.46 ± 0.02
		24	10	148.66 ± 39.78	0.28 ± 0.03
		0	100	150.29 ± 19.7	0.35 ± 0.06
		24	100	88.63 ± 4.97	0.51 ± 0.01

The ζ -potential resulted highly negative for AgNKD (-27.57 mV), slightly negative for Ag-PVP and Ag-HECs (-6.07 mV and -4.71 mV, respectively) and positive for AgHECp ($+9.92$ mV). This differential surface property of the different NPs is related to the different coating—the naked particle being the most negative compared to the coated ones—and to the coating procedure, the ζ -potential of HECs and HECp being different.

Ag NP suspensions, prepared in MilliQ water, were also analyzed by transmission electron microscopy (TEM) to qualitatively evaluate their morphology and agglomeration state (Figure 3). All the Ag NPs showed primary particles with a spherical shape in the range of 20 to 30 nm. AgHECs and AgHECp resulted better dispersed compared to AgNKD and AgPVP, which were characterized by agglomerates in the order of hundreds of nm, as already observed by DLS analysis. This difference in agglomeration is a relevant outcome of the different surface modifications which allow for a better dispersion during manufacturing processes, such as spray coating of textile, at the same time, agglomeration state greatly affects bio-interactions and effects in living cells.

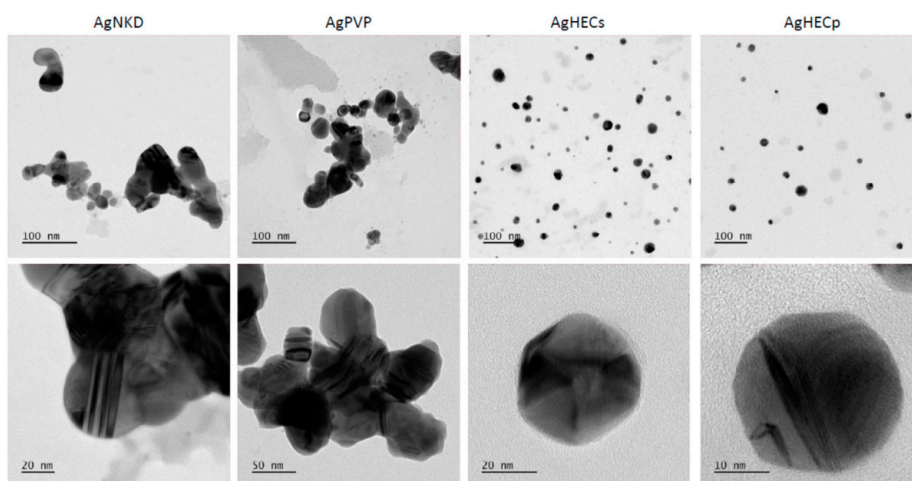


Figure 3. Transmission electron microscopy images of Ag NP suspensions. Ag NPs in MilliQ water were analyzed by TEM. The images in the upper panel show how particle suspensions are dispersed and in the lower panel is shown a detail of small agglomerates or single particles.

3.3. Cell Viability

To better assess cell viability, avoiding possible NP interference, Alamar Blue and MTT assays were tested. Finally, the Alamar Blue method was selected as the best performing assay (Figure 4, MTT data in Appendix B, Figure A2). Viability decreased concentration-dependently for all the particles tested, but the AgHECs, with a clearer effect for the AgHECp NPs. Similar results were obtained after 48 h of treatment, showing no additional toxicity to exposed cells (Appendix B, Figure A3). Given the general low cytotoxicity of the Ag NPs, the 24 h IC_{50} was correctly calculated only for AgHECp (IC_{50} equal to 57.05 $\mu\text{g/mL}$, with an upper and lower confidence values of 47.61 and 70.01 $\mu\text{g/mL}$) while for the other Ag NPs we assume that the IC_{50} is higher than 100 $\mu\text{g/mL}$.

According to its higher cytotoxic effects, AgHECp (Appendix B, Figure A4) also induced a concentration-dependent increase in annexin V/PI positive necrotic/late apoptotic cells that was statistically significant at 20 and 50 $\mu\text{g/mL}$ (5.7% and 7.2% versus 1.9% in control cells) with a consequent reduction in viable cells (90.92% and 87.8% compared to 94.8% in control cells). Additionally, AgHECs and AgPVP induced a statistical increase in necrotic/late apoptotic cells (3.4 and 3.7% at 20 and 50 $\mu\text{g/mL}$ for AgHECs and 4.1% at 50 $\mu\text{g/mL}$ for AgPVP) while the AgNKD showed no significant effect at the concentrations we tested (Appendix B, Figure A4).

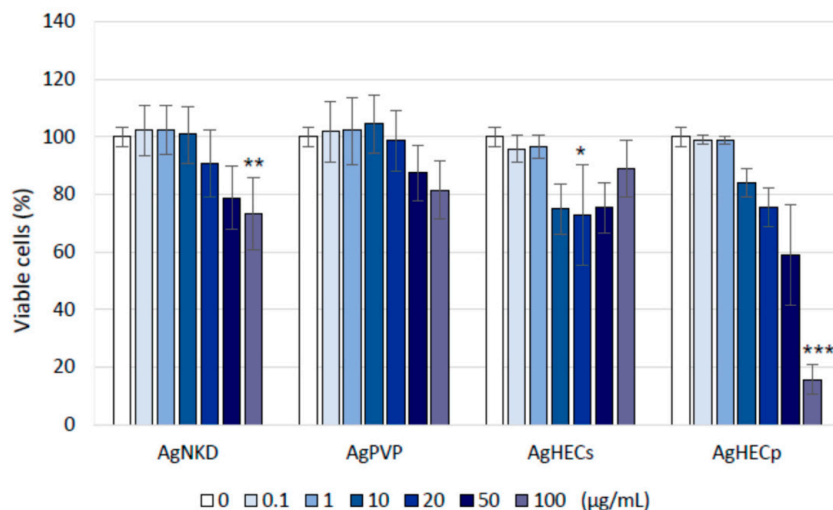


Figure 4. Cell viability. The graphs show the percentages of cell viability compared to the negative control, assessed by Alamar Blue assay after 24 h of treatment. Data are presented as the mean of at least three independent experiments \pm SE. Statistical analysis: one-way ANOVA followed by Dunnett's test. * $p < 0.05$ compared to control; ** $p < 0.01$ compared to control; *** $p < 0.001$ compared to control group.

3.4. Reactive Oxygen Species Formation

Intracellular ROS formation was selected to investigate the capability of the NPs to increase the oxidative status in exposed A549 cells. H_2DCFDA conversion to fluorescent DCFA was assessed by cytofluorimetric assay. After 90 min of treatment, AgNKD and AgPVP at the exposure concentration of 50 $\mu\text{g}/\text{mL}$ induced a significant increase in intracellular ROS. A non-significant increase was observed in AgHECp exposed cells, while absence of modulation was observed in AgHECs treatments (Figure 5). After 24 h of exposure to Ag NPs, ROS were slightly but not statistically significantly modulated by all the NPs (Appendix B, Figure A5).

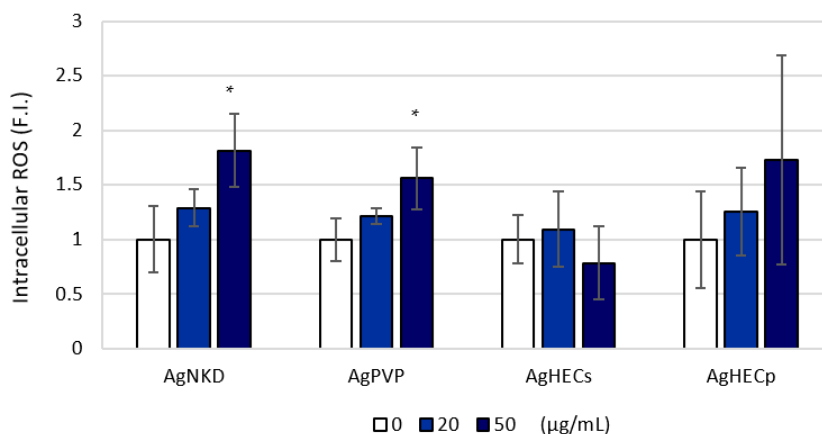


Figure 5. Reactive oxygen species were significantly increased after 90 min of treatment in AgNKD and AgPVP exposed cells (50 $\mu\text{g}/\text{mL}$). Data are presented as the mean of at least three independent experiments \pm standard deviation. Statistical analysis: one-way ANOVA followed by Dunnett's test. * $p < 0.05$ compared to control non exposed cells.

3.5. Inflammatory Response (IL-8 Release)

The release of the inflammatory mediator (IL-8) in A549 cells after 24 h of exposure to Ag NPs was modulated differently by the different NPs (Figure 6). Although some increase in the pg/mL of IL-8 in treated samples, statistically significant increases were observed only for the higher concentrations of AgHECs (100 $\mu\text{g}/\text{mL}$) and at the concentration for 50 $\mu\text{g}/\text{mL}$ of AgHECp. Among the different NPs, AgPVP was the least active in inducing IL-8 modulation. After 48 h of exposure, the modulation of the inflammatory protein IL-8 was not significant at the concentrations tested (data not shown).

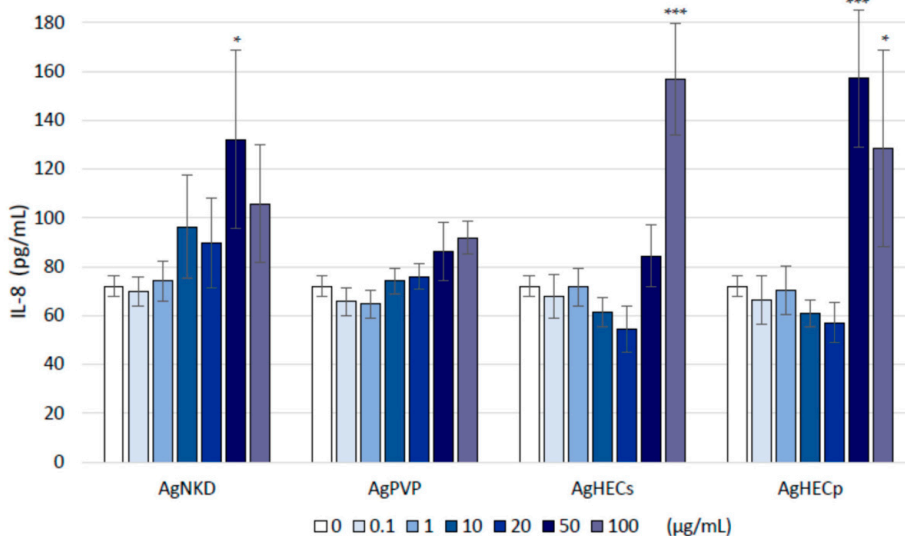


Figure 6. The inflammatory response (IL-8 release). IL-8 protein concentration was differently modulated by the NPs. Higher releases were observed at the higher exposure concentration of the AgHEC NPs (ANOVA followed by Dunnett's test) and at the concentration for 50 $\mu\text{g}/\text{mL}$ AgHECp. Data are presented as the mean of the pg/mL release by each sample ($n = 3$) \pm SE of at least three independent experiments. * $p < 0.05$ and *** $p < 0.001$ compared to control group.

3.6. Oxidative DNA Damage (γH2AX)

The DNA damaging effects of the Ag NPs was assessed by the quantification of the phosphorylated protein H2AX (γH2AX). The increase in the fluorescent signal of γH2AX (Figure 7) after A549 treatment with the different NPs was significant for all the NPs at the concentrations tested (20 and 50 $\mu\text{g}/\text{mL}$). Compared with the other NPs, the AgHEC NPs showed a high increase in H2AX phosphorylation after the exposure to 20 $\mu\text{g}/\text{mL}$.

3.7. Cell Cycle Alteration

Since damage at the DNA is a relevant endpoint in assessing the hazards of new NPs, we also tested the capability of the different NPs to induce alteration in the cell cycle progression (Figure 8). The cell cycle may be altered by different events, an increase in cells stalled in the S phase is normally related to issues with the DNA replication machinery or the presence of DNA damages that slow the replication process, while increases in cells in the G2/M phase may be still related to the presence of DNA damages to be corrected prior to mitosis or to alteration to the mitosis machinery. The results show that after treatment with the different Ag NPs at the concentration of 50 $\mu\text{g}/\text{mL}$ a significant increase in cells blocked in G2/M was observed and coupled to an increase in S phase (except for the AgPVP NPs). Again, the AgHECp NPs were able to induce cell cycle alterations at a lower concentration.

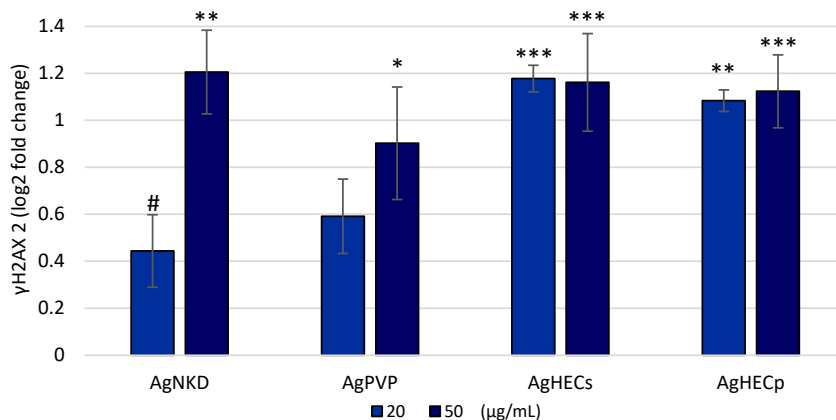


Figure 7. DNA damage (expressed as log₂ FC of γ H2AX) was determined by quantifying the increase in the γ H2AX protein. Control values are equivalent to the zero line, values above this value are actual increases in the protein content while negative values are downregulation of the protein. Increases in DNA damages in exposed cells were observed for all the Ag NPs at the concentration of 20 and 50 μ g/mL. Data are presented as the mean of at least three independent experiments \pm SE. Statistical difference analyzed by one-way ANOVA and Dunnett's test. * $p < 0.05$ compared to control; ** $p < 0.01$ compared to control, ANOVA with post hoc; *** $p < 0.001$ compared to control, ANOVA with post hoc; # $p < 0.05$ compared to the 50 μ g/mL exposure concentration.

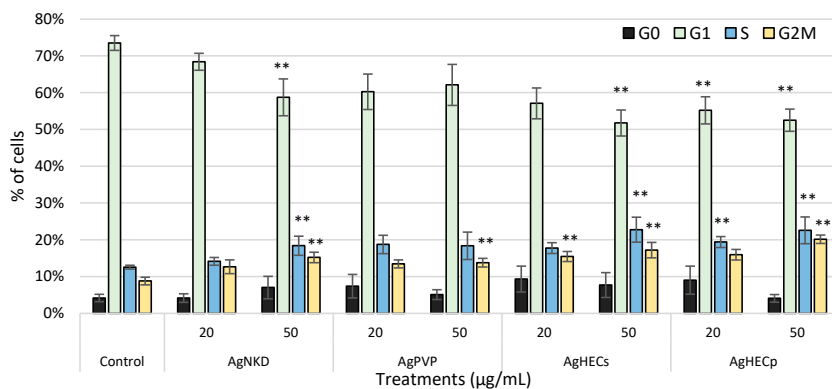


Figure 8. Cell cycle analysis. In the graph are reported the percentages of cells in the different cell cycle phases: subG0, G1, S and G2M ($n > 3$). It is possible to observe a statistically significant increase in cells in G2M phase after treatment with all the Ag NPs. Data are presented as the mean of at least three independent experiments \pm SE. Statistical analysis: one-way ANOVA followed by Dunnett's test; ** p -value = 0.01 compared to control.

3.8. Cell–Particle Bio-Interactions

To analyze the possible NP interactions and/or uptake of Ag NPs, monolayers of A549 treated for 24 h were investigated by laser beam scattering and TEM imaging. The SSC reported show (Figure 9) that A549 cells treated with AgNPD and AgPVP had the lowest scattering values and were statistically different from the control only at the higher concentration of exposure. On the contrary, cells treated with AgHECs and AgHECp resulted in higher SSC values and therefore higher cell–particle interactions (significant values different from the controls already at the concentration of 10 μ g/mL ($p < 0.001$)). TEM imaging (Appendix B, Figure A6) supports these findings. AgPVP treated cells show an ultrastructure well maintained, and different subcellular structures are recognizable.

AgHECp cells on the contrary clearly show particles internalization and particle membrane interactions. In the future, a more detailed investigation of the intracellular localization of the NPs and possible modifications induced at ultrastructural levels may support the AOP-oriented investigation strategy.

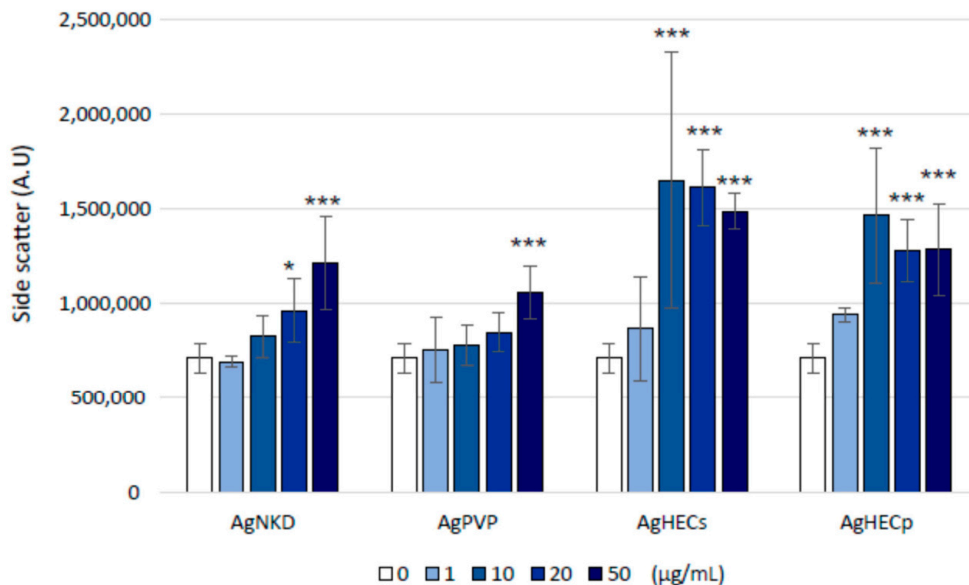


Figure 9. Bio-interaction analysis. The side scatter (SSC) values of cells exposed at different concentrations of the different Ag NPs. Clear differences among the NPs are reported, with AgHEC NPs showing higher SSC values compared to AgNKD and AgPVP treatments. Data are presented as the mean of at least three independent experiments \pm SE. Statistical analysis: one-way ANOVA followed by Dunnett's test; * p -value = 0.05; *** p -value = 0.001 compared to control.

4. Discussion

Safety of nanomaterials and nano-enabled products (NEPs) is a primary objective for more sustainable and innovative goods given the intrinsic potential hazards of objects in the nanometric scale [31,32]. The evaluation of the hazards of NPs of interest is usually performed after a synthesis procedure is set up to shape the NP of interest for the specific application it is intended for. Therefore, the toxicological evaluation has been usually performed at the end of the production, application, and disposal cycle to confirm that the particle or the product containing the particle does not pose a hazard to humans or the environment. To overcome this a posteriori evaluation of the risk for the human health and the environment of NPs or NEPs, safe-by-design (SbD) approaches have been proposed during the last years [15,33]. The basic concept is to provide a priori evidence of the absence of hazards in the new NP or NEP during their life cycle therefore minimizing or removing unwanted or unpredicted risk after exposure. One of the key questions of SbD procedure is to what extent they are predictive of potential chronic effects, given the absence of acute toxicity. To address this question, methodological approaches have been proposed such as in [33] to provide a standardized procedure to follow for different NMs with similar intended application. On the other hand, the definition of the adverse outcome pathways (AOPs) concept [34–36] provided a novel framework to support SbD approaches [15,16,37]. Within the framework of AOPs we identified AOP #173 related to lung fibrosis of substances interacting with the membrane components (e.g., receptors and lipids) of lung cells leading to fibrosis. In fact, the induction of lung fibrosis due to NP exposure has been proposed by several authors [16–19]. In our experiments, we synthesized novel Ag NPs coated with a

shell of HEC. The thorough characterization performed, confirmed the crystalline nature of the novel NPs and the presence of the external layer of HEC. These novel particles were analyzed in parallel for their toxicological properties according to the AOP selected. This AOP has, as a molecular-initiating event (MIE), the interaction of the substance with the cell membrane. The data reported confirm the interaction of Ag NPs with the plasma membrane of exposed cells and the internalization of clusters of NPs into membrane structures within the cytoplasm, interestingly this was more evident for AgHECp. Internalization of NPs is a relevant mechanism also for cytotoxicity. Indeed, the capability of some metal or metal oxide NPs, especially Ag NPs, to exert their adverse effects through the intracellular release of metal ions after internalization is largely reported [38–41]. Internalized NPs might interact with cellular macromolecules according to their affinity or by generating ROS [41,42]. The results here reported show a significant increase in ROS after 90 min of exposure. According to the expected oxidative burst usually reported few hours after exposure of *in vitro* or *in vivo* models to NPs [42–45]. We would like to speculate, that the absence of positive results with the HEC coated NPs, may be related to a quenching effect or a masking effect of the HEC over the fluorescent probe used to test ROS. In fact, according to the short life of reactive species in cells, we observed, also in HEC coated Ag NPs, the increase in γ H2AX, a marker of oxidative damage of the DNA, that is in fact also related to precedent ROS formation [46,47]. ROS formation may also be related to inflammatory mediator release [48–51] and therefore contribute to the modulation of IL-8 we reported here. The activation of the inflammatory response in exposed cells is another key event (KE) in the AOP for lung fibrosis since chronic inflammation [52–54] is a trigger of changes in the extra cellular matrix leading to fibrosis [55]. We also report here the capability of Ag NPs to alter the cell cycle of the exposed epithelial cells, adding an additional event on the path to lung fibrosis [56]. What are relevant in the SbD concept are the differences we have observed between the differentially coated NPs (Appendix B, Table A1). Considering AgNKD as a reference we report here that the AgPVP nanoparticles are likely the less active in inducing adverse events related to the selected AOP. Interestingly, we report a clear difference of Ag NPs coated with hydroxyethyl cellulose (HEC), the focus of our study, considering two different conditions. The AgHECp was the most toxic, determining the highest cytotoxicity and IL-8 modulation, while the DNA damaging potency and the cell cycle alteration were similar between the two AgHEC NPs. The higher toxicity of AgHEC NPs could be related to both their higher stability and lower agglomeration in toxicological media, lower DLS hydrodynamic diameter and TEM images as compared to reference Ag NPs [56–58] and the direct effect of the HEC coating in favoring the internalization of the Ag NPs [57]. In the SbD framework and considering the AOP outcomes we reported here, the HEC coating being the core of the newly developed Ag NPs, the production and use of HEC coated Ag NPs should follow a wet production and use procedure rather than drying the NPs for subsequent uses. The reason why AgHEC in powder form is more hazardous than the original colloidal solution may be linked to the possible physico-chemical transformations of the coating polymer during the processes. Further, considering the methodology (freeze-drying) used to obtain AgHECp, very slight modifications of the polymer structure are expected. How such possible minor modifications may influence the biological reactivity is a fascinating aspect for future investigations.

5. Conclusions

In conclusion, novel NPs (AgHEC) were here synthesized, characterized and tested in parallel for their hazards according to a SbD approach combined with relevant AOP events (Figure 9). The combination of these two relevant frameworks showed efficacy in characterizing the hazards of different Ag NPs and defining which production and use procedure should be considered with lower expected risk. The doping of the surface of Ag NPs seems to have a primary role in driving the toxicity of the newly synthesized particles and the selection of coated NPs with lower intrinsic hazards should be favored for subsequent testing and use in manufacturing procedure (Figure 10). Here, we show

that HEC coating favors the dispersion of the Ag NPs in water-based media. This, from a manufacturing point of view, is a benefit since well-dispersed NPs are less prone to clump and obstruct orifices needed for example during spraying. On the other hand, HEC coating favors particle–cell membrane interaction and cytotoxicity. Our results allowed the discrimination of the potential hazard of two different processes of AgHEC production and use, the wet (AgHECs) and dry (AgHECp) approaches, considering the first the one to favor for subsequent additional tests and manufacturing processes.

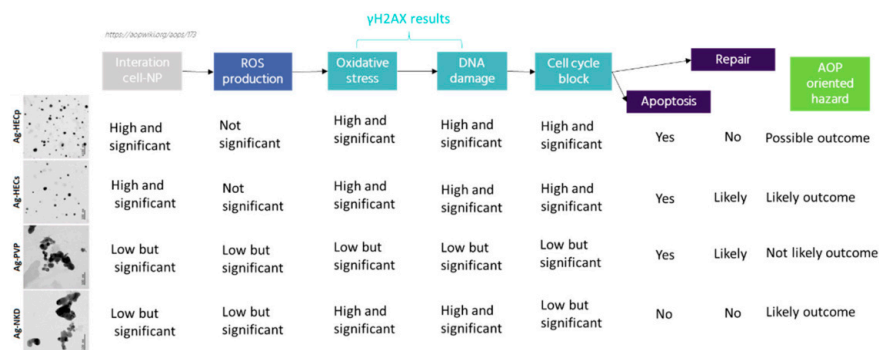


Figure 10. Summary of the AOP-oriented test analysis for the different NPs analyzed. Among the different NPs, the newly produced are the most likely to activate relevant events related to AOP #173, lung fibrosis, and therefore pose a relevant hazard for human health. The reference materials (AgNKD and AgPVP) are less relevant in the framework of the AOP selected. Significantly, the AOP events investigated clearly showed that the AgHECp are activating all the relevant events that may link the exposure to these NPs to the adverse lung outcome, while the AgHECs are less likely to determine such detrimental effects.

Author Contributions: G.M., investigation and data analysis; M.G., writing—original draft preparation and review and editing and formal analysis; M.S., manuscript review and editing and data analysis; R.B., manuscript review and editing and data analysis; A.B., AgHEC NP synthesis and investigation and manuscript review; M.C., manuscript review; P.M., manuscript review, project administration, and funding acquisition. All authors have read and agreed to the published version of the manuscript.

Funding: This work was supported by the “ASINA” (Anticipating Safety Issues at the Design Stage of Nano Product Development) European project (H2020—GA 862444).

Institutional Review Board Statement: Not applicable.

Informed Consent Statement: Not applicable for the reported research.

Data Availability Statement: No data are at the moment available due to privacy requirements.

Acknowledgments: The authors wish to thank Anna Luisa Costa and Magda Blosi (CNR-ISSMC, former ISTE, Faenza, Italy) for providing AgHEC preparations and for the valuable suggestions on their properties and applications.

Conflicts of Interest: All the authors declare no conflict of interest.

Appendix A

- MTT assay

The viability of the cells was also assessed through the MTT assay. After the exposure to nanoparticles, cell medium was removed, and cells were washed with PBS. MTT was dissolved at 5 mg/mL in PBS, then a suspension containing 62.5 μ L for each mL of cell culture medium (DMEM supplemented with 10% of FBS) was prepared and 1 mL of it was

added to each well. Cells were then incubated in the dark at 37 °C and 5% CO₂ for 2 h to allow the viable cells to reduce tetrazolium salt in formazan crystals. Then, supernatants were removed, and the precipitated crystals were solubilized using 1 mL of DMSO for each well. The plates were left for 10 min with continual shaking, then 200 µL from each well were pipetted in triplicate in a 96-well transparent plate and the absorbance was measured at 570 nm with a reference of 690 nm with a TECAN Infinite M200 Pro microplate reader. The viability is expressed as percent control ratio.

- Mycoplasma detection

The possible contamination by mycoplasma strains of the cultured cells is performed monthly according to [58]. Cells were seeded on a glass coverslip in 6 multiwell plate (2.5×10^5 cell/well) and allowed to grow until reaching confluence. The medium is then removed, and cells are washed with sterile PBS. The cells are then fixed with 1 mL of paraformaldehyde fixative for 5 min, this procedure is repeated twice. Then, the fixative is removed, and the coverslips are allowed to dry under a sterile hood. After drying, cells are stained with Hoechst 33258 for 5 min. The stained cells are rinsed with sterile PBS and then are mounted with Prolong mounting solution. Each coverslip is analyzed under an AxioObserver.Z1 Cell imaging station (Zeiss, Jena, Germany), by an immersion oil 63x objective to detect the presence into the cytoplasm of small Hoechst positive extranuclear dots. At least 100 cells per coverslip are analyzed. Images are acquired by an AxioCam MRm digital camera and elaborated with the ZEN2.3 Blue software (Zeiss). Figure 6 reports representative pictures of A549 cells after Hoechst staining at two different passages of the cell culture, passage 10 and passage 19.

Appendix B

Table A1. Summary of the toxicological outcomes and tentative ranking of the tested NPs from the less to the most toxic. Scores (in terms of number of +) were assigned considering the statistical significance of the effects, the dose response tendency of the effects and the first concentration of exposure giving a significant effect.

NPs	Cytotoxicity	ROS (90 min)	Inflammation	DNA Damage	Cell Cycle Alteration	Final Rank from Less to Most Toxic
AgNKD	+	+	+	+	+	1
AgPVP	++	+		+	+	1
AgHECs	++		++	++	++	2
AgHECp	+++		++	++	++	3

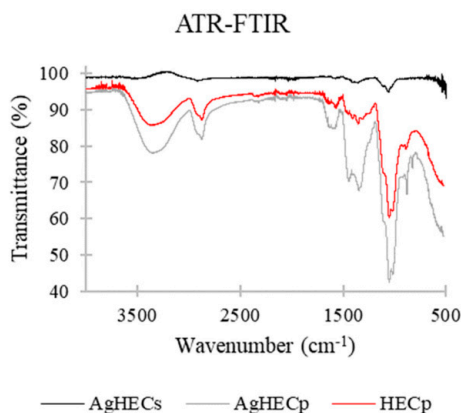


Figure A1. FTIR spectra of the AgHEC NPs. The ATR-FTIR spectrum of the hydroxyethyl cellulose (HEC) functionalized with quaternary ammonium used as capping agent (in red) show a broad band

at approximately $3500\text{--}3200\text{ cm}^{-1}$, which refers to stretching of hydroxyl group. Peaks at 2870 and 3010 cm^{-1} refer to C–H stretching. The band at approximately $1650\text{--}1580\text{ cm}^{-1}$ is related to the amine N–H bending. Peaks at 1440 and 1350 cm^{-1} refer to C–H and O–H bending. The alcohol C–O stretching peaks at 1110 and 1050 cm^{-1} are observed. Using this one as reference, it is possible to observe that AgHECp follows well the relative intensity of the absorption peaks. The AgHECs spectrum is influenced (very low signal intensity) by the water suspension.

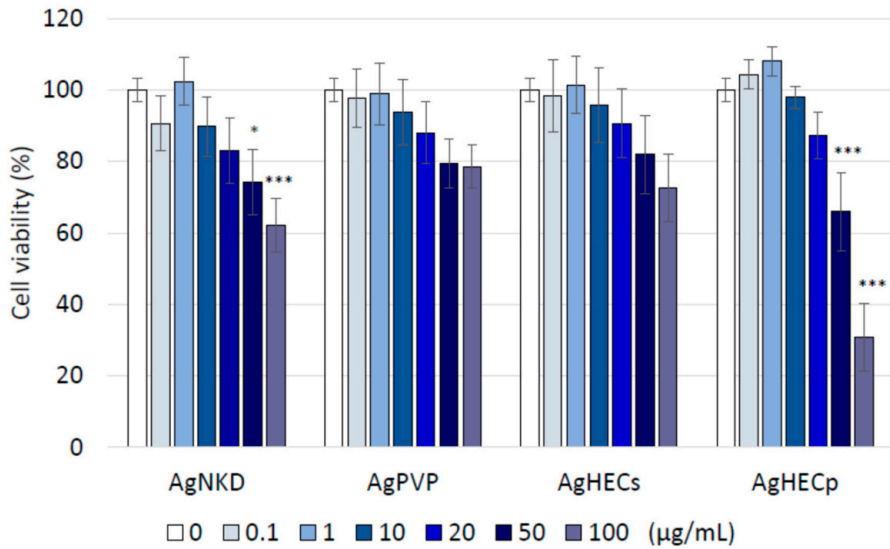


Figure A2. Cell viability assessed by MTT. Significant reduction of cell viability was observed after AgHECp and AgNKD. AgPVP and AgHECs particles were effective less. ANOVA one way followed by Dunnett test, * $p < 0.05$; *** $p < 0.001$ compared to control cells, $N = 3$.

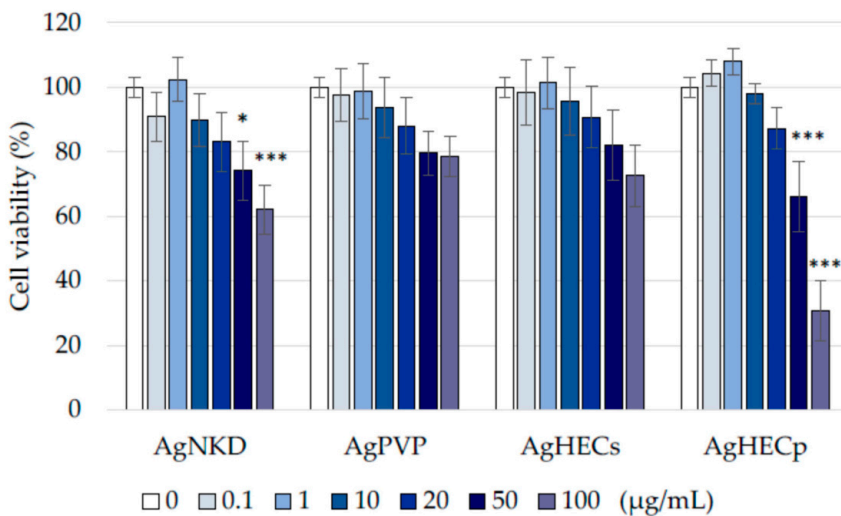


Figure A3. Cell viability assessed by Alamar Blue at 48 h. A significant reduction in cell viability was observed after AgHECp and AgNKD. AgPVP and AgHECs particles were less effective. One-way ANOVA followed by Dunnett's test; * $p < 0.05$; *** $p < 0.001$ compared to control cells. $N = 3$.

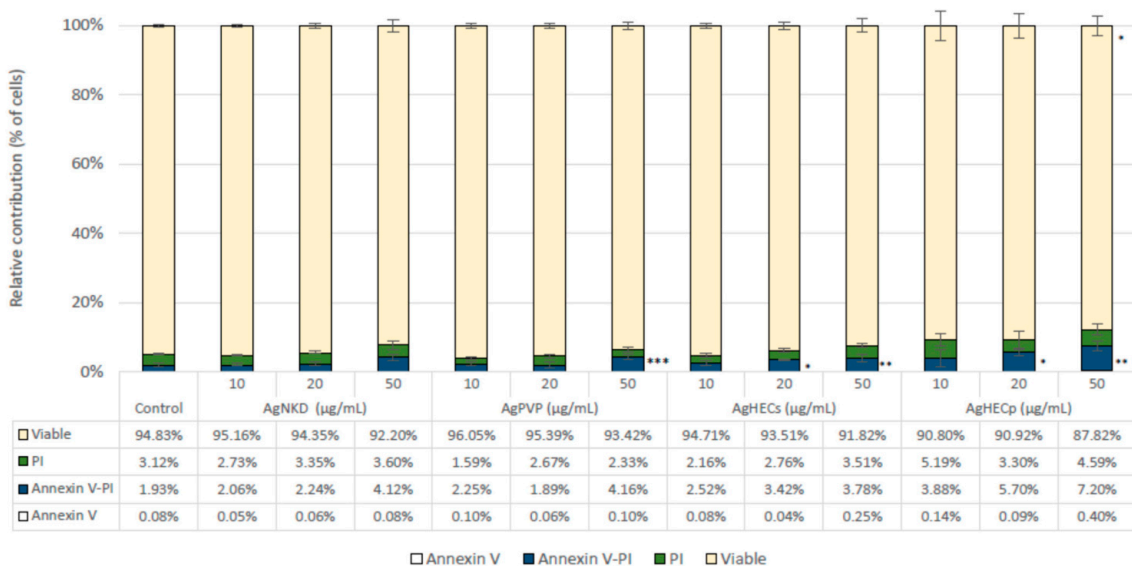


Figure A4. Cell death characterization after exposure to Ag NPs. The percentages of viable cells, apoptotic cells (Annexin V positive), late apoptotic cells (Annexin V/PI—positive) and necrotic cells (PI—positive). A549 cells after exposure for 24 h to 50 µg/mL to Ag NPs; each treatment is reported with its relative negative control (unexposed cells). Statistical analysis: one-way ANOVA followed by *t*-test; * *p* < 0.05; ** *p* < 0.01, *** *p* < 0.001 compared to control cells. N = 3.

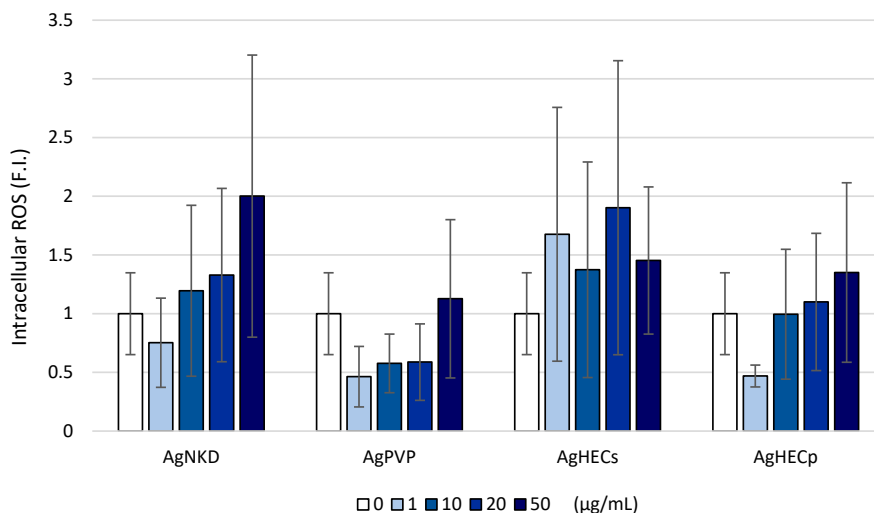


Figure A5. ROS levels in cells exposed to Ag NPs for 24 h. ROS expression was assessed using H₂DCFDA as indicator although some modulation statistically significant effects were not observed. Data are presented as the mean ± SE. Statistical analysis: one-way ANOVA followed by *t*-test.

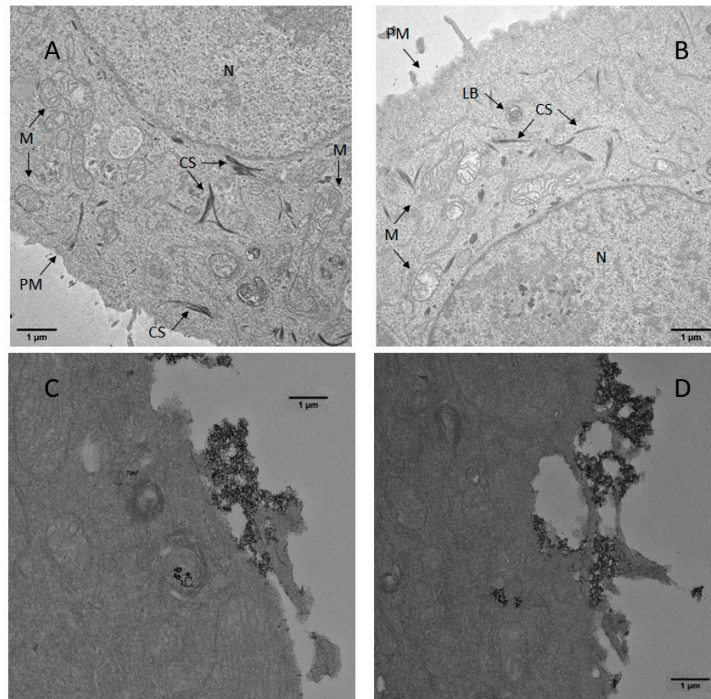


Figure A6. TEM picture of A549 exposed to AgPVP (B) or AgHECp (C,D) NPs. Increased membrane localization of NPs is evident in AgHECp treated cells and intracellular localization in lamellar bodies (C) in compared to AgPVP (B) and control cells (A). M = mitochondria, PM = plasma membrane, LB = lamellar bodies, CS = cytoskeleton, and N = nucleus.

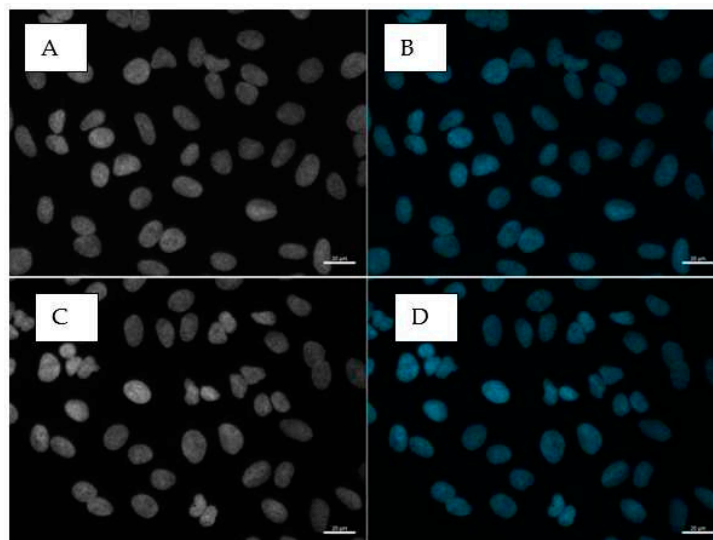


Figure A7. Hoechst stained A549 for mycoplasma screening. The absence of extranuclear cytoplasmic staining confirm the absence of mycoplasma in the cultured A549 cells. Pictures are from two different passages: passage 10 is reported in Figure A6 (A) (tones of grey channel) and (B) (Hoechst channel), passage 19 is reported in Figure A6 (C) (tones of grey channel) and (D) (Hoechst channel).

References

1. Nowack, B.; Krug, H.F.; Height, M. 120 Years of Nanosilver History: Implications for Policy Makers. *Environ. Sci. Technol.* **2011**, *45*, 1177–1183. [[CrossRef](#)] [[PubMed](#)]
2. Beyene, H.D.; Werkneh, A.A.; Bezabh, H.K.; Ambaye, T.G. Synthesis paradigm and applications of silver nanoparticles (AgNPs), a review. *Sustain. Mater. Technol.* **2017**, *13*, 18–23. [[CrossRef](#)]
3. Shanmuganathan, R.; Karuppusamy, I.; Saravanan, M.; Muthukumar, H.; Ponnuchamy, K.; Ramkumar, V.S.; Pugazhendhi, A. Synthesis of Silver Nanoparticles and their Biomedical Applications—A Comprehensive Review. *Curr. Pharm. Des.* **2019**, *25*, 2650–2660. [[CrossRef](#)] [[PubMed](#)]
4. Bruna, T.; Maldonado-Bravo, F.; Jara, P.; Caro, N. Silver Nanoparticles and Their Antibacterial Applications. *Int. J. Mol. Sci.* **2021**, *22*, 7202. [[CrossRef](#)] [[PubMed](#)]
5. Natsuki, J.; Natsuki, T.; Hashimoto, Y. A Review of Silver Nanoparticles: Synthesis Methods, Properties and Applications. *Int. J. Mater. Sci. Appl.* **2015**, *4*, 325. [[CrossRef](#)]
6. Tortella, G.; Rubilar, O.; Durán, N.; Diez, M.; Martínez, M.; Parada, J.; Seabra, A. Silver nanoparticles: Toxicity in model organisms as an overview of its hazard for human health and the environment. *J. Hazard. Mater.* **2020**, *390*, 121974. [[CrossRef](#)] [[PubMed](#)]
7. Burduşel, A.-C.; Gherasim, O.; Grumezescu, A.M.; Mogoantă, L.; Ficai, A.; Andronesu, E. Biomedical Applications of Silver Nanoparticles: An Up-to-Date Overview. *Nanomaterials* **2018**, *8*, 681. [[CrossRef](#)]
8. Garcés, M.; Cáceres, L.; Chiappetta, D.; Magnani, N.; Evelson, P. Current understanding of nanoparticle toxicity mechanisms and interactions with biological systems. *New J. Chem.* **2021**, *45*, 14328–14344. [[CrossRef](#)]
9. Ahmadian, E.; Dizaj, S.M.; Rahimpour, E.; Hasanzadeh, A.; Eftekhari, A.; Zadegan, H.H.; Halajzadeh, J.; Ahmadian, H. Effect of silver nanoparticles in the induction of apoptosis on human hepatocellular carcinoma (HepG2) cell line. *Mater. Sci. Eng. C* **2018**, *93*, 465–471. [[CrossRef](#)]
10. de Matteis, V.; Rinaldi, R. Toxicity assessment in the nanoparticle era. *Adv. Exp. Med. Biol.* **2018**, *1048*, 1–19. [[CrossRef](#)]
11. Gurunathan, S.; Kang, M.-H.; Qasim, M.; Kim, J.-H. Nanoparticle-Mediated Combination Therapy: Two-in-One Approach for Cancer. *Int. J. Mol. Sci.* **2018**, *19*, 3264. [[CrossRef](#)] [[PubMed](#)]
12. Han, J.W.; Gurunathan, S.; Jeong, J.-K.; Choi, Y.-J.; Kwon, D.-N.; Park, J.-K.; Kim, J.-H. Oxidative stress mediated cytotoxicity of biologically synthesized silver nanoparticles in human lung epithelial adenocarcinoma cell line. *Nanoscale Res. Lett.* **2014**, *9*, 459. [[CrossRef](#)] [[PubMed](#)]
13. Bobyk, L.; Tarantini, A.; Beal, D.; Veronesi, G.; Kieffer, I.; Motellier, S.; Valsami-Jones, E.; Lynch, I.; Jouneau, P.-H.; Pernet-Gallay, K.; et al. Toxicity and chemical transformation of silver nanoparticles in A549 lung cells: Dose-rate-dependent genotoxic impact. *Environ. Sci. Nano* **2021**, *8*, 806–821. [[CrossRef](#)]
14. Gulumian, M.; Cassee, F.R. Safe by design (SbD) and nanotechnology: A much-discussed topic with a prudence? *Part. Fibre Toxicol.* **2021**, *18*, 32. [[CrossRef](#)] [[PubMed](#)]
15. Halappanavar, S.; Brule, S.V.D.; Nymark, P.; Gaté, L.; Seidel, C.; Valentino, S.; Zhernovkov, V.; Danielsen, P.H.; De Vizcaya-Ruiz, A.; Wolff, H.; et al. Adverse outcome pathways as a tool for the design of testing strategies to support the safety assessment of emerging advanced materials at the nanoscale. *Part. Fibre Toxicol.* **2020**, *17*, 16. [[CrossRef](#)]
16. Ma, J.; Bishoff, B.; Mercer, R.; Barger, M.; Schwegler-Berry, D.; Castranova, V. Role of epithelial-mesenchymal transition (EMT) and fibroblast function in cerium oxide nanoparticles-induced lung fibrosis. *Toxicol. Appl. Pharmacol.* **2017**, *323*, 16–25. [[CrossRef](#)]
17. Sun, B.; Wang, X.; Ji, Z.; Wang, M.; Liao, Y.-P.; Chang, C.H.; Li, R.; Zhang, H.; Nel, A.E.; Xiang, W. NADPH Oxidase-Dependent NLRP3 Inflammasome Activation and its Important Role in Lung Fibrosis by Multiwalled Carbon Nanotubes. *Small* **2015**, *11*, 2087–2097. [[CrossRef](#)]
18. Wang, Z.; Wang, C.; Liu, S.; He, W.; Wang, L.; Gan, J.; Huang, Z.; Wei, H.; Zhang, J.; Dong, L. Specifically Formed Corona on Silica Nanoparticles Enhances Transforming Growth Factor β 1 Activity in Triggering Lung Fibrosis. *ACS Nano* **2017**, *11*, 1659–1672. [[CrossRef](#)]
19. Roda, E.; Bottono, M.; Biggiogera, M.; Milanesi, G.; Coccini, T. Pulmonary and hepatic effects after low dose exposure to nanosilver: Early and long-lasting histological and ultrastructural alterations in rat. *Toxicol. Rep.* **2019**, *6*, 1047–1060. [[CrossRef](#)]
20. Lolli, A.; Blosi, M.; Ortelli, S.; Costa, A.L.; Zanoni, I.; Bonincontro, D.; Carella, F.; Albonetti, S. Innovative synthesis of nanostructured composite materials by a spray-freeze drying process: Efficient catalysts and photocatalysts preparation. *Catal. Today* **2019**, *334*, 193–202. [[CrossRef](#)]
21. Gardini, D.; Blosi, M.; Ortelli, S.; Delpivo, C.; Bussolati, O.; Bianchi, M.; Allegri, M.; Bergamaschi, E.; Costa, A. Nanosilver: An innovative paradigm to promote its safe and active use. *Nanoimpact* **2018**, *11*, 128–135. [[CrossRef](#)]
22. Costa, A.L.; Blosi, M.; Brigliadori, A.; Zanoni, I.; Ortelli, S.; Simeone, F.C.; Delbue, S.; D’Alessandro, S.; Parapini, S.; Vineis, C.; et al. Environmental Science Eco design for Ag-based solutions against SARS-CoV-2 and *E. coli*. *Environ. Sci. Nano* **2022**, *9*, 4295–4304. [[CrossRef](#)]
23. Marassi, V.; Di Cristo, L.; Smith, S.; Ortelli, S.; Blosi, M.; Costa, A.L.; Reschiglian, P.; Volkov, Y.; Prina-Mello, A. Silver nanoparticles as a medical device in healthcare settings: A five-step approach for candidate screening of coating agents. *R. Soc. Open Sci.* **2018**, *5*, 171113. [[CrossRef](#)] [[PubMed](#)]
24. Blosi, M.; Albonetti, S.; Dondi, M.; Baldi, G.; Barzanti, A.; Bitossi, M. Process for Preparing Stable Suspensions of Metal Nanoparticles and the Stable Colloidal Suspensions Obtained Thereby. European Patent Office EP2403636A2, 10 March 2010.

25. Mello, D.F.; Trevisan, R.; Rivera, N.; Geitner, N.K.; Di Giulio, R.T.; Wiesner, M.R.; Hsu-Kim, H.; Meyer, J.N. Caveats to the use of MTT, neutral red, Hoechst and Resazurin to measure silver nanoparticle cytotoxicity. *Chem. Interact.* **2020**, *315*, 108868. [CrossRef]
26. Fragkos, M.; Jurvansuu, J.; Beard, P. H2AX Is Required for Cell Cycle Arrest via the p53/p21 Pathway. *Mol. Cell. Biol.* **2009**, *29*, 2828–2840. [CrossRef]
27. Tanaka, T.; Huang, X.; Jorgensen, E.; Gietl, D.; Traganos, F.; Darzynkiewicz, Z.; Albino, A.P. ATM activation accompanies histone H2AX phosphorylation in A549 cells upon exposure to tobacco smoke. *BMC Cell Biol.* **2007**, *8*, 26. [CrossRef]
28. Nikitaki, Z.; Hellweg, C.E.; Georgakilas, A.G.; Ravanat, J.-L. Stress-induced DNA damage biomarkers: Applications and limitations. *Front. Chem.* **2015**, *3*, 35. [CrossRef]
29. R Core Team. *R: A Language and Environment for Statistical Computing*; R Foundation for Statistical Computing: Vienna, Austria, 2019; Available online: <https://www.R-project.org/> (accessed on 5 October 2022).
30. Vishwakarma, V.; Samal, S.S.; Manoharan, N. Safety and Risk Associated with Nanoparticles-A Review. *J. Miner. Mater. Charact. Eng.* **2010**, *9*, 455–459. [CrossRef]
31. Demir, E. A review on nanotoxicity and nanogenotoxicity of different shapes of nanomaterials. *J. Appl. Toxicol.* **2021**, *41*, 118–147. [CrossRef]
32. Schmutz, M.; Borges, O.; Jesus, S.; Borchard, G.; Perale, G.; Zinn, M.; Sips, A.J.A.M.; Soeteman-Hernandez, L.G.; Wick, P.; Som, C. A Methodological Safe-by-Design Approach for the Development of Nanomedicines. *Front. Bioeng. Biotechnol.* **2020**, *8*, 258. [CrossRef]
33. Delrue, N.; Sachana, M.; Sakuratani, Y.; Gourmelon, A.; Leinala, E.; Diderich, R. The Adverse Outcome Pathway Concept: A Basis for Developing Regulatory Decision-making Tools. *Altern. Lab. Anim.* **2016**, *44*, 417–429. [CrossRef]
34. Ankley, G.T.; Edwards, S.W. The adverse outcome pathway: A multifaceted framework supporting 21st century toxicology. *Curr. Opin. Toxicol.* **2018**, *9*, 1–7. [CrossRef] [PubMed]
35. Leist, M.; Ghallab, A.; Graepel, R.; Marchan, R.; Hassan, R.; Bennekou, S.H.; Limonciel, A.; Vinken, M.; Schildknecht, S.; Waldmann, T.; et al. Adverse outcome pathways: Opportunities, limitations and open questions. *Arch. Toxicol.* **2017**, *91*, 3477–3505. [CrossRef] [PubMed]
36. Gerloff, K.; Landesmann, B.; Worth, A.; Munn, S.; Palosaari, T.; Whelan, M. The Adverse Outcome Pathway approach in nanotoxicology. *Comput. Toxicol.* **2017**, *1*, 3–11. [CrossRef]
37. Medici, S.; Peana, M.; Pelucelli, A.; Zoroddu, M.A. An updated overview on metal nanoparticles toxicity. *Semin. Cancer Biol.* **2021**, *76*, 17–26. [CrossRef] [PubMed]
38. Glinski, A.; de Souza, T.L.; da Luz, J.Z.; Junior, A.G.B.; de Oliveira, C.C.; Ribeiro, C.A.D.O.; Neto, F.F. Toxicological effects of silver nanoparticles and cadmium chloride in macrophage cell line (RAW 264.7): An in vitro approach. *J. Trace Elements Med. Biol.* **2021**, *68*, 126854. [CrossRef] [PubMed]
39. Lubick, N. Nanosilver toxicity: Ions, nanoparticles—Or both? *Environ. Sci. Technol.* **2008**, *42*, 8617. [CrossRef]
40. Studer, A.M.; Limbach, L.K.; Van Duc, L.; Krumeich, F.; Athanassiou, E.K.; Gerber, L.C.; Moch, H.; Stark, W.J. Nanoparticle cytotoxicity depends on intracellular solubility: Comparison of stabilized copper metal and degradable copper oxide nanoparticles. *Toxicol. Lett.* **2010**, *197*, 169–174. [CrossRef]
41. Niu, Y.; Tang, M. In vitro review of nanoparticles attacking macrophages: Interaction and cell death. *Life Sci.* **2022**, *307*, 120840. [CrossRef]
42. Capasso, L.; Camatini, M.; Gualtieri, M. Nickel oxide nanoparticles induce inflammation and genotoxic effect in lung epithelial cells. *Toxicol. Lett.* **2014**, *226*, 28–34. [CrossRef]
43. Moschini, E.; Gualtieri, M.; Colombo, M.; Fascio, U.; Camatini, M.; Mantecca, P. The modality of cell–particle interactions drives the toxicity of nanosized CuO and TiO₂ in human alveolar epithelial cells. *Toxicol. Lett.* **2013**, *222*, 102–116. [CrossRef] [PubMed]
44. Jr, A.D.C.M.; Azevedo, L.F.; Rocha, C.C.D.S.; Carneiro, M.F.H.; Venancio, V.P.; De Almeida, M.R.; Antunes, L.M.G.; Hott, R.D.C.; Rodrigues, J.L.; Ogunjimi, A.T.; et al. Evaluation of distribution, redox parameters, and genotoxicity in Wistar rats co-exposed to silver and titanium dioxide nanoparticles. *J. Toxicol. Environ. Health Part A* **2017**, *80*, 1156–1165. [CrossRef]
45. Rahmanian, N.; Shokrzadeh, M.; Eskandani, M. Recent advances in γ H2AX biomarker-based genotoxicity assays: A marker of DNA damage and repair. *DNA Repair* **2021**, *108*, 103243. [CrossRef] [PubMed]
46. Zhao, X.; Takabayashi, F.; Ibuki, Y. Coexposure to silver nanoparticles and ultraviolet A synergistically enhances the phosphorylation of histone H2AX. *J. Photochem. Photobiol. B Biol.* **2016**, *162*, 213–222. [CrossRef] [PubMed]
47. Hoffmann, M.H.; Griffiths, H.R. The dual role of Reactive Oxygen Species in autoimmune and inflammatory diseases: Evidence from preclinical models. *Free. Radic. Biol. Med.* **2018**, *125*, 62–71. [CrossRef]
48. Sharma, A.; Tewari, D.; Nabavi, S.F.; Habtemariam, S. Reactive oxygen species modulators in pulmonary medicine. *Curr. Opin. Pharmacol.* **2021**, *57*, 157–164. [CrossRef]
49. Delgado-Roche, L.; Mesta, F. Oxidative Stress as Key Player in Severe Acute Respiratory Syndrome Coronavirus (SARS-CoV) Infection. *Arch. Med. Res.* **2020**, *51*, 384–387. [CrossRef]
50. Castranova, V. Signaling Pathways Controlling The Production Of Inflammatory Mediators in Response To Crystalline Silica Exposure: Role Of Reactive Oxygen/Nitrogen Species. *Free. Radic. Biol. Med.* **2004**, *37*, 916–925. [CrossRef]
51. Geering, B.; StoECKle, C.; Conus, S.; Simon, H.-U. Living and dying for inflammation: Neutrophils, eosinophils, basophils. *Trends Immunol.* **2013**, *34*, 398–409. [CrossRef]

52. Alessandri, A.L.; Sousa, L.; Lucas, C.; Rossi, A.G.; Pinho, V.; Teixeira, M.M. Resolution of inflammation: Mechanisms and opportunity for drug development. *Pharmacol. Ther.* **2013**, *139*, 189–212. [[CrossRef](#)]
53. Gomez-Mejiba, S.E.; Zhai, Z.; Akram, H.; Pye, Q.N.; Hensley, K.; Kurien, B.T.; Scofield, R.H.; Ramirez, D.C. Inhalation of environmental stressors & chronic inflammation: Autoimmunity and neurodegeneration. *Mutat. Res. Toxicol. Environ. Mutagen.* **2009**, *674*, 62–72. [[CrossRef](#)]
54. Nissinen, L.; Kähäri, V.-M. Matrix metalloproteinases in inflammation. *Biochim. et Biophys. Acta (BBA) Gen. Subj.* **2014**, *1840*, 2571–2580. [[CrossRef](#)] [[PubMed](#)]
55. Selman, M.; Pardo, A. The leading role of epithelial cells in the pathogenesis of idiopathic pulmonary fibrosis. *Cell Signal.* **2019**, *66*, 109482. [[CrossRef](#)] [[PubMed](#)]
56. Sheikhi, A.; Hayashi, J.; Eichenbaum, J.; Gutin, M.; Kuntjoro, N.; Khorsandi, D.; Khademhosseini, A. Recent advances in nanoengineering cellulose for cargo delivery. *J. Control. Release* **2019**, *294*, 53–76. [[CrossRef](#)] [[PubMed](#)]
57. Ciekot, J.; Psurski, M.; Jurec, K.; Boratyński, J. Hydroxyethylcellulose as a methotrexate carrier in anticancer therapy. *Investig. New Drugs* **2020**, *39*, 15–23. [[CrossRef](#)]
58. Jung, H.; Wang, S.-Y.; Yang, I.-W.; Hsueh, D.-W.; Yang, W.-J.; Wang, T.-H.; Wang, H.-S. Detection and treatment of mycoplasma contamination in cultured cells. *Chang. Gung Med. J.* **2003**, *26*, 250–258.

Disclaimer/Publisher’s Note: The statements, opinions and data contained in all publications are solely those of the individual author(s) and contributor(s) and not of MDPI and/or the editor(s). MDPI and/or the editor(s) disclaim responsibility for any injury to people or property resulting from any ideas, methods, instructions or products referred to in the content.

ANNEX II

Data-Driven Quantitative Intrinsic Hazard Criteria for Nanoproduct Development in a Safe-by-Design Paradigm: A Case Study of Silver Nanoforms

Irini Furxhi,* Rossella Bengalli, Giulia Motta, Paride Mantecca, Ozge Kose, Marie Carriere, Ehtsham Ul Haq, Charlie O'Mahony, Magda Blosi, Davide Gardini, and Anna Costa



Cite This: *ACS Appl. Nano Mater.* 2023, 6, 3948–3962



Read Online

ACCESS |



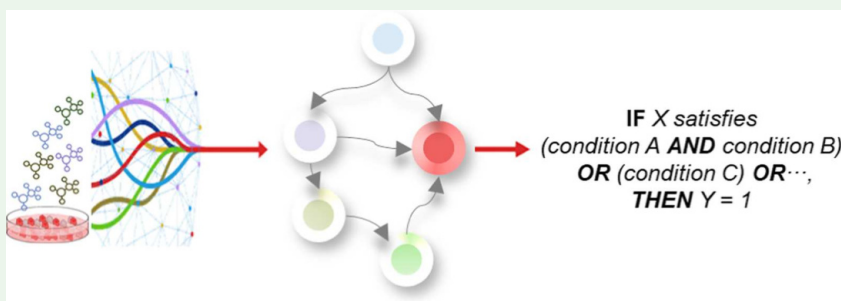
Metrics & More



Article Recommendations



Supporting Information



ABSTRACT: The current European (EU) policies, that is, the Green Deal, envisage safe and sustainable practices for chemicals, which include nanoforms (NFs), at the earliest stages of innovation. A theoretically safe and sustainable by design (SSbD) framework has been established from EU collaborative efforts toward the definition of quantitative criteria in each SSbD dimension, namely, the human and environmental safety dimension and the environmental, social, and economic sustainability dimensions. In this study, we target the safety dimension, and we demonstrate the journey toward quantitative intrinsic hazard criteria derived from findable, accessible, interoperable, and reusable data. Data were curated and merged for the development of new approach methodologies, that is, quantitative structure–activity relationship models based on regression and classification machine learning algorithms, with the intent to predict a hazard class. The models utilize system (i.e., hydrodynamic size and polydispersity index) and non-system (i.e., elemental composition and core size)-dependent nanoscale features in combination with biological in vitro attributes and experimental conditions for various silver NFs, functional antimicrobial textiles, and cosmetics applications. In a second step, interpretable rules (criteria) followed by a certainty factor were obtained by exploiting a Bayesian network structure crafted by expert reasoning. The probabilistic model shows a predictive capability of $\approx 78\%$ (average accuracy across all hazard classes). In this work, we show how we shifted from the conceptualization of the SSbD framework toward the realistic implementation with pragmatic instances. This study reveals (i) quantitative intrinsic hazard criteria to be considered in the safety aspects during synthesis stage, (ii) the challenges within, and (iii) the future directions for the generation and distillation of such criteria that can feed SSbD paradigms. Specifically, the criteria can guide material engineers to synthesize NFs that are inherently safer from alternative nanoformulations, at the earliest stages of innovation, while the models enable a fast and cost-efficient in silico toxicological screening of previously synthesized and hypothetical scenarios of yet-to-be synthesized NFs.

KEYWORDS: safe and sustainable by design, nanoforms, nanoparticles, quantitative structure–activity relationship, machine learning, Bayes rules, intrinsic hazard criteria

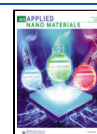
1. INTRODUCTION

The current paradigm of European (EU) policies, that is, the Green Deal, envisage safe and sustainable practices for chemicals, which include nanoforms (NFs), at the earliest stages of innovation to prevent and/or minimize safety and sustainability impacts.¹ To meet those policy goals, novel frameworks are required such as the safe and sustainable by design (SSbD) notion. The SSbD concept is under the

Received: January 11, 2023

Accepted: January 20, 2023

Published: February 16, 2023



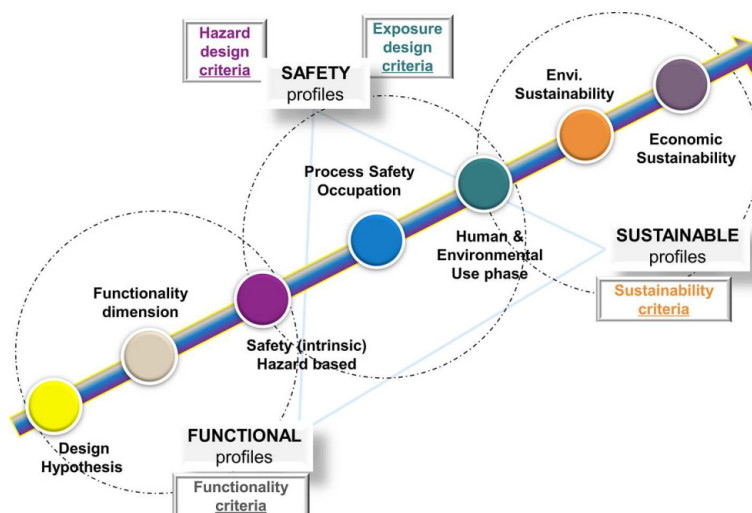


Figure 1. SSBd framework dimensions, following a hierarchical approach in which safety aspects are contemplated first, followed by environmental sustainability, and socioeconomic aspects (image adapted from the JRC framework).

spotlight of science, regulation, and engineering to achieve the goals foreseen by EU policies.⁷ Commission has funded several projects on nanotechnologies⁴ in the frame of Horizon 2020 (H2020) which, through industrial case studies, will offer to various stakeholders digital products to facilitate (i) the selection of alternative design options and (ii) the decision-making process when having to weight criteria along the life cycle of a NF and once integrated in nano-enabled products (NEPs). In relation to the aforementioned criteria, the Joint Research Center (JRC) published a theoretical SSBd framework for the description of such criteria.³ The framework provides guiding principles on the SSBd dimensions to support the design phase and aspects and indicators in each dimension to establish criteria that will guide researchers toward SSBd practices. The SSBd dimensions are shown in Figure 1 demonstrating the re-design phase supported by a hypothesis formulation and the dimensional targets of functionality, human, and environmental safety containing intrinsic hazards, human occupational safety (process stage) and human/environmental health (use phase), and the two final steps of sustainability (environmental and economic).

The first principle stressed by ref 4 that supports the SSBd framework is the need of findable, accessible, interoperable, and reusable (FAIR) data: each dimension is driven by criteria based on data (experimental or modeled) to promote safe and sustainable research and innovation. A cornerstone aspect of the implementation and reproducibility of the SSBd concept is data quality and availability, that is, data FAIRness. Data needs to be treated according to FAIR principles to safeguard its long-term use and access.^{5,6} The data management plan has been added as an inherent deliverable of any project that generates, assembles, or processes data according to the guidelines on FAIR data management. The Anticipating Safety Issues at the Design Stage of NANO Product Development (ASINA) project is generating data across the life cycle of NFs with the aim to develop a data-driven decision-making strategy based on the manufacturing of two types of enhanced antimicrobial NEPs, namely, functional textiles and cosmetics

applications.⁷ These data are currently being curated by the data shepherd^{6,8–10} In this study, we show one of the fruits of the FAIR data management process and how such an action accelerates the development of new approach methodologies (NAMs).

The second principle underlined by ref 4 is the need of NAMs: an umbrella of various applications such as computational, that is, in chemico, in silico, and other in vitro, approaches that allow multiple investigations at the same time and are expected to accelerate the implementation and validation of the SSBd concept.^{3,11–13} Machine learning (ML) is a subfield of artificial intelligence (AI) and represents the definitive implementation of the 3R principles (replacement, reduction, and refinement of animal testing). In the field of computational (nano)toxicology, one of the most essential methods are the quantitative structure–activity relationships (QSARs, “nano-QSARs”, when applied to NFs). In QSAR, the activity (e.g., toxicity) is predicted from a set of descriptors by using various ML algorithms (e.g., supporting vector machines, random forests, and artificial neural networks).¹⁴ QSARs have been widely used in the field of nanotoxicology,^{15–18} and with the blooming of the ML applications, the interpretability has become an integral part so that their reasoning processes are more understandable and easier to be used in practice.¹⁹ Bayesian networks (BNs) are ML graphical models that merge probabilistic analysis, automated reasoning, and expert judgment. Such an amalgamation is essential in a challenging domain, such as nanosafety, which faces conflicting and uncertain knowledge.^{20,21} Expert reasoning structures are interpretable, re-usable by humans, and differ from the ones generated solely by automated reasoning from data.²² Numerous studies have employed BNs in the nanosafety domain to support risk assessment and prioritize NF hazard assessment.^{16,23–27}

The third principle for a successful SSBd implementation is the extraction of quantitative criteria: during the EU high-level roundtable on chemicals strategy for sustainability,⁶ it was mentioned that the design criteria for chemicals will move

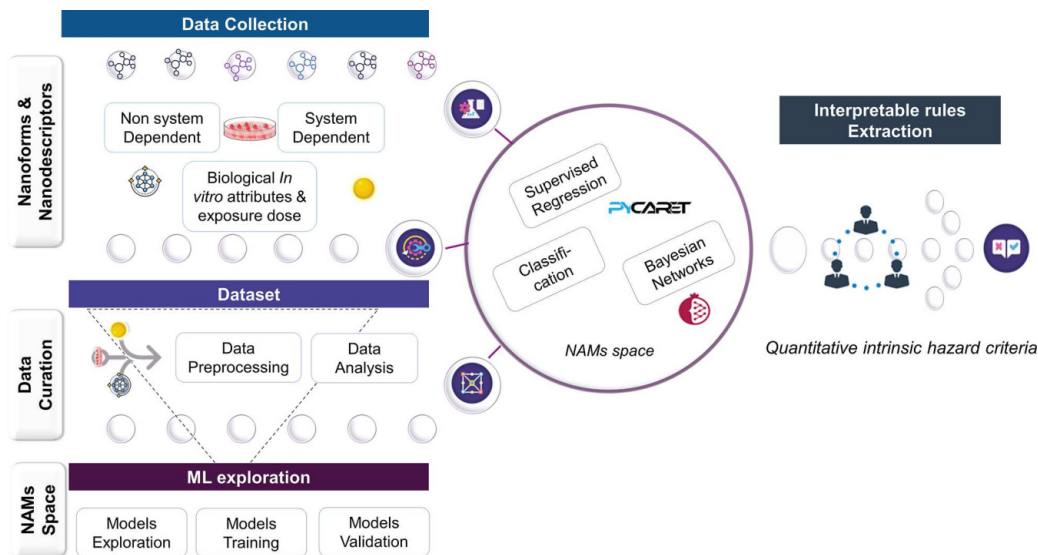


Figure 2. Interpretable rule extraction workflow. From the data collection, to dataset curation, and exploration of ML tools for the QSAR development to the final extrapolation of interpretable rules.

“from qualitative to quantitative assessments, with more data becoming available”. Recent stakeholder webinars^d, networking events^e, and nanosafety expert trainings^f stressed that a well-defined and straightforward approach to derive quantitative criteria guiding a SSbD is missing and required. The BNs fulfill the expectations of such criteria by providing a set of discrete and mutually dependent interpretable rules from the conditional probability tables (CPTs). These rules have been used to guide decision-making processes by providing experts a series of IF statements [IF X satisfies (condition A AND condition B) OR (condition C) OR..., Then $Y = 1$].^{28,29} In the nanosafety domain,³⁰ BNs were developed from the data derived from a meta-analysis of cellular viability of quantum dot NFs. In the supplementary material of the *ibid* study, the authors provide such rules derived from the CPTs of the BN structure.

To respond to the above challenges, we focused on step 1—hazard assessment of the SSbD framework³ concerning the assessment of the physicochemical (pchem) properties of materials in order to derive criteria that lead to intrinsically safer materials, before proceeding further in the SSbD execution. In this context, the term “by design” refers to a set of nanoscale features that can be modified by material designers toward synthesizing/re-designing less hazardous NFs. In this manner, our efforts align with the overall objectives of the chemicals strategy for sustainability⁸, for example, “ensure that all materials placed on the market are in themselves safe”. The methodology followed is shown in Figure 2. We combined FAIR data with NAMs comprising QSAR approaches and explainable ML techniques for the extraction of interpretable rules from BNs. Data collection: first, nanodescriptors related to silver nanoforms (AgNFs) such as system-dependent pchem properties (extrinsic properties influenced by the surrounding environment or experimental conditions aka the system) and non-system-dependent pchem properties (intrinsic), biological *in vitro* attributes, exposure

conditions, and the hazard outcome were collected (Figure 2, left). Dataset: in a second step, data is curated, merged, and processed with various techniques (such as missing value imputations and one hot encoding). Data is analyzed for visualization and insight purposes. ML explorations for QSAR development: various ML models were explored, from regression and classifications algorithms to the construction of a constrained BN based on expert judgment. Models are trained and validated to reveal predictive performance metrics. Rules extraction: finally, the quantitative intrinsic hazard criteria (rules) applicable to the safety dimension of the SSbD framework were extracted from the BN structure (Figure 2, right). From now on, in this manuscript, the interpretable rules refer to the quantitative intrinsic hazard criteria.

This work demonstrates for the first time how QSAR models in combination with FAIR data can support the development and implementation of SSbD paradigm by supporting the knowledge establishment for criteria definition.

2. EXPERIMENTAL SECTION

2.1. Data Collection. The data gathered for this study refers to AgNFs, which are currently under investigation as SSbD alternatives.^{31,32}

2.1.1. Silver NFs. Based on the intended application, data of two alternative AgNFs coated with hydroxyethylcellulose (HEC), either as powder form or suspended into a solution, are gathered. The powder is intended for incorporation into cosmetics to provide functionalities such as antimicrobial creams or lotions, while the solution is incorporated into textiles as coating for increased antimicrobial/antiviral efficiency.^{33,34} In addition to the alternative AgNFs, reference data are used to facilitate the NAM approach. Commission⁴ mentions the need of reference materials data for the validation of NAMs derived from harmonized protocols. Below, we describe the NFs along with their European Registry of Materials (ERM) identifiers which guarantee that internal documentation can be later connected to data and expertise for the particular NFs or variants³⁵

- (1) ERM00000559: AgHEC water-based solution (AgHEC sol) reduced from AgNO_3 solution by HEC catalyzed by sodium

hydroxide (NaOH). From a sustainability perception, the one-step synthesis process utilized is an environment-friendly, sol-gel-based technology obtainable at room temperature.⁴

- (2) ERM00000552: Powder AgHEC (AgHEC pwd) is derived by spray-freeze-drying the solution without affecting the organic layer producing microparticles with highly porous nanostructures (final composition of 11% Ag and 89% wt HEC). Both solution and powder contain a molar ratio of HEC/Ag = 5.5 and NaOH/Ag = 2.8.
- (3) ERM00000549: Reference uncoated material—Sigma-Aldrich (Ag ref).
- (4) ERM00000548: Reference material coated with PVP—Sigma-Aldrich (AgPVP ref) in a powder form.
- (5) ERM00000575: A variant AgHEC with a HEC/Ag: 6.4 and NaOH/Ag: 1.4 molar ratio (AgHEC 6.4/1.4 sol) as a SSbD alternative. Formulation obtained by tweaking two synthesis parameters that affect the antimicrobial effectiveness (i) concentration of HEC, acting as both reducing and chelating agents, and (ii) concentration of NaOH, acting as a catalyst. Such reagents play a fundamental role in the nucleation and growth processes, colloidal stability,³⁶ and reduction of metals,³⁷ driving the formation of the non-aggregated NFs.
- (6) ERM00000580: AgNFs with curcumin solution (AgCUR) which is a proven antibacterial/antiviral phytochemical as a SSbD alternative.³⁸

2.1.2. Input Features. It is of fundamental importance to define the nanoscale features—nanodescriptors used in the QSAR modeling since a subtle alteration may influence the output to be predicted (i.e., cellular viability). Nanodescriptors should reflect not only the substance elemental composition but also other characteristics requested by regulation when reporting a NF, for example, size distribution and other morphological characterization such as crystal structure.³⁹ Moreover, nanodescriptors should reflect the influence of the system (surrounding environment or experimental conditions) on those properties. One can differentiate between system-independent (intrinsic properties) and system-dependent (extrinsic properties) nanodescriptors.⁴⁰ In this study, both are considered. It is worth to notice that the dataset solely refers to AgNFs, rendering those descriptors collectively unique, acting as a fingerprint. This enables NFs belonging in the same elemental composition group to be differentiated.⁴⁰ Commission⁴ remarks the development of substance-specific hazard assessments and the exploration of the determinants that drive the toxicity.

2.1.2.1. System-Independent Nanodescriptors. Those descriptors contain the (i) quantification of the atomic concentrations of elemental compositions derived by X-ray photoelectron spectroscopy (XPS) analysis, a technique for analyzing material's surface chemistry,⁴¹ (ii) core size and morphology by transmission electron microscopy (TEM), and (3) crystallographic structure-related information by X-ray diffraction analysis (XRD).⁴² System-dependent nanodescriptors: a crucial aspect of NF toxicity exploration is their characterization in relevant biological media since properties could change in relation to the environment, influencing their cytotoxicity potential. Therefore, NFs should be characterized as pristine (system independent) and as applied in biological fluids,^{43,44} which in this case is the cell culture medium [Dulbecco's modified Eagle's medium (DMEM) and 1% fetal bovine serum (FBS) with pH = 7, 2–7, and 4]. The nanodescriptors contain particle's hydrodynamic size (z-average and peak maximum value) and polydispersity indexes (PDI), which represent the sample's heterogeneity, derived from dynamic light scattering (DLS). DLS analysis is recommended from the ISO standard⁴ and from the OECD's Working Party on Manufactured Nanomaterials (WPMN) testing programme.⁴ Since DLS measurements of size distribution depend on sample dispersion, PDI should be considered.⁴⁵ PDI values vary from 0.01 to 0.5–0.7 (monodispersed particles) and PDI >0.7 (broad particle size distribution).⁴⁶ Moreover, size distribution could change at time 0 (t_0) and the time after in vitro exposure (in our case 24 h, for cell viability assessment, t_{24}). To

account for alterations of properties in time,⁴⁷ we considered measurements (hydrodynamic size and PDIs) performed at t_0 and t_{24} .

2.1.2.2. Biological Attributes. The criteria definition in the SSbD framework was based on hazard categories established within the CLP [no. 1272/2008 (EU, 2008)] and REACH (no. 1907/2006 (EU, 2006)] regulations containing carcinogenicity, reproductive toxicity, target organ toxicity, and so forth. However, those endpoints are assessed with in vivo testing. In our case, the in vitro lines represent different target organs, alveolar lung cells (A549, human adenocarcinoma), and intestinal (HCT-116, human colon carcinoma) at a cellular level of biological representation. The cell lines represent different exposure routes, that is, inhalation and ingestion. Inhalation is a major route of human exposure to airborne NFs, and it may occur at workplaces, and A549 cells are a well-established line used for inhalation toxicological testing,⁴⁸ including AgNFs.⁴⁹ Ingestion is another important route of exposure,⁵⁰ and with regard to intestinal exposure, ingested NFs pass through various environments before reaching the intestinal cells, such as saliva, gastric, and intestinal fluids.^{51,52} Due to the complex nature of these fluids such as acidic conditions, the presence of salts and biomolecules, the pchem properties of NFs could be altered before, during, and after passing the gastrointestinal tract, affecting their bioactivity.^{53,54} To mimic the fate of NFs, simulated digestive fluids were prepared based on ref 55, and NF preparation in simulated digestion cascade was performed according to ref 56. Finally, digested and non-digested NFs were exposed to HCT-116 cells, a well-accepted model for testing NF intestinal cytotoxicity.⁵⁷

2.1.2.3. Outcome and Exposure Conditions. Hazard evaluation was performed via cytotoxic measurements based on cell viability, a means to a preliminary hazard screening in a quick, cheap, and efficient manner.⁵⁸ Several in vitro assays are available to assess cell viability, including the 3-(4,5-dimethylthiazol-2-yl)-2,5-diphenyltetrazolium bromide (MTT), Alamar blue, and WST-1 tests, which are rapid, high-throughput, and low-cost assays.⁵⁹ The cell viability for the lung cells (%) was estimated with MTT and Alamar blue protocols (ISO10993-5:2009) at various concentrations (0.1–100 ppm). MTT is used in several ISO standards (ISO10993-5:2009) and OECD test guidelines (OECD 431, 439, 492). The inclusion of the different assays as output-related features is also relevant since NFs could interfere with the tests and the final outcome.^{60,61} Intestinal cells are exposed with either digested or non-digested AgNFs at concentrations ranging from 1.25 to 100 ppm with the WST-1 assay. All experiments refer to a 24 h duration of exposure.

2.2. Dataset. **2.2.1. Dataset Curation.** The three different datasets are as follows: toxicological attributes in (i) lung and (ii) intestinal cell lines along with system-dependent features and (iii) system-independent pchem properties were merged. Each row represents one set of experimental testing conditions and related system-dependent nanodescriptors based on the exposure dose and NF pre-treatment (for intestinal assessments). The system-independent inputs are NF specific and independent of experimental conditions. Data is captured via FAIR principles where the reader can find the origin (institution) of each data, the responsible data creators (experimentalists), the raw measurements, the protocols followed, and the instrumentations used for each experiment. More information regarding the worksheet used for data capturing can be found here.⁸

2.2.2. Data Preprocessing. Missing value imputation methodology is commonly used for ML studies since it is a basic assumption that (i) certain relationship exists between the different attributes and (ii) missing value fill-in is a learning process.⁶² Missing value imputation: for the missing values of system-dependent nanodescriptors, imputation was performed by linearly interpolating data in cases where the corresponding variable was known in a smaller and larger dose; for example, if the hydrodynamic size at t_0 was known for a 10 and 50 ppm solution, interpolation for the 20 and 40 ppm solution was feasible (neighboring points according to the corresponding values). The cases above and below those known values were left blank. The missing value interpolation was performed on a dose, cell line, and NF's pretreatment-reliant manner. Meaning, if the

Table 1. FAIR Data Gathered Related to Intrinsic Hazard Properties of the Safety Dimension

nanodescriptors	category	protocol	input nanodescriptors	feature type	Unit	missing value imputation
system-independent intrinsic pchem properties. OECD guiding principles: ENV/JM/MONO(2019)	surface properties. Elemental and chemical composition	XPS	Na 1s_Atomic concentration O 1s_Atomic concentration Ag 3d_Atomic concentration C 1s_Atomic concentration N 1s_Atomic concentration	numerical	%	none
system-dependent extrinsic pchem properties	particle size properties	none	coating	categorical		none
	crystallographic properties ^c	TEM (ISO/DIS 19749)	core size ^a spherical surface area ^b crystallinity	numerical	nm nm ² %	none 19% → yes none
	particle size properties	DLS (ISO 22412:2017)	average crystallite sizes hydrodynamic size (Z-average) $t_{0.1}$	numerical	nm	none
	particle size quality/heterogeneity measurements		hydrodynamic size (Z-average) t_{24} polydispersity index t_0	numerical	nm	47% → yes
biological attributes	in vitro characteristics (human-derived cell lines)	none	polydispersity index t_{24} organ	categorical		47% → yes none
	exposure conditions		cell line (code) cell type multiwell	numerical		none none none
	output related features	Alamar blue, WST-1, MTT [ISO 10993-5:2009]	exposure dose	numerical	μg/mL (ppm)	none
	output to be predicted		exposure duration assay	categorical	h	none none
			cellular viability	numerical	%	none

^aAverage cumulative size of 50, 100, and 400 kX magnifications. ^bAssumption that the particle is perfectly spherical in shape ($A = 4\pi r^2$). ^cAll the samples in the dataset have a cubic crystal structure, and the amorphous phase is at the crystalline state.

hydrodynamic size at a 50 ppm solution for one specific digested NF was known, the same value did not apply for the non-digested NFs at the same 50 ppm solution. In this manner, we kept the missing value imputation uncertainty at minimum levels. For the system-independent missing values and for the ones left blank from the interpolation, an iterative sequential imputation process was executed via regression with the Light Gradient Boosting Machine (lightgbm) algorithm.⁶³ Each feature is modeled as a function of the other features, allowing prior values to be used into predicting subsequent features. The dataset with the ML-based imputed values can be found in the supplementary material (Supporting Information: tab v01 in the excel). It is worth to notice that during the ML imputation, the ERM codes of the NFs were left in the dataset (dropped after for modeling) since it is the only feature that distinguishes the dataset into fragments, greatly easing the lightgbm algorithm with targeted imputations, lowering the uncertainties.

2.2.2.1. One Hot Encoding. One hot encoding was performed on the categorical attributes for the ML regression models and the BNs. This technique converts categorical features into numerical dummy variables with values 0/1 indicating the absence or presence of the originally feature.⁶⁴

2.2.2.2. SMOTE. For the ML classifiers and BNs, the outcome was discretized into three classes: safe, toxic, and very toxic depending on the corresponding values of cell viability. A challenge in the criteria development is the threshold definition for deciding when a material is deemed safe.¹ The lower the viability value, the higher the cytotoxic potential. Thus, safe were the data points with cell viability $\geq 70\%$, toxic where the viability ranged from 30 to 70% in a precautionary manner, and very toxic where the viability was $<30\%$ (ISO10933-5). However, discretizing the outcome leads to unbalanced classes. To address this issue, we adjusted the relative frequency of the instances by applying SMOTE (synthetic minority oversampling technique), a supervised algorithm that uses the k -nearest neighbors algorithm in the training set (80%) to oversample minority instances.⁶⁵

2.2.2.3. Discretization. In the case of BNs, a quantile-based discretization function was performed on the numerical inputs to discretize them into three equal-sized bins to facilitate the interpretation of the rules. Instead of utilizing the actual numeric edges of the bins, the function defines the bins using percentiles based on the data distribution.

2.2.3. Data Analysis and Visualization. **2.2.3.1. UMAP and MAPPER.** Uniform manifold approximation and projection (UMAP), like principal component analysis methodology, is a dimension reduction technique for 3D data structure visualization. UMAP is constructed from a theoretical framework based in Riemannian geometry and algebraic topology.⁶⁶ Prior to patching together their local fuzzy simplicial set representations, it first builds a topological representation of the high-dimensional data with local manifold approximations.⁶⁷ Similarly, the Mapper algorithm was used for visualization purposes, a method for extracting simple descriptions of the dataset in the forms of simplicial complexes.⁶⁸ The methodology is qualitative based on topological ideas and on partial clustering guided by a set of functions defined on the min–max scaled data. Mapper is essentially providing a simplified version of the UMAP scatterplot via topology.⁶⁹

2.2.3.2. Correlation. Spearman's was performed on numerical–numerical correlations which ranks correlation coefficient (ρ) as a measure of monotonic correlation between -1 and $+1$, where -1 indicates the negative correlation, 0 denotes the absence of association, and 1 shows the positive correlation.⁷⁰ Cramér's V , an association measure for categorical variables,⁷¹ was utilized for numerical–categorical and categorical–categorical features with coefficients ranging from 0 to 1 , with 0 denoting independence and 1 indicating perfect correlation.

2.3. QSAR Development. **2.3.1. ML Exploration.** Several QSAR models were developed exploring various ML algorithms via PyCaret, a low-code AutoML-augmented Data Pipeline library implemented in Python version 3.7.⁷² Regression algorithms include lightgbm, random forest regressor (rfr), extra trees regressor (etr), Lasso regression (lasso), elastic net (en), linear regression (lr), AdaBoost

regressor (ada), and so forth; classification algorithms include gradient boosting classifier (gbc), random forest classifier (rfr), extra trees classifier (etr), decision tree classifier (dt), ridge classifier (ridge), linear discriminant analysis (lda), and so forth. All models are trained with a randomly split sample containing 80% of the initial dataset, with 20% withheld for an out-of-sample validation.

2.3.2. BNs and Rules Extraction. BNs are directed acyclic graphical models where features are nodes and connections are arrows, each of which denotes a conditional reliance of a child to a parent node. The Bayes' rule updates the probabilities in light of new data, and the network as a whole represents the joint probability distribution of features.^{73–75} The probability distribution of all nodes is specified by the artifact of all CPTs in the BN model. For the development of the BN structure and the CPTs, we utilized an open source ML package for probabilistic modeling in Python, pomegranate.⁷⁶ We initialized the BN structure development in a two-fold manner. First, the optimal unconstrained structure was built on the basis of the exact algorithm with knowledge learned directly from data without interference. Second, the structure was then refined by guidance upon expert judgment and inclusion of enforced expected dependencies.⁷⁷ The BN constructed in this manner encodes the expert's reasoning process and allows the system to explain the inference through interpretable rules.^{22,78}

Structure learning and rules extraction are independent with the latter being described as an explainability method.⁷⁷ Each rule is followed with a certainty factor (CF), which is the likelihood ratio for and against an outcome (T) when presented with evidence (X): that is, IF ($X = 0$) THEN $T = 0$ with CF = 0.25. By adding CF to rules, we reveal model's uncertainty in the nanosafety domain.²²

2.3.3. Models Validation. QSAR models were validated based on the OECD guiding principles, containing a defined endpoint (biological effect can be measured and modeled, i.e., cellular viability); unambiguous algorithms and measurements of goodness-of-fit, robustness (internal 10-fold cross-validation, 80%), and predictivity (external validation, 20%).^{79,80} Since the focus of this study is QSAR based on the BN algorithm, the domain of applicability is defined solely for this case. Regression QSAR models were validated with various performance metrics such as the mean absolute error (MAE), which is the mean value of individual prediction errors over all instances, root-mean-square error (RMSE), the standard deviation of residuals (prediction errors), and the coefficient of determination (R^2) that measures how well a model predicts an outcome. Classification QSAR models and BNs were validated via multiclass classification metrics⁸¹ such as balanced accuracy (overall measure of correctly predicted instances with classes having the same weight), precision (true negative rate or specificity), recall (true positive rate or sensitivity), F1 score (weighted average of precision and recall), and Mathews correlation coefficient (MCC), a metric that accounts all confusion matrix categories. In the case of multiclass outcome, those metrics are calculated per class, for example, the metrics for the toxic class consider toxic as true and the union of the remaining classes as false.

3. RESULTS

3.1. Data Merging and Pre-processing. Table 1 shows the information related to the nanodescriptors and toxicological data. System-independent variables contain information derived by XPS, TEM, and XRD analysis. System-dependent variables contain DLS measurements in two different times. The toxicological data contain information related to (1) in vitro characteristics such as the cell line exposed, the cell type, cell origin, and cell number; (2) exposure conditions such as the exposure dose and duration; and (3) output-related information such as the assay for the cellular viability determination. The FAIR dataset is enriched and annotated with information of the origin of the data, the protocols, and instrumentation and can be found in the Supporting Information and in the open repository Zenodo.^k

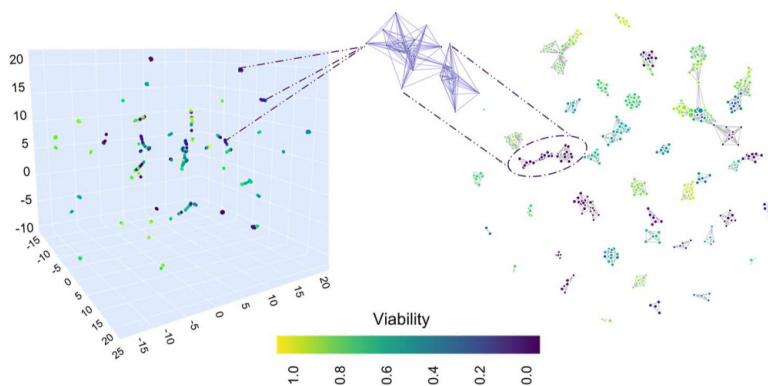


Figure 3. UMAP for dimension reduction (left) and topological network representing the dataset (right). The axes coordinates of UMAP are dimensionless representing an Euclidean space with points distributed so that the low dimensional representation has a similar topological structure to the original data. 3D visualizations of the dataset with respect to viability are colored by a scaled order of viability.

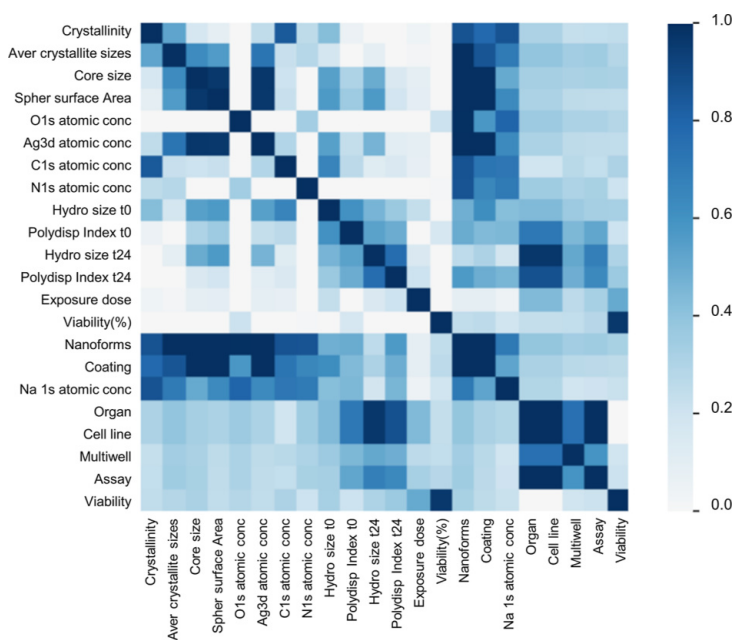


Figure 4. Inter-relationship correlations of input variables and between the inputs and output.

3.2. Data Analysis. In Figure 3, UMAP and Mapper topological network projecting data into lower dimensional spaces demonstrating the structure of the data. Even with missing value imputations, the experimental data are quite sparse with relatively low variance, with the local dimension varying across the data and the dataset uniformly distributed on the Riemannian manifold (Figure 3, left). This was expected since the dataset contains (i) triplicates of toxicological experiments (rows with identical inputs but different outcomes) and (ii) rows where the only feature varying is the exposure dose or the assay. UMAP places related experiments near to one another with the color differentiating the 3D experimental space based on cellular viability-scaled

values. The gaps between the points signify the experiments that could have been hypothetically performed.

Data are projected into a two low-dimensional simplicial complex with the Mapper algorithm including clusters varying by color and size containing cubes (Figure 3, right). The color indicates the value of the function at a representative point (cell viability), and the size indicates the number of dots in the set (experiments), providing information about the nature of the output.⁶⁸ Each dot belongs to a rule/criteria (cube) and finding the input's association of the cubes within the cluster provides the output.

The pairwise correlation among the features based on Spearman's ρ for the numeric features and based on Cramer's V for the categorical relationships is shown in Figure 4.

The output (viability expressed either as % or multiclass) shows no correlation with input features. The NFs (ERM identifiers) which are utilized during missing value imputation with the lightgbm algorithm shows high correlation with nearly half of the features in the dataset. Thus, including it during the imputation helped the algorithm to efficiently allocate missing values. Crystallinity is correlated with the C 1s atomic concentration, while Ag 3d atomic concentration is correlated with the core size, coating, and surface area of NFs. The average crystallite sizes are correlated with the coating along with other features such as the C 1s atomic concentration. This information is useful for the reasoning construction of the BN structure since some correlation among features is required. Negative linear correlation is shown among O 1s with Ag 3d and C 1s atomic concentrations (see Supporting Information Figure S1: Pearson r correlation). The cell line is highly correlated with the organ, multiwell, assay, and the hydrodynamic size at t_{24} . Thus, we kept only the cell line as a final feature to be used in the modeling part since it encapsulates the information regarding the organ. Such input features would be valuable in case of diverse targeted organs to reveal any target-specific toxicities. Assay is kept which includes information of the multiwell used. Regarding the correlation of the above-mentioned features with hydrodynamic size at t_{24} , correlation does not signify causation, and this information is not deemed redundant in our case. In BNs, determining the conditional dependencies among the features goes beyond the correlation concept revealing the causal effect probabilities among the features (Pearl's ladder of causation).⁸³

Table 2 shows the final modeling features along with their skewness and the transformed bins for the BN training, which also represent the applicability domain of the QSAR model. Skewness quantifies distribution asymmetry, and values between -2 and $+2$ are acceptable to demonstrate a normal univariate distribution.⁸³ All features show good skewness except hydrodynamic size at t_{24} . However, the feature is included since it contributes greatly to the information gain analysis of the dataset (see Supporting Information Table S1: attribute selection). All the experiments refer to a 24 h acute in vitro toxicological screening, thus from the exposure conditions, only the exposure dose was considered. Na 1s and N 1s atomic concentrations were not considered for the modeling due to redundant zero values and the fact that those features are related to the synthesis process and precursors utilized and have no causal effect to hazard effects.

3.3. QSAR Development and Validation. **3.3.1. ML Exploration.** QSAR models trained either as regression or classification ML tasks are able to predict cellular viability with satisfactory results. Table 3 shows the top three regressor and classifier algorithm's external performance metrics. Random forest regressor (rf) slightly outperforms the other regressors achieving $R^2 = 0.7$, MAE = 12.77, and RMSE = 19.55. Extra trees classifier (et) faintly outperforms rf, reaching a balanced accuracy of 85%, a F1 score (a harmonized metric including precision and recall) of $\approx 85\%$, and a MCC of 77%. Additional algorithms with their internal 10-fold cross-validation, hyperparameterization, and external performance metrics can be found in the Supporting Information (Tables S2–S5: additional algorithms' validation metrics).

3.3.2. BNs and Rules Extraction. For the development of the constrained reasoned structured network, expert judgment was applied to conditional dependencies. Some alterations of arcs include polydispersity index t_{24} and hydrodynamic size t_0 ,

Table 2. Features in the Final Dataset for Modeling Purposes^a

input features	metric	skewness	bins [for the BN structure training]
O 1s_Atomic	%	0.78	"low": [14.16 → 14.54], "medium": [14.54 → 34.02], "high": ≥ 34.02
Ag 3d_Atomic	%	-0.21	"low": [0.08 → 0.19], "medium": [0.19 → 15.53], "high": ≥ 15.53
C 1s_Atomic	%	-0.19	"low": [54.23 → 60.61], "medium": [60.61 → 61.83], "high": ≥ 61.83
core size	nm	0.60	"low": [7.0 → 17.8], "medium": [17.8 → 20.00], "high": ≥ 20.00
spherical surface area	N m ²	1.03	"low": [3981.53 → 3981.59], "medium": [3981.59 → 5023.55], "high": ≥ 5023.55
crystallinity	%	1.61	"low": [22.9 → 60.0], "medium": [60.0 → 61.0], "high": ≥ 61.0
av crystallite sizes	nm	0.35	"low": [46.0 → 98.0], "medium": [98.0 → 117.0], "high": ≥ 117.0
coating			HEC, PVP, CUR, none (one hot encoded)
hydrodynamic size t_0	nm	1.79	"low": [55.91 → 209.97], "medium": [209.97 → 363.31], "high": ≥ 363.31
hydrodynamic size t_{24}	nm	2.67	"low": [63.74 → 149.34], "medium": [149.34 → 266.90], "high": ≥ 266.90
pol index t_0		-0.72	"low": [0.18 → 0.47], "medium": [0.47 → 0.59], "high": ≥ 0.59
pol index t_{24}		0.31	"low": [0.04 → 0.28], "medium": [0.28 → 0.49], "high": ≥ 0.49
cell line			AS49, HCT-116 (one hot encoded)
exposure dose	ppm	0.32	"low": [0.0 → 20.0], "medium": [20.0 → 58.35], "high": ≥ 58.35
assay			WST-1, MTT, Alamar blue (one hot encoded)
output feature	metric	skewness	bins [for the BNs structure training]
cellular viability	%	-0.28	very toxic [0 → 30.0%], toxic [30.0 → 70.0%], safe >70%

^a900 rows transformed into the final dataset of 1682 rows through SMOTE implementation for the classification modeling and BNs. The bins also demonstrate the applicability domain of the QSAR model based on BN algorithm in which the model makes predictions with a given reliability.

Table 3. Performance Metrics (External Validation/Predictivity with 20% of the Dataset) for the Top Three Regressors and Classifiers

task	models	performance metrics		
		MAE	RMSE	R^2
regression	rfr	12.77	19.55	0.70
	lightgbm	12.91	19.71	0.70
	gbr	14.17	20.18	0.68
classification	et	ACC	F1	MCC
	rf	0.85	0.85	0.77
	lightgbm	0.84	0.84	0.77
	lightgbm	0.84	0.83	0.76

where t_{24} features were parents to exposure dose in the unconstrained structure (see Supporting Information Figure S2: unconstrained BN structure); however, such a dependency is not realistic; that is, the external exposure dose cannot be

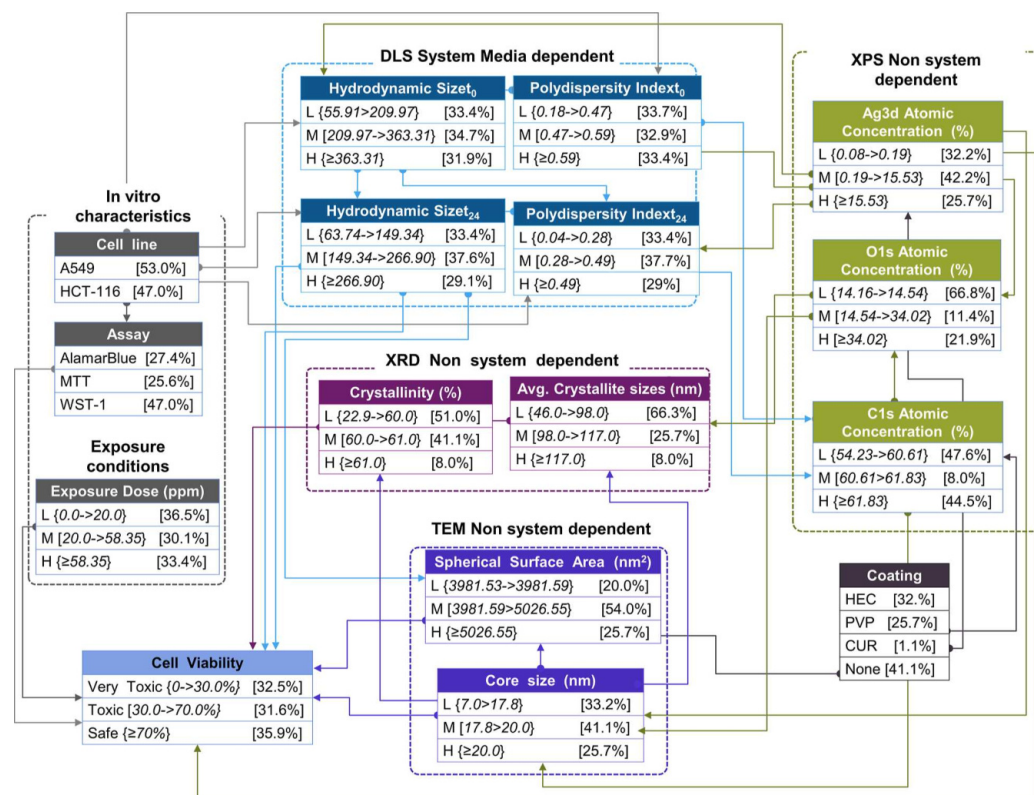


Figure 5. Graphical structure of the constrained BN representing the variables (input features and toxicological attributes) along with the conditional probabilities. Arcs represent the conditional dependencies between the features. The different color represents the categories of the input features containing system-dependent and system-independent pchem properties measured with different protocols, biological attributes (in vitro characteristics), and exposure conditions.

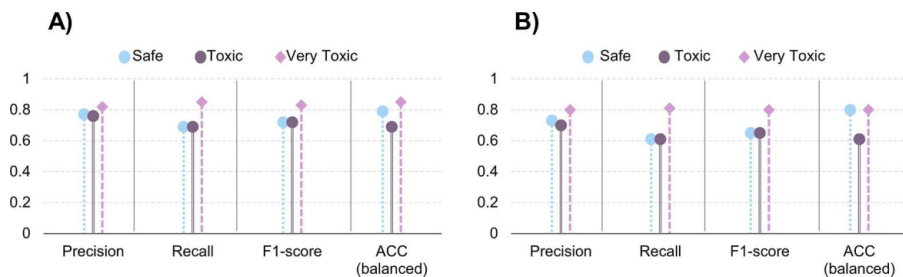


Figure 6. External validation metrics containing precision (PREC), recall (REC), and F1 score and balanced accuracy (ACC) per class label of the constrained structure (A) and the unconstrained structure (B).

determined by the hydrodynamic size; however, the exposure dose did not feed the cell viability node, which is kept in the constrained structure, eliminating the other relationships. The exposure dose was forced to act as an independent global parameter⁸⁴ (see Figure 5, node: exposure dose, color gray). The same reasoning was applied for the assay, which affects the output to be predicted. Coating is fed by the core size in the unconstrained structure, but knowing the coating has no effect on predicting the core size; instead, the coating feature determines the surface area and the Ag 3d atomic

concentration in the case of uncoated AgNFs. Polydispersity index at t_0 appeared at the end of the structure with hydrodynamic size at t_0 and the cell line feeding it. Thus, one constrain included in the structure was that the output should be the only feature receiving prior knowledge at the terminate point. Core size fed many nodes in the unconstrained structure, and the pattern was kept in the constrain as well. Features measured at t_0 should act like parents to features at t_{24} and not vice versa (see Figure 5, system media dependent, color blue). The constrained structure follows a

reasoning pathway of scale information starting from a higher level such as coating to → structure level → to atomic system-independent properties, while the system-dependent features are fed by medium information encapsulated within the cell line. With the above manipulations of the conditional dependencies based on expert judgment, the constrained model displayed slightly higher predictive capacity for some classes, but most importantly, the structure has reasoning, in order for the rules to make sense.

Exploring the Weka software for automated BN construction (estimator: simple, $a = 0.5$, search algorithm: local hill climber, six parents limit configuration), the unconstrained structure also demonstrated the exposure dose, hydrodynamic size at t_{24} , core size, and assay being connected to the outcome, reinforcing the reasoning on some arcs (see [Supporting Information](#) Figure S3: unconstrained Bayesian structure derived from WEKA software).

Figure 6 demonstrates the external validation results of the QSAR BN-based model tested with the 20% test set. The metrics are quite similar for both structures. However, we demonstrate that even with constrains, the predictability of the BNs is slightly increased (MCC for unconstrained: 62% vs constrained 67%, data not shown in figure since MCC considers all classes into a single metric).

The focus on the validation was to surpass the performance for the very toxic instances from the structure learned with no reasoning. The constrain model has higher performance metrics for the very toxic instances. This is significant especially in the case of the high recall (REC: 85% constrained vs 81% unconstrained), meaning a false negative instance (safe or toxic) rarely gets predicted instead of very toxic. The BN performed better also for safe instances (PREC: 77% constrained vs 73% unconstrained). Regarding the toxic instances, the constrained BN scores 69% ACC (vs 61% unconstrained).

3.3.2.1. Rules Extraction. The extraction of the interpretable rules related to the quantitative intrinsic hazard properties of AgNFs was filtered down to the cases where the hazard class was present and with the highest CF as an example. For the theoretical scenarios where the input ranges fall outside those given rules (or the ones provided in the [Supporting Information](#), Section 4: extra rules), Bayesian inference (or the regressors/classifiers) can be used to determine the hazard class with a given CF. The higher the CF, the higher the posterior probability of that statement/rule to be true. Infinite confidence probabilities, an instance that occurs due to a divide-by-zero runtime exception when comparing the likelihood of events with no counterexamples, were discarded.

The following rules are mentioned based on the BN structure's CPTs solely as examples, where L denotes low, M medium, H high values in the representative bins (see [Table 2](#)), and the logical symbol for *and*:

(1) Quantitative intrinsic hazard criteria for lung cells (under MTT assay)

IF (crystallinity) = M(60 → 61) core size = M(18 → 20) spherical surface area = M(3982 → 5026) Ag 3d at. % = M(0.2 → 15) hydrodynamic size t_{24} = L(64 → 149) THEN AgNFs are toxic if tested under low (0.0 → 58) dose with an average 0.82 probability.

IF (crystallinity) = H(>61) core size = L(7 → 18) spherical surface area = L(3981.53 → 3981.59) Ag 3d at. % = L(0.08 → 0.2) hydrodynamic size t_{24} = L(64 → 149) THEN AgNFs are

safe if tested under low (0.0 → 58) dose with an average 0.81 probability.

(2) Quantitative intrinsic hazard criteria for lung cells (under Alamar blue assay)

IF (crystallinity) = L(23 → 60) core size = L(7 → 18) spherical surface area = M(3982 → 5026) Ag 3d at. % = L(0.08 → 0.2) hydrodynamic size t_{24} = M(149 → 267) OR.

IF (crystallinity) = H(>61) core size = L(7 → 18) spherical surface area = L(3981.53 → 3981.59) Ag 3d at. % = L(0.08 → 0.2) hydrodynamic size t_{24} = L(64 → 149) THEN AgNFs are very toxic if tested under low dose (0 → 20) or medium dose (20 → 58), respectively, with a 0.87 probability (CF = 6.7).

(3) Quantitative intrinsic hazard criteria for intestinal cells (under WST-1 assay)

IF (crystallinity) = L(23 → 60) core size = L(7 → 18) spherical surface area = M(3982 → 5026) Ag 3d at. % = L(0.08 → 0.2) hydrodynamic size t_{24} = M(149 → 267) THEN AgNFs are safe if tested under any exposure range with an average 0.87 probability (CF = 35).

The rules mentioned are only a sub-part of all the rules and serve as a technical extract example of the model that can be used as a formula, ad hoc. The structure of the BN contains the decision structure and the rules within—a total of rules extracted from this case is ~150.

4. DISCUSSION

4.1. Data. For the moment, a great amount of information produced by H2020 projects is stored online in private servers, locked to external users, making the data re-usability unfeasible, hindering progress and data integration, especially for modeling purposes.⁸⁵ Commission⁴ remarks that research and innovation are needed in open platforms to ensure access and data integration from different databases enabling exchanges between different stakeholders in line with data governance acts, meaning an overarching level.¹ Metadata capturing is not frequently promoted in regular academic practice, despite its importance. This is due to a lack of data management training. This FAIR challenge requires the active involvement, participation, and collaboration of participants with different expertise. In this work, we used data captured by the data shepherd,⁸ which demonstrates that this role is essential in a project where data are generated, modeled, and used.⁸⁵ The role of the shepherd is to capture data, protocols, and instrumentations and to help with data reporting, merging, and harmonization. The most important part of this role is the implementation of the FAIRification process with multiple stakeholders who are unaccustomed with the notion of FAIRification process.^{8–10} It is outside of the scope of this manuscript to provide details regarding the FAIR initiatives and the efforts in place in the EU. The reader can refer to the following footnotes^{1,76} to get an appreciation of the current initiatives regarding FAIR data.

The size of the dataset used in this study is not remarkable (in comparison to common experimental computer science fields), but in comparison to the dataset sizes used in the nanocomputational domain literature, the data size is sufficiently large.¹⁶ To tackle this sparsity, the approach in this work is twofold, the data is augmented by a standard method to oversample sparse data with SMOTE leading to 1682 data points and by applying BN ML algorithm, which is a robust learning paradigm in the sparse data regime. In addition, the interoperability of data is high due to the annotation with ontological identifiers from eNanoMapper and

with ERM identifiers which ensure that internal project documentation can later be linked to released data for specific NFs.³⁵ The dataset contains harmonized features derived from different laboratories; for example, the system-dependent properties reported in the toxicological datasets were similar across the two partners, greatly facilitating the merging. By capturing the measurements at two time points, we were able to account for variations that might occur to the size when dispersed and once when in contact with cellular medium.⁴⁷ By incorporating the polydispersity index, we increase the quality of the measurements and consequently the modeling.⁴⁵ The data is targeting cellular viability, which is the majority of the re-usable data that exist in the literature and databases,^{27,85} implying a potentiality of further merging. Also, exposure conditions and in vitro characteristics are commonly considered as input features.⁵⁹ The exposure aspects are not part of step 1—hazard assessment of the SSbD framework.³ In this work, we go a step further considering, besides the system and non-system-dependent properties, also the in vitro characteristics and exposure conditions to better represent how those properties are altered depending on the dose and the cellular target. We argue that inherently safer NFs should be cell line (organ)-target specific; that is, NFs safe for skin cells could be harmful for lung cells. Taking into account in vitro features for the hazard criteria, we capture the dynamic and complex nature of NFs when surrounded by a biological environment.⁴³ In addition, from a toxicological point of view, dose should be considered at each dimension. Including exposure conditions increase the performance as this information is always reported in in vitro studies but could also reduce the biological accuracy by grouping this information in a node of exposure features not readily comparable; for example, exposure doses for different tissues cannot be grouped. However, the nodes were included as exposure criterion, which is a crucial variable in the hazard notion.

4.2. Data Pre-processing. Commission⁴ mentions the need of improved methods to address missing data such as ML-based methods. In this study, an iterative sequential imputation process was executed via regression with the lightgbm algorithm. Other techniques have been proposed such as a hybrid missing data imputation method incorporating records similarity using the global correlation structure by using *k*-nearest neighbors and iterative imputation algorithms⁸⁶ or by merits integration of decision trees and fuzzy clustering into an iterative learning approach.⁸⁷

A quantile-based discretization function was performed in this study to discretize features into bins. For this step, alternative methods have been proposed, for example,⁸⁸ introduced a dynamic programming search strategy and a Bayesian score for the evaluation and the discretization of variables.

UMAP places related experiments (each row of the dataset) near to one another. Such an approach could hypothetically be helpful to identify the experimentations that should be prioritized during a project, in a data gap filling manner, supporting the application of QSAR modeling. Since the axes in UMAP are non-dimensional, input features could be used to predict *x*, *y*, *z* values. On a second step, a SHapley Additive exPlanations (SHAP) analysis could reveal the most important features determining the space and were experimentations should focus.⁸⁹ In addition, the dimensionality reduction algorithms could be more interpretable only for some cases

due to complexity.¹⁹ However, this field is under research, with hyperparameter choice appearing to play an important role.

4.3. NAMs. QSAR models based on random forest (rf) and extra tress (et) algorithms showed good validation metrics in our study. Throughout the literature, rf has been shown to surpass other algorithms.^{90–92} Et algorithm generates a large number of unpruned decision trees from the dataset and then combines the predictions. Et similarly to rf randomly samples the features at each split point. However, et splits the nodes by selecting cut points randomly, in comparison to rf, and fits each decision tree to the entire training dataset whose structures are independent of the output values.⁹³

The theoretical framework from ref 3 and the recent report by ref 4 both mention NAM approaches as helpful tools in the implementation and validation of the SSbD approach, without providing instructions. This study is a contribution of an iterative consolidation of modeling and experimental domain expertise. We demonstrate how experimentalists in conduction with modelers can act in a complementary manner, accelerating the progress in the nanosafety domain. Bringing the gaps between the three fields (toxicology, material designers, and modelers) demanded strong communication, interaction, while transferring experimental domain knowledge, adopting a multidisciplinary approach.⁹⁴ In this work, we demonstrated in a detailed manner how QSAR tools based on BNs coupled with expert judgment can be used for the definition and extraction of quantitative intrinsic hazard criteria. The same approach can be used in datasets targeting different outputs.

The modeling approach is unique in some points: (i) the BN model is crafted by expert reasoning integrating system-dependent and -independent nanodescriptors in combination with in vitro experimental conditions derived from a FAIR process to predict a biological effect, (ii) the data refer to NFs that have the same chemical identity but a unique fingerprint that allows a NF-dependent differentiation among the same substance, (iii) the interpretable rules can guide material developers into synthesizing (re-synthesizing) inherently safer NFs, and (iv) the models (BN, regressors, and classifiers) can enable the fast and cost-efficient in silico toxicological screening of previously synthesized NFs and hypothetical scenarios of yet-to be synthesized NFs. It is worth noting that the methodology strongly improves given variables that material designers have the most control over modifying in the laboratory. For the development of the BN structure and the CPTs, we utilized an open source ML package pomegranate.⁷⁶ Other packages for the implementation of BN are documented.⁹⁵

In the nanosafety, there are no clear understandings of causal relations among nanodescriptors and hazardous attributes, only statistical relevance information. Such relevance is insufficient to fully capture causal relations. This means that any explanation proven wrong may have to be prohibited within the structure.⁷⁸ The BNs can perform an incremental learning, meaning, as more data become available in the nanosafety domain, the existing structure can remain the same, or updated to novel modifications of parameters (inclusion of additional nanodescriptors or hazard endpoints), and even a new structure, to fit the new data.²² The BN can also perform with multiple outcomes, rendering it an optimum solution in the case of multiple hazard criteria⁹⁶ while also providing a robust learning paradigm in the sparse data regime.⁹⁷ The extraction of the rules from the CPTs is performed with the

aim to extract quantitative intrinsic hazard design criteria that can be used in SSbD paradigms. The interpretable rules can act in a hierarchic manner, meaning that the last descriptors have to be measured only if the previous IF statements are met. Identifying quantitative criteria to address the SSbD multi-criteria decision problem is one of the most significant goals where collective robust efforts are currently placed. The rules are followed with CFs, which is the likelihood ratio for and against an outcome when presented with evidence, as a means of expressing domain knowledge and creating expert systems that can take into account quantitative uncertainties. The quantifiable CFs for each rule deliver a convenient system to manage uncertainties in a criteria-based framework. As a result, such a rule-based system will have practical ways to elicit expert knowledge and clearly communicate the reasoning process. This methodology proposed entails a flexible, nuanced, and promising approach applicable at each SSbD dimension with a goal to extract a set of quantitative criteria in a data-driven manner.

5. CONCLUSIONS

Collaborative efforts are required among data shepherds, experimentalists, experts, and modelers to merge information in an iterative manner that can reveal valuable information for each SSbD dimension. BNs are promising probabilistic ML tools helpful to (i) derive interpretable rules from FAIR data, (ii) capable and flexible in updating their conditional dependencies from new data while (iii) allowing the quantification of the uncertainties. In addition, they present graphical structures developed from expert reasoning in combination with automated inference. In this work, utilizing system (i.e., hydrodynamic size and polydispersity index) and non-system (i.e., elemental composition and core size)-dependent nanodescriptors in combination with biological in vitro attributes and experimental conditions, we demonstrate how such a methodology can be used for extracting quantitative intrinsic hazard criteria for silver NFs, synthesized with the intend of antimicrobial/antiviral functional textiles and antimicrobial creams or lotions (cosmetics) applications, which can guide materials designers toward intrinsically safer materials while saving time, effort, and money for the toxicologists.

■ ASSOCIATED CONTENT

Supporting Information

The Supporting Information is available free of charge at <https://pubs.acs.org/doi/10.1021/acsanm.3c00173>.

FAIR dataset used for the modeling can be found in the supplementary file and in open repository Zenodo (<https://zenodo.org/record/7335039#.Y3emqnbMIQ8>) (XLSX)

Additional data analysis, QSAR development, validation metrics of algorithms, and additional BN rules extracted (PDF)

■ AUTHOR INFORMATION

Corresponding Author

Irini Furxhi – *Transgero Ltd, Limerick V42V384, Ireland; Department of Accounting and Finance, Kemmy Business School, University of Limerick, Limerick V94T9PX, Ireland;* orcid.org/0000-0002-2263-0279; Phone: +353 85 106 9771; Email: irini.furxhi@transgero.eu, irini.furxhi@ul.ie

Authors

Rossella Bengalli – *Department of Earth and Environmental Sciences, University of Milano-Bicocca, Milano 20126, Italy*

Giulia Motta – *Department of Earth and Environmental Sciences, University of Milano-Bicocca, Milano 20126, Italy*

Paride Mantecca – *Department of Earth and Environmental Sciences, University of Milano-Bicocca, Milano 20126, Italy;* orcid.org/0000-0002-6962-049X

Ozge Kose – *Univ. Grenoble Alpes, CEA, CNRS, Grenoble INP, IRIG, SYMMES, Grenoble 38000, France*

Marie Carriere – *Univ. Grenoble Alpes, CEA, CNRS, Grenoble INP, IRIG, SYMMES, Grenoble 38000, France;* orcid.org/0000-0001-8446-6462

Ehtsham Ul Haq – *Department of Physics, and Bernal Institute, University of Limerick, Limerick V94TC9PX, Ireland*

Charlie O'Mahony – *Department of Physics, and Bernal Institute, University of Limerick, Limerick V94TC9PX, Ireland*

Magda Blosi – *Istituto di Scienza e Tecnologia dei Materiali Ceramici (CNR-ISTEC), Faenza 48018 Ravenna, Italy;* orcid.org/0000-0001-8841-247X

Davide Gardini – *Istituto di Scienza e Tecnologia dei Materiali Ceramici (CNR-ISTEC), Faenza 48018 Ravenna, Italy*

Anna Costa – *Istituto di Scienza e Tecnologia dei Materiali Ceramici (CNR-ISTEC), Faenza 48018 Ravenna, Italy*

Complete contact information is available at: <https://pubs.acs.org/doi/10.1021/acsanm.3c00173>

Author Contributions

The manuscript was written through contributions of all authors. All authors have given approval to the final version of the manuscript.

Funding

This work was supported by the European Union's Horizon 2020 research and innovation programme under grant number no. 862444.

Notes

The authors declare no competing financial interest.

■ ACKNOWLEDGMENTS

The authors thank Prof. Syed A. Tofail, Prof. Christophe Sillien, Dr. Pritam Khan, Dr. Vasily Labedev, and Na Jia from the Department of Physics and Bernal Institute, University of Limerick, Ireland, for their contributions in nanoscale characterization.

■ ADDITIONAL NOTES

^a<https://zenodo.org/record/4652587#.Y1eVGnZBwQ8>.

^bThe data shepherd not only oversees the data management, handling, and quality control processes but also communicates in a simple language with all parties. Data shepherds combine experimental, computational, and technical background and lead the data quality control and FAIRness evaluation facilitating the data curation.⁶

^c<https://webcast.ec.europa.eu/3rd-meeting-of-the-high-level-roundtable-on-the-chemicals-strategy-for-sustainability> [Accessed November 2022].

^dhttps://www.youtube.com/watch?v=R3_QEZIShf0&t=1578s [Accessed November 2022].

^e<https://www.asina-project.eu/asina-1st-stakeholder-workshop-bioceramics-2022/> [Accessed November 2022].
^f<https://www.h2020sunshine.eu/events/nanosafety-training-school-venice-2022> [Accessed November 2022].
^g<https://eur-lex.europa.eu/legal-content/EN/TXT/?uri=COM%3A2020%3A667%3AFIN> [Accessed November 2022].
^hPatent number granted in USA: US10525432B2.
ⁱ<https://www.iso.org/standard/65410.html> [Accessed November 2022].
^j[https://one.oecd.org/document/ENV/JM/MONO\(2016\)7/en/pdf](https://one.oecd.org/document/ENV/JM/MONO(2016)7/en/pdf) [Accessed November 2022].
^k<https://zenodo.org/record/7335039#Y3emqnbMIQ8>.
^l<https://www.go-fair.org/implementation-networks/overview/advancednano/> [Accessed November 2022].
^m<https://worldfair-project.eu/> [Accessed November 2022].

REFERENCES

- (1) Mech, A.; Gottardo, S.; Amenta, V.; Amodio, A.; Belz, S.; Bowadt, S.; Drbohlavová, J.; Farcial, L.; Jantunen, P.; Malyska, A.; Rasmussen, K.; Riego Sintes, J.; Rauscher, H. Safe- and sustainably-by-design: The case of Smart Nanomaterials. A perspective based on a European workshop. *Regul. Toxicol. Pharmacol.* **2022**, *128*, 105093.
- (2) Gottardo, S.; Mech, A.; Drbohlavová, J.; Malyska, A.; Bowadt, S.; Riego Sintes, J.; Rauscher, H. Towards safe and sustainable innovation in nanotechnology: State-of-play for smart nanomaterials. *NanoImpact* **2021**, *21*, 100297.
- (3) European Union; Caldeira, C.; Farcial, L.; Garmendia Aguirre, I.; Mancini, L.; Tosches, D.; Amelio, A.; Rasmussen, K.; Rauscher, H.; Riego Sintes, J.; Sala, S. *Safe and Sustainable by Design Chemicals and Materials: Framework for the Definition of Criteria and Evaluation Procedure for Chemicals and Materials*; Publications Office of the European Union, 2022.
- (4) Commission, E. Directorate-General for, R *Innovation, Strategic Research and Innovation Plan for Safe and Sustainable Chemicals and Materials*; Publications Office of the European Union, 2022.
- (5) Jeliakzova, N.; Apostolova, M. D.; Andreoli, C.; Barone, F.; Barrick, A.; Battistelli, C.; Bossa, C.; Botea-Petcu, A.; Châtel, A.; De Angelis, I.; Dusinska, M.; El Yamani, N.; Gheorghe, D.; Giusti, A.; Gómez-Fernández, P.; Grafström, R.; Gromelski, M.; Jacobsen, N. R.; Jeliakzov, V.; Jensen, K. A.; Kochev, N.; Kohonen, P.; Manier, N.; Mariussen, E.; Mech, A.; Navas, J. M.; Paskaleva, V.; Precupas, A.; Puzyn, T.; Rasmussen, K.; Ritchie, P.; Llopis, I. R.; Rundén-Pran, E.; Sandu, R.; Shandilya, N.; Tanasescu, S.; Haase, A.; Nymark, P. Towards FAIR nanosafety data. *Nat. Nanotechnol.* **2021**, *16*, 644–654.
- (6) Papadiamantis, A. G.; Klaessig, F. C.; Exner, T. E.; Hofer, S.; Hofstaetter, N.; Himly, M.; Williams, M. A.; Doganis, P.; Hoover, M. D.; Afantitis, A.; Melagraki, G.; Nolan, T. S.; Rumble, J.; Maier, D.; Lynch, I. Metadata Stewardship in Nanosafety Research: Community-Driven Organisation of Metadata Schemas to Support FAIR Nanoscience Data. *Nanomaterials* **2020**, *10*, 2033.
- (7) Furchi, I.; Perucca, M.; Blosi, M.; Lopez de Ipiña, J.; Oliveira, J.; Murphy, F.; Costa, A. L. ASINA Project: Towards a Methodological Data-Driven Sustainable and Safe-by-Design Approach for the Development of Nanomaterials. *Front. Bioeng. Biotechnol.* **2022**, *9*, 805096.
- (8) Furchi, I.; Arvanitis, A.; Murphy, F.; Costa, A.; Blosi, M. Data Shepherding in Nanotechnology. The Initiation. *Nanomaterials* **2021**, *11*, 1520.
- (9) Furchi, I.; Koivisto, A. J.; Murphy, F.; Trabucco, S.; Del Secco, B.; Arvanitis, A. Data Shepherding in Nanotechnology. The Exposure Field Campaign Template. *Nanomaterials* **2021**, *11*, 1818.
- (10) Furchi, I.; Varesano, A.; Salman, H.; Mirzaei, M.; Battistello, V.; Tomasoni, I.; Blosi, M. Data shepherding in nanotechnology. The antimicrobial functionality data capture template. *Coatings* **2021**, *11*, 1818.
- (11) Doak, S. H.; Clift, M. J. D.; Costa, A.; Delmaur, C.; Gosens, I.; Halappanavar, S.; Kelly, S.; Pejinenburg, W. J. G. M.; Rothen-
- Rutishauser, B.; Schins, R. P. F.; Stone, V.; Tran, L.; Vijver, M. G.; Vogel, U.; Wohlleben, W.; Cassee, F. R. The Road to Achieving the European Commission's Chemicals Strategy for Nanomaterial Sustainability-A PATROLS Perspective on New Approach Methodologies on New Approach Methodologies. *Small* **2022**, *18*, 2200231.
- (12) Ramanarayanan, T.; Szarka, A.; Flack, S.; Hinderliter, P.; Corley, R.; Charlton, A.; Pyles, S.; Wolf, D. Application of a new approach method (NAM) for inhalation risk assessment. *Regul. Toxicol. Pharmacol.* **2022**, *133*, 105216.
- (13) Stucki, A. O.; Barton-Maclaren, T. S.; Bhuller, Y.; Henriquez, J. E.; Henry, T. R.; Hirn, C.; Miller-Holt, J.; Nagy, E. G.; Perron, M. M.; Ratzlaff, D. E.; Stedeford, T. J.; Clippinger, A. J. Use of new approach methodologies (NAMs) to meet regulatory requirements for the assessment of industrial chemicals and pesticides for effects on human health. *Front. Toxicol.* **2022**, *4*, 964553.
- (14) Puzyn, T.; Leszczynska, D.; Leszczynski, J. Toward the development of "nano-QSARs": advances and challenges. *Small* **2009**, *5*, 2494–2509.
- (15) Puzyn, T.; Rasulev, B.; Gajewicz, A.; Hu, X.; Dasari, T. P.; Michalkova, A.; Hwang, H. M.; Toropov, A.; Leszczynska, D.; Leszczynski, J. Using nano-QSAR to predict the cytotoxicity of metal oxide nanoparticles. *Nat. Nanotechnol.* **2011**, *6*, 175–178.
- (16) Furchi, I.; Murphy, F.; Mullins, M.; Arvanitis, A.; Poland, C. A. Practices and Trends of Machine Learning Application in Nanotoxicology. *Nanomaterials* **2020**, *10*, 116.
- (17) Mikolajczyk, A.; Gajewicz, A.; Mulkiwicz, E.; Rasulev, B.; Marchelek, M.; Diak, M.; Hirano, S.; Zaleska-Medynska, A.; Puzyn, T. Nano-QSAR modeling for ecotoxicity of heterogeneous TiO₂-based nano-photocatalysts. *Environ. Sci.: Nano* **2018**, *5*, 1150–1160.
- (18) Tantra, R.; Oksel, C.; Puzyn, T.; Wang, J.; Robinson, K. N.; Wang, X. Z.; Ma, C. Y.; Wilkins, T. Nano(Q)SAR: Challenges, pitfalls and perspectives. *Nanotoxicology* **2015**, *9*, 636–642.
- (19) Rudin, C.; Chen, C.; Chen, Z.; Huang, H.; Semenova, L.; Zhong, C. Interpretable machine learning: Fundamental principles and 10 grand challenges. *Statt. Surv.* **2022**, *16*, 1–85.
- (20) Kim, I. Y.; Kwak, M.; Kim, J.; Lee, T. G.; Heo, M. B. Comparative Study on Nanotoxicity in Human Primary and Cancer Cells. *Nanomaterials* **2022**, *12*, 993.
- (21) Chun, A. L. Conflicting results. *Nat. Nanotechnol.* **2007**, DOI: 10.1038/nnano.2007.257.
- (22) Thirumuruganathan, S.; Huber, M. Building Bayesian Network based expert systems from rules. *2011 IEEE International Conference on Systems, Man, and Cybernetics, 9–12 Oct 2011, 2011*; pp 3002–3008.
- (23) Marvin, H. J. P.; Bouzembrak, Y.; Janssen, E. M.; et al. Application of Bayesian networks for hazard ranking of nanomaterials to support human health risk assessment. *Nanotoxicology* **2017**, *11*, 123–133.
- (24) Murphy, F.; Sheehan, B.; Mullins, M.; et al. A Tractable Method for Measuring Nanomaterial Risk Using Bayesian Networks. *Nanoscale Res. Lett.* **2016**, *11*, S03.
- (25) Sheehan, B.; Murphy, F.; Mullins, M.; Furchi, I.; Costa, A.; Simeone, F.; Mantecca, P. Hazard Screening Methods for Nanomaterials: A Comparative Study. *Int. J. Mol. Sci.* **2018**, *19*, 649.
- (26) Furchi, I.; Murphy, F.; Sheehan, B.; Mullins, M.; Mantecca, P. *Bayesian Networks Application for the Prediction of Cellular Effects from Genome-wide Transcriptomics Studies of Exposure to Nanoparticles*; University of Limerick, 2019.
- (27) Furchi, I.; Murphy, F.; Mullins, M.; Arvanitis, A.; Poland, C. A. Nanotoxicology data for in silico tools: a literature review. *Nanotoxicology* **2020**, *14*, 612–637.
- (28) Letham, B.; Rudin, C.; McCormick, T. H.; Madigan, D. Interpretable classifiers using rules and Bayesian analysis: Building a better stroke prediction model. *Ann. Appl. Stat.* **2015**, *9*, 1350–1371.
- (29) Wang, T.; Rudin, C.; Doshi-Velez, F.; Liu, Y.; Klampfl, E.; MacNeille, P. A Bayesian Framework for Learning Rule Sets for Interpretable Classification. *J. Mach. Learn. Res.* **2017**, *18*, 1–37.

- (30) Bilal, M.; Oh, E.; Liu, R.; Breger, J. C.; Medintz, I. L.; Cohen, Y. Bayesian Network Resource for Meta-Analysis: Cellular Toxicity of Quantum Dots. *Small* **2019**, *15*, 1900510.
- (31) Costa, A. L. Applying Safety by Molecular Design Concepts to Nanomaterials Risk Management. In *Managing Risk in Nanotechnology: Topics in Governance, Assurance and Transfer*; Murphy, F., McAlea, E. M., Mullins, M., Eds.; Springer International Publishing: Cham, 2016; pp 171–195.
- (32) Gardini, D.; Blosi, M.; Ortelli, S.; Delpivo, C.; Bussolati, O.; Bianchi, M. G.; Allegri, M.; Bergamaschi, E.; Costa, A. L. Nanosilver: An innovative paradigm to promote its safe and active use. *NanoImpact* **2018**, *11*, 128–135.
- (33) Marassi, V.; Di Cristo, L.; Smith, S. G. J.; Ortelli, S.; Blosi, M.; Costa, A. L.; Reschiglian, P.; Volkov, Y.; Prina-Mello, A. Silver nanoparticles as a medical device in healthcare settings: a five-step approach for candidate screening of coating agents. *R. Soc. Open Sci.* **2018**, *5*, 171113.
- (34) Costa, A. L.; Blosi, M.; Brigladori, A.; Zanon, I.; Ortelli, S.; Simeone, F. C.; Delbue, S.; D'Alessandro, S.; Parapini, S.; Vineis, C.; Varesano, A.; Toprak, M. S.; Hamawandi, B.; Gardini, D. Eco design for Ag-based solutions against SARS-CoV-2 and E. coli. *Environ. Sci.: Nano* **2022**, *9*, 4295–4304.
- (35) van Rijn, J.; Afantitis, A.; Culha, M.; Dusinska, M.; Exner, T. E.; Jeliakova, N.; Longhin, E. M.; Lynch, I.; Melagraki, G.; Nymark, P.; Papadimitriou, A. G.; Winkler, D. A.; Yilmaz, H.; Willighagen, E. European Registry of Materials: global, unique identifiers for (undisclosed) nanomaterials. *J. Cheminf.* **2022**, *14*, 57.
- (36) Blosi, M.; Albonetti, S.; Ortelli, S.; Costa, A. L.; Ortolani, L.; Dondi, M. Green and easily scalable microwave synthesis of noble metal nanosols (Au, Ag, Cu, Pd) usable as catalysts. *New J. Chem.* **2014**, *38*, 1401–1409.
- (37) Blosi, M.; Albonetti, S.; Dondi, M.; Martelli, C.; Baldi, G. Microwave-assisted polyol synthesis of Cu nanoparticles. *J. Nanoparticle Res.* **2011**, *13*, 127–138.
- (38) Yang, X. X.; Li, C. M.; Huang, C. Z. Curcumin modified silver nanoparticles for highly efficient inhibition of respiratory syncytial virus infection. *Nanoscale* **2016**, *8*, 3040–3048.
- (39) ECHA Appendix for Nanofoms Applicable to the Guidance on Registration and Substance Identification, 2022.
- (40) Wyrzykowska, E.; Mikolajczyk, A.; Lynch, I.; Jeliakova, N.; Kochev, N.; Sarimveis, H.; Dogan, P.; Karatzas, P.; Afantitis, A.; Melagraki, G.; Serra, A.; Greco, D.; Subbotina, J.; Lobaskin, V.; Bañares, M. A.; Valsami-Jones, E.; Jagiello, K.; Puzyn, T. Representing and describing nanomaterials in predictive nanoinformatics. *Nat. Nanotechnol.* **2022**, *17*, 924–932.
- (41) Andrade, J. D. X-ray Photoelectron Spectroscopy (XPS). *Surface and Interfacial Aspects of Biomedical Polymers: Volume 1 Surface Chemistry and Physics*; Andrade, J. D., Ed.; Springer US: Boston, MA, 1985; pp 105–195.
- (42) Epp, J. X-ray diffraction (XRD) techniques for materials characterization. *Materials Characterization Using Nondestructive Evaluation (NDE) Methods*; Hübschen, G.; Altpeter, I.; Tschuncky, R.; Herrmann, H.-G., Eds.; Woodhead Publishing, 2016; pp 81–124.
- (43) Dusinska, M.; Tulinska, J.; El Yamani, N.; Kuricova, M.; Liskova, A.; Rollovera, E.; Rundén-Pran, E.; Smolkova, B. Immunotoxicity, genotoxicity and epigenetic toxicity of nanomaterials: New strategies for toxicity testing? *Food Chem. Toxicol.* **2017**, *109*, 797–811.
- (44) Riaz Ahmed, K. B.; Nagy, A. M.; Brown, R. P.; Zhang, Q.; Malghan, S. G.; Goering, P. L. Silver nanoparticles: Significance of physicochemical properties and assay interference on the interpretation of in vitro cytotoxicity studies. *Toxicol. in Vitro* **2017**, *38*, 179–192.
- (45) Rasmussen, K.; Rauscher, H.; Mech, A.; Riego Sintes, J.; Gilliland, D.; González, M.; Kearns, P.; Moss, K.; Visser, M.; Groenewold, M.; Bleeker, E. A. J. Physico-chemical properties of manufactured nanomaterials - Characterisation and relevant methods. An outlook based on the OECD Testing Programme. *Regul. Toxicol. Pharmacol.* **2018**, *92*, 8–28.
- (46) Johnston, S. T.; Faria, M.; Crampin, E. J. An analytical approach for quantifying the influence of nanoparticle polydispersity on cellular delivered dose. *J. R. Soc., Interface* **2018**, *15*, 20180364.
- (47) Maiorano, G.; Sabella, S.; Sorce, B.; Brunetti, V.; Malvindi, M. A.; Cingolani, R.; Pompa, P. P. Effects of Cell Culture Media on the Dynamic Formation of Protein–Nanoparticle Complexes and Influence on the Cellular Response. *ACS Nano* **2010**, *4*, 7481–7491.
- (48) Martin, A.; Sarkar, A. Overview on biological implications of metal oxide nanoparticle exposure to human alveolar A549 cell line. *Nanotoxicology* **2017**, *11*, 713–724.
- (49) Schlinkert, P.; Casals, E.; Boyles, M.; Tischler, U.; Hornig, E.; Tran, N.; Zhao, J.; Himly, M.; Riediker, M.; Oostingh, G. J.; Puentes, V.; Duschl, A. The oxidative potential of differently charged silver and gold nanoparticles on three human lung epithelial cell types. *J. Nanobiotechnol.* **2015**, *13*, 1.
- (50) Brito, S. D. C.; Bresolin, J. D.; Sivieri, K.; Ferreira, M. D. Low-density polyethylene films incorporated with silver nanoparticles to promote antimicrobial efficiency in food packaging. *Food Sci. Technol.* **2020**, *26*, 353–366.
- (51) Böhmert, L.; Girod, M.; Hansen, U.; Maul, R.; Knappe, P.; Niemann, B.; Weidner, S. M.; Thünemann, A. F.; Lampen, A. Analytically monitored digestion of silver nanoparticles and their toxicity on human intestinal cells. *Nanotoxicology* **2014**, *8*, 631.
- (52) Antonello, G.; Marucco, A.; Gazzano, E.; Kainourgiou, P.; Ravagli, C.; Gonzalez-Paredes, A.; Sprio, S.; Padín-González, E.; Soliman, M. G.; Beal, D.; Barbero, F.; Gasco, P.; Baldi, G.; Carriere, M.; Monopoli, M. P.; Charitidis, C. A.; Bergamaschi, E.; Fenoglio, I.; Riganti, C. Changes of physico-chemical properties of nanomaterials by digestion fluids affect the physiological properties of epithelial intestinal cells and barrier models. *Part. Fibre Toxicol.* **2022**, *19*, 49.
- (53) Ault, A. P.; Stark, D. I.; Axson, J. L.; Keeney, J. N.; Maynard, A. D.; Bergin, I. L.; Philbert, M. A. Protein corona-induced modification of silver nanoparticle aggregation in simulated gastric fluid. *Environ. Sci.: Nano* **2016**, *3*, 1510–1520.
- (54) Laloux, L.; Kastrati, D.; Cambier, S.; Gutleb, A. C.; Schneider, Y.-J. The Food Matrix and the Gastrointestinal Fluids Alter the Features of Silver Nanoparticles. *Small* **2020**, *16*, 1907687.
- (55) Sohal, I. S.; Cho, Y. K.; O'Fallon, K. S.; Gaines, P.; Demokritou, P.; Bello, D. Dissolution Behavior and Biodurability of Ingested Engineered Nanomaterials in the Gastrointestinal Environment. *ACS Nano* **2018**, *12*, 8115–8128.
- (56) Marucco, A.; Prono, M.; Beal, D.; Alasonati, E.; Fisicaro, P.; Bergamaschi, E.; Carriere, M.; Fenoglio, I. Biotransformation of Food-Grade and Nanometric TiO₂ in the Oral-Gastro-Intestinal Tract: Driving Forces and Effect on the Toxicity toward Intestinal Epithelial Cells. *Nanomaterials* **2020**, *10*, 2132.
- (57) Jia, M.; Zhang, W.; He, T.; Shu, M.; Deng, J.; Wang, J.; Li, W.; Bai, J.; Lin, Q.; Luo, F.; Zhou, W.; Zeng, X. Evaluation of the Genotoxic and Oxidative Damage Potential of Silver Nanoparticles in Human NCM460 and HCT116 Cells. *Int. J. Mol. Sci.* **2020**, *21*, 1618.
- (58) Stone, V.; Johnston, H.; Schins, R. P. Development of in vitro systems for nanotoxicology: methodological considerations. *Crit. Rev. Toxicol.* **2009**, *39*, 613–626.
- (59) Hillegass, J. M.; Shukla, A.; Lathrop, S. A.; MacPherson, M. B.; Fukagawa, N. K.; Mossman, B. T. Assessing nanotoxicity in cells in vitro. *Wiley Interdiscip. Rev.: Nanomed. Nanobiotechnol.* **2010**, *2*, 219–231.
- (60) Hamid, R.; Rotshteyn, Y.; Rabadi, L.; Parikh, R.; Bullock, P. Comparison of alamar blue and MTT assays for high through-put screening. *Toxicol. Vitro* **2004**, *18*, 703–710.
- (61) Longhin, E. M.; El Yamani, N.; Rundén-Pran, E.; Dusinska, M. The alamar blue assay in the context of safety testing of nanomaterials. *Front. Toxicol.* **2022**, *4*, 981701.
- (62) Li, H. Missing Values Imputation Based on Iterative Learning. *Int. J. Intell. Sci.* **2013**, *03*, 50.
- (63) Fazakis, N.; Kostopoulos, G.; Kotsiantis, S.; Mporas, I. Iterative Robust Semi-Supervised Missing Data Imputation. *IEEE Access* **2020**, *8*, 90555–90569.

- (64) Cassel, M.; Lima, F. Evaluating one-hot encoding finite state machines for SEU reliability in SRAM-based FPGAs, *12th IEEE International On-Line Testing Symposium (IOLTS'06)*, 10–12 July 2006, 2006; p 6.
- (65) Chawla, N. V.; Bowyer, L. O.; Hall, K. W.; Kegelmeyer, W. P. SMOTE: Synthetic Minority Over-sampling Technique. *J. Artif. Intell. Res.* **2002**, *16*, 321–357.
- (66) McInnes, L.; Healy, J.; Melville, J. UMAP: Uniform Manifold Approximation and Projection for Dimension Reduction. **2018**, arXiv:1802.03426.
- (67) Cao, J.; Spielmann, M.; Qiu, X.; Huang, X.; Ibrahim, D. M.; Hill, A. J.; Zhang, F.; Mundlos, S.; Christiansen, L.; Steemers, F. J.; Trapnell, C.; Shendure, J. The single-cell transcriptional landscape of mammalian organogenesis. *Nature* **2019**, *566*, 496–502.
- (68) Singh, G. K. C.; Mémoli, F.; Carlsson, G. E. *Topological Methods for the Analysis of High Dimensional Data Sets and 3D Object Recognition*; PBG@Eurographics, 2007.
- (69) He, Y.; Tan, H.; Luo, W.; Mao, H.; Ma, D.; Feng, S.; Fan, J. MR-DBSCAN: An Efficient Parallel Density-Based Clustering Algorithm Using MapReduce. *2011 IEEE 17th International Conference on Parallel and Distributed Systems*, 7–9 Dec 2011, 2011; pp 473–480.
- (70) Hauke, J.; Kossowski, T. Comparison of Values of Pearson's and Spearman's Correlation Coefficients on the Same Sets of Data. *Quaest. Geogr.* **2011**, *30*, 87–93.
- (71) Akoglu, H. User's guide to correlation coefficients. *Turk. J. Emerg. Med.* **2018**, *18*, 91–93.
- (72) Gain, U.; Hotti, V. Low-code AutoML-augmented Data Pipeline - A Review and Experiments. *J. Phys.: Conf. Ser.* **2021**, *1828*, 012015.
- (73) Zabinski, J. W.; Garcia-Vargas, G.; Rubio-Andrade, M.; Fry, R. C.; Gibson, J. M. Advancing Dose-Response Assessment Methods for Environmental Regulatory Impact Analysis: A Bayesian Belief Network Approach Applied to Inorganic Arsenic. *Environ. Sci. Technol. Lett.* **2016**, *3*, 200–204.
- (74) Zabinski, J. W.; Pieper, K. J.; Gibson, J. M. A Bayesian Belief Network Model Assessing the Risk to Wastewater Workers of Contracting Ebola Virus Disease During an Outbreak. *Risk Anal.* **2017**, *38*, 376.
- (75) Friedman, N.; Linal, M.; Nachman, I.; Pe'er, D. Using Bayesian networks to analyze expression data. *J. Comput. Biol.* **2000**, *7*, 601.
- (76) Schreiber, J. Pomegranate: fast and flexible probabilistic modeling in python. *J. Mach. Learn. Res.* **2018**, *18*, 1.
- (77) Gopalakrishnan, V.; Lustgarten, J. L.; Visweswaran, S.; Cooper, G. F. Bayesian rule learning for biomedical data mining. *Bioinformatics* **2010**, *26*, 668–675.
- (78) Yuan, C.; Lim, H.; Lu, T.-C. Most Relevant Explanation in Bayesian Networks. *J. Artif. Intell. Res.* **2011**, *42*, 309–352.
- (79) OECD *Guidance Document on the Validation of (Quantitative) Structure-Activity Relationship [(Q)SAR] Models*, 2014.
- (80) Puzyn, T.; Jeliakova, N.; Sarimveis, H.; Marchese Robinson, R. L.; Lobaskin, V.; Rallo, R.; Richarz, A. N.; Gajewicz, A.; Papadopoulos, M. G.; Hastings, J.; Cronin, M. T. D.; Benfenati, E.; Fernández, A. Perspectives from the NanoSafety Modelling Cluster on the validation criteria for (Q)SAR models used in nanotechnology. *Food Chem. Toxicol.* **2018**, *112*, 478–494.
- (81) Grandini, M.; Bagli, E.; Visani, G. J. A. Metrics for Multi-Class Classification: an Overview. **2020**, arXiv:2008.05756.
- (82) Carey, A.; Wu, X. The Fairness Field Guide: Perspectives from Social and Formal Sciences. **2022**, arXiv:2201.05216
- (83) George, D.; Mallery, P. *SPSS for Windows Step-by-step: A Simple Guide and Reference, 14.0 Update*, 7th ed.; Pearson Education, 2003; [http://lst-iiiep.iiep-unesco.org/cgi-bin/wwwi32.exe/\[in=epidoc1.in\]/?t2000=026564/\(100\)](http://lst-iiiep.iiep-unesco.org/cgi-bin/wwwi32.exe/[in=epidoc1.in]/?t2000=026564/(100)).
- (84) Furchi, I.; Murphy, F.; Poland, C. A.; Sheehan, B.; Mullins, M.; Mantecca, P. Application of Bayesian networks in determining nanoparticle-induced cellular outcomes using transcriptomics. *Nanotoxicology* **2019**, *13*, 827–848.
- (85) Furchi, I. Health and environmental safety of nanomaterials: O Data, Where Art Thou? *NanoImpact* **2022**, *25*, 100378.
- (86) Fouad, K. M.; Ismail, M. M.; Azar, A. T.; Arafa, M. M. Advanced methods for missing values imputation based on similarity learning. *PeerJ Comput. Sci.* **2021**, *7*, No. e619.
- (87) Nikfalazar, S.; Yeh, C.-H.; Bedingfield, S.; Khorshidi, H. A. Missing data imputation using decision trees and fuzzy clustering with iterative learning. *Knowl. Inf. Syst.* **2020**, *62*, 2419–2437.
- (88) Lustgarten, J. L.; Visweswaran, S.; Gopalakrishnan, V.; Cooper, G. F. Application of an efficient Bayesian discretization method to biomedical data. *BMC Bioinf.* **2011**, *12*, 309.
- (89) Nohara, Y.; Matsumoto, K.; Soejima, H.; Nakashima, N. Explanation of machine learning models using shapley additive explanation and application for real data in hospital. *Comput. Methods Progr. Biomed.* **2022**, *214*, 106584.
- (90) Mirzaei, M.; Furchi, I.; Murphy, F.; Mullins, M. A machine learning tool to predict the antibacterial capacity of nanoparticles. *Nanomaterials* **2021**, *11*, 1774.
- (91) Mirzaei, M.; Furchi, I.; Murphy, F.; Mullins, M. A Supervised Machine-Learning Prediction of Textile's Antimicrobial Capacity Coated with Nanomaterials. *Coatings* **2021**, *11*, 1532.
- (92) Furchi, I.; Murphy, F.; Mullins, M.; Poland, A. Machine learning prediction of nanoparticle in vitro toxicity: A comparative study of classifiers and ensemble-classifiers using the Copeland Index. *Toxicol. Lett.* **2019**, *312*, 157–166.
- (93) Geurts, P.; Ernst, D.; Wehenkel, L. Extremely randomized trees. *Mach. Learn.* **2006**, *63*, 3–42.
- (94) Forest, V. Experimental and Computational Nanotoxicology-Complementary Approaches for Nanomaterial Hazard Assessment. *Nanomaterials* **2022**, *12*, 1346.
- (95) Atienza, D.; Bielza, C.; Larrañaga, P. PyBNesian: An extensible python package for Bayesian networks. *Neurocomputing* **2022**, *504*, 204–209.
- (96) Marvin, H. J. P.; Bouzembrak, Y.; Janssen, E. M.; van der Zande, M.; Murphy, F.; Sheehan, B.; Mullins, M.; Bouwmeester, H. Application of Bayesian networks for hazard ranking of nanomaterials to support human health risk assessment. *Nanotoxicology* **2017**, *11*, 123–133.
- (97) Furchi, I.; Murphy, F.; Mullins, M.; Poland, C. A. Machine learning prediction of nanoparticle in vitro toxicity: A comparative study of classifiers and ensemble-classifiers using the Copeland Index. *Toxicol. Lett.* **2019**, *312*, 157–166.

Data-Driven Quantitative Intrinsic Hazard Criteria for Nanoproduct Development in a Safe-by-Design Paradigm: A Case Study of Silver Nanoforms.

*Irini Furxhi^{*1,2}, Rossella Bengalli³, Giulia Motta³, Paride Mantecca³, Ozge Kose⁴, Marie Carriere⁴, Ehtsham Ul Haq⁵, Charlie O'Mahony⁵, Magda Blosi⁶, Davide Gardini⁶ and Anna Costa⁶*

¹Transgero Ltd, Limerick, V42V384, Ireland.

²Dept. of Accounting and Finance, Kemmy Business School, University of Limerick, V94T9PX, Ireland.

³ University of Milano-Bicocca, Dept. of Earth and Environmental Sciences, Piazza della Scienza 1, 20126 Milano , Italy

⁴Univ. Grenoble Alpes, CEA, CNRS, Grenoble INP, IRIG, SYMMES, 38000 Grenoble, France

⁵Department of Physics, and Bernal Institute, University of Limerick, Limerick V94T9PX, Ireland

⁶Istituto di Scienza e Tecnologia dei Materiali Ceramici (CNR-ISTEC), Via Granarolo, 64, 48018 Faenza RA, Italy

*Correspondence: irini.furxhi@transgero.eu, irini.furxhi@ul.ie. Tel: +353 85 106 9771

Experimental Section

1 Data Preprocessing

1.1 Attribute selection

Information gain analysis of the training dataset (80%) based on average impurity decrease (and number of nodes using that attribute). Search Method: Attribute ranking. Attribute Evaluator (supervised, Class (nominal): 16 viability): Information Gain Ranking Filter. Selected attributes: 9,11,10,12,13,6,3,7,2,4,8,5,1,15,14.

Table S1- Attribute Selection.

Information Gain		Ranked attributes
0.656963	9	Hydro_size_t0_nm
0.647354	11	Hydro_size_t24_nm
0.582135	10	PI_t0
0.573924	12	PI_t24
0.565378	13	Exposure_dose_PPM
0.153672	6	O_1s_Concent_%
0.153672	3	Aver_crystallite_sizes_nm
0.153672	7	Ag_3d_Concent_%
0.153672	2	Crystallinity_%
0.150748	4	Core_size
0.146015	8	C_1s_Concent_%
0.107264	5	Spherical_surface_Area_nm^2_TEM
0.098697	1	Coating
0.069231	15	Assay
0.00051	14	Cell_line

1.2 Correlation Analysis

The Pearson's correlation coefficient (r) is a measure of linear correlation between two variables. It's value lies between -1 and $+1$, -1 indicating total negative linear correlation, 0 indicating no linear correlation and 1 indicating total positive linear correlation. Furthermore, r is invariant under separate changes in location and scale of the two variables, implying that for a linear function the angle to the x -axis does not affect r .

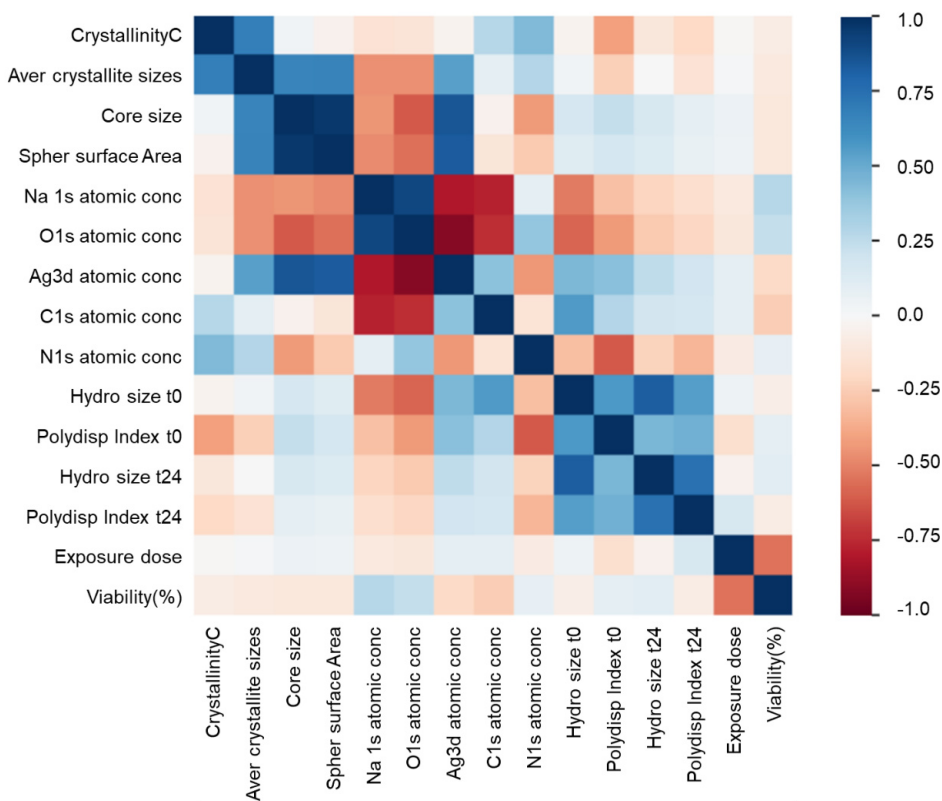


Figure S1- Pearson r correlation.

2 QSAR development and Validation

2.1 Regression algorithms

QSAR models trained either as regression or classification ML tasks, are able to predict cellular viability with satisfactory results. Additional algorithms with their internal 10-fold cross validation, hyper parameterization and external performance metrics.

Table S2- Additional regression algorithms external predictivity performances metrics. Regression algorithms are derived from PyCaret library.

	Model	MAE	MSE	RMSE	R2	RMSLE	MAPE	TT (Sec)
rf	Random Forest Regressor	1.277600e+01	3.874638e+02	1.955080e+01	7.053000e-01	0.8154	3.369500e+00	1.657
lightgbm	Light Gradient Boosting Machine	1.291420e+01	3.952788e+02	1.971850e+01	7.000000e-01	0.8147	3.268300e+00	0.212
gbr	Gradient Boosting Regressor	1.417130e+01	4.120250e+02	2.018230e+01	6.875000e-01	0.8601	3.445100e+00	0.406
et	Extra Trees Regressor	1.265830e+01	4.220538e+02	2.035510e+01	6.784000e-01	0.8292	3.334900e+00	1.123
dt	Decision Tree Regressor	1.352500e+01	5.156505e+02	2.256230e+01	6.064000e-01	0.8843	3.324700e+00	0.046
ada	AdaBoost Regressor	1.757810e+01	5.262554e+02	2.292110e+01	6.010000e-01	0.9418	3.740200e+00	0.073
ridge	Ridge Regression	1.752050e+01	5.373334e+02	2.310810e+01	5.924000e-01	1.0021	3.595300e+00	0.053
br	Bayesian Ridge	1.767000e+01	5.426961e+02	2.322050e+01	5.885000e-01	1.0093	3.674800e+00	0.046
lasso	Lasso Regression	1.846020e+01	5.711001e+02	2.382630e+01	5.681000e-01	1.0228	3.890700e+00	0.075
knn	K Neighbors Regressor	1.627680e+01	5.909606e+02	2.424100e+01	5.548000e-01	0.9469	4.405700e+00	0.065
en	Elastic Net	1.950880e+01	6.404212e+02	2.521680e+01	5.167000e-01	1.0267	4.475900e+00	0.090
omp	Orthogonal Matching Pursuit	2.041900e+01	6.621426e+02	2.568250e+01	4.971000e-01	1.1234	4.110000e+00	0.036
lr	Linear Regression	1.915100e+01	6.833052e+02	2.563940e+01	4.862000e-01	1.0358	3.684100e+00	0.030
huber	Huber Regressor	2.626660e+01	1.183424e+03	3.429290e+01	1.029000e-01	1.1137	4.961900e+00	0.307
llar	Lasso Least Angle Regression	3.208570e+01	1.347116e+03	3.667230e+01	-1.860000e-02	1.3682	7.244700e+00	0.026
dummy	Dummy Regressor	3.208570e+01	1.347116e+03	3.667230e+01	-1.860000e-02	1.3682	7.244700e+00	0.005
par	Passive Aggressive Regressor	1.410491e+02	4.597176e+04	1.845018e+02	-3.388820e+01	2.0405	2.633870e+01	0.024
lar	Least Angle Regression	7.576682e+08	6.058722e+20	8.153330e+09	-4.371112e+17	9.6370	6.391748e+08	0.053

Table S3- Internal 10-fold validation of lightgbm regression algorithm (left) and hyperparameters tuning (right) results.

	MAE	MSE	RMSE	R2	RMSLE	MAPE		MAE	MSE	RMSE	R2	RMSLE	MAPE
Fold							Fold						
0	13.0210	362.8833	19.0495	0.6939	0.6374	1.0460	0	13.3310	361.6793	19.0179	0.6949	0.6262	1.1164
1	11.9836	327.1305	18.0867	0.7648	0.8972	3.2214	1	11.8613	307.3331	17.5309	0.7790	0.8991	3.0610
2	12.6223	386.5662	19.6613	0.6944	0.8521	3.2695	2	12.7953	397.2119	19.9302	0.6860	0.8678	3.1065
3	10.8628	231.2104	15.2056	0.8480	0.7137	1.5745	3	10.9606	243.4240	15.6021	0.8399	0.7172	1.5383
4	10.3974	268.6802	16.3915	0.8230	0.6744	1.3669	4	11.0776	283.5458	16.8388	0.8132	0.6833	1.3283
5	12.9043	472.9354	21.7471	0.6776	0.9504	3.6544	5	12.9984	429.9490	20.7352	0.7069	0.8982	3.3964
6	15.2028	610.9565	24.7175	0.5585	1.0391	4.9407	6	14.7015	523.7986	22.8866	0.6215	1.0192	4.5988
7	13.0543	378.5734	19.4570	0.7176	0.6915	1.4132	7	12.5535	337.8803	18.3815	0.7480	0.7090	1.3543
8	13.6376	406.4968	20.1618	0.6919	0.7040	2.4023	8	14.1569	434.6923	20.8493	0.6705	0.7560	2.5743
9	11.5706	355.9808	18.8675	0.7255	0.6983	1.9183	9	11.3882	328.3799	18.1213	0.7468	0.6792	1.8345
Mean	12.5257	380.1413	19.3345	0.7195	0.7858	2.4807	Mean	12.5824	364.7894	18.9894	0.7307	0.7855	2.3909
Std	1.3260	100.4592	2.5133	0.0768	0.1307	1.1909	Std	1.2079	78.8404	2.0477	0.0641	0.1206	1.0838

2.2 Classification algorithms

Table S4- Additional classification algorithms external predictivity performances metrics. Classification algorithms are derived from PyCaret library.

	Model	Accuracy	AUC	Recall	Prec.	F1	Kappa	MCC	TT (Sec)
et	Extra Trees Classifier	0.8530	0.9352	0.8503	0.8560	0.8527	0.7781	0.7798	1.120
rf	Random Forest Classifier	0.8463	0.9489	0.8428	0.8503	0.8456	0.7678	0.7701	1.552
lightgbm	Light Gradient Boosting Machine	0.8403	0.9478	0.8370	0.8439	0.8397	0.7586	0.7608	0.286
gbc	Gradient Boosting Classifier	0.8267	0.9475	0.8221	0.8290	0.8253	0.7381	0.7403	0.749
dt	Decision Tree Classifier	0.8199	0.8969	0.8157	0.8257	0.8195	0.7278	0.7307	0.020
knn	K Neighbors Classifier	0.7757	0.9114	0.7728	0.7837	0.7761	0.6610	0.6637	0.057
ada	Ada Boost Classifier	0.7367	0.8333	0.7359	0.7440	0.7377	0.6041	0.6061	0.183
lda	Linear Discriminant Analysis	0.6814	0.8585	0.6728	0.6813	0.6763	0.5189	0.5228	0.035
ridge	Ridge Classifier	0.6602	0.0000	0.6457	0.6546	0.6377	0.4825	0.4961	0.030
lr	Logistic Regression	0.6380	0.8127	0.6294	0.6403	0.6296	0.4512	0.4580	0.815
nb	Naive Bayes	0.5718	0.7754	0.5762	0.5869	0.5709	0.3608	0.3660	0.019
svm	SVM - Linear Kernel	0.4875	0.0000	0.4788	0.4683	0.4150	0.2233	0.2527	0.116
qda	Quadratic Discriminant Analysis	0.3764	0.5000	0.3333	0.1417	0.2059	0.0000	0.0000	0.017
dummy	Dummy Classifier	0.3764	0.5000	0.3333	0.1417	0.2059	0.0000	0.0000	0.012

Table S5- Internal 10-fold validation of *lightgbm* classification algorithm (left) and hyperparameters tuning (right) results.

	Accuracy	AUC	Recall	Prec.	F1	Kappa	MCC		Accuracy	AUC	Recall	Prec.	F1	Kappa	MCC
Fold								Fold							
0	0.8475	0.9423	0.8471	0.8492	0.8480	0.7708	0.7711	0	0.7881	0.9275	0.7899	0.7995	0.7890	0.6824	0.6869
1	0.8475	0.9488	0.8454	0.8527	0.8477	0.7703	0.7727	1	0.8475	0.9348	0.8471	0.8480	0.8471	0.7707	0.7713
2	0.7627	0.9353	0.7645	0.7637	0.7615	0.6442	0.6457	2	0.7966	0.9286	0.7967	0.7980	0.7970	0.6948	0.6951
3	0.8136	0.9446	0.8086	0.8117	0.8081	0.7191	0.7229	3	0.7627	0.9368	0.7580	0.7584	0.7590	0.6430	0.6443
4	0.8644	0.9577	0.8625	0.8738	0.8660	0.7957	0.7990	4	0.8051	0.9561	0.8040	0.8148	0.8070	0.7068	0.7092
5	0.7627	0.9325	0.7616	0.7697	0.7645	0.6434	0.6447	5	0.7881	0.9332	0.7881	0.8017	0.7917	0.6825	0.6853
6	0.8475	0.9525	0.8449	0.8532	0.8479	0.7703	0.7727	6	0.8475	0.9463	0.8452	0.8548	0.8470	0.7705	0.7741
7	0.8803	0.9663	0.8774	0.8800	0.8782	0.8201	0.8218	7	0.8120	0.9300	0.8094	0.8110	0.8103	0.7174	0.7184
8	0.7863	0.9425	0.7863	0.7845	0.7848	0.6793	0.6798	8	0.8034	0.9409	0.8021	0.8026	0.8024	0.7045	0.7051
9	0.8632	0.9635	0.8589	0.8669	0.8612	0.7938	0.7976	9	0.8547	0.9638	0.8542	0.8591	0.8560	0.7814	0.7822
Mean	0.8276	0.9486	0.8257	0.8305	0.8268	0.7407	0.7428	Mean	0.8106	0.9398	0.8095	0.8148	0.8106	0.7154	0.7172
Std	0.0411	0.0108	0.0401	0.0420	0.0412	0.0615	0.0620	Std	0.0287	0.0116	0.0290	0.0295	0.0291	0.0430	0.0428

3 Bayesian Network Structure Learning

3.1 Unconstrained– Python

For the development of the constrained reasoned structured network , expert judgment was applied to conditional dependencies. Some alterations of arcs include: Polydispersity index t24 and hydrodynamic size t0,t24 features were parents to exposure dose in the unconstrained structure built with the exact algorithm and no constraints in the parents relationships, however such a dependency is not realistic i.e., the external exposure dose can not be determined by the hydrodynamic size; However, the exposure dose did fed the cell viability node, which is kept in the constrained structure, eliminating the other relationships.

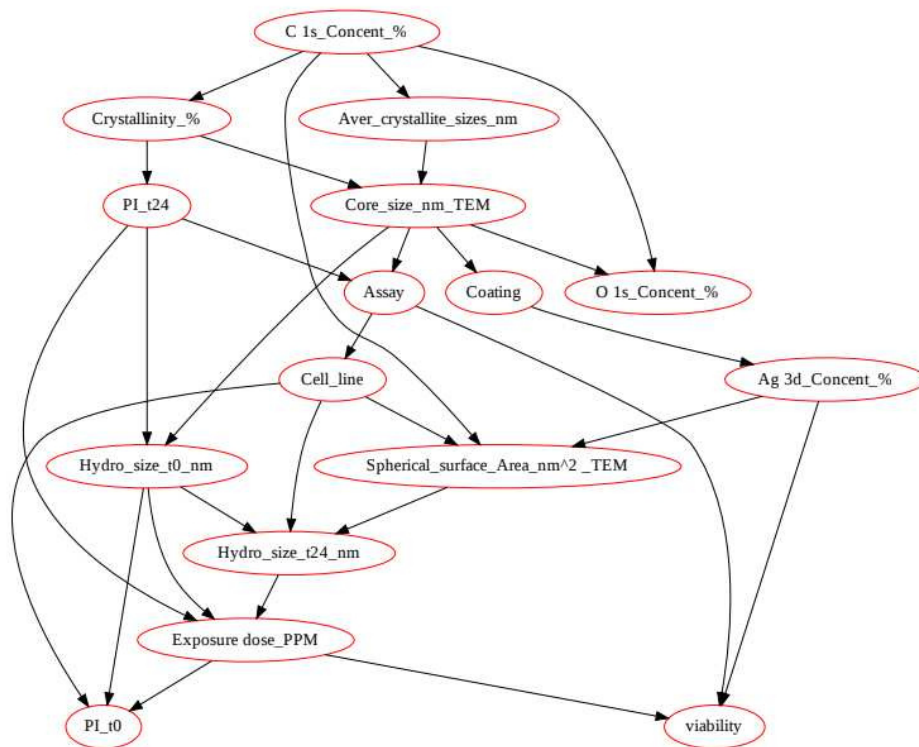


Figure S2- Unconstrained Bayesian Network Structure.

3.2 Unconstrained– Weka

Exploring the Weka software for automated BN construction (estimator: simple, $a=0.5$, search algorithm: local hill climber, six parents limit configuration), the unconstrained structure also demonstrated the exposure dose, hydrodynamic size at t24, core size and assay being connected to the outcome, reinforcing the reasoning on some arcs.

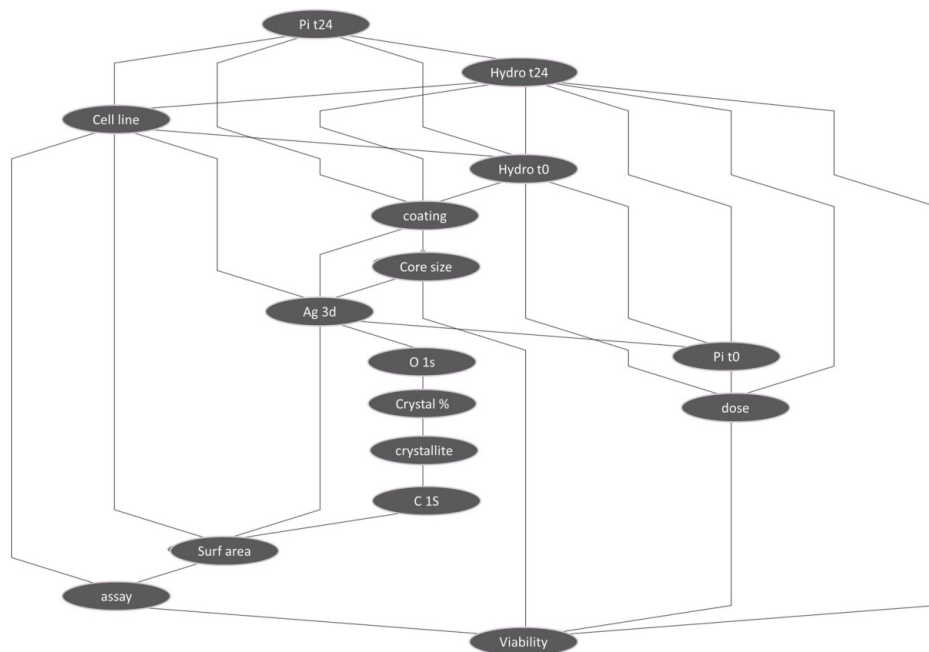


Figure S3- Unconstrained Bayesian structure derived from WEKA software (estimator: simple, $a=0.5$, search algorithm: local hill climber, six parents limit configuration).

Unconstrained Bayesian Network – Weka - Cross validation metrics

=== Stratified cross-validation === [all dataset]

Correctly Classified Instances 1324 78.7158 %

Incorrectly Classified Instances 358 21.2842 %

Total Number of Instances 1682

=== Detailed Accuracy By Class ===

	TP	FP	Prec	Rec	F-1	MCC	ROC	PRC	Class
	0.852	0.12	0.774	0.852	0.811	0.715	0.961	0.931	very toxic
	0.854	0.131	0.785	0.854	0.818	0.711	0.946	0.903	safe
	0.645	0.07	0.809	0.645	0.718	0.615	0.914	0.848	Toxic
Weighted Avg.	0.787	0.108	0.789	0.787	0.784	0.682	0.941	0.894	

=== Confusion Matrix ===

a b c <-- classified as

465 32 49 | a = very_toxic

56 516 32 | b = safe

80 109 343 | c = Toxic

3.3 BN model Validation

Internal Cross validation metrics derived from the constrained BN structure from Python

	precision	recall	f1-score	support
Toxic	0.75	0.69	0.72	427
safe	0.80	0.79	0.79	492
very_toxic	0.80	0.87	0.83	427
accuracy			0.78	1346
macro avg	0.78	0.78	0.78	1346
weighted avg	0.78	0.78	0.78	1346

```

very_toxic
Acc: 0.8665
Acc (balanced): 0.8665

```

```

safe
Acc: 0.7886
Acc (balanced): 0.7886

```

```

Toxic
Acc: 0.6932
Acc (balanced): 0.6932

```

```
MCC: 0.6746025781279282
```

Figure S4- Internal cross validation (80% training data) performance metrics of the constrained BN network.

4 Extra rules derived from the BN constrained structure

The extraction of the interpretable rules related to the quantitative intrinsic hazard properties of AgNFs, was filtered down to the cases where the hazard class was present and with the highest certainty factors (CF) as an example. The higher the CF the higher the posterior probability of that statement / rule to be true. Infinite confidence probabilities, an instance that occurs due to a divide-by-zero runtime exception when comparing the likelihood of events with no counterexamples, were discarded.

- IF (Ag 3d atomic= High (> 15.53) ^ Hydro_size_t0_nm = Medium (209.97 -> 363.31) ^ Cell line = A549) THEN (PI_t24 = Low (0.04 -> 0.28)) 60 0.98
- IF (Hydro_size_t0_nm = Medium (209.97 -> 363.31) ^ PI_t24 = Medium (0.28 -> 0.499763) ^ Cell line = A549) THEN (Hydro_size_t24= Medium (149.34 -> 266.9)) 18 0.94
- IF (Coating = HEC ^ Core size = Low (7.0 -> 17.8) ^ Hydro_size_t24= Low (63.74 -> 149.34)) THEN (Spherical_surface_Area_nm^2_TEM = Low (3981.53 -> 3981.59)) 16.69 0.94
- IF (Ag 3d atomic= Low (0.08 -> 0.19) ^ PI_t0 = Low (0.18 -> 0.47) ^ Cell line = A549) THEN (Hydro_size_t0_nm = Low (55.91 -> 209.97)) 13.5 0.93
- IF (Coating = HEC ^ PI_t24 = Medium (0.28 -> 0.49)) THEN (C 1s_Concent_% = Low (54.23 -> 60.61)) 6.19 0.86

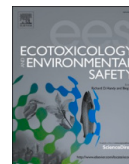
- IF (Ag 3d atomic= High (> 15.53) ^ Hydro_size_t0_nm = High (> 363.315) ^ Cell line = HCT-116) THEN (PI_t24 = High (> 0.499763)) 6 0.85
- IF (Hydro_size_t0_nm = Low (55.91 -> 209.97) ^ PI_t24 = Low (0.04 -> 0.28) ^ Cell line = A549) THEN (Hydro_size_t24= Low (63.74 -> 149.34)) 5.83 0.85
- IF (Ag 3d atomic= High (> 15.53) ^ Hydro_size_t0_nm = Medium (209.97 -> 363.31) ^ Cell line = HCT-116) THEN (PI_t24 = Medium (0.28 -> 0.499763)) 5.61 0.84
- IF (Ag 3d atomic= Low (0.08 -> 0.19) ^ Cell line = A549) THEN (PI_t0 = Low (0.18 -> 0.47)) 4.75 0.82
- IF (Ag 3d atomic= High (> 15.53) ^ Hydro_size_t0_nm = High (> 363.31) ^ Cell line = A549) THEN (PI_t24 = Low (0.04 -> 0.28)) 4 0.8
- IF (Ag 3d atomic= Medium (0.19 -> 15.53) ^ Hydro_size_t0_nm = High (> 363.31) ^ Cell line = A549) THEN (PI_t24 = Low (0.04 -> 0.28)) 3.69 0.78
- IF (Hydro_size_t0_nm = Medium (209.97 -> 363.31) ^ PI_t24 = Medium (0.28 -> 0.499763) ^ Cell line = HCT-116) THEN (Hydro_size_t24= High (> 266.9)) 3.58 0.78
- IF (Hydro_size_t0_nm = Medium (209.97 -> 363.315) ^ PI_t24 = Low (0.04 -> 0.28) ^ Cell line = A549) THEN (Hydro_size_t24= Medium (149.34 -> 266.9)) 3.53 0.77
- IF (Hydro_size_t0_nm = High (> 363.315) ^ PI_t24 = Medium (0.28 -> 0.49) ^ Cell line = HCT-116) THEN (Hydro_size_t24= Medium (149.34 -> 266.9)) 3 0.75
- IF (Ag 3d atomic= Medium (0.19 -> 15.53) ^ Hydro_size_t0_nm = Medium (209.97 -> 363.315) ^ Cell line = A549) THEN (PI_t24 = Medium (0.28 -> 0.499763)) 2.88 0.74
- IF (Hydro_size_t0_nm = Low (55.91 -> 209.97) ^ PI_t24 = Medium (0.28 -> 0.49) ^ Cell line = A549) THEN (Hydro_size_t24= Low (63.74 -> 149.34)) 2.84 0.73
- IF (Ag 3d atomic= Low (0.08 -> 0.19) ^ Cell line = HCT-116) THEN (PI_t0 = High (> 0.59)) 2.68 0.72826087
- IF (Hydro_size_t0_nm = High (> 363.315) ^ PI_t24 = Low (0.04 -> 0.28) ^ Cell line = A549) THEN (Hydro_size_t24= Low (63.74 -> 149.34)) 2.43 0.70
- IF (Ag 3d atomic= High (> 15.53) ^ PI_t0 = High (> 0.59) ^ Cell line = HCT-116) THEN (Hydro_size_t0_nm = Medium (209.97 -> 363.315)) 2.23 0.69
- IF (Hydro_size_t0_nm = High (> 363.315) ^ PI_t24 = Medium (0.28 -> 0.499763) ^ Cell line = A549) THEN (Hydro_size_t24= Low (63.74 -> 149.34)) 2.21 0.68
- IF (Ag 3d atomic= Low (0.08 -> 0.19) ^ PI_t0 = Medium (0.47 -> 0.59) ^ Cell line = HCT-116) THEN (Hydro_size_t0_nm = Low (55.91 -> 209.97)) 2.1 0.67
- IF (Coating = HEC ^ PI_t24 = Low (0.04 -> 0.28)) THEN (C_1s_Concent_% = Medium (60.61 -> 61.83)) 2.02 0.66
- IF (Ag 3d atomic= Medium (0.19 -> 15.53) ^ Cell line = HCT-116) THEN (PI_t0 = High (> 0.59)) 1.97 0.66
- IF (Coating = HEC ^ PI_t24 = High (> 0.49)) THEN (C_1s_Concent_% = Low (54.23 -> 60.61)) 1.94 0.65
- IF (Ag 3d atomic= High (> 15.53) ^ PI_t0 = Medium (0.47 -> 0.59) ^ Cell line = A549) THEN (Hydro_size_t0_nm = Medium (209.97 -> 363.315)) 1.87 0.651567944
- IF (Ag 3d atomic= High (> 15.53) ^ Cell line = A549) THEN (PI_t0 = Low (0.18 -> 0.47)) 1.37 0.57

- IF (Hydro_size_t0_nm = High (> 363.315) ^ PI_t24 = High (> 0.499763) ^ Cell line = HCT-116) THEN (Hydro_size_t24= High (> 266.9)) 1.33 0.57
- IF (Ag_3d_atomic= Medium (0.19 -> 15.53) ^ PI_t0 = Low (0.18 -> 0.47) ^ Cell line = A549) THEN (Hydro_size_t0_nm = Medium (209.97 -> 363.315)) 1.29 0.56
- IF (Ag_3d_atomic= High (> 15.53) ^ Cell line = HCT-116) THEN (PI_t0 = Medium (0.47 -> 0.59)) 1.24 0.55
- IF (Ag_3d_atomic= Medium (0.19 -> 15.53) ^ PI_t0 = Medium (0.47 -> 0.59) ^ Cell line = A549) THEN (Hydro_size_t0_nm = Medium (209.97 -> 363.315)) 1.21 0.54
- IF (Ag_3d_atomic= Medium (0.19 -> 15.53) ^ PI_t0 = High (> 0.59) ^ Cell line = HCT-116) THEN (Hydro_size_t0_nm = High (> 363.315)) 1.18 0.54
- IF (Ag_3d_atomic= Low (0.08 -> 0.19) ^ Hydro_size_t0_nm = Low (55.91 -> 209.97) ^ Cell line = A549) THEN (PI_t24 = Low (0.04 -> 0.28)) 1.16 0.53
- IF (Crystallinity = Low (22.9 -> 60.0) ^ Core size = Low (7.0 -> 17.8) ^ Spherical_surface_Area_nm^2_TEM = Medium (3981.59 -> 5026.55) ^ Ag_3d_atomic= Low (0.08 -> 0.19) ^ Hydro_size_t24= Medium (149.34 -> 266.9) ^ Exposure_dose = Medium (20.0 -> 58.35) ^ Assay = WST-1) THEN (viability = safe) 35 0.97
- IF (Crystallinity = Low (22.9 -> 60.0) ^ Core size = Low (7.0 -> 17.8) ^ Spherical_surface_Area_nm^2_TEM = Low (3981.53 -> 3981.59) ^ Ag_3d_atomic= Low (0.08 -> 0.19) ^ Hydro_size_t24= Low (63.74 -> 149.34) ^ Exposure_dose = Low (0.0 -> 20.0) ^ Assay = MTT) THEN (viability = safe) 33 0.97
- IF (Crystallinity = Low (22.9 -> 60.0) ^ Core size = Low (7.0 -> 17.8) ^ Spherical_surface_Area_nm^2_TEM = Medium (3981.59 -> 5026.55) ^ Ag_3d_atomic= Low (0.08 -> 0.19) ^ Hydro_size_t24= Medium (149.34 -> 266.9) ^ Exposure_dose = Low (0.0 -> 20.0) ^ Assay = WST-1) THEN (viability = safe) 22 0.95
- IF (Crystallinity = Medium (60.0 -> 61.0) ^ Core size = Medium (17.8 -> 20.0) ^ Spherical_surface_Area_nm^2_TEM = Medium (3981.59 -> 5026.55) ^ Ag_3d_atomic= Medium (0.19 -> 15.53) ^ Hydro_size_t24= High (> 266.9) ^ Exposure_dose = Medium (20.0 -> 58.35) ^ Assay = WST-1) THEN (viability = Toxic) 10 0.9
- IF (Crystallinity = Low (22.9 -> 60.0) ^ Core size = High (> 20.0) ^ Spherical_surface_Area_nm^2_TEM = High (> 5026.55) ^ Ag_3d_atomic= High (> 15.53) ^ Hydro_size_t24= Medium (149.34 -> 266.9) ^ Exposure_dose = Low (0.0 -> 20.0) ^ Assay = MTT) THEN (viability = safe) 9.5 0.90
- IF (Crystallinity = High (> 61.0) ^ Core size = Low (7.0 -> 17.8) ^ Spherical_surface_Area_nm^2_TEM = Low (3981.53 -> 3981.59) ^ Ag_3d_atomic= Low (0.08 -> 0.19) ^ Hydro_size_t24= Low (63.74 -> 149.34) ^ Exposure_dose = Low (0.0 -> 20.0) ^ Assay = MTT) THEN (viability = safe) 7.75 0.88
- IF (Crystallinity = High (> 61.0) ^ Core size = Low (7.0 -> 17.8) ^ Spherical_surface_Area_nm^2_TEM = Low (3981.53 -> 3981.59) ^ Ag_3d_atomic= Low (0.08 -> 0.19) ^ Hydro_size_t24= Low (63.74 -> 149.34) ^ Exposure_dose = Medium (20.0 -> 58.35) ^ Assay = MTT) THEN (viability = safe) 7 0.875
- IF (Crystallinity = Medium (60.0 -> 61.0) ^ Core size = Medium (17.8 -> 20.0) ^ Spherical_surface_Area_nm^2_TEM = Medium (3981.59 -> 5026.55) ^ Ag_3d_atomic=

- Medium (0.19 -> 15.53) ^ Hydro_size t24= Low (63.74 -> 149.34) ^ Exposure dose = High (> 58.35) ^ Assay = MTT) THEN (viability = Toxic) 7 0.87*
- *IF (Crystallinity = Low (22.9 -> 60.0) ^ Core size = Low (7.0 -> 17.8) ^ Spherical_surface_Area_nm^2_TEM = Medium (3981.59 -> 5026.55) ^ Ag 3d atomic= Low (0.08 -> 0.19) ^ Hydro_size t24= Medium (149.34 -> 266.9) ^ Exposure dose = Low (0.0 -> 20.0) ^ Assay = Alamar Blue) THEN (viability = very_toxic) 6.67 0.86*
 - *IF (Crystallinity = High (> 61.0) ^ Core size = Low (7.0 -> 17.8) ^ Spherical_surface_Area_nm^2_TEM = Low (3981.53 -> 3981.59) ^ Ag 3d atomic= Low (0.08 -> 0.19) ^ Hydro_size t24= Low (63.74 -> 149.34) ^ Exposure dose = Medium (20.0 -> 58.35) ^ Assay = Alamar Blue) THEN (viability = very_toxic) 6.5 0.86*
 - *IF (Crystallinity = Low (22.9 -> 60.0) ^ Core size = High (> 20.0) ^ Spherical_surface_Area_nm^2_TEM = High (> 5026.55) ^ Ag 3d atomic= High (> 15.53) ^ Hydro_size t24= Medium (149.34 -> 266.9) ^ Exposure dose = Low (0.0 -> 20.0) ^ Assay = Alamar Blue) THEN (viability = very_toxic) 3.57 0.78*
 - *IF (Crystallinity = Low (22.9 -> 60.0) ^ Core size = High (> 20.0) ^ Spherical_surface_Area_nm^2_TEM = High (> 5026.55) ^ Ag 3d atomic= High (> 15.53) ^ Hydro_size t24= Medium (149.34 -> 266.9) ^ Exposure dose = Medium (20.0 -> 58.35) ^ Assay = Alamar Blue) THEN (viability = very_toxic) 3.5 0.77*
 - *IF (Crystallinity = Medium (60.0 -> 61.0) ^ Core size = Medium (17.8 -> 20.0) ^ Spherical_surface_Area_nm^2_TEM = Medium (3981.59 -> 5026.55) ^ Ag 3d atomic= Medium (0.19 -> 15.53) ^ Hydro_size t24= Low (63.74 -> 149.34) ^ Exposure dose = High (> 58.35) ^ Assay = Alamar Blue) THEN (viability = Toxic) 3.17 0.76*
 - *IF (Crystallinity = Medium (60.0 -> 61.0) ^ Core size = Medium (17.8 -> 20.0) ^ Spherical_surface_Area_nm^2_TEM = Medium (3981.59 -> 5026.55) ^ Ag 3d atomic= Medium (0.19 -> 15.53) ^ Hydro_size t24= Low (63.74 -> 149.34) ^ Exposure dose = Medium (20.0 -> 58.35) ^ Assay = MTT) THEN (viability = Toxic) 3.12 0.75*
 - *IF (Crystallinity = High (> 61.0) ^ Core size = Low (7.0 -> 17.8) ^ Spherical_surface_Area_nm^2_TEM = Low (3981.53 -> 3981.59) ^ Ag 3d atomic= Low (0.08 -> 0.19) ^ Hydro_size t24= Low (63.74 -> 149.34) ^ Exposure dose = High (> 58.35) ^ Assay = MTT) THEN (viability = safe) 3 0.75*
 - *IF (Crystallinity = Medium (60.0 -> 61.0) ^ Core size = Medium (17.8 -> 20.0) ^ Spherical_surface_Area_nm^2_TEM = Medium (3981.59 -> 5026.55) ^ Ag 3d atomic= Medium (0.19 -> 15.53) ^ Hydro_size t24= Medium (149.34 -> 266.9) ^ Exposure dose = High (> 58.35) ^ Assay = Alamar Blue) THEN (viability = Toxic) 2.75 0.733*
 - *IF (Crystallinity = Medium (60.0 -> 61.0) ^ Core size = Medium (17.8 -> 20.0) ^ Spherical_surface_Area_nm^2_TEM = Medium (3981.59 -> 5026.55) ^ Ag 3d atomic= Medium (0.19 -> 15.53) ^ Hydro_size t24= Medium (149.34 -> 266.9) ^ Exposure dose = Low (0.0 -> 20.0) ^ Assay = Alamar Blue) THEN (viability = safe) 2.75 0.73*
 - *IF (Crystallinity = Medium (60.0 -> 61.0) ^ Core size = Medium (17.8 -> 20.0) ^ Spherical_surface_Area_nm^2_TEM = Medium (3981.59 -> 5026.55) ^ Ag 3d atomic= Medium (0.19 -> 15.53) ^ Hydro_size t24= Medium (149.34 -> 266.9) ^ Exposure dose = Low (0.0 -> 20.0) ^ Assay = MTT) THEN (viability = safe) 2.2 0.68*

- IF (Crystallinity = Low (22.9 -> 60.0) ^ Core size = Low (7.0 -> 17.8) ^ Spherical_surface_Area_nm^2_TEM = Medium (3981.59 -> 5026.55) ^ Ag 3d atomic= Low (0.08 -> 0.19) ^ Hydro_size t24= Medium (149.34 -> 266.9) ^ Exposure dose = High (> 58.35) ^ Assay = WST-1) THEN (viability = safe) 2.14 0.6815
- IF (Crystallinity = Low (22.9 -> 60.0) ^ Core size = High (> 20.0) ^ Spherical_surface_Area_nm^2_TEM = High (> 5026.55) ^ Ag 3d atomic= High (> 15.53) ^ Hydro_size t24= High (> 266.9) ^ Exposure dose = Medium (20.0 -> 58.35) ^ Assay = WST-1) THEN (viability = Toxic) 2.08 0.67
- IF (Crystallinity = Medium (60.0 -> 61.0) ^ Core size = Medium (17.8 -> 20.0) ^ Spherical_surface_Area_nm^2_TEM = Medium (3981.59 -> 5026.55) ^ Ag 3d atomic= Medium (0.19 -> 15.53) ^ Hydro_size t24= High (> 266.9) ^ Exposure dose = Low (0.0 -> 20.0) ^ Assay = WST-1) THEN (viability = safe) 2 0.66

**ANNEX
III**



Microplastics from miscellaneous plastic wastes: Physico-chemical characterization and impact on fish and amphibian development

Patrizia Bonfanti^{a,1}, Anita Colombo^{a,1}, Melissa Saibene^a, Giulia Motta^a, Francesco Saliu^a, Tiziano Catelani^b, Dora Mehn^c, Rita La Spina^c, Jessica Ponti^c, Claudia Cella^c, Pamela Floris^a, Paride Mantecca^{a,*}

^a Department of Earth and Environmental Sciences, Research Centre POLARIS, University of Milano – Bicocca, Milano, Italy

^b Interdepartmental Microscopy Platform, University of Milano – Bicocca, Milano, Italy

^c European Commission, Joint Research Centre (JRC), Ispra, Italy

ARTICLE INFO

Edited by: Professor Bing Yan

Keywords:

Microplastics
Zebrafish
Xenopus laevis
Developmental toxicity
Chorion
Intestine

ABSTRACT

Microplastic pollution represents a global problem with negative impacts on aquatic environment and organisms' health. To date, most of the laboratory toxicological studies on microplastics (MPs) have made use of single commercial micro and nano-polymers, which do not reflect the heterogeneity of environmental MPs. To improve the relevance of the hazard assessment, micrometer-sized plastic particles of miscellaneous non-reusable waste plastics, with size <100 µm and <50 µm (waste microplastics, wMPs), were characterized by microscopic and spectroscopic techniques and tested on developing zebrafish and *Xenopus laevis* by FET and FETAX assays respectively. Moreover, the modalities of wMP interaction with the embryonic structures, as well as the histological lesions, were explored by light and electron microscopy.

We have shown that wMPs had very heterogeneous shapes and sizes, were mainly composed of polyethylene and polypropylene and contained metal and organic impurities, as well as submicrometric particle fractions, features that resemble those of environmental occurring MPs. wMPs (0.1–100 mg/L) caused low rate of mortality and altered phenotypes in embryos, but established species-specific biointeractions. In zebrafish, wMPs by adhering to chorion were able to delay hatching in a size and concentration dependent manner. In *Xenopus* embryos, which open stomodeum earlier than zebrafish, wMPs were accumulated in intestinal tract, where produced mechanical stress and stimulated mucus overproduction, attesting an irritation response.

Although wMP biointeractions did not interfere with morphogenesis processes, further studies are needed to understand the underlying mechanisms and long-term impact of these, or even smaller, wMPs.

1. Introduction

Microplastics (MPs) have become an emerging concern worldwide for both human and environmental health due to their enormous intentional or unintended release to the environment, particularly in marine and freshwater aquatic systems, where they are accumulated (Auta et al., 2017; Li et al., 2020).

MPs (average particle size 1–5000 µm Ø, GESAMP, 2015) gather together a large variety of organic polymers and include both primary MPs produced for specific commercial purposes (e.g. microbeads in tooth paste or cosmetics, Cole et al., 2011; Fendall and Sewell, 2009) and secondary MPs derived by breakdown of any plastic good (Barnes

et al., 2009; Eriksen et al., 2014). It is estimated that primary MPs represent only a small part of the MPs present in the environment (Andrady, 2011; Rist and Hartmann, 2018). Most of them are instead represented by secondary MPs, whose spread rate is almost impossible to control due to indiscriminate disposal and inadequate waste management systems without proper recycling. Land based plastic sources end up into aquatic ecosystems and here, despite their recalcitrance, they are embrittled and fragmented by mechanical, chemical and biological processes, thus contributing to about 80% of plastic debris found in these environmental compartments (Andrady, 2017).

Secondary MPs usually result to have irregular in size, shape and composition, physico-chemical (P-chem) features that in different ways

* Corresponding author.

E-mail address: paride.mantecca@unimib.it (P. Mantecca).

¹ These authors contributed equally to the work

may pose a risk to organisms (de Sá et al., 2018; Jabeen et al., 2018; Mazurais et al., 2015). In addition to the hazards arising from MPs direct toxicity and bioaccumulation, particularly if their size reaches the nanoscale, the health concerns may also derive from their ability to adsorb and convey other hydrophobic chemical pollutants, such as persistent organic pollutants and endocrine disruptors (Lee et al., 2014; O'Donovan et al., 2018; Rainieri et al., 2018; Wang et al., 2018). At the same time, plastic additives, such as alkyl-phenols, bisphenol and phthalates, can be leached out from MPs, adding further harmful chemicals to those absorbed from the environment (Barnes et al., 2009; Browne et al., 2013).

Several studies conducted under controlled laboratory conditions have recently reported that commercial polystyrene MPs possess the capability to accumulate into various aquatic organisms (Lu et al., 2016; Pitt et al., 2018). Field studies have evidenced that starting from the primary consumers, mainly represented by the zooplankton (Cole et al., 2013; Setälä et al., 2014), all the organisms composing the aquatic food web, from invertebrates to seabirds and fish (Alomar and Deudero, 2017; Cau et al., 2019; Giani et al., 2019; Sfriso et al., 2020) seem to be involved in the bioaccumulation process, including edible and commercial species (Bouwmeester et al., 2015; Browne et al., 2008; EFSA, 2016; Koongolla et al., 2020; Markic et al., 2019; Neves et al., 2015; Savoca et al., 2020).

In aquatic vertebrates, MPs accumulate especially within the digestive system, which is also the main primary target (Markic et al., 2019). Laboratory studies on larval and adult fish evidenced that, at the intestinal level, MPs can cause damages at the gut epithelium compromising the feeding activity and bringing to negative effects on growth parameters and survival (Jabeen et al., 2018; Lei et al., 2018; Naidoo and Glassom, 2019; Pannetier et al., 2020; Pedà et al., 2016). In addition, some studies on marine and freshwater fish species reported MP translocation from the gut to the circulatory system and consequent histological and metabolic injuries to other organs such as liver (Espinoso et al., 2019; Jabeen et al., 2018; Lu et al., 2016).

In the extensive literature regarding the impact of MPs on aquatic organisms, it is noteworthy the knowledge gap on their potential adverse effects on development, when embryos mainly undergo passive exposure to MPs during the delicate phase of morphogenesis and organ functional differentiation.

However, most of the studies on invertebrates and vertebrates, including embryonic stages, have investigated the uptake and distribution of commercial micro- and nanopolymers, mainly spherical and monodisperse polystyrene (PS) (De Felice et al., 2018; Duan et al., 2020; Messinetti et al., 2018; Pitt et al., 2018). Alternatively, other studies assessed the impact of leaching by comparing virgin versus beach-stranded pellets or artificially contaminated commercial MPs (Batel et al., 2018; Nobre et al., 2015). Despite having appropriate dimensions, the commercial MPs are overly simplified and do not reflect the modality of interaction with organisms of the heterogeneous environmental MPs (Phuong et al., 2016). Environmental secondary MPs, intended as mixtures of fragments of different shapes, composition and aggregation capacity are therefore worthy of additional research efforts.

To improve the knowledge on the possible effects of environmental MPs during the development of sensible target organisms, like fish and amphibians, in the present study we used the zebrafish (*Danio rerio*) and the African frog (*Xenopus laevis*) as ecologically-relevant experimental models. Recently, these animal models have been extensively used to study the biointeractions and toxicity of micro- and nano-particles (NPs) (Bonfanti et al., 2019, 2015; Colombo et al., 2017; Fiandra et al., 2020; Haque and Ward, 2018; Mantecca et al., 2015), confirming their capability to efficiently predict the hazard of environmental and biomedical particles. Moreover, the specific developmental strategies of fish and amphibians offer the opportunity to study how the interactions of MPs with different embryonic structures may affect the development.

In order to improve the relevance of the toxicological hazard assessment of the MP environmental pollution, micrometer-sized plastic

particles were produced by fragmentation of miscellaneous plastics derived from the collection of miscellaneous plastic wastes in municipal ecological platforms. After mechanical sieving of the particles, the two smallest fractions with size ranges 100–50 µm and less than 50 µm were retrieved. These samples have been considered representative of the environmentally occurring and measurable MPs, with a micron-scaled dimension conferring them the ability to effectively interact and be taken up by aquatic organisms. After a detailed P-chem characterization of the wMPs by microscopy (light, SEM, TEM) and spectroscopy (ATR-FTIR, Raman, TXRF) techniques, the toxic responses have been investigated by the Fish Embryo acute Toxicity (FET) test using zebrafish, and the Frog Embryo Teratogenesis Assay-*Xenopus* (FETAX); the modalities of the MP interaction with the biological structures, as well as the histological lesions, have been investigated by microscopy techniques.

2. Materials and methods

2.1. Production of waste plastic granules and microparticles

Plastic granulates were obtained from industrial partners in the framework of the project ECOPAVE (POR FESR 2014–2020, Reg. Lombardia), in which a pilot value chain has been established to collect and reuse plastic wastes. After being collected, the plastic waste of various origins was treated to obtain fractions of plastic granules of decreasing size (Text S2, Supporting Information) on which the ATR-FTIR analysis was carried out.

The finest wMP fractions, with at least one of the dimensions of 50 µm <wMPs <100 µm and wMPs <50 µm (named F1 and F2 respectively), have been used for further chemical-physical and toxicological analyses.

2.2. Waste microplastic characterization

2.2.1. ATR-FTIR spectroscopy

Attenuated total reflection-Fourier-transform infrared (ATR-FTIR) spectroscopy analysis was performed using a Nicolet In5 FTIR instrument (Thermo Fisher Scientific) with 128 scans at 2 cm⁻¹ of resolution in the range of 4000–550 cm⁻¹. Four sampling replicates were collected from each of the six different size fractions (Fig. S1 C). Applied contact force was increased until a constant ratio between the C-H stretching bands at 2900 cm⁻¹ and the CH₂ rocking bands at 720 cm⁻¹ was ensured. Spectral acquisition, analysis and library research were performed by using the OMNIC Spectra software. Identity confirmation was established with 95% match obtained with the patented comparison algorithm provided by the software.

2.2.2. Raman spectroscopy

Raman spectroscopic analysis of the F1 and F2 wMP particles was performed using an alpha300 confocal Raman microscope (WITec, Ulm, Germany) applying a 532 nm laser. Particles were deposited using a stainless-steel spatula on a polished, clean silicon wafer placed on the motorized stage of the Raman microscope. For both fractions, spectra of 50 particles were collected using a 10x objective typically at 1 s integration times by averaging 10 accumulations. Materials were identified after baseline subtraction of the raw spectra, using the ACDLabs UVVis manager software and an in-house built polymer database. For the identification of materials not present in our database (polyethylene-octene copolymer) an open spectral database, OpenSpecy (www.openspecy.org) (Cowger et al., 2021) was utilized. Spectra without specific Raman features (only wide fluorescent signal) were considered to be not-identified.

2.2.3. Total reflection X-ray fluorescence (TXRF)

TXRF measurements were performed after sample digestion as previously described (Bobba et al., 2021) with some modification. Briefly wMP F1 and F2 samples (0.3 g) were placed in dried glass microwave

digestion tubes and dispersed in 800 μL of aqua regia plus 100 μL of 30% H_2O_2 solution, added drop by drop. Three replicates for each WMP fraction were prepared. Samples were digested by an automatized CEM Explorer SPD microwave digestion system and treated at 220 $^\circ\text{C}$ for 10 min (after 10 min ramping to the final temperature). The digestion step was repeated twice by adding again the same amount of reagents in the same glass tube. Three blank samples were processed with the same digestion protocol operated with only aqua regia and H_2O_2 . Samples and blanks were then purified using an Amicon Ultra-4 centrifugal filter, 100 kDa (Millipore), and diluted 1:1 in water. Mixture for TXRF analysis were prepared in triplicate by adding 10 μL of each sample to 77 μL of HNO_3 at 14% w/v, 3 μL Ga internal standard (3.3 mg/L final concentration), and 10 μL Triton X-100 at 1.0% w/v. 5 μL of the final mixture were spotted on acrylic sample holder, dried and placed in the TXRF spectrometer (S4 T-Star 4 TXRF spectrometer, Bruker) equipped with a Mo X-ray source. Measurement data were collected for 1200 s.

2.2.4. Particle size and particle size distribution

The size and particle size distribution of F1 and F2 were determined by the laser diffraction method (Malvern Mastersizer 3000). The measurements were performed either in ethanol and 0.1% w/v Triton X-100 and kept under continuous stirring (850 rpm) during the analysis. Each measurement was performed in five replicates.

The model for data analysis assumes that the particles are not-spherical, while refractive index and absorption value were set to 1.5 and 0.010, respectively, on the base of the chemical composition of the material. Laser obscuration was kept between 10% and 20%. Data were reported as size distribution, calculated from the volume size distribution.

2.2.5. Microscopy characterization

Light, Fluorescence, Scanning and Transmission Electron Microscopy (LM, FM, SEM and TEM-EDX) were used to characterize morphology, optical properties and elemental composition of F1 and F2. For LM analysis, small amounts of F1 and F2 granulates were mounted onto glass slides and observed under a Zeiss Axioplan microscope equipped with an Axiocam MRc5 digital camera. For FM, the slides were observed with an inverted Zeiss Observer.Z1 microscope, equipped with a Zeiss AxioCam MRm digital camera, selecting UV, eGFP and DsRed filters. For SEM analysis, F1 and F2 samples were attached with adhesive carbon tape onto stubs and sputter-coated with 10 nm gold. SEM-SE imaging was performed using a TESCAN Vega@XM 5136 SEM operating at 20 kV acceleration voltage. For TEM analysis, F1 and F2 fractions were directly embedded in epoxy resin and ultrafine slices were cut using Leica EM-UC7 ultramicrotome (Leica, Milan, Italy). Slices were analyzed by EDX in STEM mode using JEOL-JEM 2100 at 120 kV (JEOL, Italy) coupled with Bruker X-flash detector 5030 (Bruker Italy). The QUANTAX 200 software, in Hypermap mode, assessed elemental composition.

2.3. Embryotoxicity test

2.3.1. Preparation of the WMP treatment suspensions

To obtain the suspensions for the embryos' treatment, F1 and F2 were suspended in FET (in mg/L NaHCO_3 100, Instant ocean salt 100, CaSO_4 190 for zebrafish) or FETAX (in mg/L NaCl 625, NaHCO_3 96, KCl 30, CaCl_2 15, $\text{CaSO}_4 \cdot 2\text{H}_2\text{O}$ 60, and MgSO_4 70 for *X. laevis*) solution (pH 7.5–8.5) to achieve the maximum working concentration of 100 mg WMPs/L. These suspensions were vortexed to obtain a uniform distribution of particles and then sequentially diluted to generate the additional treatment concentrations (0.1, 1 and 10 mg/L). To date, MP amounts measured in the aquatic environment are extremely variable, therefore we have chosen a range comprising an environmental relevant concentration (0.1 mg/L) with reference to the contaminated areas (Naidoo and Glassom, 2019) up to concentrations likely representing hotspot pollution events (10 and 100 mg/L).

According to the guidelines of the FET (OECD TG 236, 2013) and

FETAX (ASTM, 1998), embryos of zebrafish and *Xenopus* control groups were incubated in standard FET and FETAX solution respectively and all the solutions/suspensions were changed daily.

2.3.2. Fish embryo acute toxicity (FET)

Wild-type (AB strain) zebrafish were maintained as described in S3.

The acute toxicity of WMPs was determined as recommended by the OECD (OECD, 2013), with minor modifications. Within 3 h post-fertilization (hpf), groups of 20 embryos at same development stage, obtained by natural spawning of adult wild type AB zebrafish pairs ($n = 6$), were randomly subdivided in four Petri dishes (\varnothing 6.0 cm) containing 10 mL of FET solution (control group) or treatment suspension (F1 and F2 WMPs at 0.1–1–10–100 mg/L). Embryos were exposed in a thermostatic chamber at 26 ± 0.5 $^\circ\text{C}$, under static conditions. Lethal (coagulation, lack of somite formation, lack of detachment of the tail from the yolk sac, lack of the heartbeat) indicating acute toxicity and sublethal (e.g. oedemas, hatching rate and tail malformations) endpoints, were monitored at 24, 48, 72 and 96 hpf.

At the end of the exposure period, randomly selected embryos from each experimental group were anesthetized in 0.16 mg/mL MS-222 and 10 embryos were processed for histological analysis while the remaining were fixed with 10% neutral buffered formalin for head-tail length measurement with the digitizing software AxioVision (Zeiss, Germany).

2.3.3. Frog embryo teratogenesis assay *Xenopus* - FETAX

Xenopus embryos were obtained by natural breeding of pairs ($n = 3$) of adult *X. laevis* injected with HCG into the dorsal lymph sac (females: 300 IU; males: 150 IU) as previously described (Bonfanti et al., 2015). Embryotoxicity tests were conducted according to the standard guide for the FETAX (ASTM, 1998) performing three replicate definitive tests in the same experimental conditions, each conducted using embryos from a different male/female pair of *X. laevis*. Groups of 25 embryos at the midblastula stage (Stage 8), 5 hpf (Nieuwkoop and Faber, 1956) were randomly placed in Petri dishes (\varnothing 6.0 cm) containing 10 mL of FETAX solution (control group) or treatment suspension. Two replicate dishes were used for each test concentration (F1 and F2 0.1–1–10–100 mg/L) while for control group four replicate dishes were used.

All Petri dishes were incubated in a thermostatic chamber at 23 ± 0.5 $^\circ\text{C}$ and daily dead embryos were counted and removed. FETAX endpoints (i.e. mortality, malformations and growth inhibition) were considered at the end of the assay (stage 46, 96 hpf). At the end of the analysis, embryos ($n = 75$ randomly selected from each experimental group) were fixed in 10% neutral buffered formalin to evaluate the growth retardation by measuring head-tail lengths with the digitizing software AxioVision (Zeiss, Germany). The remaining embryos were processed for the subsequent morphological analyses.

2.4. Fluorescence stereomicroscopy analysis of zebrafish and *Xenopus* embryos

The optical property of some WMPs emitting fluorescence has been exploited to localize the WMPs particles in order to evaluate their bio-interactions with embryonic tissues. To this aim, groups ($n = 10$) of living zebrafish embryos at 24 hpf and formalin fixed *Xenopus* embryos at 96 hpf were randomly sampled from control and 100 mg/L F1 and F2 experimental groups and observed under a dissection microscope (Leica, M205FA equipped with LAS X Expert software) in brightfield and fluorescence mode with GFP long pass and DsRed filter settings.

2.5. Histological analyses

At the end of FET and FETAX (96 hpf), embryos ($n = 10$) were randomly selected from control and 100 mg/L F1 and F2 experimental groups, fixed in Bouin's solution and processed for paraffin embedding. Samples were transversely cut from eye to proctodeum into 6 μm thick serial sections, mounted on glass slides and stained with haematoxylin

and eosin (H&E) or Periodic acid–Schiff (PAS). The slides were screened under a Zeiss Axioplan optical microscope equipped with an Axiocam MRC5 digital camera.

2.6. Scanning electron microscopy of *Xenopus* embryos' intestines

For SEM analysis, 96 hpf embryos randomly selected at the end of the FETAX from the control, F1 and F2 wMPs 100 mg/L groups ($n = 6$ each) were euthanized with MS-222 (300 mg/L). The intestinal tubes were dissected, immediately fixed overnight (ON) with 2% glutaraldehyde in Na-cacodylate (CAC) buffer (0.1 M), washed with CAC buffer (0.1 M) and post-fixed with 1% osmium tetroxide in CAC buffer (0.1 M) for 90 min at room temperature (RT). After dehydration with a graded ethanol series up to 100%, specimens were infiltrated with hexamethyldisilazane and left to dry ON at RT. After drying, the samples were placed on a conductive tape mounted on aluminum stubs and coated with 10 nm chromium using high vacuum Quorum Q150T-ES sputtering system. SEM-SE micrographs were acquired by means Zeiss Gemini 500 FEG-SEM operating with an acceleration voltage of 5 kV.

2.7. Data collection and statistical analysis

The number of dead embryos versus their total number at the beginning of the tests led to the mortality percentages and the number of malformed embryos versus the total number of surviving ones gave the

malformed embryo percentages. Data were expressed as the average \pm standard error (SE) or standard deviation (SD) and the percentage relative standard deviation (RSD %). Data were tested for homogeneity and normality and one-way analysis of variance (ANOVA) was performed. The daily and cumulative hatching percentages were investigated by chi-square method, using Yates's correction for continuity (χ^2 test) or Fisher's exact tests. The elaboration of cumulative hatching data of zebrafish embryos by probit analysis (Finney, 1971) allowed obtaining the median Hatching Time (HT_{50}) value, which is the hatching time for 50% of the embryos. All statistical test were applied with at least 95% confidence interval using the IBM SPSS statistic 25 software.

3. Results

3.1. Microplastic characterization

The preliminary chemical characterization of the plastic granulates obtained from the collected plastic waste showed that poly-olefins were the main components (data not shown). After the dimension-based fractionation of the wMP granulate by manual sieving, additional chemical characterizations were performed to identify the type of polyolefin prevalent and any change in chemical structure induced by the grinding process in the different granule subpopulations. Representative ATR-FTIR spectra of these different sized fractions are presented in Fig. 1 A. The list of the main peaks detected is reported in

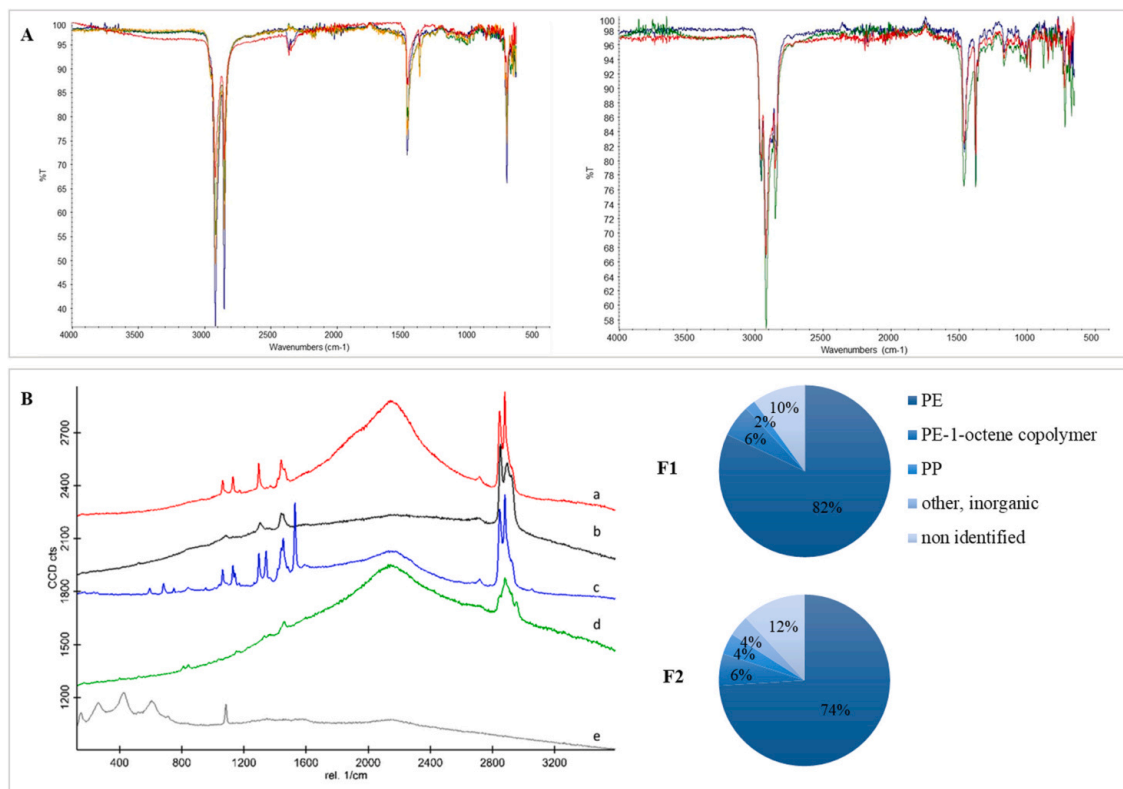


Fig. 1. Polymer characterization of wMPs. Panel A: superimposed ATR-FTIR spectra of polyethylene (left) and polypropylene (right) granulates obtained from each of the six dimensional fractions of wMPs. Panel B: Raman spectroscopy analysis of wMPs. On the right: examples of raw Raman spectra of the analyzed particles before baseline subtraction, many of them showing wide fluorescence peaks in addition to the Raman lines. From top to bottom: a) polyethylene, b) polyethylene-octene copolymer, c) polyethylene with phthalocyanine blue additive, d) polypropylene in fraction F1, e) metal oxide (rutile) containing particle in fraction F2. On the left: summary of the chemical composition of the wMP particles in fractions F1 and F2.

Table S1.

Considering a >85% match, library research enabled the identification of two main polymers: polyethylene (PE) and polypropylene (PP) in a 8:1 ratio. No other polymers were identified. Considering the same identified polymer in the different size fractions the spectra resulted similar, indicating that no remarkable transformation were induced in the chemical structure of the bulk material during the sorting and grinding process. However, some aliquots displayed peaks not detected in the reference virgin pellets, indicating that the original plastic materials were probably containing different ingredients that were retained during the processing and/or faced a different degradation pathway. Specifically, seven samples display signals at 1719 cm^{-1} that may originate from oxidation processes of the aliphatic chain.

The finest fractions obtained in appreciable quantities from the sieving of initial granulate were F1 and F2 (Fig. S1 C), which comprise plastic particles with at least one nominal dimension between 100 and $50\ \mu\text{m}$ and less than $50\ \mu\text{m}$ respectively. These fractions were selected to study the impact on zebrafish and *Xenopus* embryonic development and their biointeraction potential. To support toxicological data, F1 and F2 wMPs were further characterized in terms of chemical compositions by Raman spectroscopy, TXRF and EDX, and of shape and dimension by laser diffraction and LM, FM, SEM and TEM analysis.

Characterization of F1 and F2 wMPs by Raman spectroscopy confirms the results obtained by FTIR on "bulk" aliquots, suggesting that most of the plastic particles are made of polyolefins (Fig. 1 B). Many of them also show fluorescence at the excitation wavelength applied, underlining that the waste plastic material contains several other ingredients beside the synthetic polymers. In the two fractions, about 74–82% of the particles were PE, 6% was PE copolymer, 2–4% were PP. Some of them contained also inorganic materials, like TiO_2 . This is also confirmed by the TEM-EDX analysis, which shows the presence of different elements in nano-form such as Ti, Pb, Fe, Si, Al (Fig. 3 B). In

other cases, complex spectra revealed that many wMPs contained colorants like phthalocyanine blue (Simon and Röhrs, 2018). However, about 10–12% of the particles remained unidentified, in most cases because of the strong fluorescent signal of colorants/additives hiding the Raman features of polymers.

F1 and F2 fractions were also analysed by Total reflection X-ray fluorescence spectrometry (TXRF) to evaluate the presence of trace elements (Table S2). Overall, the F2 fraction shows higher concentration of extracted metals in comparison to F1. A more detailed analysis carried out by TEM-EDX shows the presence of Ti, Pb, Fe and Si in nanoform in the F1 fraction (Fig. 3 B, F1) whereas in the F2 fraction they were distributed more homogeneously inside the plastic particles (Fig. 3 B, F2).

The size and the volume size distribution of the two fractions were measured by the Mastersizer using ethanol and 0.1% Triton X-100 as dispersants (Table S3). The obtained values, which resulted higher than the nominal dimensions, might be affected by the presence of aggregates or agglomerates, as confirmed also by the variation of the volume size distribution observed in the different dispersant.

LM analysis confirmed the different size of the F1 and F2 wMP fractions and that particles are characterized by highly variable dimensions (even if within the limits imposed by the sieve), thickness, shapes and colours (Fig. 2 A). In addition to the round granules, also fibres and flakes with rough and sharp edges were observed. Moreover, since it is well known that plastic materials show significant autofluorescence when excited by near-UV or even visible radiation, F1 and F2 wMPs were observed with an inverted fluorescence microscope after selecting UV, GFP and DsRed filters (Fig. 2 B). Fluorescence images showed that the particles behaved differently in terms of fluorescence wavelength and intensity of emission. Considering that the fluorescence emission at a specific wavelength is intrinsic to the bulk polymer and can depend also on additives, pigments, impurities or degradation products

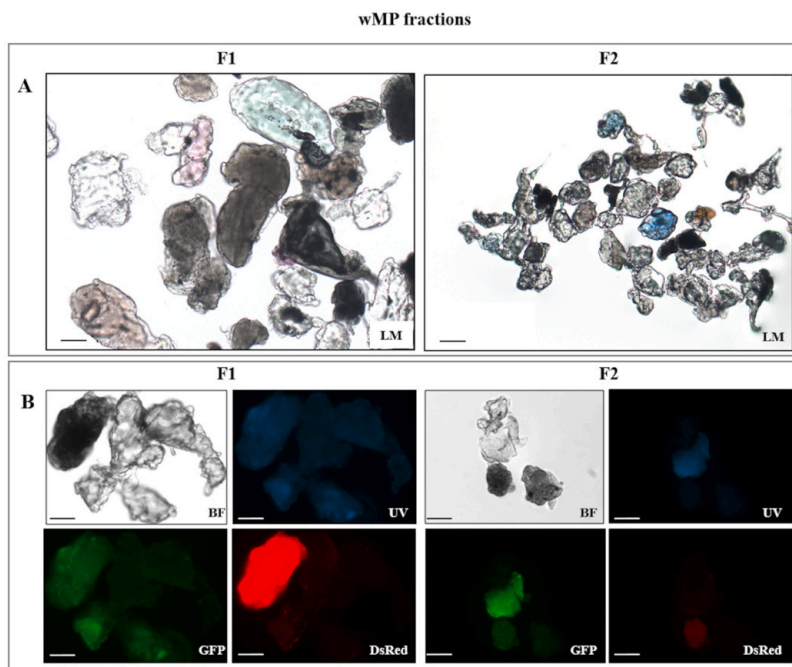


Fig. 2. Morphological characterization of wMPs. Representative light (A) and fluorescence microscope images (B) that highlight heterogeneity in terms of shapes, colors, sizes and optical properties of the particles contained in F1 and F2 fractions. LM=light microscope, BF=bright field. Filter setting for fluorescence microscope: UV= 358 nm, and GFP= 488 nm, DsRed= 563 nm. Scale bar = $50\ \mu\text{m}$.

used in the production process (Hawkins and Yager, 2003; Qiu et al., 2015), this result confirms the presence of different polymers and various associated molecules in the selected fractions.

SEM analysis, performed to better characterize the wMP F1 and F2 morphology, confirmed that many particles have an irregular and rough surface and that submicrometric particles are aggregated to the surface of the larger ones (Fig. 3). TEM coupled with EDX confirmed the presence of nanoparticles inside F1 fraction slices and representative analysis showed Ti, Pb, Fe, Si alone or combined in nanoform of min Feret diameter around 100–200 nm (Fig. 3 B, F1). In the F2 fraction, elements such as Al, Pb, Fe and Si were more homogeneously distributed in the fraction, including also plastics particles of 1 μm size or less (Fig. 3 B, F2).

3.2. Effects of the wMPs on zebrafish and *Xenopus* embryos

A comparative evaluation of embryotoxicity of the F1 and F2 wMP fractions was conducted on zebrafish and *Xenopus laevis* during the first 96 h of development, a sensitive period that include important processes leading to organ formation.

FET results have evidenced that the exposure to both wMP fractions did not induce a significant increase in mortality and malformation rates in zebrafish embryos at 96 hpf (Fig. 4 A). The head-tail length of the embryos was also not substantially affected (Fig. S2). In contrast, a dose-dependent pattern was evidenced in the ability of zebrafish embryos exposed to both F1 and F2 wMPs to hatch successfully (Fig. 4 B). In particular, the evaluation of the daily hatching showed that the percentage of embryos exposed to F1 hatched mainly at 72 hpf with a dose-dependent decrease compared to unexposed ones. Instead, zebrafish embryos exposed to 0.1–10 mg/L F2 hatched at the same extent at 72 and 96 hpf, but those exposed to 100 mg/L hatched mainly at 96 hpf. The cumulative hatching rate highlighted the trend of embryos to delay the release from the chorion in a concentration-dependent manner, more marked for the finest fraction F2. However, at 96 hpf almost 100% of treated embryos were able to hatch similarly to controls. HT_{50} values calculated at the different wMP concentrations confirmed that the time taken for hatching of 50% embryos was significantly delayed starting from 10 mg/L for F1 ($\text{HT}_{50} = 68.99$ hpf) and from 1 mg/L for F2 ($\text{HT}_{50} = 74.30$ hpf) respect to the control ($\text{HT}_{50} = 65.89$ hpf) (Table S4).

We exploited the fluorescence of some plastic particles to highlight their adhesion to the chorion of 24 hpf zebrafish embryos as this interaction could be one of the causes influencing hatching (Fig. 4 B).

In control embryos, chorion surface appeared smooth and transparent unlike treated embryos, where some wMP aggregates attached to the chorion surface were observed as fluorescent spots. This result was more pronounced in F2 treated embryos. No fluorescent wMPs were detected in the periovular fluid and not even in the yolk sac or in other embryo tissues.

As with zebrafish, wMPs did not elicit mortality in *Xenopus* embryos since mortality rates for both fractions were not significantly different from control (Fig. 5 A). Malformation rates statistically different from controls (but never exceeding 10%) occurred sporadically, in particular to embryos exposed to F1 and F2 at 10 and 0.1 mg/L respectively, without any correlation with wMP concentration (Fig. 5 A).

However, the score of single malformations showed that the slight increase in malformation rates in treated embryos was mainly attributable to the loosening of the intestinal loops (Fig. 5 C). Observing embryos' abdominal region under dissecting microscope, the presence of debris in the loops of these slightly altered intestines was detected (Fig. 5 C). Taking advantage of the fluorescence emission properties of F1 and F2 fractions previously highlighted, the debris were identified to be mainly plastic particles (Fig. 5 C). It is likely that the presence of these wMP agglomerates in the gut lumen has interfered to a small extent with the tight coiling of the intestinal tube that characterizes *Xenopus* gut development. Furthermore, wMPs were only observed in the digestive tracts of F1 and F2 treated embryos while no particle was observed on

the epidermis or within other organs.

As far as it concerns the head-tail length of *Xenopus* embryos, a statistically significant increase respect to control was observed at all concentrations for the F1 and at 1 and 10 mg/L for F2 fractions (Fig. 5 B). Interestingly, a slight biphasic behaviour of the concentration-response curves of both fractions was observed, with the tendency of head-tail length to be greater at low or intermediate concentrations and lower at the high concentrations.

3.3. Bio-interactions of the wMPs with zebrafish and *Xenopus* embryonic tissues

In order to highlight the interactions of the wMPs with embryonic tissues and evaluate any damage induced to primitive organs, H&E transversal sections of control and 100 mg/L F1 and F2 exposed zebrafish and *Xenopus* embryos at 96 hpf were examined.

No histological and organ morphology alterations were detected in zebrafish embryos exposed to wMPs and no wMP fragments have been visualized inside the lumen or at the level of the yolk even in finest fraction (F2) treated embryos (Fig. S3). Furthermore, no altered phenotype of intestinal epithelium nor delay in intestinal development has been recorded in wMP treated embryos (Fig. 6, line D). Additional histological evidences regarding the distinct intestinal segments are reported in Fig. S3B.

In *Xenopus* embryos, although exposure to neither fractions of wMPs did result in morphological alterations of the primitive organs in the abdominal cavity (Fig. 6, line A) as in zebrafish, single heterogeneous fragments or agglomerates of wMPs were detected inside the lumen of several intestinal loops (Fig. 6, line B). In particular, the wMP particles seemed to adhere and press on the intestinal epithelium of these tracts, without causing apparent morphological damage to the epithelium.

Since mucus secreted by goblet cells provides a physical protection of intestinal epithelium and its hyper-production represents a physiological response to an undesirable irritant, a PAS staining was also performed. In the lumen of the intestinal loops of the control embryos, the reaction revealed a PAS positivity at the brush border level, consistent with the glycocalyx of microvilli membrane and the thin protective mucus layer stratified on the enterocytes (Fig. 6, line C). Instead, in the embryos exposed to both fractions of the wMPs, the reaction revealed a large amount of mucus into the lumen of some intestinal loops that wrap wMP particles (Fig. 6, line C). No presence of infiltrating inflammatory tissue was anyway observed at the level of the developing gut mucosa. At the level of the gill basket no wMP particle has been observed (Fig. S4).

SEM observation of isolated intestinal tube of *Xenopus* embryos exposed to 100 mg/L F1 and F2 has confirmed the accumulation of heterogeneous shaped and sized wMP particles in the digestive tract, which were so abundant to stuff the lumen (Fig. 7). The particles were found to be enclosed in a mucus coating and besides to pressing the microvilli of the enterocytes, some fibre-shaped and pointed fragments were wedged in the epithelium.

4. Discussion

MPs are recognized to pose a serious threat to various aquatic organisms, from detritus feeders to filter feeders and predators that, accidentally or intentionally, ingest them due to the similarities of these particles, so heterogeneous in size, shapes and colours, with their natural food sources (Botterell et al., 2019; Lusher, 2015).

The right concern that these plastic particles can accumulate in the digestive tract and starve wildlife triggered a rapid increasing number of studies especially focusing on the hazard deriving from the oral exposure route (Carbery et al., 2018).

Although these investigations still require attention to elucidate the modality of interaction of MPs with gut and the resulting mechanical and metabolic damage as well as the transfer of smaller particles to other

wMP fractions

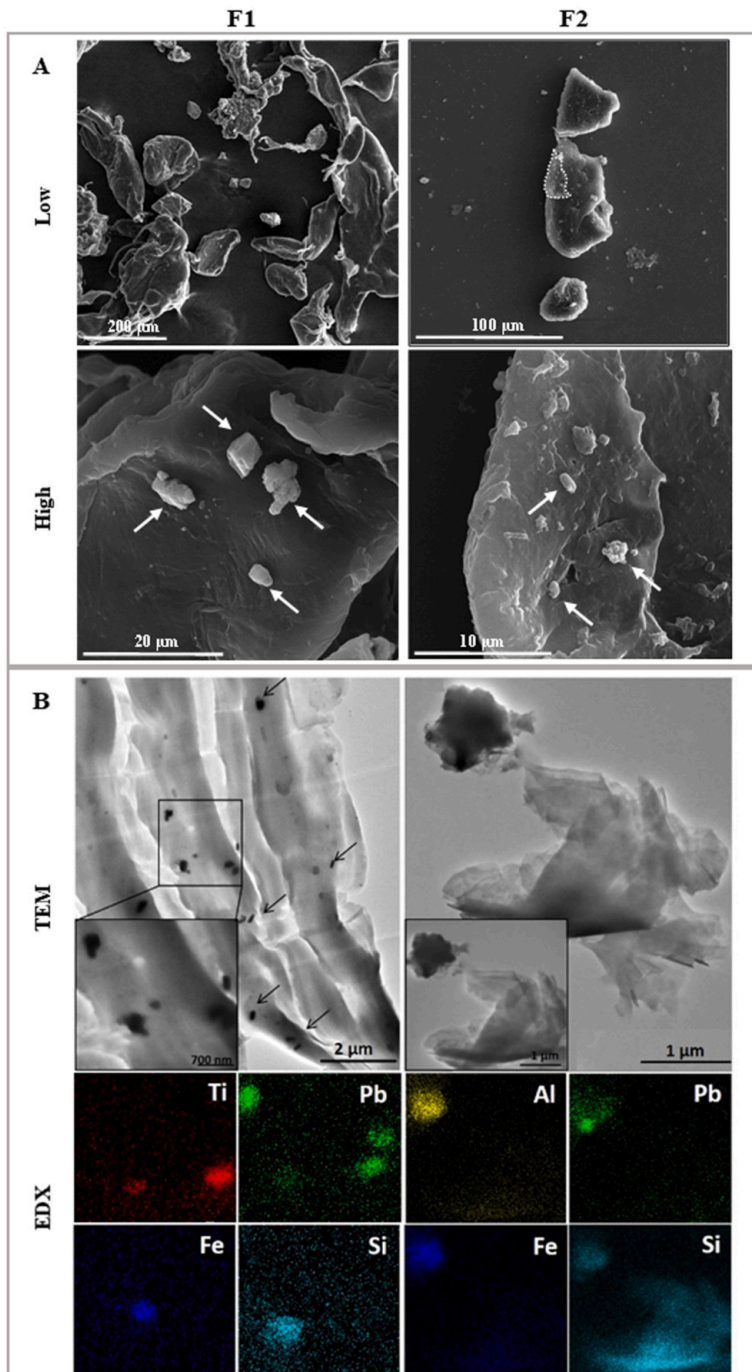


Fig. 3. Electron Microscopy analysis of wMPs. Panel A: SEM representative images at low and high magnification of F1 and F2 particles. It is possible to observe heterogeneous shapes and dimensions and the irregular surface of wMPs with the presence of sub-micrometric particles deposited on them (arrows). The high magnification of F2 corresponds to the white dotted area in low magnification image. Panel B: TEM images of F1 and F2 fractions ultrafine slices and corresponding EDX analysis in STEM mode (square selection and elemental maps). F1 fraction shows the presence of nanoparticles inside material of min Feret diameter around 100–200 nm (arrows) and the F2 fraction shows particles of min Feret diameter of 1 μm or less. The elemental composition of both fractions confirm the presence of Ti, Pb, Fe and Si in nano-form (F1 fraction) or distributed in the material (Al, Pb, Fe and Si in F2 fraction).

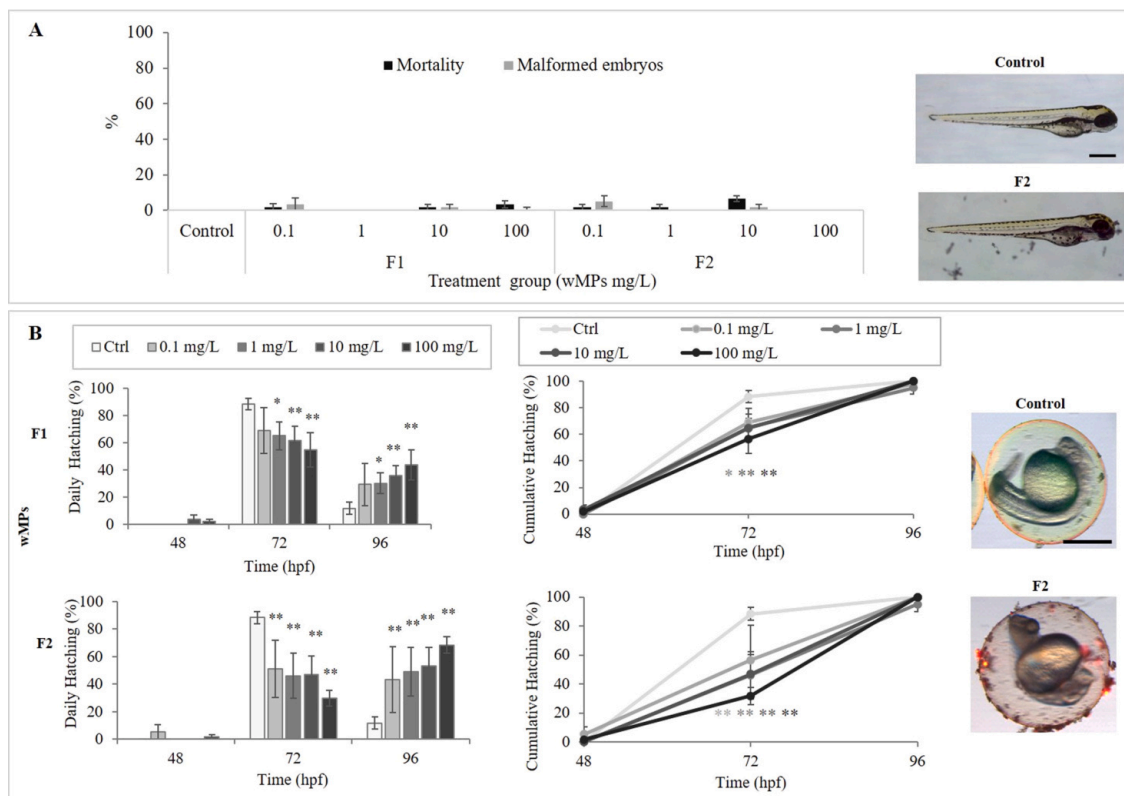


Fig. 4. Embryotoxicity of wMPs evaluated by FET. Panel A: mortality and malformation rates in 96 hpf embryos after exposure to F1 and F2 fractions (0.1–100 mg/L). On the right, representative stereomicroscopy images of a control embryo and a F2 exposed embryo at the end of assay (96 hpf). Panel B: daily and cumulative percentage of hatched control and wMPs exposed zebrafish embryos during FET. On the right, fluorescence stereomicroscopy representative images of control and F2 exposed zebrafish embryos at 24 hpf obtained by merging the red and green channels with bright field photographs. In wMP treated embryos, chorion surface is less smooth and transparent than in control and fluorescent wMP spots are observable. All values in the graphs are given as mean \pm SE of three independent assays. * $p < 0.05$, ** $p < 0.01$ indicate statistical difference from control (Chi-squared test). Scale bars = 500 μ m.

organs, it is important to advance knowledge on MP impact on embryonic life stage, before exogenous feeding, when the delicate phase of organogenesis is taking place. Moreover, on those aspects, almost none studies evaluated the impact of environmental secondary MPs deriving from wastes.

Thus, considering that of all the plastic produced less than 10% is recycled and the rest, if not destined for waste-to-energy, ends up into the environment (Alimi et al., 2018; Geyer et al., 2017), in this study we involved the finest MPs (100–50 μ m and < 50 μ m) retrievable by the mechanical fragmentation and sieving of non-reusable miscellaneous plastic waste. After a detailed P-chem characterization of the wMPs, we reported their effects on early development of two model organisms, *D. rerio* and *X. laevis*, widely exploited for (eco)toxicological studies on freshwater vertebrates under laboratory conditions.

The wMPs appear to share similarities with environmental MPs as referred to their chemical nature and morphology, without substantial differences between the two dimensional fractions considered. First of all, as suggested by Eitzen et al. (2019), the environmental relevance of the plastic materials tested should be one of the requirements for toxicological studies. According to FTIR and Raman analyses, our wMPs are mainly composed of PE and PP, a mixture of polymers highly representative of environmental MPs (Law, 2017).

The prevalence of these polymers was evidenced also in fragmented plastic samples collected on the beaches of known plastic accumulation

areas such as the North Atlantic (El Hadri et al., 2020) and North and South Pacific Ocean gyres (Pannetier et al., 2020). In addition, according to the origin of the starting plastic materials, some of the analysed wMP specimens showed a certain level of degradation such as oxidation, an aging process typical of environmental MP samples caused by atmospheric agents (Chen et al., 2019; Song et al., 2017). In this regard, testing in the laboratory a mixture of MPs composed of the most abundant polymers in the environment rather than a single commercial polymer, represents an innovative aspect of this study, which adds to the other environmentally relevant properties highlighted by the morphological characterization. Indeed, the heterogeneous shapes, the irregular surface texture and the highly variable particle size of our wMPs, are morphometric characteristics comparable to those of MPs sampled in the environment or extracted from the intestine of oceanic fish (Pannetier et al., 2020; Wang et al., 2017). Similar polymorphic MPs have also been reported by studies focusing on the standardization of procedures for the preparation of realistic MP suspensions, which are strongly recommended to improve the representativeness of aquatic MP laboratory research (Eitzen et al., 2019; El Hadri et al., 2020; Gigault et al., 2016). Another noteworthy result related to the surface of our wMPs is the presence of smaller particles with sub-micrometric dimensions attached to larger fragments, which leads us to hypothesize that this aggregation is due to wMP electrostatic and hydrophobic interactions, property that can be exploited to separate MPs from

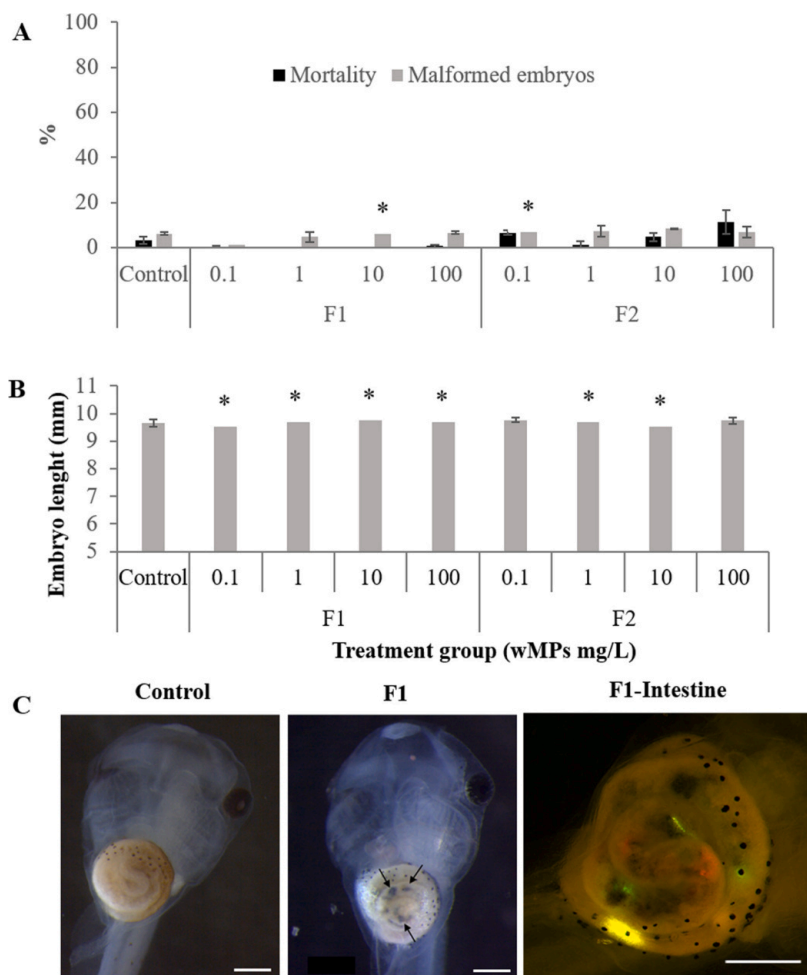


Fig. 5. Embryotoxicity of wMPs evaluated by FETAX. Mortality and malformation rates (A) and head-tail length (B) in 96 hpf embryos after exposure to F1 and F2 fractions (0.1–100 mg/L). All values are given as mean \pm SE of three independent assays. (*) statistically different from control ($p < 0.05$, ANOVA + Fisher LSD Method). Panel C shows representative stereomicroscopic images of control and 100 mg/L F1 exposed embryos at the end of FETAX (stage 46–96 hpf), showing debris in the intestinal loops (arrows) of the latter. In the magnification of intestine of the 100 mg/L F1 exposed embryo observed at fluorescence stereomicroscopy (merge of the green and red fluorescence channels with the bright field photographs), it was ascertained that the most of the debris is represented by fragments of wMPs that emit fluorescence when excited in the GFP (green) or DsRed (red) channels. Scale bars = 500 μ m.

environmental samples (Felsing et al., 2018). This wide heterogeneity is highly representative of an environmental exposure, where MPs undergo to progressive size reduction, resulting in defragmentation into nanoplastics with diameter $< 1 \mu$ m. These nanoscale plastic particles could be a significantly hazardous component even if hardly detectable in the environment (El Hadri et al., 2020; Ter Halle et al., 2017). In our case, the TEM-EDX analysis of F1 showed the presence of Ti, Pb, Fe, Si alone or combined in nanoform of min Feret diameter around 100–200 nm (Fig. 3 B, F1). In F2, elements such as Al, Pb, Fe and Si were mainly distributed inside the plastic particles. These particles a few μ m in size or in the nanoscale could be even more harmful for organisms due to the greater ease of translocation through biological barriers and distribution with the circulatory system to the different tissues as demonstrated in mussels and zebrafish exposed to PS nanospheres (Browne et al., 2008; Lu et al., 2016; Pitt et al., 2018). Taking into consideration that our different polymeric wMPs also contain additives, impurities or degradation products used in the production process of the initial plastic materials, we verified that they show fluorescence emission at different wavelengths. This rarely used visualization strategy can be useful for detecting and isolating MPs from environmental samples (Fu et al., 2020; Savoca et al., 2020) but has also been proven well suitable for tracking wMPs in whole zebrafish and *Xenopus* embryos.

Based on FET and FETAX results, neither lethality nor phenotypic alterations were observed in neither zebrafish nor *Xenopus* embryos even at the highest F1 and F2 concentration tested. These results are in line with those obtained in zebrafish and *Xenopus* embryos exposed to commercial nano e microplastics that despite being distributed from the yolk sac to different organs or ingested did not affect survival and development (Batel et al., 2018; De Felice et al., 2018; Pitt et al., 2018). However, zebrafish embryo treatment with high PS nanoplastic concentrations via injection or waterborne exposure resulted in growth inhibition, increased frequency of malformations, hypoactivity and changes in neural and ocular genes expression (Zhang et al., 2020). Moreover, an anomalous embryonic development in two species of sea urchin and a slowdown of ascidian juveniles' metamorphosis were observed after external exposure to virgin PE pellets or after ingestion of PS beads (Messinetti et al., 2018; Nobre et al., 2015).

As regards the length of *Xenopus* embryos, recognized as one of the most sensitive indicator of developmental toxicity (ASTM, 1998), wMPs have led to a faint biphasic response related to the concentrations. This glimpses a possible hormetic effect that has been previously observed in developing amphibian exposed to other environmental stressors such as pesticides or metal oxide nanoparticles (Bolis et al., 2020). In particular, the stimulation of growth could be explained as an adaptive stress

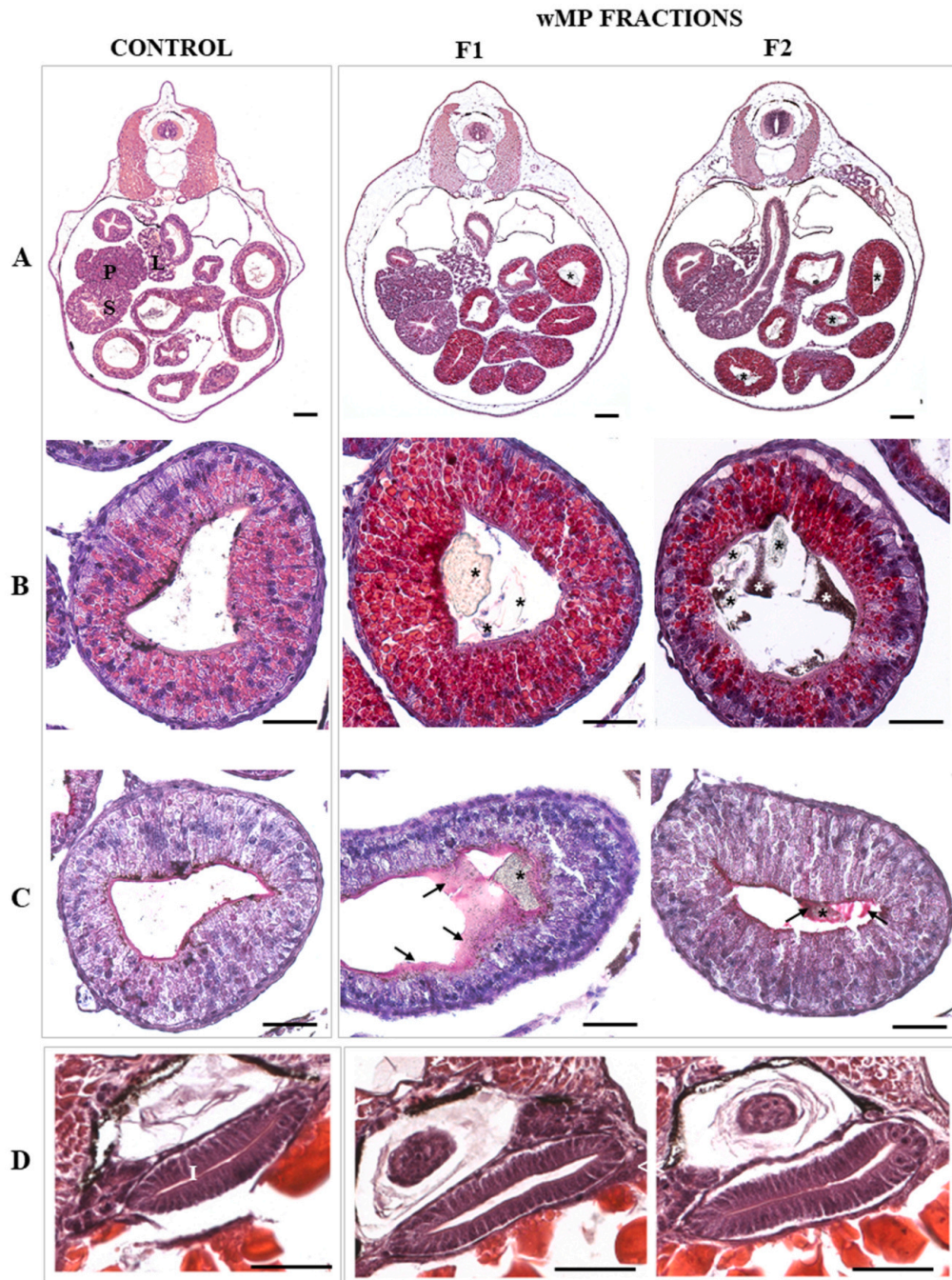


Fig. 6. Histological transversal sections of 96 hpf *Xenopus laevis* and zebrafish embryos at 96 hpf. Low magnification representative images H&E stained of whole *X. laevis* embryos showing that the localization and morphology of primitive organs in the abdominal cavity such as liver (L), pancreas (P), oesophagus-stomach transition (S) and intestine are not altered in wMP treated embryos compared to control. B) Magnification of an intestinal loop of a *Xenopus* embryo showing that several wMP particles (*) are visible into the lumen, mainly attached to the surface of the lining epithelium, where they appeared to result in mechanical damage. C) PAS stained sections evidencing that mucus (arrows) is abundant and wrap wMPs in the F1 and F2 treated embryos. D) Magnifications of representative images of zebrafish embryos middle segment of intestine. No wMPs are detectable in intestinal lumen and intestinal epithelium is not altered in wMP treated embryos compared to control. (A-C) Scale bars = 100 μ m. (D) Scale bars = 50 μ m.

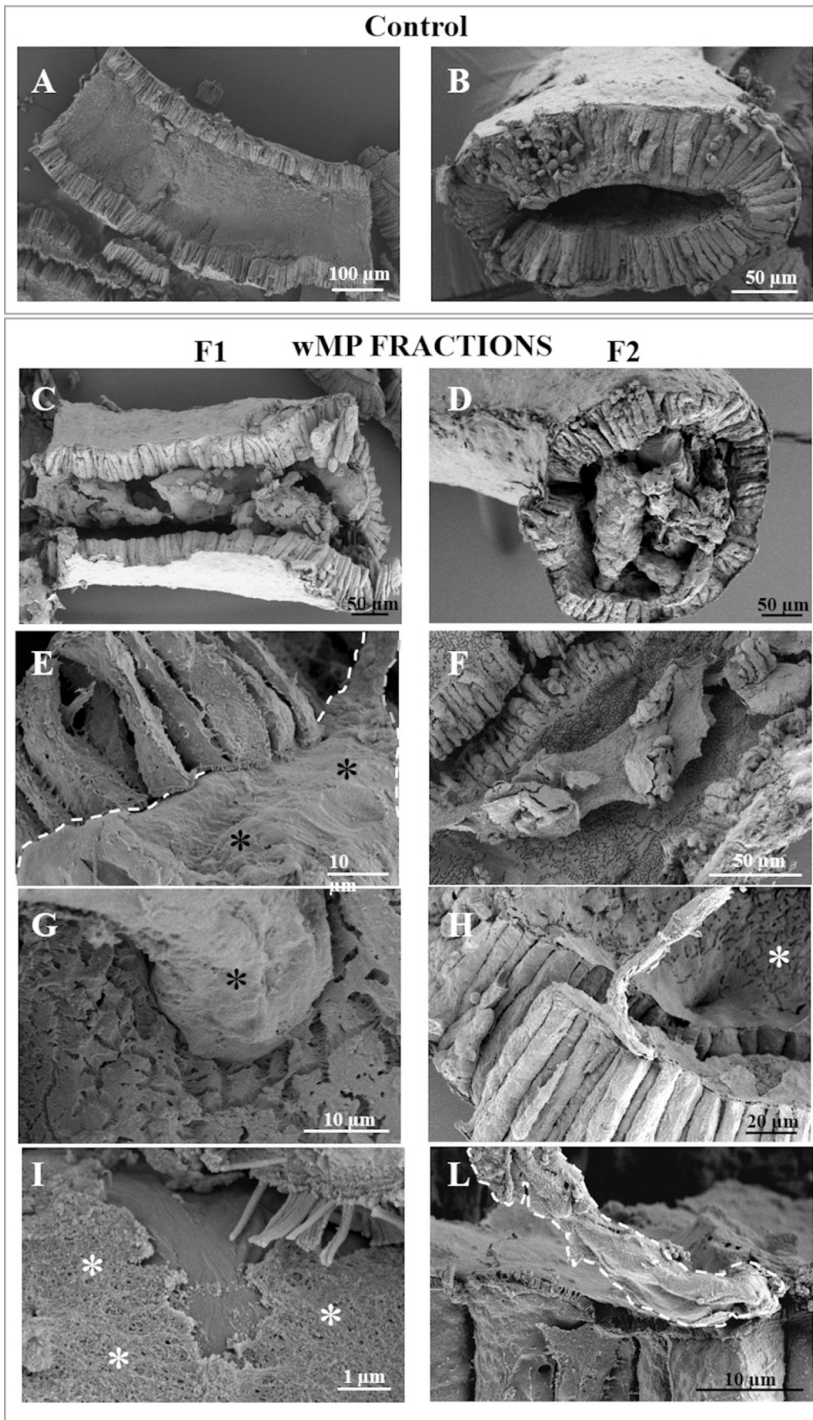


Fig. 7. SEM analysis of intestinal tube isolated from control and F1 and F2 wMP exposed *Xenopus* embryos. Representative images of intestinal epithelium from a control *Xenopus* embryo intestine (A, B) where the columnar morphology of enterocytes and the characteristic brush border facing to the lumen can be appreciated. In the representative images of the intestine isolate from embryos exposed to F1 (C, E, G, I) and F2 (D, F, H, L), the wMP fragments are crammed into the intestinal lumen and contact the microvilli, causing mechanical damage and hypersecretion of mucus that envelops them (white and black asterisks). In G the detail of a fibrous wMPs is visible that deepens in the epithelium. The dotted lines in E and L mark the wMP particles.

response to low, non-toxic concentrations of the environmental stressor.

Although not affecting the development of embryonic primary organs, morphological and histological analysis evidenced that wMPs interact with embryos' structures in species-specific manner due to the different morpho-functional peculiarities that characterize fish and amphibian development.

In particular, wMP treated zebrafish embryos displayed a temporary delayed hatching more marked in F2 fraction. By taking advantage of autofluorescence properties of some wMPs, we observed F2 much more than F1 particle aggregates attached to the chorion surface of 24 hpf zebrafish embryos. This analysis underestimates the amount of particles adhering to the chorion, as it does not highlight the non-fluorescent ones. Taking this into account, more particles may have adhered to the chorion, interfering with the mechanical tearing of the outermost thin layer caused by the tail movements of the embryo. Alternatively, the hatching delay could be attributed to a chemical action of the plastic additives, such as flame retardants as suggested by Lema et al. (2007) or of the metals present in both fractions. Reduced or delayed hatching has been reported after exposure to several metal oxide nanoparticles and attributed to the interaction of the nanoparticles with the zebrafish hatching enzymes (Ong et al., 2014). Batel et al. (2018) also observed that the 1–5 µm MPs accumulated more on the outer surface of the zebrafish chorion than 10–20 µm PE particles, but unfortunately did not report hatching data. Duan et al. (2020) found that PS particles have a high affinity for zebrafish chorions, causing a covering layer of PS particles on their outer surface. Since delayed hatching, more pronounced with nano PS, was observed, they hypothesized that PS could modify the mechanical properties of the chorions or affect the patency of their pores, leading to a hypoxic microenvironment in the embryos. It remains to establish if the wMPs effect on hatching is related to inhibition of hatching enzymes, change in mechanical properties of chorions or to environmental hypoxia and consequent impairment of embryo spontaneous movements.

No wMP fluorescent signals were instead observed in the periovular fluid. As expected, due to the pore size (500–700 nm), the chorion was found to be an effective barrier to all particles present in the two tested fractions, including those with sub-micrometric size. Similar results were reported in zebrafish embryos exposed to fluorescent PS particles ranging from 25 to 700 nm, which were excluded from the passage through chorion pores due to the surface charges or tendency to aggregation (van Pomeran et al., 2017). The barrier function of zebrafish chorions was also confirmed for nano PS in the diameter of 100 nm (Duan et al., 2020). Conversely, fluorescent PS and latex particles of about 50 nm used at low concentrations have proven to be able to penetrate zebrafish and medaka chorion respectively, initially accumulating in the yolk sac and later in other organs (Manabe et al., 2011; Pitt et al., 2018). These data suggest that the chorion represents a barrier capable of protecting the embryo in the crucial early stages of development from the impact with micrometric-sized MPs, while it does not exclude the passage of nanometric ones if present at low concentrations and not in aggregated form. Probably, the submicrometric particles present in our wMPs remained aggregated to the larger ones on the surface of the chorion or alternatively we were unable to map them with light microscopy inside the embryo.

Even in the post-hatching exposure interval up to 96 hpf, wMPs did not interact with the zebrafish embryonic tissues such as gills, epidermis or intestine via ingestion as confirmed both by microscopy observation. Similar results were obtained in zebrafish embryos treated with virgin and benzo [a] pyrene loaded MPs that after hatching remained mainly attached to the fish chorion, while not at all were found on the larval surface and only occasionally appeared within the gastrointestinal tract at 96 hpf (Batel et al., 2018). The absence of MP ingestion is consistent with the morpho-functional characteristics of the zebrafish embryo in the exposure window set by the FET protocol, in which the autonomous feeding is not yet active being the intestine not completely differentiated with the anus still closed and the yolk still available (Ng et al., 2005).

Consequently, uptake of the wMPs via the oral route cannot take place. Instead, by prolonging the exposure to 120 hpf, when the intestinal tract is a completely open-ended tube, the oral uptake of plastic particles becomes predominant as described by van Pomeran and colleagues (2017).

On the other hand, considering the amphibian *Xenopus*, the wMPs did not interfere with the hatching of embryo from the fertilization envelope that acts as a protective barrier up to stage 28 (32 hpf). Conversely, we found in a previous study that nanomaterials such as branched polyethyleneimine coated silver nanoparticles were able to modify fertilization envelope reducing and sometimes preventing *Xenopus* embryo hatching (Colombo et al., 2017). In the post hatching period, starting from stage 39–40 (56–66 hpf) when the stomodeum opens, *Xenopus* embryos acquire a characteristic swallowing and grazing behaviour facilitating intake of particles present in the surrounding environment (Bonfanti et al., 2019; Colombo et al., 2017). This behaviour caused a not selective assumption of wMPs via ingestion as occurs in aquatic filter feeding organisms such as copepods, cladocerans and ascidian juveniles (Cole et al., 2013; Messinetti et al., 2018; Rist et al., 2017).

The wMPs fluorescence optical properties facilitated the visualization of fluorescent spots in the intestinal lumen of whole embryos, discriminating them from any other debris physiologically present even in unexposed embryos. Histological and SEM analysis confirmed the presence of heterogeneous sized and shaped particles in the gut lumen and their interaction with the intestinal epithelium. wMPs, without any difference between F1 and F2 fractions, were visible close to or lying on the thin microvilli of enterocytes and sometimes entangled between them as evidenced by SEM images. This suggests a mechanical friction of wMPs on the apical surface of epithelium during intestinal transit depending on their irregular shapes, thus triggering an inflammatory response. It is well established that perturbed conditions such as infections or mechanical injury can induce mucin hypersecretion by goblet cells as a first defence strategy in mammals and fish (Cornick et al., 2015; Pedà et al., 2016). A gut responsiveness in terms of a hyper-secretion of mucus that trapped and enveloped wMPs in *Xenopus* embryos gut was observed. The property of mucus to entrap particles could avoid their contact with enterocytes' microvilli and protect the underlying tissues. Such a role had been highlighted in a previous study on *ex-vivo* pig ileum mucus blanket by implemented atomic force microscope, which proved to be able of binding and trapping particles up to 15 µm in size (Sotres et al., 2017). The mucus trapping ability has been also observed towards plastic microfibers in other mucus secreting epithelia such as the skin of *Sardinia pilchardus* juveniles (Savoca et al., 2020). This finding shows how the mucus hypersecretion is an effective defence strategy already in developing *Xenopus* embryos, and confirms this model as a promising alternative to the use of adults in ingestion toxicology of environmental particles (Bonfanti et al., 2019).

To the best our knowledge, this is the first study that has investigated the interactions of environmentally relevant MPs from waste with *Xenopus* embryos' intestinal epithelium at histological level. In a previous study, De Felice and collaborators (2018) evidenced the ingestion of commercial 3 µm PS beads by *Xenopus* embryos which, although clogging the lumen, did not cause any mechanical damage to the intestinal wall. Our results also confirm that wMPs induced slight damages to the intestinal epithelium, contrary to what we observed in *Xenopus* embryos exposed to more reactive metal-based nanoparticles (Bacchetta et al., 2012; Bonfanti et al., 2015; Colombo et al., 2017).

However, the mucus hypersecretion observed in this study highlights that the irregular shapes of the wMP fragments with sharp edges and rough surfaces and fibre-like structure can represent a physical risk for organism compared to those with spherical smooth shape, confirming the results of previous studies in adult fish (Jabeen et al., 2018). SEM images, where some wMPs appear even inserted into the epithelium, also support this idea.

Furthermore, no evidence that the two wMP fractions could invade

Xenopus embryos by routes other than the gastrointestinal tract were obtained. The same results were obtained also in zebrafish embryos exposed to PS MPs between 72 and 120 hpf, where the oral route was identified as the main one while skin exposure only marginally contributed to uptake and subsequent biodistribution (van Pomeroy et al., 2017). In contrast, PS 70 nm nanoplastics, unlike PS 50 µm, were able to penetrate muscle tissue through the epidermis of the goldfish *Carassius auratus* larvae, causing damage to muscle and nerve fibers (Yang et al., 2020).

For *Xenopus* embryos, the ingestion of environmentally relevant waste MPs does not interfere with growth as long as vitelline platelets are present in the enterocytes, but after 120 hpf the persistence of MPs knots in the gastrointestinal tract could cause obstruction leading to feeding impairment and death as described in *A. obstetricans* tadpoles feeding (from day 5) on periphyton contaminated with MPs (Boyer et al., 2020).

In addition, mucus hypersecretion could alter the physiological diffusion of ions and nutrients as well as the equilibrium of commensal bacteria, which in turn may contribute to chronic inflammatory diseases. For zebrafish embryos, the wMPs mainly impact by delaying hatching which may affect predatory escape behaviour and the later larval developmental stages, thus finally mining the fitness of the species.

5. Conclusion

In conclusion, wMPs obtained from miscellaneous plastic wastes and representative of environmental MP were characterized, confirming the highly heterogeneous size, morphology and composition, with PE and PP as main polymers. Submicrometric particles, as well as the presence of metals and other organic co-contaminants are additional peculiarities of these MP samples. However, our results suggest that the effects of these complex materials are likely related to the shapes, texture surface and size of plastic particles rather than their chemical composition. Although wMPs did not severely interfere with early developmental processes and morphogenesis in zebrafish and *Xenopus*, they were able to establish specific biointeractions, depending on the peculiar structures and timing of the developmental patterning of the two species.

First, we demonstrated that wMPs are able to adhere to zebrafish chorion and delay hatching in a size and concentration dependent manner, without penetrating it, and confirming its role as an efficient physical barrier to micrometric plastic particles. Neither the epidermis nor the ingestion represented significant exposure route for zebrafish embryos to wMPs.

Instead, *Xenopus* embryos become more susceptible to wMPs exposure by ingestion during development. Due to swallowing behaviour, gastrointestinal tract was found to be the target organ of wMPs in this embryo model. The particle accumulation in the digestive diverticula likely produced a mechanical stress at the intestinal epithelium, resulting in blind morphological lesions and in an overproduction of mucus, which attests an irritation response of this tissue. These effects, occurring during development, may endanger the intestinal microenvironment, influence the organism's ability to feed and finally the possibility to correctly develop through larval and metamorphosis processes. Nevertheless, further experiments would be needed to evaluate changes in gene expression or metabolism to fully understand the toxicity of these wMPs.

In conclusion, the results of the present study strengthen the need of improving the knowledge on the biointeractions and mechanistic toxic effects of smaller MPs, including nanoplastics, from environmentally relevant waste plastic mixtures.

Disclaimer

The scientific output expressed does not imply a policy position of the European Commission. Neither the European Commission nor any

person acting on behalf of the Commission is responsible for the use that might be made of this publication.

Funding

This work was supported by ECOPAVE Project, Call Accordi per la Ricerca e l'Innovazione Cofin. POR FESR 2014–2020, Regione Lombardia.

CRedit authorship contribution statement

Patrizia Bonfanti: Conceptualization, Methodology, Formal analysis, Writing – original draft, Writing – review & editing. **Anita Colombo:** Conceptualization, Methodology, Formal analysis, Writing – original draft, Writing – review & editing. **Melissa Saibene:** Investigation (FETAX test, LM, FM and SEM analysis), Formal analysis. **Giulia Motta:** Investigation (FET, FETAX test, LM and FM analysis). **Francesco Saliu:** Methodology, Investigation, Chemical analysis (ATR-FTIR). **Tiziano Catelani:** Methodology, Morphological analysis (SEM). **Dora Mehn:** Methodology, Investigation (Raman analysis). **Rita La Spina:** Methodology, Investigation (TXRF). **Jessica Ponti:** Methodology, Investigation (TEM-EDX analysis). **Claudia Cella:** Methodology, Investigation (Mastersizer analysis). **Pamela Floris:** Methodology, Investigation (FET, LM and FM analysis). **Paride Mantecca:** Conceptualization, Resources, Writing – review & editing, Supervision.

Declaration of Competing Interest

The authors declare that they have no known competing financial interests or personal relationships that could have appeared to influence the work reported in this paper.

Acknowledgements

This paper is dedicated to the memory of Prof. Marina Camatini, President of the Research Center POLARIS, University of Milano-Bicocca. Part of experimental data used in this research were generated through access to the Nanobiotechnology Laboratory under the Framework of access to the Joint Research Centre Physical Research Infrastructures of the European Commission (Wasteplastics project, Research Infrastructure Access Agreement Nr. RIAA_35559). Authors thanks Pascal Colpo, Giacomo Ceccone, Francesco Fumagalli, European Commission, Joint Research Centre – Ispra. Authors wish also to thank the companies involved in the project ECOPAVE for the production of the waste plastic granules (Itechimica srl, GEco srl) and the precious technical support of Mr. S. Cisani in this phase.

Appendix A. Supporting information

Supplementary data associated with this article can be found in the online version at [doi:10.1016/j.ecoenv.2021.112775](https://doi.org/10.1016/j.ecoenv.2021.112775).

References

- Alimi, O.S., Farnier Budarz, J., Hernandez, L.M., Tufenkji, N., 2018. Microplastics and nanoplastics in aquatic environments: aggregation, deposition, and enhanced contaminant transport. *Environ. Sci. Technol.* 52, 1704–1724. <https://doi.org/10.1021/acs.est.7b05559>.
- Alomar, C., Deudero, S., 2017. Evidence of microplastic ingestion in the shark *Galeus melastomus Rafinesque*, 1810 in the continental shelf off the western Mediterranean Sea. *Environ. Pollut.* 223, 223–229. <https://doi.org/10.1016/j.envpol.2017.01.015>.
- Andrady, A.L., 2011. Microplastics in the marine environment. *Mar. Pollut. Bull.* 62, 1596–1605. <https://doi.org/10.1016/j.marpolbul.2011.05.030>.
- Andrady, A.L., 2017. The plastic in microplastics: a review. *Mar. Pollut. Bull.* 119, 12–22. <https://doi.org/10.1016/j.marpolbul.2017.01.082>.
- ASTM, A.S. for T., 1998. Standard guide for conducting the frog embryo teratogenesis assay—*Xenopus* (FETAX). *Am. Soc. Test. Mater. Int.*
- Auta, H.S., Emenike, C.U., Fauziyah, S.H., 2017. Distribution and importance of microplastics in the marine environment: a review of the sources, fate, effects, and

- potential solutions. *Environ. Int.* 102, 165–176. <https://doi.org/10.1016/j.envint.2017.02.013>.
- Bacchetta, R., Santo, N., Fascio, U., Moschini, E., Freddi, S., Chirico, G., Camatini, M., Mantecca, P., 2012. Nano-sized CuO, TiO₂ and ZnO affect *Xenopus laevis* development. *Nanotoxicology* 6, 381–398. <https://doi.org/10.3109/17435390.2011.579634>.
- Barnes, D.K.A., Galgani, F., Thompson, R.C., Barlaz, M., 2009. Accumulation and fragmentation of plastic debris in global environments. *Philos. Trans. R. Soc. B Biol. Sci.* 364, 1985–1998. <https://doi.org/10.1098/rstb.2008.0205>.
- Batel, A., Borchert, F., Reinwald, H., Erdinger, L., Braunbeck, T., 2018. Microplastic accumulation patterns and transfer of benzo[a]pyrene to adult zebrafish (*Danio rerio*) gills and zebrafish embryos. *Environ. Pollut.* 235, 918–930. <https://doi.org/10.1016/j.envpol.2018.01.028>.
- Bobba, S., Marques Dos Santos, F., Maury, T., Tecchio, P., Mehn, D., Weiland, F., Pekar, F., Mathieux, F., Ardente, F., 2021. Sustainable use of Materials through automotive remanufacturing to boost resource efficiency in the road transport system (SMART). *Publ. Off. Eur. Union, Luxemb.* <https://doi.org/10.2760/84767>.
- Bolis, A., Gazzola, A., Pellitteri-Rosa, D., Colombo, A., Bonfanti, P., Bellati, A., 2020. Exposure during embryonic development to Roundup® Power 2.0 affects lateralization, level of activity and growth, but not defensive behaviour of marsh frog tadpoles. *Environ. Pollut.* 263, 114395. <https://doi.org/10.1016/j.envpol.2020.114395>.
- Bonfanti, P., Moschini, E., Saibene, M., Bacchetta, R., Rettighieri, L., Calabri, L., Colombo, A., Mantecca, P., 2015. Do nanoparticle physico-chemical properties and developmental exposure window influence nano ZnO embryotoxicity in *Xenopus laevis*? *Int. J. Environ. Res. Public Health* 12, 8828–8848. <https://doi.org/10.3390/ijerph12088828>.
- Bonfanti, P., Colombo, A., Saibene, M., Fiandra, L., Armenia, I., Gamberoni, F., Gornati, R., Bernardini, G., Mantecca, P., 2019. Iron nanoparticle bio-interactions evaluated in *Xenopus laevis* embryos, a model for studying the safety of ingested nanoparticles. *Nanotoxicology* 14, 196–213. <https://doi.org/10.1080/17435390.2019.1685695>.
- Botterell, Z.L.R., Beaumont, N., Dorrington, T., Steinke, M., Thompson, R.C., Lindeque, P. K., 2019. Bioavailability and effects of microplastics on marine zooplankton: a review. *Environ. Pollut.* 245, 98–110. <https://doi.org/10.1016/j.envpol.2018.10.065>.
- Bouwmeester, H., Hollman, P.C.H., Peters, R.J.B., 2015. Potential health impact of environmentally released micro- and nanoplastics in the human food production Chain: experiences from nanotoxicology. *Environ. Sci. Technol.* 49, 8932–8947. <https://doi.org/10.1021/acs.est.5b01090>.
- Boyer, L., López-Rojas, N., Bosch, J., Alonso, A., Correa-Araneda, F., Pérez, J., 2020. Microplastics impair amphibian survival, body condition and function. *Chemosphere* 244, 125500. <https://doi.org/10.1016/j.chemosphere.2019.125500>.
- Browne, M.A., Dissanayake, A., Galloway, T.S., Lowe, D.M., Thompson, R.C., 2008. Ingested microscopic plastic translocates to the circulatory system of the mussel, *Mytilus edulis* (L.). *Environ. Sci. Technol.* 42, 5026–5031. <https://doi.org/10.1021/es800249a>.
- Browne, M.A., Niven, S.J., Galloway, T.S., Rowland, S.J., Thompson, R.C., 2013. Microplastic moves pollutants and additives to worms, reducing functions linked to health and biodiversity. *Curr. Biol.* 23, 2388–2392. <https://doi.org/10.1016/j.cub.2013.10.012>.
- Carbery, M., O'connor, W., Thavamani, P., 2018. Trophic transfer of microplastics and mixed contaminants in the marine food web and implications for human health. *Environ. Int.* 115, 400–409. <https://doi.org/10.1016/j.envint.2018.03.007>.
- Cau, A., Avio, C.G., Dessì, C., Follesa, M.C., Moccia, D., Regoli, F., Puseddu, A., 2019. Microplastics in the crustaceans *Nepherops norvegicus* and *Aristeus antennatus*: Flagship species for deep-sea environments? *Environ. Pollut.* 255, 113107. <https://doi.org/10.1016/j.envpol.2019.113107>.
- Chen, Q., Allgeier, A., Yin, D., Hollert, H., 2019. Leaching of endocrine disrupting chemicals from marine microplastics and mesoplastics under common life stress conditions. *Environ. Int.* 130, 104938. <https://doi.org/10.1016/j.envint.2019.104938>.
- Cole, M., Lindeque, P., Halsband, C., Galloway, T.S., 2011. Microplastics as contaminants in the marine environment: a review. *Mar. Pollut. Bull.* 62, 2588–2597. <https://doi.org/10.1016/j.marpolbul.2011.09.025>.
- Cole, M., Lindeque, P., Fileman, E., Halsband, C., Goodhead, R., Moger, J., Galloway, T. S., 2013. Microplastic ingestion by zooplankton. *Environ. Sci. Technol.* 47, 6646–6655. <https://doi.org/10.1021/es400663f>.
- Colombo, A., Saibene, M., Moschini, E., Bonfanti, P., Collini, M., Kasemets, K., Mantecca, P., 2017. Teratogenic hazard of BPEI-coated silver nanoparticles to *Xenopus laevis*. *Nanotoxicology* 11, 405–418. <https://doi.org/10.1080/17435390.2017.1309703>.
- Cornick, S., Tawiah, A., Chadec, K., 2015. Roles and regulation of the mucus barrier in the gut. *Tissue Barriers* 3, 982426. <https://doi.org/10.4161/21688370.2014.982426>.
- Cowger, W., Steinmetz, Z., Gray, A., Munno, K., Lynch, J., Hapich, H., Primpke, S., De Frond, H., Rochman, C., Herodotou, O., et al., 2021. Microplastic Spectral Classification Needs an Open Source Community: Open Specky to the Rescue! *Analytical Chem.* <https://doi.org/10.1021/acs.analchem.1c00123>.
- De Felice, B., Bacchetta, R., Santo, N., Tremolada, P., Parolini, M., 2018. Polystyrene microplastics did not affect body growth and swimming activity in *Xenopus laevis* tadpoles. *Environ. Sci. Pollut. Res.* 25, 34644–34651. <https://doi.org/10.1007/s11356-018-3408-x>.
- Duan, Z., Duan, X., Zhao, S., Wang, X., Wang, J., Liu, Y., Peng, Y., Gong, Z., Wang, L., 2020. Barrier function of zebrafish embryonic chorions against microplastics and nanoplastics and its impact on embryo development. *J. Hazard. Mater.* 395, 122621. <https://doi.org/10.1016/j.jhazmat.2020.122621>.
- EFSA, 2016. Presence of microplastics and nanoplastics in food, with particular focus on seafood. *EFSA J.* 14, 4501. <https://doi.org/10.2903/j.efsa.2016.4501>.
- Eitzen, L., Paul, S., Braun, U., Altmann, K., Jekel, M., Ruhl, A.S., 2019. The challenge in preparing particle suspensions for aquatic microplastic research. *Environ. Res.* 168, 490–495. <https://doi.org/10.1016/j.envres.2018.09.008>.
- El Hadri, H., Gigault, J., Maxit, B., Grassl, B., Reynaud, S., 2020. Nanoplastic from mechanically degraded primary and secondary microplastics for environmental assessments. *NanoImpact* 17, 100206. <https://doi.org/10.1016/j.impact.2019.100206>.
- Eriksen, M., Lebreton, L.C.M., Carson, H.S., Thiel, M., Moore, C.J., Borero, J.C., Galgani, F., Ryan, P.G., Reisser, J., 2014. Plastic pollution in the world's oceans: more than 5 trillion plastic pieces weighing over 250,000 tons afloat at sea. *PLoS One* 9, 111913. <https://doi.org/10.1371/journal.pone.0111913>.
- Espinosa, C., Esteban, M.A., Cuesta, A., 2019. Dietary administration of PVC and PE microplastics produces histological damage, oxidative stress and immunoregulation in European sea bass (*Dicentrarchus labrax* L.). *Fish Shellfish Immunol.* 95, 574–583. <https://doi.org/10.1016/j.fsi.2019.10.072>.
- Felsing, S., Kochleus, C., Buchinger, S., Brennholt, N., Stock, F., Reifferscheid, G., 2018. A new approach in separating microplastics from environmental samples based on their electrostatic behavior. *Environ. Pollut.* 234, 20–28. <https://doi.org/10.1016/j.envpol.2017.11.013>.
- Fendall, L.S., Sewell, M.A., 2009. Contributing to marine pollution by washing your face: microplastics in facial cleansers. *Mar. Pollut. Bull.* 58, 1225–1228. <https://doi.org/10.1016/j.marpolbul.2009.04.025>.
- Fiandra, L., Bonfanti, P., Piuono, Y., Navgenkar, A.P., Perlestein, I., Gedanken, A., Saibene, M., Colombo, A., Mantecca, P., 2020. Hazard assessment of polymer-capped CuO and ZnO nanocolloids: a contribution to the safe-by-design implementation of biocidal agents. *NanoImpact* 17, 100195. <https://doi.org/10.1016/j.impact.2019.100195>.
- Finney, D.J., 1971. *Probit Analysis*. Cambridge Univ. Press, London.
- Fu, W., Min, J., Jiang, W., Li, Y., Zhang, W., 2020. Separation, characterization and identification of microplastics and nanoplastics in the environment. *Sci. Total Environ.* 721, 137561. <https://doi.org/10.1016/j.scitotenv.2020.137561>.
- GESAMP Joint Group of Experts on the Scientific Aspects of Marine Environmental Protection, 2015. Sources, fate and effects of microplastics in the marine environment: a global assessment. Reports Stud. GESAMP 90, 96. <https://doi.org/10.13140/RG.2.1.3803.7925>.
- Geyer, R., Jambeck, J.R., Law, K.L., 2017. Production, use, and fate of all plastics ever made. *Sci. Adv.* 3, 1700782. <https://doi.org/10.1126/sciadv.1700782>.
- Giani, D., Baini, M., Galli, M., Casini, S., Fossi, M.C., 2019. Microplastics occurrence in edible fish species (*Mullus barbatus* and *Merluccius merluccius*) collected in three different geographical sub-areas of the Mediterranean Sea. *Mar. Pollut. Bull.* 140, 129–137. <https://doi.org/10.1016/j.marpolbul.2019.01.005>.
- Gigault, J., Pedrono, B., Maxit, B., Ter Halle, A., 2016. Marine plastic litter: the unanalyzed nano-fraction. *Environ. Sci. Nano* 3, 346–350. <https://doi.org/10.1039/c6en00008h>.
- Haque, E., Ward, A., 2018. Zebrafish as a model to evaluate nanoparticle toxicity. *Nanomaterials* 8, 561. <https://doi.org/10.3390/nano8070561>.
- Hawkins, K.R., Yager, P., 2003. Nonlinear decrease of background fluorescence in polymer thin-films - a survey of materials and how they can complicate fluorescence detection in μ TAS. *Lab Chip* 3, 248–252. <https://doi.org/10.1039/b307772c>.
- Jabeen, K., Li, B., Chen, Q., Su, L., Wu, C., Hollert, H., Shi, H., 2018. Effects of virgin microplastics on goldfish (*Carassius auratus*). *Chemosphere* 213, 323–332. <https://doi.org/10.1016/j.chemosphere.2018.09.031>.
- Koongolla, J.B., Lin, L., Pan, Y.F., Yang, C.P., Sun, D.R., Liu, S., Xu, X.R., Maharana, D., Huang, J.S., Li, H.X., 2020. Occurrence of microplastics in gastrointestinal tracts and gills of fish from Beibu Gulf, South China Sea. *Environ. Pollut.* 258, 113734. <https://doi.org/10.1016/j.envpol.2019.113734>.
- Law, K.L., 2017. Plastics in the Marine Environment. *Ann. Rev. Mar. Sci.* 9, 205–229. <https://doi.org/10.1146/annurev-marine-010816-060409>.
- Lee, H., Shim, W.J., Kwon, J.H., 2014. Sorption capacity of plastic debris for hydrophobic organic chemicals. *Sci. Total Environ.* 470–471, 1545–1552. <https://doi.org/10.1016/j.scitotenv.2013.08.023>.
- Lei, L., Wu, S., Lu, S., Liu, M., Song, Y., Fu, Z., Shi, H., Raley-Susman, K.M., He, D., 2018. Microplastic particles cause intestinal damage and other adverse effects in zebrafish *Danio rerio* and nematode *Caenorhabditis elegans*. *Sci. Total Environ.* 619–620, 1–8. <https://doi.org/10.1016/j.scitotenv.2017.11.103>.
- Lema, S.C., Schultz, I.R., Scholz, N.L., Incardona, J.P., Swanson, P., 2007. Neural defects and cardiac arrhythmia in fish larvae following embryonic exposure to 2,2',4,4'-tetrabromodiphenyl ether (PBDE 47). *Aquat. Toxicol.* 82, 296–307. <https://doi.org/10.1016/j.aquatox.2007.03.002>.
- Li, C., Busquets, R., Campos, L.C., 2020. Assessment of microplastics in freshwater systems: a review. *Sci. Total Environ.* <https://doi.org/10.1016/j.scitotenv.2019.135578>.
- Lu, Y., Zhang, Y., Deng, Y., Jiang, W., Zhao, Y., Geng, J., Ding, L., Ren, H., 2016. Uptake and accumulation of polystyrene microplastics in zebrafish (*Danio rerio*) and toxic effects in liver. *Environ. Sci. Technol.* 50, 4054–4060. <https://doi.org/10.1021/acs.est.6b00183>.
- Lusher, A., 2015. Microplastics in the marine environment: distribution, interactions and effects. In: *Marine Anthropogenic Litter*. Springer International Publishing, pp. 245–307. https://doi.org/10.1007/978-3-319-16510-3_10.
- Manabe, M., Tatarazako, N., Kinoshita, M., 2011. Uptake, excretion and toxicity of nano-sized latex particles on medaka (*Oryzias latipes*) embryos and larvae. *Aquat. Toxicol.* 105, 576–581. <https://doi.org/10.1016/j.aquatox.2011.08.020>.

- Mantecca, P., Moschini, E., Bonfanti, P., Fascio, U., Perelshtein, I., Lipovsky, A., Chirico, G., Bacchetta, R., Del Giacco, L., Colombo, A., Gedanken, A., 2015. Toxicity evaluation of a new Zn-doped CuO nanocomposite with highly effective antibacterial properties. *Toxicol. Sci.* 146, 16–30. <https://doi.org/10.1093/toxsci/kfv067>.
- Markic, A., Gaertner, J.C., Gaertner-Mazouini, N., Koelmans, A.A., 2019. Plastic ingestion by marine fish in the wild. *Crit. Rev. Environ. Sci. Technol.* 50, 657–697. <https://doi.org/10.1080/10643389.2019.1631990>.
- Mazurais, D., Ermande, B., Quazuquel, P., Severe, A., Huelvan, C., Madec, L., Mouchel, O., Soudant, P., Robbens, J., Huvet, A., Zambonino-Infante, J., 2015. Evaluation of the impact of polyethylene microbeads ingestion in European sea bass (*Dicentrarchus labrax*) larvae. *Mar. Environ. Res.* 112, 78–85. <https://doi.org/10.1016/j.marenvres.2015.09.009>.
- Messinetti, S., Mercurio, S., Parolini, M., Sugni, M., Pennati, R., 2018. Effects of polystyrene microplastics on early stages of two marine invertebrates with different feeding strategies. *Environ. Pollut.* 237, 1080–1087. <https://doi.org/10.1016/j.envpol.2017.11.030>.
- Naidoo, T., Glassom, D., 2019. Decreased growth and survival in small juvenile fish, after chronic exposure to environmentally relevant concentrations of microplastic. *Mar. Pollut. Bull.* 145, 254–259. <https://doi.org/10.1016/j.marpolbul.2019.02.037>.
- Neves, D., Sobral, P., Ferreira, J.L., Pereira, T., 2015. Ingestion of microplastics by commercial fish off the Portuguese coast. *Mar. Pollut. Bull.* 101, 119–126. <https://doi.org/10.1016/j.marpolbul.2015.11.008>.
- Ng, A.N.Y., De Jong-Curtain, T.A., Mawdsley, D.J., White, S.J., Shin, J., Appel, B., Dong, P.D.S., Stainier, D.Y.R., Heath, J.K., 2005. Formation of the digestive system in zebrafish: III. Intestinal epithelium morphogenesis. *Dev. Biol.* 286, 114–135. <https://doi.org/10.1016/j.ydbio.2005.07.013>.
- Nieuwkoop, P., Faber, J., 1956. Nieuwkoop PD, Faber J (1956) Normal table of *Xenopus laevis* (DAUDIN). A systematic and chronological survey of the development from the fertilized egg till the end. Amsterdam: North Holland Publishing Co. 260 p. - Open Access Library [WWW Document]. <https://www.oalib.com/references/10915515> (Accessed 21 July 2020).
- Nobre, C.R., Santana, M.F.M., Maluf, A., Cortez, F.S., Cesar, A., Pereira, C.D.S., Turra, A., 2015. Assessment of microplastic toxicity to embryonic development of the sea urchin *Lytechinus variegatus* (Echinodermata: Echinoidea). *Mar. Pollut. Bull.* 92, 99–104. <https://doi.org/10.1016/j.marpolbul.2014.12.050>.
- O'Donovan, S., Mestre, N.C., Abel, S., Fonseca, T.G., Carteny, C.C., Cormier, B., Keiter, S. H., Bebianno, M.J., 2018. Ecotoxicological effects of chemical contaminants adsorbed to microplastics in the Clam *Scrobicularia plana*. *Front. Mar. Sci.* 5, 143. <https://doi.org/10.3389/fmars.2018.00143>.
- OECD, 2013. Test No. 236: Fish Embryo Acute Toxicity (FET) Test. OECD Guidel. Test. Chem. Sect. 2, OECD Publ. 1–22. <https://doi.org/10.1787/9789264203709-en>.
- Ong, K.J., Zhao, X., Thistle, M.E., Maccormack, T.J., Clark, R.J., Ma, G., Martinez-Rubi, Y., Simard, B., Loo, J.S.C., Veinot, J.G.C., Goss, G.G., 2014. Mechanistic insights into the effect of nanoparticles on zebrafish hatch. *Nanotoxicology* 8, 295–304. <https://doi.org/10.3109/17435390.2013.778345>.
- Pannetier, P., Morin, B., Le Bihanic, F., Dubreil, L., Clérandeau, C., Chouvellon, F., Van Arkel, K., Danion, M., Cachot, J., 2020. Environmental samples of microplastics induce significant toxic effects in fish larvae. *Environ. Int.* 134, 105047. <https://doi.org/10.1016/j.envint.2019.105047>.
- Pedà, C., Caccamo, L., Fossi, M.C., Gai, F., Andaloro, F., Genovese, L., Perdicchi, A., Romeo, T., Maricchiolo, G., 2016. Intestinal alterations in European sea bass *Dicentrarchus labrax* (Linnaeus, 1758) exposed to microplastics: preliminary results. *Environ. Pollut.* 212, 251–256. <https://doi.org/10.1016/j.envpol.2016.01.083>.
- Phuong, N.N., Zalouk-Vergnoux, A., Poirier, L., Kamari, A., Châtel, A., Mouneyrac, C., Lagarde, F., 2016. Is there any consistency between the microplastics found in the field and those used in laboratory experiments? *Environ. Pollut.* 211, 111–123. <https://doi.org/10.1016/j.envpol.2015.12.035>.
- Pitt, J.A., Kozal, J.S., Jayasundara, N., Massarsky, A., Trevisan, R., Geitner, N., Wiesner, M., Levin, E.D., Di Giulio, R.T., 2018. Uptake, tissue distribution, and toxicity of polystyrene nanoparticles in developing zebrafish (*Danio rerio*). *Aquat. Toxicol.* 194, 185–194. <https://doi.org/10.1016/j.aquatox.2017.11.017>.
- Qiu, Q., Peng, J., Yu, X., Chen, F., Wang, J., Dong, F., 2015. Occurrence of microplastics in the coastal marine environment: first observation on sediment of China. *Mar. Pollut. Bull.* 98, 274–280. <https://doi.org/10.1016/j.marpolbul.2015.07.028>.
- Rainieri, S., Conlledo, N., Larsen, B.K., Granby, K., Barranco, A., 2018. Combined effects of microplastics and chemical contaminants on the organ toxicity of zebrafish (*Danio rerio*). *Environ. Res.* 162, 135–143. <https://doi.org/10.1016/j.envres.2017.12.019>.
- Rist, S., Hartmann, N.B., 2018. Aquatic ecotoxicity of microplastics and nanoplastics: lessons learned from engineered nanomaterials. In: *Handbook of Environmental Chemistry*. Springer Verlag, pp. 25–49. https://doi.org/10.1007/978-3-319-61615-5_2.
- Rist, S., Baun, A., Hartmann, N.B., 2017. Ingestion of micro- and nanoplastics in *Daphnia magna* – quantification of body burdens and assessment of feeding rates and reproduction. *Environ. Pollut.* 228, 398–407. <https://doi.org/10.1016/j.envpol.2017.05.048>.
- de Sá, L.C., Oliveira, M., Ribeiro, F., Rocha, T.L., Futter, M.N., 2018. Studies of the effects of microplastics on aquatic organisms: what do we know and where should we focus our efforts in the future? *Sci. Total Environ.* 645, 1029–1039. <https://doi.org/10.1016/j.scitotenv.2018.07.207>.
- Savoca, S., Bottari, T., Fazio, E., Bonsignore, M., Mancuso, M., Luna, G.M., Romeo, T., D'Urso, L., Capillo, G., Panarello, G., Greco, S., Compagnini, G., Lanteri, G., Crupi, R., Neri, F., Spanò, N., 2020. Plastics occurrence in juveniles of *Engraulis encrasicolus* and *Sardina pilchardus* in the Southern Tyrrhenian Sea. *Sci. Total Environ.* 718, 137457. <https://doi.org/10.1016/j.scitotenv.2020.137457>.
- Setälä, O., Fleming-Lehtinen, V., Lehtiniemi, M., 2014. Ingestion and transfer of microplastics in the planktonic food web. *Environ. Pollut.* 185, 77–83. <https://doi.org/10.1016/j.envpol.2013.10.013>.
- Sfriso, A.A., Tomio, Y., Rosso, B., Gambaro, A., Sfriso, A., Corami, F., Rastelli, E., Corinaldesi, C., Mistri, M., Munari, C., 2020. Microplastic accumulation in benthic invertebrates in Terra Nova Bay (Ross Sea, Antarctica). *Environ. Int.* 137, 105587. <https://doi.org/10.1016/j.envint.2020.105587>.
- Simon, S., Röhrs, S., 2018. Between fakes, forgeries, and illicit artifacts—authenticity studies in a heritage science laboratory. *Arts* 7, 20. <https://doi.org/10.3390/arts7020020>.
- Song, Y.K., Hong, S.H., Jang, M., Han, G.M., Jung, S.W., Shim, W.J., 2017. Combined effects of UV exposure duration and mechanical abrasion on microplastic fragmentation by polymer type. *Environ. Sci. Technol.* 51, 4368–4376. <https://doi.org/10.1021/acs.est.6b06155>.
- Sotres, J., Jankovskaja, S., Wannerberger, K., Arnebrant, T., 2017. Ex-vivo force spectroscopy of intestinal mucosa reveals the mechanical properties of mucus blankets. *Sci. Rep.* 7, 1–14. <https://doi.org/10.1038/s41598-017-07552-7>.
- Ter Halle, A., Jeanneau, L., Martignac, M., Jardé, E., Pedrono, B., Brach, L., Gigault, J., 2017. Nanoplastic in the North Atlantic subtropical gyre. *Environ. Sci. Technol.* 51, 13689–13697. <https://doi.org/10.1021/acs.est.7b03667>.
- van Pomeroy, M., Brun, N.R., Peijnenburg, W.J.G.M., Vijver, M.G., 2017. Exploring uptake and biodistribution of polystyrene (nano)particles in zebrafish embryos at different developmental stages. *Aquat. Toxicol.* 190, 40–45. <https://doi.org/10.1016/j.aquatox.2017.06.017>.
- Wang, F., Wong, C.S., Chen, D., Lu, X., Wang, F., Zeng, E.Y., 2018. Interaction of toxic chemicals with microplastics: a critical review. *Water Res.* <https://doi.org/10.1016/j.watres.2018.04.003>.
- Wang, Z.M., Wagner, J., Ghosal, S., Bedi, G., Wall, S., 2017. SEM/EDS and optical microscopy analyses of microplastics in ocean trawl and fish guts. *Sci. Total Environ.* 603–604, 616–626. <https://doi.org/10.1016/j.scitotenv.2017.06.047>.
- Yang, H., Xiong, H., Mi, K., Xue, W., Wei, W., Zhang, Y., 2020. Toxicity comparison of nano-sized and micron-sized microplastics to Goldfish *Carassius auratus* Larvae. *J. Hazard. Mater.* 388, 122058. <https://doi.org/10.1016/j.jhazmat.2020.122058>.
- Zhang, R., Silic, M.R., Schaber, A., Wasel, O., Freeman, J.L., Sepúlveda, M.S., 2020. Exposure route affects the distribution and toxicity of polystyrene nanoplastics in zebrafish. *Sci. Total Environ.* 724, 138065. <https://doi.org/10.1016/j.scitotenv.2020.138065>.

Supporting Information

Microplastics from miscellaneous plastic wastes: physico-chemical characterization and impact on fish and amphibian development

*Patrizia Bonfanti^{1§}, Anita Colombo^{1§}, Melissa Saibene¹, Giulia Motta¹, Francesco Saliu¹,
Tiziano Catelani², Dora Mehn³, Rita La Spina³, Jessica Ponti³, Claudia Cella³, Pamela
Floris¹, Paride Mantecca^{1*}*

¹ *Department of Earth and Environmental Sciences, Research Centre POLARIS, University of Milano – Bicocca, Piazza
della Scienza 1, 20126 Milano, Italy*

² *Interdepartmental Microscopy Platform, University of Milano – Bicocca Piazza della Scienza 2, 20126 Milano, Italy*

³ *European Commission, Joint Research Centre (JRC), , Italy*

This Supporting Information document (SI) contains one text section, four figures and 4
tables

[§] These authors contributed equally to the work

* Corresponding author (paride.mantecca@unimib.it)

S1: Chemicals

All analytical-grade reagents, human chorionic gonadotropin (HCG), 3-amino-benzoic acid ethyl ester (MS222), hydrochloric acid, nitric acid, ethanol, hydrogen peroxide and Triton X-100, reagents for histology and scanning and transmission electron microscopy analysis, salts for FETAX and FET solution, except Instant Ocean (Aquarium systems, Sarrebourg, France) were purchased from Sigma-Aldrich S.r.l., Italy.

S2: Production of waste plastic granules and microparticles

Plastic wastes of miscellaneous origin were collected, separated manually from the eventual metallic parts and then transferred to a plastic recycling plant, where, after washing and controlled flotation, were mechanically fragmented to obtain plastic granulates (Figure S1 A). Granulates were additionally milled and grinded to achieve fine plastic granules with size less than 3 mm (Figure S1 B).

The plastic granulates obtained were transferred to the laboratory and mechanically sieved using stainless steel sieves with decreasing mesh sizes (1 mm – 500 μm – 250 μm – 150 μm – 100 μm – 50 μm). The residual fraction from each sieve was stored in glass vials (Figure S1 C) to perform ATR-FTIR analysis.

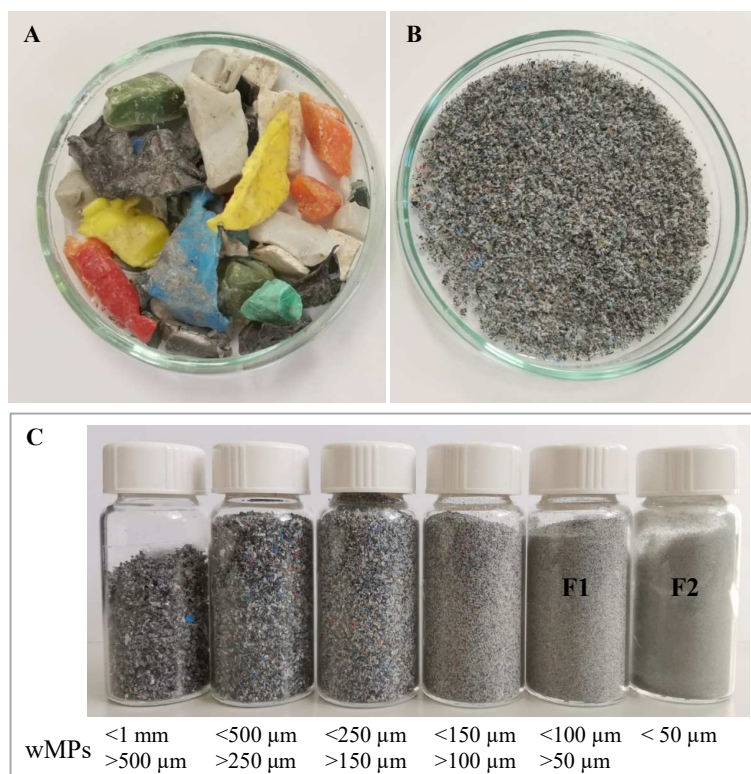


Figure S1. Waste microplastic (wMP) granulates. Large plastic granulates obtained by mechanical fragmentation of collected plastic waste (A), fine plastic granules with size less than 3 mm (B) achieved by additional milling and residual wMP fractions recovered after sieving (C). It is appreciable the decreasing graininess in all fractions. The two finest wMP fractions named F1 and F2 were used for chemical-physical and toxicological analyses.

S3: Animals

Wild-type (AB strain) zebrafish were maintained in a breeding colony at University of Milano-Bicocca, Dept. of Environmental and Earth Sciences (Italy), according to standard zebrafish breeding protocols. Adults were maintained at 28 °C with a lighting schedule of 14 h light and 10 h dark in a closed flow-through system (TECNIPLAST, BUGUGGIATE Italy). Water supplied to the system was filtered by reverse osmosis (pH 7.5–8), and Instant Ocean® salt was added to the water to raise the conductivity to ~1500 S/cm (system water).

Zebrafish embryos were obtained from natural spawning of adult wild-type AB line zebrafish pairs. Two pairs of breeders were located in breeding tanks (n=3) and separated by sex with a barrier overnight (ON). The next morning at the onset of light, the barrier was removed and adults were allowed to mate. Fertilized eggs from each tank were collected in a strainer within 30 min after mating, rinsed several times in FET solution to eliminate faeces and scales, then selected under a stereomicroscope (Zeiss, Germany) to remove unfertilized eggs and damaged embryos.

Table S1. Functional groups at the corresponding FTIR spectra

Wavenumbers (cm ⁻¹)	Assignment	Detection in samples
3200 – 3450	OH - stretching (intermolecular)	2
2950	C-H stretching (PP)	21
2916	C-H asymmetric stretching (PE)	24
2840	C-H asymmetric stretching (PE)	
1719	C=O stretching (possible oxidation)	7
1635	C=C (alkene)	3
1466	CH bending (alkane)	24
1380	OH bending	2
1377-1366	C-H bend; CH ₂ and CH ₃ groups	23
1352	C-H bend; CH ₂ and CH ₃ groups wagging	3
1306	Twisting deformation	7
1170	Wagging deformation	10
1167	C-O	6
1017		9
997	C=C (alkene)	3
973-968	C=C (alkene)	16
874-879		19
730-719	CH ₂ rocking	24

Note:

Numbers reported in the “Detection in samples” column are the frequencies that the specified peak might be observed in the 24 analysis (four aliquots from each of the 6 fractions)

Table S2. TXRF result for wMP F1 and F2 fractions

Atomic number	Element	F1			F2		
		mg/g	SD	RSD (%)	mg/g	SD	RSD (%)

20	Calcium	0.3893	0.0409	10.5198	3.3442	0.3713	11.1031
22	Titanium	0.0036	0.0014	39.023	0.0124	0.0021	16.8583
24	Chromium	0.0033	0.0005	14.3312	0.0140	0.0022	15.5668
26	Iron	0.0993	0.0057	5.7700	0.3886	0.0338	8.6990
28	Nickel	0.0011	0.0003	26.1586	0.0094	0.0014	14.4602
29	Copper	ND	-	-	0.0164	0.0022	13.2366
30	Zinc	0.0085	0.0012	14.1373	0.0257	0.0036	13.9178
82	Lead	0.0141	0.0005	3.8858	0.0244	0.0035	14.4460

Note:

The following elements were considered for spectrum deconvolution: Aluminium, Sulfur, Calcium, Titanium, Chromium

Manganese, Iron, Nickel, Copper, Zinc, Bromine, Strontium, Zirconium, Palladium, Silver, Tin, Antimony, Barium, Gold, Lead. The amount of single elements is expressed as mg of the element per unit (in gram) of the starting material. All values are presented as the mean \pm standard deviation (SD) and the percent relative standard deviation per each element (% RSD). ND= Not Detectable

Table S3. D₁₀, D₅₀ and D₉₀ values for the volume size distribution of the wMPs fractions F1 and F2.

	Dx (10) (μ m)	Dx (50) (μ m)	Dx (90) (μ m)
F1 (ethanol)	79.523 \pm 0.515	192.443 \pm 5.967	662.851 \pm 77.253
F2 (ethanol)	31.047 \pm 0.029	60.682 \pm 0.236	141.659 \pm 4.660
F1 (Triton X-100)	62.830 \pm 0.978	118.010 \pm 1.908	241.540 \pm 10.445
F2 (Triton X-100)	29.618 \pm 0.161	59.595 \pm 0.640	127.334 \pm 8.933

Note:

D₅₀ represents the average particle size, which means 50% of the particles' size was below the reported value.

D₁₀ and D₉₀ mean that 10 and 90% of the particles' size were less than the corresponding values, respectively.

Data are referred to average \pm SD of five replicates.

Table S4. Median hatching time (HT₅₀) of zebrafish embryos at different concentrations of wMPs

	Control	(mg/L)			
		0.1	1	10	100
F1	65.89 \pm 1.74	68.66 \pm 7.45	67.21 \pm 3.22	68.99 \pm 0.28*	70.84 \pm 2.32*
F2		69.98 \pm 10.19	74.30 \pm 4.4*	72.51 \pm 3.34*	74.54 \pm 1.79*

Note:

HT50 stands for time, expressed as hpf, required for 50% hatching of embryos

All values are presented as the mean \pm standard deviation
* $p < 0.05$ versus the control group.

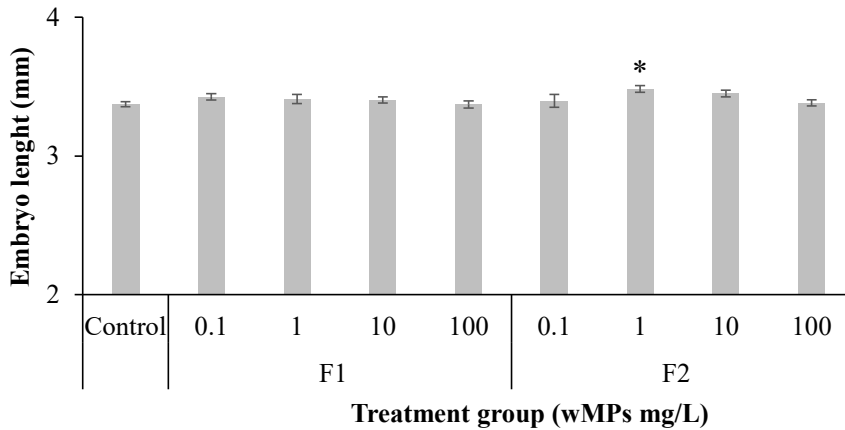


Figure S2. Head-tail length in 96 hpf zebrafish embryos after exposure to F1 and F2 fractions (0.1-100 mg/L). All values are given as mean \pm SE of three independent assays. (*) statistically different from control ($p < 0.05$, ANOVA + Fisher LSD Method).

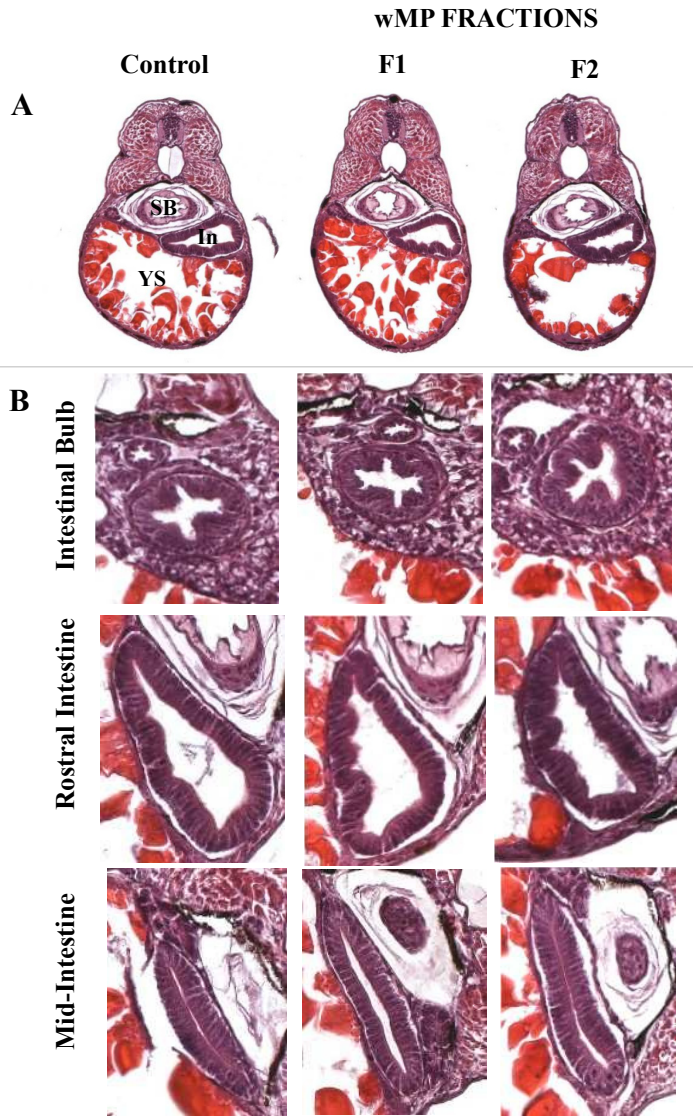


Figure S3. Histological transversal sections of Zebrafish embryos at 96 hpf. A) Representative images of whole embryos at level of intestine stained with H&E. B) Magnifications at different level of intestine (from intestinal bulb to mid-intestine). No wMPs are detectable in intestinal lumen and no differences in the histological differentiation are appreciable. SB = Swim bladder; In = Intestine; YS = Yolk sac. Scale bars = 50 μ m.

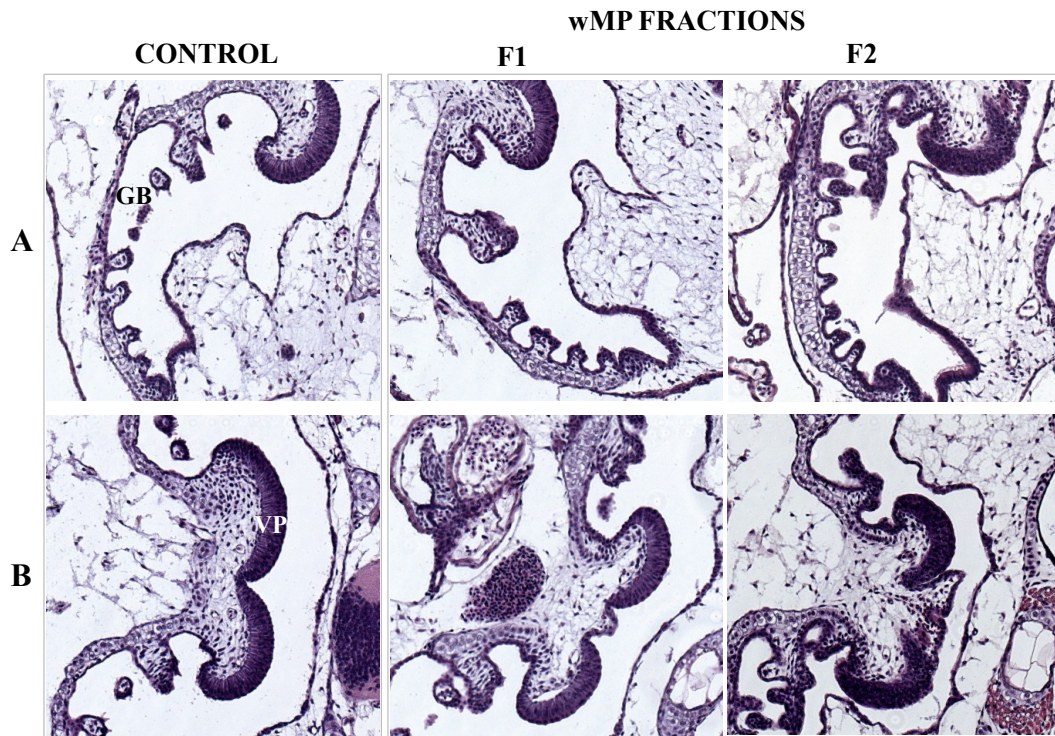


Figure S4. Histological transversal sections of stage 46 (96 hpf) *Xenopus laevis* embryos. Representative images stained with H&E at level of gill basket (GB) (line A) and velar plate (VP) (B). No wMPs are detectable in these anatomical regions. Scale bars = 100 μ m.